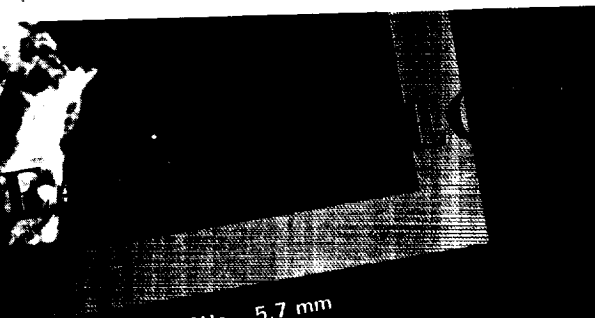


RESEARCH AND TECHNOLOGY,
GODDARD SPACE FLIGHT CENTER (NASA)
233 0

497-26324

Unclas
63/99 0093249



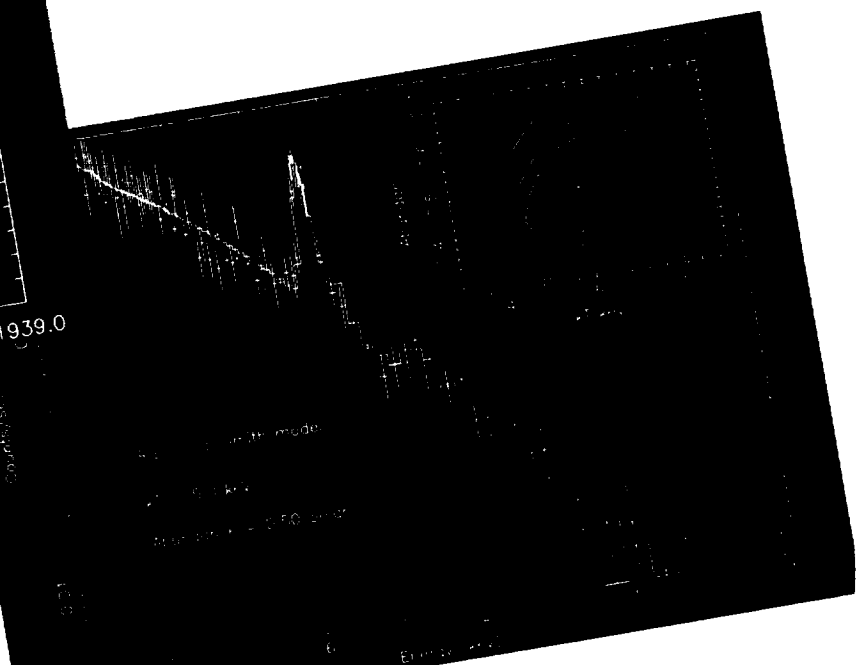
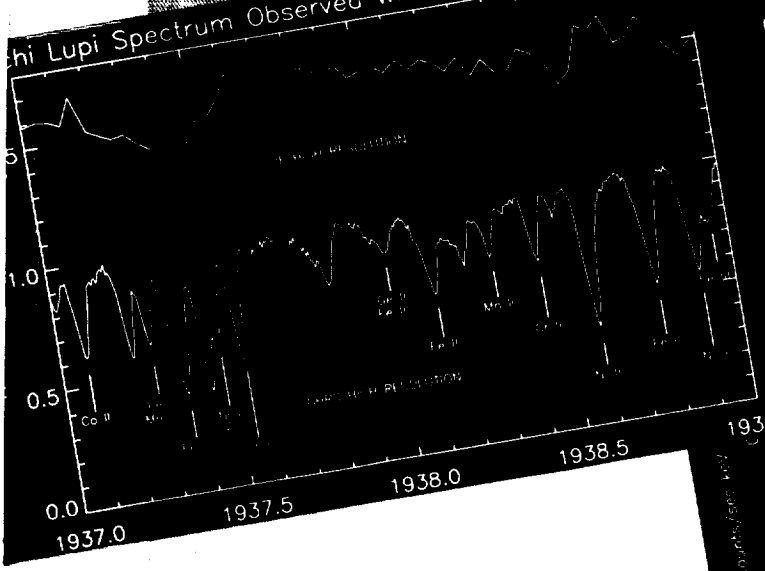
53 GHz 5.7 mm



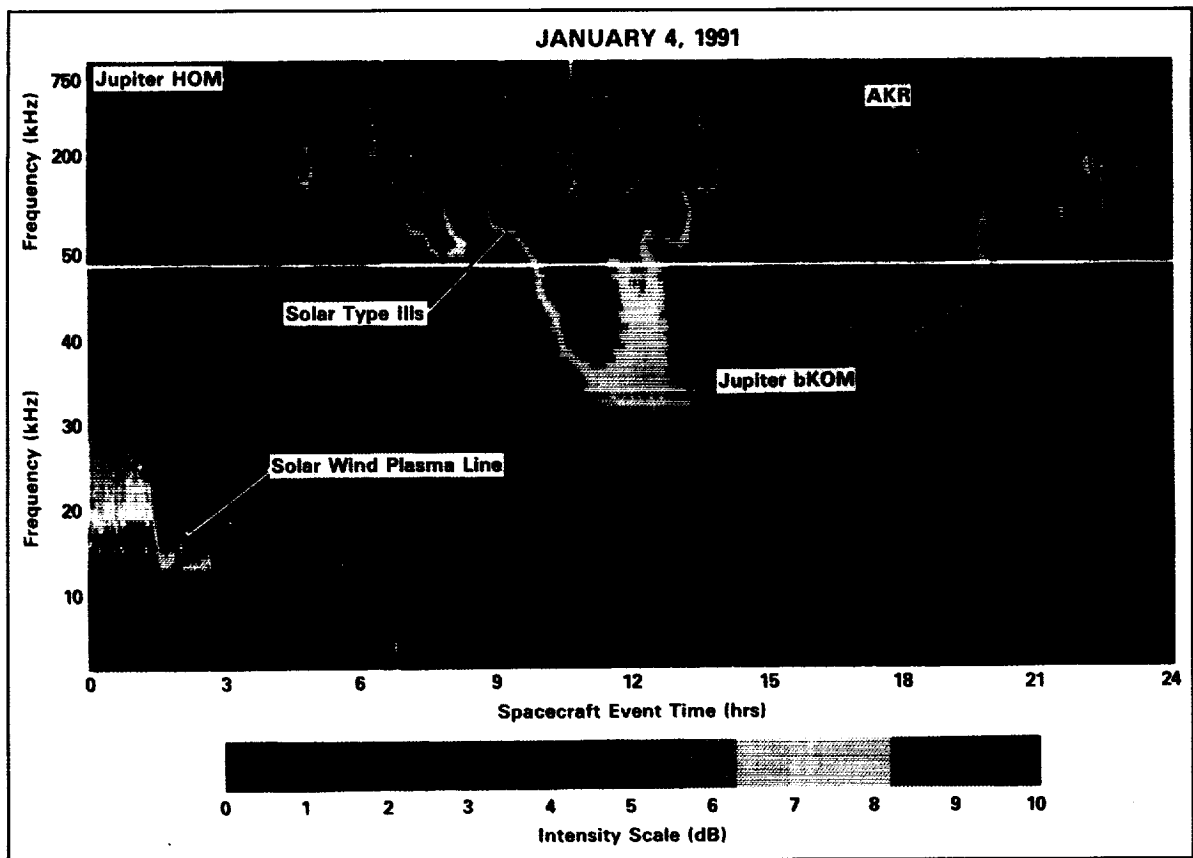
1990 Goddard Space Flight Center

-6.6 +6.6

Chi Lupi Spectrum Observed With IUE and HST/C



NASA



The Unified Plasma and Radio Wave Experiment (UPRWE) on board the Ulysses spacecraft captured the above dynamic spectrum of solar radio bursts, the solar wind, and radiations from Jupiter during Ulysses' multi-year billion mile journey to study the heliospheric plasma near and distant from the sun, within and out of the ecliptic plane. UPRWE was developed in a Goddard lead collaboration with the University of Minnesota, the Observatoire de Paris-Meudon and the Centre de Recherches en Physique de l'Environnement Terrestre et Planetaire in France.

The year 1990 was a banner year for Goddard Space Flight Center (GSFC) space-based astronomy projects (back cover). The front cover (from top to bottom) shows samples of the new science capabilities and findings which came from these projects:

The Cygnus Loop, a supernova remnant photographed by the GSFC Ultraviolet Imaging Telescope (UIT) in the light of C IV (1548Å), demonstrates the broad field of view and high spatial resolution which allowed UIT to return a wealth of data on stellar populations in galaxies and on intergalactic flow of matter within clusters of galaxies. UIT was part of the Astro-1 payload orbited on the Space Shuttle Columbia in December, 1990.

A previously undetected supernova remnant (labeled "new SNR") was discovered by the Max Planck Institute's Position-Sensitive Proportional Counter (PSPC) on the Roentgen Satellite (ROSAT). ROSAT is a German, United Kingdom and United States collaboration in x-ray astronomy; the U.S. ROSAT Science Data Center (RSDC) was developed at and is operated by GSFC.

A plot in galactic coordinates of the Cosmic Microwave Background (CMB) Radiation obtained by the University of California Differential Microwave Radiometer (DMR) on the Goddard-developed and -managed Cosmic Background Explorer (COBE) heralds the beginning of a new era in experimental cosmology. No anisotropy in the CMB is evident except for that due to COBE's own motion relative to the CMB.

A false-color composite picture of the Galactic Center in infrared light (1.2, 2.2, and 3.4 μm) illustrates the capabilities of Goddard's Diffuse Infrared Background Experiment (DIRBE). DIRBE and its companion Goddard instrument, the Far Infrared Absolute Spectrophotometer (FIRAS), are also part of the COBE science payload.

The ultraviolet spectrum of Chi Lupi, a chemically peculiar binary star, dramatically illustrates the unprecedented spectral resolution brought by the Goddard High Resolution Spectrograph (GHRS) on the Hubble Space Telescope (HST) as compared to a previous spectrum obtained with the International Ultraviolet Explorer satellite (IUE).

An x-ray spectrum (crosses) obtained with Goddard's Broad Band X-Ray Telescope (BBXRT) of iron lines from the Perseus Cluster of galaxies is compared to a theoretical model (solid line) in order to determine the abundance of iron in the emitting region. Also part of the Astro-1 mission, BBXRT with its innovative x-ray mirror technology greatly expanded our knowledge of the spectral characteristics and hence the physical conditions in cosmic x-ray sources.

RESEARCH AND TECHNOLOGY

GODDARD SPACE FLIGHT CENTER *R&T* —

Foreword

Goddard Space Flight Center celebrates 1990 as a banner year in space-based astronomy. From above the Earth's obscuring atmosphere, four major orbiting observatories examined the heavens at wavelengths that spanned the electromagnetic spectrum. In the infrared and microwave, the Cosmic Background Explorer (COBE), conceived and built at Goddard, measured the spectrum and angular distribution of the cosmic background radiation to extraordinary precision. The measurements confirm the basic Big Bang picture very well, but also may require new laws of physics or new kinds of matter to explain the development of the large-scale structure of the Universe. In the optical and ultraviolet, the Hubble Space Telescope (HST), launched in April 1990 with operations management centered at Goddard, has been returning spectacular high-resolution images and spectra of a wealth of astronomical objects. The Goddard High-Resolution Spectrograph (GHRS) has resolved dozens of ultraviolet spectral lines which are as yet unidentified because they have never before been seen in any astronomical spectrum and therefore have not been studied in laboratory settings. In x-rays, the Roentgen Satellite (ROSAT), launched in June 1990 and carrying Goddard's High-Resolution Imager (HRI), has begun returning equally spectacular images of high-energy objects within our own and other galaxies.

The year ended with the successful December flight of the Astro-1 Observatory on the Space Shuttle Columbia with two Goddard-built instruments, the Ultraviolet Imaging Telescope (UIT) and the Broad Band X-Ray Telescope (BBXRT), and one Goddard-based astronaut, Dr. Ron Parise, on board. As we go to press, 1991 promises to be equally important for Space Sciences with new discoveries likely from COBE, HST and ROSAT. The launch of Goddard's Energetic Gamma Ray Experiment Telescope (EGRET) aboard the Gamma Ray Observatory (GRO) will bring us new knowledge of gamma radiation, the most energetic process in the Universe.

In the Earth Sciences, Goddard continues preparations for Mission to Planet Earth. On the ground, Earth system science—the integrated study of air, water, vegetation and soil interactions—is being developed as the theoretical framework for understanding global change.

In the air and in orbit, instrumentation and remote-sensing techniques are being fine-tuned as a prelude to developing the Earth Observing System (EOS), with the Upper Atmosphere Research Satellite (UARS), scheduled to launch in late 1991, as its first flight project. Around the globe, data transmission networks and computer systems are being readied for handling the vast amount of information that EOS will produce.

In short, Goddard is holding firm to its mission of conducting scientific investigations from the unique vantage point of space. Looking upward to the Universe and downward to Planet Earth, we at Goddard also look forward to our continued preeminence in the Space and Earth Sciences.



John M. Klineberg



Contents



SPACE SCIENCES

The Hubble Space Telescope (HST) <i>Stephen P. Maran</i>	1
Observing The Big Bang With The Cosmic Background Explorer (COBE) <i>Nancy W. Boggess</i>	2
Antiprotons in the Cosmic Radiation <i>Robert E. Streitmatter, Jonathan F. Ormes, and Steven J. Stochaj</i>	5
X-Ray Spectroscopy and Variability Studies: A Probe of the Central Regions of Active Galaxies <i>T. Jane Turner, G. M. Madejski</i>	6
The All-Sky Extragalactic X-Ray Foreground <i>Elihu Boldt, Takamitsu Miyaji</i>	7
Fabry-Perot Images of a Distant Quasar <i>Ronald J. Oliverson, Paul M. N. Hintzen</i>	9
Outburst From an Unusual Interacting Binary Star System <i>A. G. Michalitsianos</i>	10
Particle Acceleration and Transport in Solar Flares <i>James A. Miller</i>	12
On the Contrast and Structure of Faculae <i>Kenneth H. Schatten, Hans G. Mayr</i>	13
Shocks and Twists in the Solar Wind <i>M. L. Goldstein, D. A. Roberts, and A. F. Vinas</i>	16
Chaos in the Geospace Environment <i>Daniel N. Baker, D. A. Roberts, and Alex Klimas</i>	17
Rocket Observations of Spread-F Plasma Turbulence From Kwajalein Atoll <i>Robert F. Pfaff, Jr.</i>	19
Determination of the Water Abundance on Jupiter <i>Barbara E. Carlson</i>	21
Reaction Rate Kinetics of H + GeH₄ and the Implication for Modeling Germane Photochemistry in the Atmospheres of Jupiter and Saturn <i>David F. Nava, Walter A. Payne, and Louis J. Stief</i>	22
Magnetic Fields of Uranus and Neptune <i>J. E. P. Connerney, M. H. Acuña</i>	23
What is Driving the Neptune Emission? <i>Michael D. Desch</i>	25
Source Location of Neptune's Radio Bursts: Implications for the Auroral Zone <i>William M. Farrell</i>	25

PRECEDING PAGE BLANK NOT FILMED

INTENTIONALLY BLANK

Contents

Structure and Dynamics of Neptune's Atmosphere From Voyager IRIS Measurements <i>B. J. Conrath, F. M. Flasar, and A. L. Weir</i>	26
Laboratory Simulation of Complex Chemistry in Titan's Atmosphere <i>Paul Mahaffy</i>	29
New Astronomical Images With a 5- to 14-Micron Array Camera <i>Daniel Y. Gezari</i>	30
An All-Sky Monitor for a Soviet High-Energy Astrophysics Observatory <i>Robert M. Joyce, Richard L. Kelley</i>	32
The Goddard High-Resolution Spectrograph (GHRS) <i>Sara R. Heap</i>	34
High-Resolution Magnetograph for the Southwest Solar Facility <i>Harrison Jones</i>	36
A Solar Infrared Magnetograph <i>Drake Deming, Donald E. Jennings</i>	38
Multilayer Coating on High-Density Toroidal Extreme-Ultraviolet (EUV) Grating <i>Roger J. Thomas</i>	39
Photodissociation of the OH Radical <i>Regina J. Cody, John E. Allen Jr., and Carol Moralejo</i>	41
Microgravity Nucleation Experiments on the KC-135 Reduced Gravity Research Aircraft <i>J. A. Nuth, F. Ferguson, L. Lilleleht, and J. E. Allen</i>	42

EARTH SCIENCES

Heterogeneous Reactions in the Northern Polar Vortex and Their Effect on Middle Latitude Chemistry <i>Anne R. Douglass, Richard B. Rood</i>	47
Transfer Function Model for Thermospheric Gravity Waves <i>Hans G. Mayr, Isadore Harris, and W. Dean Pesnell</i>	49
Heat Fluxes and Roll Circulations Over the Western Gulf Stream During an Intense Cold Air Outbreak <i>Shu-Hsien Chou</i>	51
Diabatic Initialization in the Goddard Laboratory for Atmospheres (GLA) Data Assimilation System <i>Michael S. Fox-Rabinovitz, Brian D. Gross</i>	53
Global-Scale Circulation Anomalies and Tropical-Extratropical Interactions <i>Siegfried Schubert, Chung-Kyu Park</i>	54
Global Backscatter Experiment (GLOBE) <i>James Spinhirne</i>	56
Remote Sensing of Aerosol and Trace Gas Emissions from Biomass Burning in Brazil <i>Brent Holben, Yoram Kaufman, and Didier Tanré</i>	57

Contents



New Doppler Lidar Methods for Atmospheric Wind Measurements—The Edge Technique <i>C. Laurence Korb, Bruce M. Gentry</i>	59
International Satellite Cloud Climatology Project (ISCCP) Cloud Climatology Complete through 4 Years <i>William B. Rossow</i>	60
Effect of Cloud Water Variations on Global Climate Model (GCM) Cloud Feedback <i>Anthony D. Del Genio</i>	62
Radiative Forcing of Climate Changes in the Vertical Distribution of Ozone <i>Andrew A. Lacis</i>	64
Lidar Measurements of Temperature and Ozone <i>Thomas J. McGee</i>	65
The Derivation of Cloud Parameters From Satellite-Measured Radiances for Use in Surface Radiation Calculations <i>Ming-Dah Chou</i>	67
Tropical Rainfall and Global Change <i>David A. Short, Otto W. Thiele, and Daniel Rosenfeld</i>	69
Monthly Oceanic Rainfall Indices From Special Sensor Microwave/Imager (SSM/I) Data <i>Alfred Chang</i>	70
The Impact of Severe Storms on Satellite Radar Altimeter Measurements <i>Chester J. Koblinsky, Edward J. Walsh, and Prabhakara Cuddapah</i>	71
Precipitation Estimates Derived from Satellite Data <i>Man-Li C. Wu</i>	73
Airborne Lidar Detection of Subsurface Oceanic Scattering Layers <i>Frank E. Hoge</i>	75
Polar Cap F Region Ion Composition—The Measurements <i>Joseph M. Grebowsky, Walter R. Hoegy</i>	76
Arctic and Antarctic Sea Ice, 1978-1987: Satellite Passive Microwave Observations and Analysis <i>Per Gloersen, Donald J. Cavalieri, Josefino C. Comiso, Claire L. Parkinson, H. Jay Zwally, and William J. Campbell</i>	77
The Botswana Water and Energy Balance Field Experiment <i>Manfred Owe</i>	80
Ocean Wind Wave Modeling <i>Hendrik L. Tolman, Dean G. Duffy</i>	82
Recent Applications of Space Geodesy <i>John J. Degnan</i>	84
Geodynamic Effects of Atmospheric Variation <i>Benjamin Fong Chao</i>	87
Active and Passive Microwave Modeling of Grasslands <i>Sasan S. Saatchi</i>	89

Contents

Subpixel Parameterization of Fractional Vegetation Distribution <i>Michael F. Jasinski</i>	90
A Model of a Vegetated Land Surface for Use in Studies of Long-Term Climate Variability <i>Randal Koster, Max Suarez</i>	93

FLIGHT PROJECTS

Gamma Ray Observatory (GRO) <i>Donald A. Kniffen</i>	95
Gamma Ray Observatory (GRO) Science Support Center <i>Donald A. Kniffen, Jay P. Norris</i>	96
High-Energy Gamma-Ray Astronomy on the Gamma Ray Observatory (GRO) and Beyond <i>Carl E. Fichtel, Stanley D. Hunter</i>	97
High-Resolution, Coordinated Solar Observations by the Orbiting Solar Laboratory (OSL) <i>Roger A. Mattson</i>	98
Pegsat—The First Pegasus Payload <i>B.R. Pincus, J.E. Pownell, and J.J. Rast</i>	100
Earth Observing System (EOS) <i>Jeff Dozier, Jeremiah J. Madden</i>	103
Version 0 of the Earth Observing System (EOS) Data and Information System (EOSDIS) <i>H.K. Ramapriyan, G.R. McConaughy, and T.D. Taylor</i>	106
Astromag <i>George Anikis</i>	107
Expendable Explorer Spacecraft (EES) <i>James E. Phenix</i>	109
The Total Ozone Mapping Spectrometer Missions (TOMS) <i>Donald L. Margolies</i>	110
Lunar Transit Telescope (LTT) <i>John J. O'Brien</i>	113
Geosynchronous Environmental Mission (GEM) <i>Harry Montgomery</i>	113
The Next-Generation Geostationary Operational Environmental Satellite (GOES-N) <i>Harry Montgomery</i>	114
The Tropical Rainfall Measuring Mission (TRMM) <i>Thomas Keating</i>	116
The Advanced Composition Explorer (ACE) Mission <i>Jonathan F. Ormes, Ed Thomas</i>	117

ENGINEERING TECHNOLOGY

Characterization of High-Temperature Superconductor (HTSC) Electrical Leads <i>Petar Arsenovic</i>	121
------------------------------------------------------------------------------------------------------------------------	-----

Contents



A Quantitative Eddy Current Imaging System for Nondestructive Evaluation <i>E. James Chern, J. Timothy Van Zant</i>122
A New, Novel Antifoaming Agent for Epoxy Material Processing <i>S. Yen Lee</i>123
Planar, Active-Element Waveguides in CdTe-Doped Borosilicate Glass for Enhancement of High-Speed Computing Performance <i>Stephen J. Pagano</i>124
Cryogenic Characterization of High-Temperature Superconducting (HTSC) Current Leads <i>Charles E. Powers, Gloria Oh</i>125
An Instrument for Spatial Conductivity Measurements of High-T_c Superconducting (HTSC) Materials <i>J. Timothy Van Zant</i>127
Determination of Fiber Volume in Graphite Epoxy Materials Using Computer Image Analysis <i>Michael J. Viens</i>129
Flight Telerobotic Servicer (FTS) Evolution <i>James F. Andary</i>130
The Goddard Energy Balance Program: Direct Energy Transfer (DET) and Modular Power Subsystem (MPS) <i>James M. Jagielski</i>132
Performance of a Prototype, 5-Year-Lifetime, Stirling Cycle Refrigerator for Space Applications <i>Max G. Gasser</i>133
“Capaciflector” Collision-Avoidance Sensors for Robots <i>John M. Vranish</i>134
Magnetostrictive Direct-Drive Motors <i>John M. Vranish</i>135
A Novel Approach to Array-Detector Timing Generation <i>Jeffrey W. Travis, Peter K. Shu</i>137
The Development of 50-Megabits per Second (Mbit/s) Transmit/Receive Electronic Components for Optical Communication Systems <i>John Maruschak, Robert Patschke, Michael Powers, and Catherine Long</i>138
Low-Frequency Electric and Magnetic Fields <i>John F. Sutton, G. Craig Spaniol</i>140
Reed-Solomon Encoder Controller Network <i>Douglas Ross</i>141
High-Compression Data Reduction Scheme for Space Applications <i>Pen-Shu Yeh, Warner H. Miller</i>142

Contents

Development of Dimensionally Stable, Fiber-Reinforced Composite Structural Elements for use in Spacecraft and Instrument Optical Support Platforms <i>Daniel F. Mark, Perry Wagner</i>143
Attitude Control System (ACS) Simulator on the MIL-STD-Bus <i>Thomas P. Flatley, Edward J. Hicks, and Thomas E. Correll</i>144
The Enhanced Capillary-Pumped Loop (CAPL) Flight Experiment <i>Dan Butler, Roy McIntosh</i>145
Instrument Thermal Test Bed (ITTb) <i>T. D. Swanson</i>146
The Effect of Molecular Diffusion on Outgassing Behavior <i>Philip T. Chen, Sharon A. Straka, and Dannelle M. Shover</i>147
Reduction of Flight-Trajectory Dispersion for Unguided Launch Vehicles Utilizing Boost-Stage Spin System <i>Bobby J. Flowers</i>148
Sounding Rocket Payload Attitude Control Referenced to an Undefined Magnetic Field Vector <i>Richard Olsen</i>149
Lightweight, Self-Contained Balloon Measurement Instrumentation <i>Michael Martone</i>150
Determination of Balloon Lift (Gas Mass) from Launch Acceleration <i>Edward Robbins</i>151
Finite Element Solution for the Structural Behavior of a Scientific Balloon <i>Willi W. Schur, Joel Simpson</i>152

DATA AND COMMUNICATIONS TECHNOLOGY

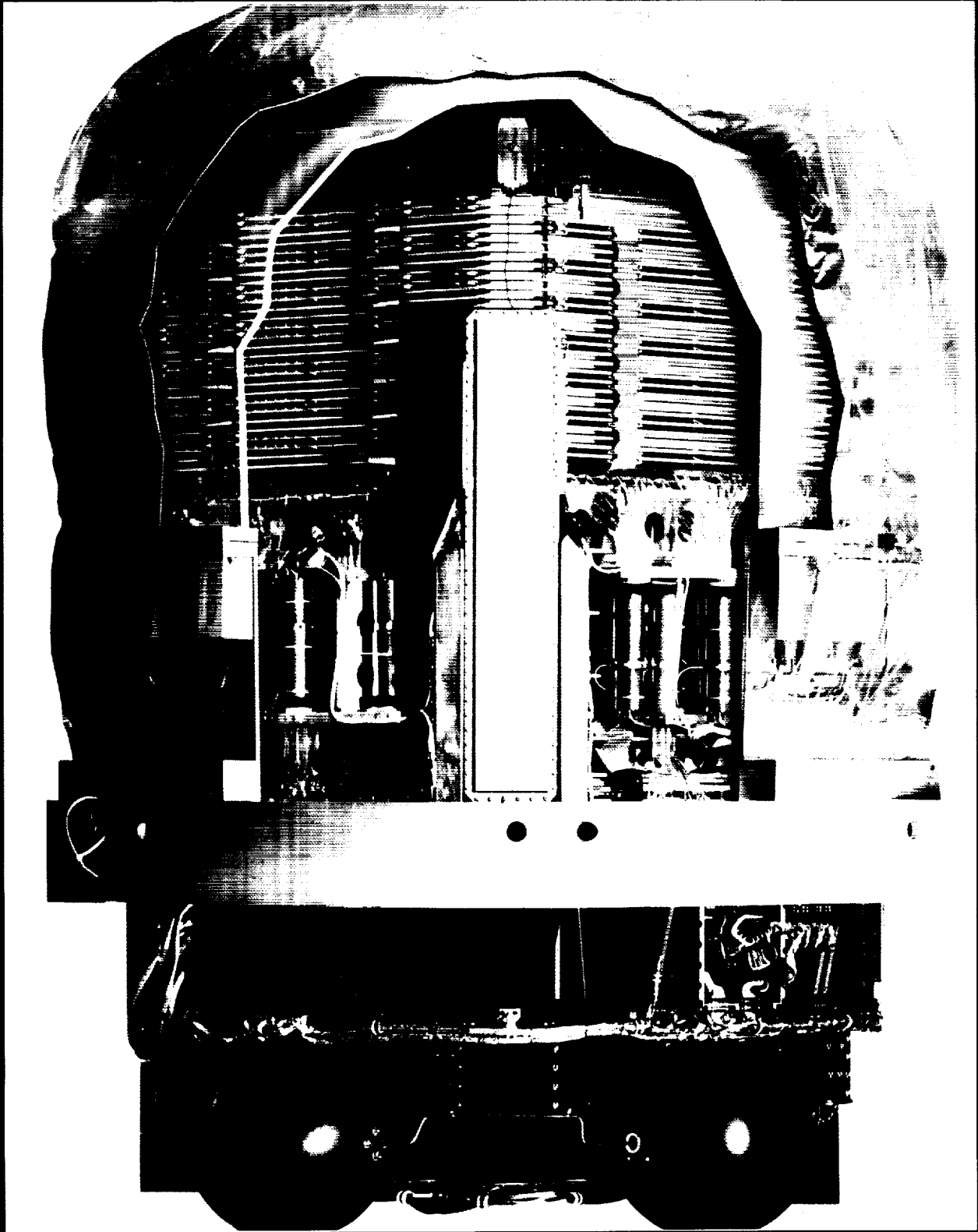
Data Distribution Media Study <i>Mary Repp, Patricia Carreon</i>157
Highly Portable, Airborne, Expendable Bathythermograph (AXBt) Data System <i>Charles W. Wright</i>159
Development of Real-Time Software Environments for NASA's Modern Telemetry Systems <i>Ward Horner, Stephen Sabia, and Stanley Hilinski</i>161
Frame Synchronization at 300 MBPS <i>Kristin Looney, Toby Bennett</i>164
High-Speed Packet Processor <i>Gerald J. Grebowski</i>167
Multifunctional Bit Generator Subsystem <i>Caleb M. Principe</i>168
High-Rate VLSI-Based Level-Zero Processing (LZP) System <i>Ward P. Horner, Jianfei Shi</i>169

Contents



Transportable Telemetry Workstation (TTW) System <i>Carol Dominy, Kevin Kay</i>173
Open System for Coordinating Automated Resources (OSCAR) <i>Robert E. Dominy</i>175
Polynomial Time Algorithm for Single-Resource Scheduling <i>Larry Hull</i>176
The TDRSS Onboard Navigation System (TONS) Simulated Flight Environment Software <i>Terri L. Wood</i>178
Satellite Communication Hardware Emulation System (SCHES) <i>Ted Kaplan, Robert Godfrey</i>179
An Interference Mitigation Methodology for Scheduling in Space Communications <i>Yen F. Wong, James L. Rash</i>185
The Generic Spacecraft and Analyst Assistant (GenSAA) <i>Peter M. Hughes</i>188
Advanced Telemetry-Processing Technology Research and Technology Operating Plan <i>James A. Pritchard</i>189
Communications Data Formatter (CDF) Enhancement <i>Lou F. Kalil</i>190
A Multiple-Access (MA) Calibrated Receiver Using Programmable Charge-Coupled Devices (CCDs) <i>Harley Mann</i>191
The Multisatellite Operations Control Center (MSOCC) Applications and Resource Scheduler (MARS) <i>Mike Bracken</i>192
The Transportable Applications Environment (TAE) <i>Martha Szczur</i>194
The Scheduling Concepts, Architecture, and Networks (SCAN) Testbed <i>Karen Thorn</i>195
Advanced Command Management System <i>Stephen G. Edwards</i>196
Combined Operational Mission Planning and Analysis System (COMPASS) <i>Ed Seidewitz</i>198
A Personal Computer-Based, Multitasking Data Acquisition System <i>Steven A. Bailey</i>199
Intelligent Tutoring Systems <i>Troy J. Ames</i>200

Space Sciences





Goddard cites its monumental and continued research in the space sciences, including astronomy, cosmology, and physics. Many successes are attributable to recent launches and their payloads—DIRBE and FIRAS on COBE, the GHRS on HST, the UIT and BBXRT on Astro-1, EGRET on GRO, and the HRS on ROSAT.

SPACE SCIENCES

THE HUBBLE SPACE TELESCOPE (HST)

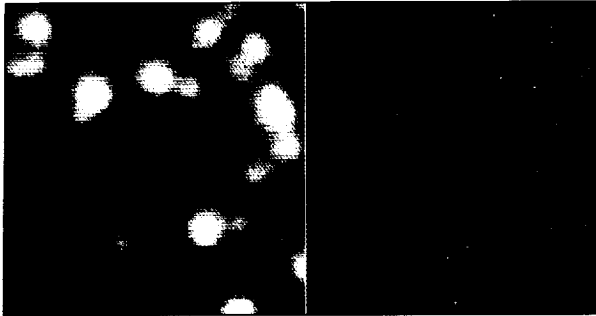
The Hubble Space Telescope (HST) was launched into near-Earth orbit by the Space Shuttle Discovery on April 24, 1990. The payload of two cameras, two spectrographs, and a high-speed photometer is supplemented by three fine-guidance sensors that can be used for astrometry as well as for star tracking. A widely reported spherical aberration in the primary mirror causes HST to produce images of much lower quality than intended. Nevertheless, the images still are fine enough to enable HST to make scientific contributions beyond those possible with any other telescope.

Computer processing, or deconvolution, to sharpen the images and to restore the spectral resolution of spectroscopic observations made with HST help make this possible. A Space Shuttle repair mission in late 1993 or 1994 will install small corrective mirrors that will restore the full intended optical capability of the HST. Meanwhile, among the many early scientific findings made with HST, studies of globular star clusters especially are revealing of its inherent advantages over telescopes on the ground.

Such a cluster is a roughly spherical aggregation of hundreds of thousands of stars, each orbiting the center of mass in its densely packed core. In a study of a region in the globular cluster Messier 14 with HST's Faint Object Camera (FOC), the HST images revealed at least six distinct stars within the tiny area occupied by the image of what appears to be a single star on telescopic photographs made from the ground. Astronomers believe that globular clusters evolve with time, as the orbiting stars exert changing gravitational pulls on one another, sometimes raising tides in one another and even colliding or merging, and sometimes ejecting stars from the cluster. According to this theory, certain clusters may have formed dense cusps (extremely dense concentrations of stars) in their centers, where a huge black hole may have formed. The prime example of such an object, according to pre-HST analyses, is the globular cluster Messier 15. Ground-based telescopic photographs of Messier 15 were consistent with the existence of a cusp, but not sharp enough to prove that it actually exists.

However, early studies of Messier 15 with the Planetary Camera mode of HST's Wide Field/Planetary Camera show that there is no such cusp and presumably, no massive black hole. Because previous work indicates that there must be much dark matter in Messier 15, the HST

◆ *The Energetic Gamma Ray Experiment Telescope (EGRET) flown on the Gamma Ray Observatory (GRO). This 4,000-pound high-sensitivity instrument records gamma rays in the energy range from 20 MeV to approximately 30 BeV.*



This pair of images of a region in the globular star cluster M-14 clearly demonstrates HST's high spatial resolution as compared to ground-based telescopes. The image on the left, taken with a ground-based telescope, has a resolution of 1.5 arc seconds. The image on the right, taken with the HST's Faint Object Camera, yields stellar diameters of 0.08 arc second. The HST image reveals literally hundreds of separate stars in a tiny region of the cluster where only dozens are distinguishable on the ground-based image.

findings suggest that it may be present as a diffuse distribution of subatomic particles of unknown type, rather than as a black hole as previously had been thought.

Among HST's payload, the Goddard High Resolution Spectrograph (GHRS), developed by Goddard's Laboratory for Astronomy and Solar Physics, stands out as the most powerful and sensitive instrument for the analysis of ultraviolet light ever launched. Ultraviolet light is blocked by the ozone layer and other components of the Earth's atmosphere and therefore must be observed from space. In studies of the peculiar star Chi Lupi, the GHRS found dozens of previously unobserved absorption lines in just a small portion of the ultraviolet spectrum, including many which cannot be identified with known atoms, because they have not been studied in the laboratory.

Further, the GHRS measurements show that a particular line in the spectrum of Chi Lupi may be produced predominantly by atoms of a single isotope of the element mercury, although six mercury isotopes are thought to be present in the stars. Such observations enable astronomers to investigate the detailed structure of stellar atmospheres including physical conditions of temperature, density, chemical composition, turbulence, and gas streaming. For example, GHRS observations of the massive star Melnick 42, located about 170,000 light-years from Earth, indicate that it is shedding gas at an enormous rate, losing an amount of mass equal to that of our Sun in a time span of

just 100,000 years. GHRS observations of the red giant star Aldebaran, in the constellation Taurus, show that the chromosphere (color sphere) layer of the red star roils with turbulence, with flow conditions changing from one altitude to another, in cosmic exaggeration of what an airline pilot might term "wind shear."

In other findings, HST was used to monitor the development of the Great White Spot, a huge storm that appeared on Saturn in the fall of 1990, to spatially resolve the debris ejected in the explosion of Supernova 1987A, to make an accurate measurement of the distance to the Large Magellanic Cloud, and to study material ejected in high-speed jets from the central cores of active galaxies.

Contact: Stephen P. Maran (Code 680)
(301) 286-8607

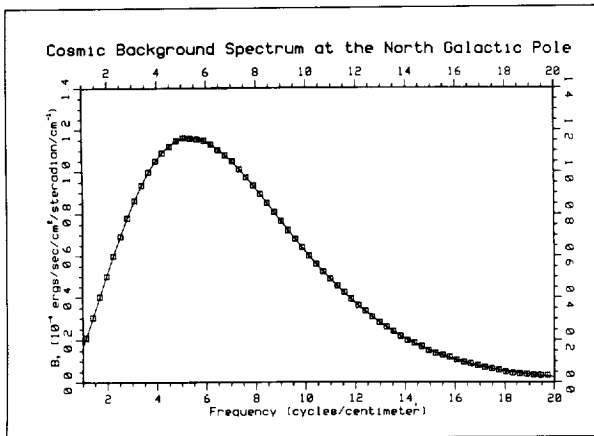
Sponsor: Hubble Space Telescope Project

Dr. Stephen P. Maran is a senior scientist in the Laboratory for Astronomy and Solar Physics with 22 years of service at Goddard. He earned a BS in physics at Brooklyn College and an MA and a PhD in astronomy from the University of Michigan. He received the NASA Medal for Exceptional Achievement for his contributions to the HST project. Dr. Maran's research interests include stars, nebulae, and galaxies.

OBSERVING THE BIG BANG WITH THE COSMIC BACKGROUND EXPLORER (COBE)

Ever since the discovery in 1964 of the cosmic microwave background, interpreted as relic radiation from the Big Bang, scientists have tried to make accurate measurements of its spectrum and anisotropies. With the launch of the Cosmic Background Explorer (COBE) in late-November 1989, major advances in our understanding of the very early universe have been achieved.

COBE—managed, developed, and operated by Goddard—was designed specifically to achieve major improvements in our knowledge of cosmological facts. It carries a complement of scientific instruments covering a significant wavelength range and operating in a well-controlled thermal environment. Essential to meeting the scientific objectives are an all-sky observing strategy, periodic absolute calibrations of the instruments, high sensitivity, and extensive care in the experimental design to minimize potential systematic errors.

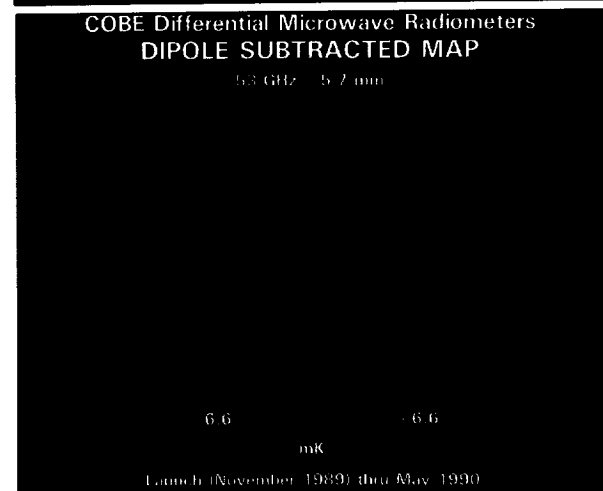
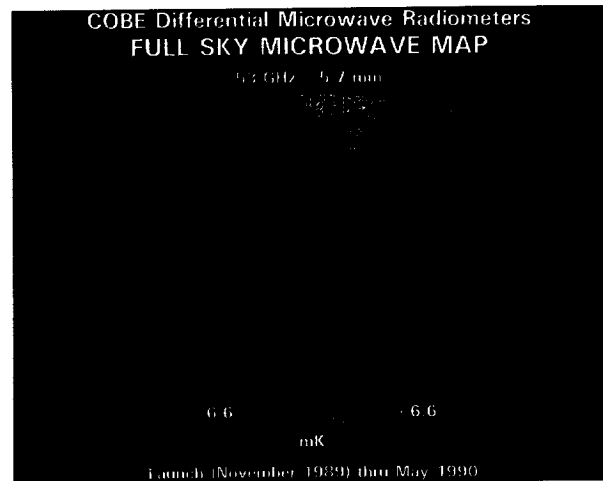


The spectrum of the cosmic microwave background, obtained by the Far Infrared Absolute Spectrophotometer (FIRAS) on COBE, from only 9 minutes of data. The data were taken in a region near the north galactic pole of our galaxy, where emission from dust is known to be low. This spectrum confirms the prediction of the Big Bang model to remarkable precision. It shows that there are no deviations from a blackbody spectrum, shown by the solid curve, greater than 1 percent of the peak intensity of the cosmic microwave background.

COBE carries three scientific instruments to achieve its objectives. They are the Far Infrared Absolute Spectrophotometer (FIRAS), the Differential Microwave Radiometer (DMR), and the Diffuse Infrared Background Experiment (DIRBE). Both the FIRAS and DIRBE are located inside a liquid-helium cryostat which kept them operating at 1.5 K while the helium lasted. The DMR receivers are located around the outside of the cryostat.

The objective of the FIRAS is to measure the spectrum of the cosmic microwave background over the wavelength range 0.1 to 10 mm with an accuracy of 0.1 percent of the peak brightness. This instrument, a Michelson interferometer, has a spectral resolution of 0.2 cm^{-1} (or 6 GHz) and an angular resolution of 7 degrees. It was designed specifically to measure small deviations in the shape of the cosmic microwave background spectrum from that of a blackbody.

The DMRs were designed to search for spatial anisotropies with a sensitivity of 0.15 mK at frequencies of 53 and 90 GHz, and 0.3 mK at 31 GHz, per 7-degree pixel on the sky. There are two independent channels at each frequency. These frequencies were selected to allow separation of the cosmic microwave background radiation from galactic synchrotron emission, free-free emission, and emission by interstellar dust in the analysis of the data.



All-sky maps at 53 GHz, one of three microwave frequencies of the Differential Microwave Radiometer (DMR) instruments aboard COBE. The maps are shown in galactic coordinates, with the plane of the Milky Way horizontally across the middle and the Galactic Center in the center. The top panel shows a smooth variation between hot areas (shown in pink, upper right) and cold (shown in light blue, lower left). This variation, only 0.2 percent from pink to light blue, is believed to be due to the motion of the Solar System relative to the distant matter in the universe. The lower panel shows the sky with the motion of the Solar System removed. The galactic emission features, seen horizontally across the middle, are only one thousandth the brightness of the sky at 53 GHz. This map shows very strictly that there are no anisotropies, or "lumpiness," in the early universe larger than one part in 25,000.

The DIRBE was designed to make a sensitive search for the cosmic infrared background, resulting from the cumulative emissions of luminous objects formed after the universe cooled sufficiently to permit the first galaxies



All-sky images of the infrared sky, taken with the Diffuse Infrared Background Explorer (DIRBE) instrument aboard COBE. The maps are shown in galactic coordinates, with the plane of the Milky Way horizontally across the middle and the Galactic Center in the center. The top panel combines data from the far infrared wavelengths of 25, 60, and 100 μm shown in blue, green, and red, respectively. The dominant features in the sky are radiation from cold dust located in vast clouds of dust and gas between the stars in our galaxy. Artifacts in the image arise from combining data obtained at different times of the year, and will be removed from the data with further processing. The lower panel combines data at the near-infrared wavelengths of 1.2, 2.2, and 3.4 μm . The image shows the distribution of the stellar population of our galaxy, with the thin disk and the bulge near the Galactic Center in our galaxy.

and stars to form. The DIRBE objectives are to discern and measure the spectrum and angular distribution of this diffuse infrared background radiation to a sensitivity of 10^{-13} W/(cm² sr), or 1 percent of the total background, whichever is greater, in 10 photometric bands from 1 to 300 μm . The instrument has a field of view of 0.7 degree. DIRBE also measures linear polarization from 1 to 3 μm in wavelength to help distinguish the sunlight that is scattered from interplanetary dust.

COBE was launched into a 99-degree-inclination, 900-km-altitude circular orbit with a 6 p.m. ascending node. With this orientation, the spin axis of the satellite always is pointed away from the Earth and about 94 degrees away from the Sun. The orbital

period is approximately 103 minutes. The satellite rotates at 0.8 rpm. This rotation helps reduce potential systematic errors in the DMR and provides DIRBE a range of solar elongation angles from which to view scattering and emission from interplanetary dust.

The cryostat cover was ejected 3 days after the COBE launch, and all three instruments began obtaining sky data. During the first month in orbit, various spacecraft maneuvers were undertaken to test the performance of the instruments and spacecraft and to optimize instrument parameters. During this entire period, the instruments were obtaining high-quality data. All three instruments had completed their full-sky coverage by mid-June 1990, and continued with a second survey.

On September 21, 1990, the liquid helium was depleted, ending more than 10 months of operation for FIRAS and DIRBE at < 2 K. After helium depletion, the FIRAS was turned off, since this instrument requires liquid-helium temperatures. The DMR, located outside the cryostat, continues to operate normally in all of its six channels. From examination of the quick-look data, it appears the four short-wavelength bands have been turned off because of the elevated temperatures. Continued data collection by these two instruments is expected to be important in further understanding any systematic errors and for complete closure on the sky as the Earth completes its annual cycle around the Sun.

COBE has obtained several of the major cosmological results of this century within its first year of operation. Results from the FIRAS have confirmed the Big Bang model's prediction that the cosmic microwave background would have a thermal spectrum. The temperature of the universe was found to be $2.735 \pm .06$ K. The DMR experiment has obtained the most precise maps of the cosmic microwave background ever made and has established that any anisotropy in the cosmic microwave background brightness on angular scales greater than 7 degrees must be $< 4 \times 10^{-5}$, a result with significant implications for large-scale structure and geometry of the universe. COBE also has obtained with DIRBE the most extensive infrared absolute sky brightness measurements and maps ever made, providing spectacular new views of the Milky Way and permitting the first serious search for cumulative light from the first objects in the universe. Even more dramatic results are expected as the collection and analysis of space data proceed.



The operational demands for DIRBE and the DMR are expected to be minimal now that the liquid helium has been depleted, and the additional data acquired until December 1991 are not expected to affect seriously the analysis effort for the data acquired during the first 10 months. With the bulk of the raw data in hand, the main emphasis for the science team has shifted toward data processing and analysis.

The software now must be completed and tested before reliable sky maps can be made. Proper characterization, analysis, and removal of systematic error sources must be done using flight data. The amount of work is somewhat instrument-independent, but is expected to take several years. A detailed understanding of the systematic errors in the three instruments is crucial to the ultimate usefulness of the COBE data sets for cosmology, galactic astronomy, and Solar System science.

The work on COBE described in this article resulted from collaborative efforts of the COBE Science Working Group (SWG). COBE is a NASA/Goddard mission. NASA was responsible for the design, development, and operation of the COBE, under the guidance of the COBE SWG. Goddard also is responsible for the entire software development for final processing of the space data.

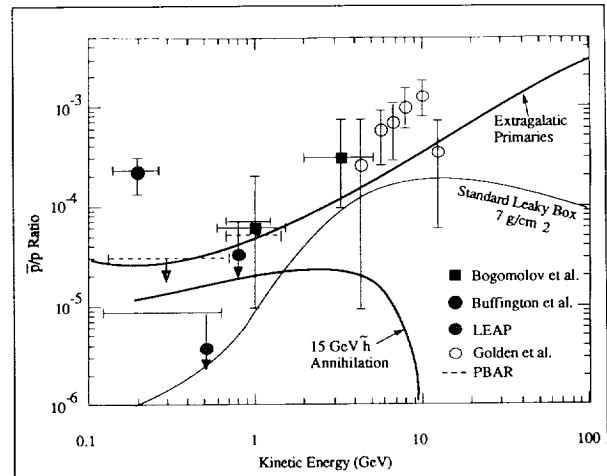
Contact: Nancy W. Boggess (Code 685)
(301) 286-6989

Sponsor: Office of Space Science and Applications

Dr. Nancy W. Boggess is an astrophysicist in the Infrared Astrophysics Branch of the Laboratory for Astronomy and Solar Physics. She is a member of the COBE SWG and is Deputy Project Scientist for Science Operations. She received a PhD in astrophysics from the University of Michigan. Dr. Boggess has nearly 4 years of service at Goddard.

ANTIPROTONS IN THE COSMIC RADIATION

Ever since postulation of antimatter existence by Dirac in 1928 and the subsequent discovery of positrons by Anderson in 1933, the question of the antimatter content of the cosmic radiation has been of interest. In particular, one expects a small fraction of antiprotons—about one in 10,000 protons—in the cosmic



The antiproton/proton ratio in the cosmic radiation versus energy. All existing positive reports are shown, as well as theoretical models.

radiation since collisions of high-energy cosmic rays with the interstellar medium will produce antiproton-proton pairs in strong interactions. The first positive measurement of antiprotons in the cosmic radiation was reported by Robert Golden in 1979. The surprising result was that the ratio of antiprotons to protons in the 5- to 12-GeV energy range was about a factor of four higher than one would expect from calculations based on known proton spectra, antiproton production cross sections, and the Standard Leaky Box cosmic ray propagation model. Far more surprising was the report of Buffington in 1981, who made a measurement of antiprotons in the few-hundred-MeV energy range. Because the probability for collision-production of antiprotons in this energy range is very small (kinetically limited), one expected antiproton/proton ratios in the range of 10^{-6} . Buffington reported a ratio several orders of magnitude higher, around 2×10^{-4} . In the next few years, various suggestions were put forward to explain the excess of antiprotons at low energy. These theories included the evaporation of primordial black holes, the annihilation of supersymmetric particles, and the existence of antimatter galaxies whose antimatter cosmic rays escape to reach us.

In 1985, scientists of the High-Energy Cosmic Ray group at Goddard entered into a collaboration, the purpose of which was to make a definitive measurement of antiprotons in low-energy, few-hundred-MeV cosmic rays. To accomplish this, they designed and carried out the Low-Energy Antiproton experiment (LEAP). The

LEAP instrument was a balloon-borne mass spectrometer using a superconducting magnet, time-of-flight system, and Cherenkov detector. In summer 1987, it was flown from Prince Albert, Canada, and spent 22 hours at a float altitude of 119,000 feet.

Analysis of the data in the energy range from 120 MeV to 640 MeV (top of the atmosphere) has been completed. After all cuts, 322,281 protons and one antiproton were found. Following small corrections for atmospheric production of protons, losses in the instrument, etc., the measured antiproton/proton ratio is 4.2×10^{-6} . This is shown in the figure, along with all other existing measurements of antiprotons in the cosmic radiation and curves showing expectation from several models.

The LEAP result is more than a factor of 50 below the report of Buffington, and places strong constraints on models suggested to explain the previously assumed excess of low-energy antiprotons. Primordial black holes are no longer needed to explain the low-energy antiproton results. Rather, the low-energy cosmic ray antiproton measurement may be used to set limits on the density of primordial black holes in the galaxy. Calculation of such limits is constrained by the ability to deconvolve solar modulation of low-energy particle fluxes.

Should extragalactic antiprotons exist and reach our galaxy, one knows what their spectral slope should be (they presumably would be produced by processes similar to our own cosmic rays), but one would not know their absolute intensity. As may be seen from the figure, the spectrum of hypothetical extragalactic antiprotons can be normalized so as to explain the excess of antiprotons measured by Golden in the 5- to 12-GeV range or to fit the low-energy LEAP result. It cannot fit both simultaneously. The conclusion is that the excess antiprotons in the 5- to 12-GeV range cannot be extragalactic.

Expectation from the Standard Leaky Box model is not in serious conflict with the new LEAP measurement.

The expected antiproton flux which would be seen by the LEAP experiment due to production of antiprotons in the atmosphere by incident primary cosmic rays has been calculated. The expectation from this mechanism is 0.6 antiproton, whereas one was seen. Since atmospherically produced antiprotons are indistinguishable from interstellar antiprotons, this suggests that balloon-borne experiments cannot be used to measure the antiproton/proton ratio to much lower limits. Substantial improvements must be

done from satellites, which are not subject to an atmospheric overburden.

Contact: Robert E. Streitmatter (Code 661)
(301) 286-5481

Jonathan F. Ormes (Code 661)
(301) 286-5705

Steven J. Stochaj
Particle Astrophysics Laboratory
New Mexico State University
(505) 646-1556

Additional collaborators in this work were: Robert Golden, Ted Bowen, Louis Barbier, Jeremy Lloyd-Evans, and S. Alfred Stephens.

Sponsor: Office of Space Science and Applications

Dr. Robert E. Streitmatter, an astrophysicist, received his PhD from the University of Chicago. He is the leader of the High-Energy Cosmic Ray group at Goddard and is interested in the experimental measurement of cosmic-ray spectra as well as theoretical work on cosmic-ray origins. He has been at Goddard for 10 years.

Dr. Jonathan F. Ormes is Chief of the Laboratory for High-Energy Astrophysics. He currently is Project Scientist for Astromag and Principal Investigator for the Large Isotope Spectrometer for Astromag. Dr. Ormes received the NASA Exceptional Service Medal in 1986.

Dr. Steven J. Stochaj received his PhD from the University of Maryland for his work on all phases of the LEAP experiment, from experiment design to data analysis. He has accepted a post-doctoral appointment at New Mexico State University.

X-RAY SPECTROSCOPY AND VARIABILITY STUDIES: A PROBE OF THE CENTRAL REGIONS OF ACTIVE GALAXIES

The nature of active galactic nuclei (AGN) has inspired tremendous interest since the discovery of the first of these objects some 40 years ago. The primary question always has been: what is the source of the tremendous energy output? Despite many decades of research, and many advances in understanding various parts of the puzzle, this most basic question remains unanswered. It is, however, generally agreed that the primary source of power for AGN is conversion of gravitational energy into



electromagnetic radiation, from matter falling onto a compact, massive object. Theory predicts that the flow, or accretion, of the surrounding matter should occur via a disk, to conserve the rotational momentum. However, the very small implied angular scales involved do not allow direct measurement of the physical structure. Thus, it is necessary to employ indirect methods. Recent intensive monitoring of the Seyfert galaxy NGC 5548 showed that one can map the outer regions of the active nucleus (scales of approximately 10^{16} cm) using variability of optical emission lines as compared to the ultraviolet ionizing continuum. For the study of the structure of the innermost regions, where the energy conversion takes place and most energetic radiation is produced, X-ray variability studies offer the best promise.

Recently, Goddard scientists in collaboration with co-workers at Nagoya University in Japan have been able to shed some light on the nature of the accretion disks around AGN. They observed the X-ray emitting Seyfert I galaxy NGC 6814 with the Japanese satellite Ginga during April 1989. This relatively nearby (about 30 kiloparsecs), low luminosity (about 5×10^{43} ergs/s) AGN was known to vary rapidly in X-rays, but the previous observations obtained with Goddard's group experiment on the High Energy Astronomy Observatory (HEAO-1) satellite in 1978 lacked the signal-to-noise ratio to allow detailed studies. During the Ginga observation, the X-ray flux changed by a factor of more than five, with the shortest observed doubling time scale of approximately 50 seconds. That clearly indicates that the dimension of the X-ray emitting source cannot be much larger than about 50 light-seconds (approximately 1.5×10^{12} cm) or sharp features observed in the time series would be washed out. Since theoretical arguments suggest that the continuum emission cannot arise from closer than five gravitational radii, the mass of the central source is less than a few million solar masses.

The ability of Ginga to perform moderate-resolution X-ray spectroscopy allowed detailed study of the 6.4-keV emission line, which is due to fluorescence from cold—or partly ionized—iron (ionization states below iron XXVII). Such iron fluorescence lines are a common feature of the X-ray spectra of Seyfert I galaxies; their presence implies that cold gas, expected to be the main constituent of an accretion disk, has a large covering fraction around the central source. Perhaps the most important discovery, however, is that the iron line flux also is highly variable on time scales of a few hundred

seconds and is positively correlated with the continuum flux on this timescale. Cross-correlation techniques limit the possible lag behind the continuum emission to < 250 seconds. Thus, the iron reprocessing region must be very close to the source of the X-ray emission, probably the central engine of NGC 6814.

By light travel-time arguments, an upper limit to the extent of that region can be established as approximately 10^{13} cm. In addition, the limits that can be put on the intrinsic width of the iron line confirm the estimate of the mass of the central source as derived from the continuum variability arguments.

The X-ray studies of NGC 6814 with the Ginga satellite clearly increased our knowledge of Seyfert galaxies, but a complete understanding of these enigmatic sources will have to await better resolution X-ray spectroscopy, so the detailed structure of the iron line can be studied.

Contact: T. Jane Turner (Code 666)
(301) 286-5190

G. M. Madejski (Code 666)
(301) 286-8099

Sponsor: Laboratory for High-Energy Astrophysics

Dr. T. Jane Turner has nearly 3 years of service with the Universities Space Research Association in the Goddard Laboratory for High-Energy Astrophysics. She earned a BS in mathematics and a PhD in X-ray astronomy from the University of Leicester in England.

Dr. G. M. Madejski has been a research scientist for Universities Space Research Association in the Laboratory for High-Energy Astrophysics since 1986. He holds a BS in physics from the Massachusetts Institute of Technology and a PhD in astronomy from Harvard University. His research focuses on the astrophysics of AGN, with emphasis on BL-Lac objects. Dr. Madejski currently is involved in the development of the X-Ray Spectrometer, a novel, low-temperature device scheduled to fly on Advanced X-Ray Astrophysics Facility (AXAF).

THE ALL-SKY EXTRAGALACTIC X-RAY FOREGROUND

Recent analysis of archival data from the High-Energy Astronomy Observatory (HEAO-1) mission gives strong indications that the general distribution of all the

underlying mass (dark as well as visible) in the nearby universe may be well traced by the X-radiation observed from active galactic nuclei (AGN). These data from the HEAO-1 mission remain unique in that they constitute the only available set providing coverage of the entire sky over a broad band of X-ray energies. This has enabled us to make a successful first-cut at using X-radiation to trace out the anisotropic distribution of all the gravitational matter pulling the Local Group of galaxies (LG) into its peculiar state of motion.

Although there seem to be structures in the universe on scales up to about one-tenth of the event horizon, a basic tenet of modern cosmology is that the universe on larger scales is isotropic and homogeneous. Under the assumption that the cosmic X-ray background is dominated by X rays emitted at high redshifts, the only global anisotropy that would be expected is the weak dipole variation of apparent surface brightness arising from the Solar System's motion with respect to the proper frame of this radiation (an effect first discussed within the context of cosmic rays by Compton and Getting in 1935). The global anisotropy of the X-ray foreground, however, involves additional considerations. In particular, the coherent 600-km/s velocity of the LG with respect to the proper frame of the microwave background is at least an order of magnitude larger than the individual velocities of recession for constituent galaxies expected from the general Hubble expansion of the universe. This indicates an appreciable gravitational acceleration from a highly anisotropic mass distribution outside the LG. To the extent that radiation traces matter, the associated X-ray foreground should exhibit a corresponding anisotropy as well.

Observations of galaxies in the infrared and optical wavelengths suggest that the 600-km/s peculiar velocity of the LG arises mainly from a foreground of anisotropically distributed mass within a look-back, light-travel time of about 300 million years (relatively small compared to the age of the universe). Since the X-ray luminosity of bright, extragalactic X-ray sources provides a good mass measure of the radiating objects involved and can be observed relatively free of galactic obscuration effects, such sources are likely candidates for serving as reliable tracers of the total underlying mass responsible for the acceleration of the LG. In this connection, we note that the local gravitational dipole implied by the 50 X-ray bright clusters of galaxies at redshifts (z) greater than 0.013 is relatively small compared with that inferred from the only three bright clusters at lower redshifts. The local

space density of AGN is about two orders of magnitude greater than rich clusters, however, such compact sources have the potential of providing a vastly improved statistical sample for tracing mass in the low-redshift region of particular interest. Furthermore, recent dipole analysis of the X-ray flux from bright AGN observed with HEAO-1 indicates that they are indeed strong tracers of this matter. The implications of this for the very pronounced large-scale foreground anisotropies to be measured via low-redshift AGN resolved in more sensitive all-sky surveys are of considerable interest for future observations. In particular, an all-sky, broad-band, X-ray survey (2 to 10 keV) at the point-source sensitivity level of the HEAO-2 Einstein Observatory would be suitable for obtaining a statistically well-defined picture of how the putative, supermassive black holes associated with X-radiating AGN trace the underlying mass distribution responsible for the peculiar velocity of the LG.

For the total extragalactic X-ray sky (including the relatively large cosmic X-ray background as well as the contribution of resolved sources) the dipole moment is small compared to the monopole. Because of the large, peculiar velocity of the LG, however, it is found that the value for this total dipole moment, currently estimated from HEAO-1 data, already can be used to set remarkably severe constraints on the volume emissivity arising from all X-ray sources within the present epoch. This provides highly restrictive limits on the possible cosmic X-ray background contributions of source populations such as faint radio galaxies and low-luminosity AGN. In particular, without evolution, all source populations other than the known class of luminous X-radiating AGN can make no more than a 20-percent contribution to the cosmic X-ray background (2 to 10 keV).

Contact: Elihu Boldt (Code 666)
(301) 286-5853

Takamitsu Miyaji (Code 666)
(301) 286-5853

Sponsor: HEAO Data Analysis Program

Dr. Elihu Boldt is Head of the X-ray Astrophysics Branch of the Laboratory for High-Energy Astrophysics and is Principal Investigator of the Goddard HEAO-1 experiment.



Mr. Takamitsu Miyaji is a University of Maryland graduate student who is a Goddard research assistant under a joint program between the Laboratory for High-Energy Astrophysics and the Astronomy Program of the university.

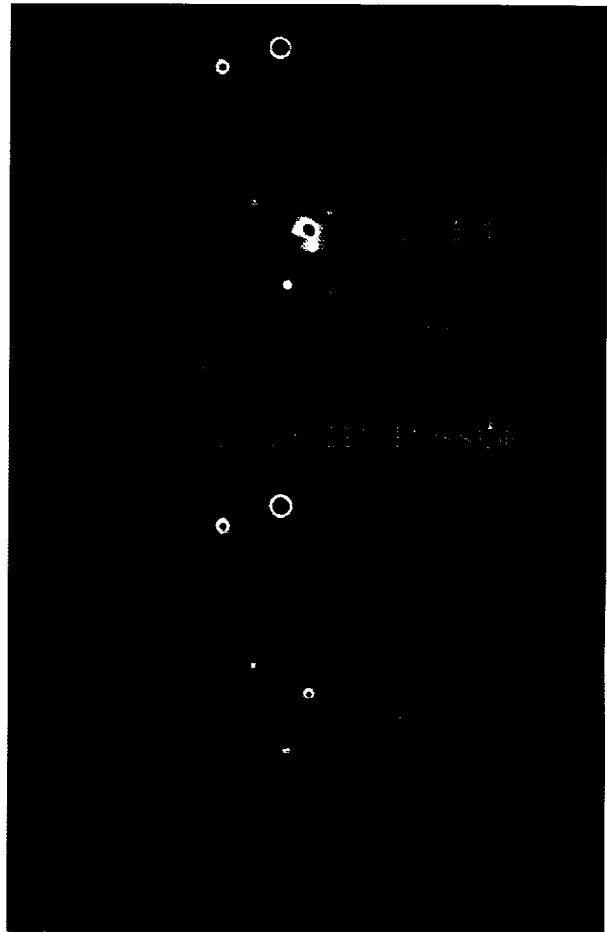
FABRY-PEROT IMAGES OF A DISTANT QUASAR

Astronomers have used a variety of instruments to produce images of extragalactic objects such as other galaxies, quasars, and clusters of galaxies, from X-ray to visible to radio wavelengths. These images allow astronomers to study the morphologies, dynamics, and kinematics of extragalactic objects. One important aspect of determining the nature of extragalactic objects comes from studying the interstellar and intergalactic gases via their emission lines. These distinctive emission lines are used to identify the components within the gases, their ionic states, and their velocities. From the emission lines we can deduce the physical conditions within the gas, including the gas temperature and density, the energy required to heat or accelerate the gas, and the mechanism which supplied the energy (e.g., a supernova).

To study the emission lines from extragalactic objects, we at the Laboratory for Astronomy and Solar Physics built a Fabry-Perot Imager. The main advantage of our Fabry-Perot Imager is its ability to tune to any visible wavelength and, using the Fabry-Perot's narrow passband, to isolate the emission line from the adjacent continuum. This is particularly important for extragalactic objects, since one property of the expanding universe is that the more distant a galaxy, the faster that galaxy is moving away from us. This expansion has the effect of shifting an emission line to longer wavelengths, otherwise referred to as a redshift. The image is recorded on a solid-state detector called a charge-coupled device (CCD), which is about 50 times more sensitive than photographic film.

One very interesting extragalactic object we have investigated with the Fabry-Perot Imager at the Kitt Peak National Observatory 4-meter telescope is the very distant quasar 3C 275.1, which is about 7 billion light-years from Earth. Thus, we now are looking at conditions as they existed 7 billion years ago, more than one-third of the way back to the explosion that began the universe. Earlier observations of 3C 275.1 had demonstrated that the quasar lies at the center of an

extremely rich cluster of galaxies. The quasar and associated galaxies are moving away from us at approximately 42 percent of the speed of light, or 78,000 miles per second. An important emission line for studying quasars and other active luminous galaxies is produced by singly ionized oxygen gas. This emission line, normally found in the far violet part of the visible spectrum, is shifted into the yellow region for 3C 275.1 due to the quasar's high recessional velocity. Shown in the figure are maps of 3C 275.1 and associated galaxies in the light of the singly ionized oxygen and the adjacent continuum. There are several striking differences with viewing this



Images of the quasar 3C 275.1 and associated galaxies taken in the light of singly ionized oxygen emission (a) and adjacent continuum (b). The labeled objects show strong oxygen emission (i.e., they are brighter in panel "a" than in panel "b," or in the case of 3C 275.1, they exhibit a halo of bright gas). The images are approximately 100 arc seconds on a side.

cluster in the light of singly ionized oxygen compared to the continuum. These include:

- three emission-line galaxies (denoted by A, B, and C) in the cluster,
- a bright galaxy (labeled G) just south of the quasar, and
- a large, extended gas cloud surrounding the quasar.

The cloud surrounding the quasar is apparently intracluster gas accreting onto the quasar at the cluster center. This accreting gas almost certainly fuels the nuclear engine—a black hole?—which provides the quasar's power. On the other hand, the gas emission lines detected in several galaxies in the cluster indicate massive, large-scale star formation. A comparison of these star formation rates with those in clusters of galaxies near our Milky Way will allow us to study the evolution of galaxies and their constituents over the last 5 to 10 billion years.

Contact: Ronald J. Oliverson (Code 684)
(301) 286-6290

Paul M. N. Hintzen (Code 681)
(301) 286-8549

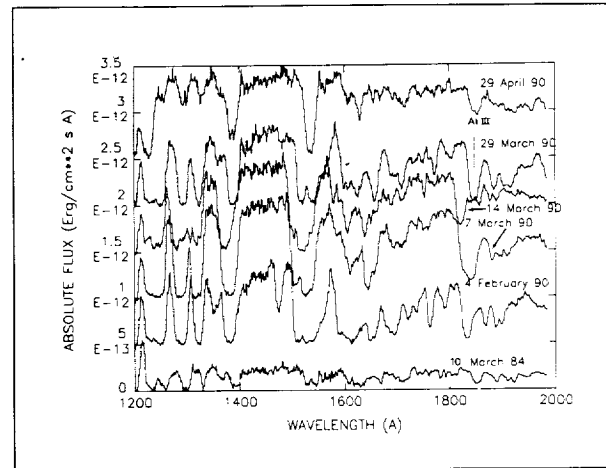
Sponsor: Office of Space Science and Applications

Dr. Ronald J. Oliverson works in the Science Operations Branch of the Laboratory for Astronomy and Solar Physics. His research interests during his 5 years at Goddard have included optical and ultraviolet instrumentation and diffuse emission nebulae. Dr. Oliverson earned a PhD in physics from the University of Wisconsin.

Dr. Paul M. N. Hintzen has 12 years of service at Goddard. An astronomer in the Astronomy Branch of the Laboratory for Astronomy and Solar Physics, his interests include the evolution and age of galaxies and the late stages of stellar evolution. He holds a PhD in astronomy from the University of Arizona.

OUTBURST FROM AN UNUSUAL INTERACTING BINARY STAR SYSTEM

The physical conditions of a binary star system immediately preceding a catastrophic outburst have been observed for the first time in the far-ultraviolet with the International Ultraviolet Explorer (IUE). Nearly 40 percent of stars in our galaxy are members of binary star systems,



Ultraviolet spectra obtained of MWC 560 with IUE in 1984 and in 1990 when the entire spectrum appeared to exhibit large velocity displacements. The deep absorption features throughout the spectra are caused by blends of thousands of singly ionized metals such as iron, silicon, and chromium.

in which two stars orbit each other with periods of revolution that can be as short as a few hours or as long as many years. If the distance that separates binary stars is sufficiently small, the gravitational force acting between the stars can be so large that material from one star can be drawn onto the surface of its companion, a process known as accretion. Material transferred in this manner is believed to provide the basis for a variety of energetic processes in interacting binary systems. The accretion process is relevant particularly to the nova phenomenon.

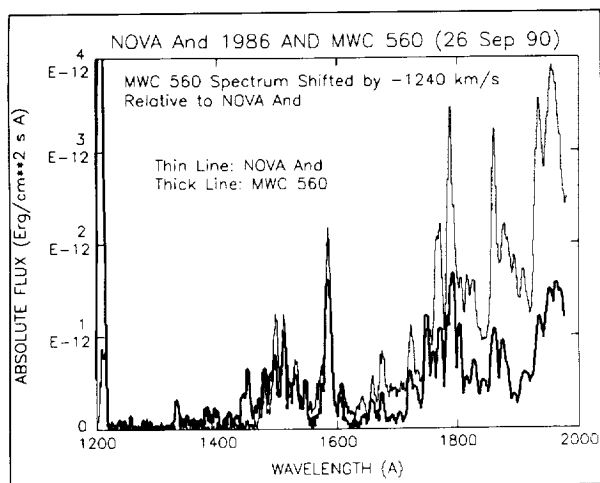
Novae are characterized by a sudden increase in light, accompanied by the ejection of high-velocity material. Nova outbursts can develop on time scales of < 1 day. Novae are believed to be binary stars which contain a small, cool red dwarf, whose radius is comparable to, or slightly smaller than, the Sun. However, the dwarf star's comparatively low surface temperature of 2,500 °C explains its characteristic red color. In contrast, the companion star is a white dwarf, which is several hundred times smaller than our Sun, but whose surface temperature is many times hotter than the solar surface, ranging from 25,000° to 100,000 °C.

Symbiotic systems comprise a category of interacting binary systems which resemble classical novae. However, one important difference distinguishes a classical nova from a symbiotic one: the presence of a red giant. These red giants



are typically hundreds to a few thousand times larger than the Sun. Our galaxy contains several hundred symbiotic systems. They can be identified by their distinctive visible light spectra, which are characteristic of red giants. In a symbiotic system, superimposed on the red giant spectrum are numerous spectral emission lines that arise from multiply ionized atomic species of oxygen, nitrogen, neon, and iron. The presence of these emission lines is indicative of a strong source of photoionizing continuum radiation, probably a white dwarf or a central star of a planetary nebula.

Symbiotic stars are associated with a cloud of extremely highly ionized gas in which the binary system is embedded. The formation of this nebula is believed to occur when the red giant's companion ejects its outer stellar envelope, exposing the remnant nuclear stellar core which slowly cools and evolves into a white dwarf. Exposed to intense ionizing radiation of the white dwarf, the surrounding nebula produces strong spectral emission lines throughout the optical and ultraviolet regions of the spectrum. The outburst responsible for the formation of this tenuous, ionized gas in symbiotic stars must be quite short, because this transitory phase never previously has been observed.



The dramatic change in the ultraviolet flux distribution of MWC 560 (thick line) is evident on September 26, 1990, when compared with IUE spectra obtained on April 29, 1990. The ultraviolet spectrum of MWC 560 now resembles a classical nova a few days following outburst. MWC 560 is shown for comparison with an IUE spectrum of Nova Andromeda 1986 (thin line) obtained 5 days after outburst.

However, data obtained with the IUE recently afforded astronomers an opportunity to observe such a rare event. IUE observations revealed unusual dynamic motion in a symbiotic-like object designated as MWC 560. Several months preceding the ejection of a dense shell of material from this object, ultraviolet spectra obtained with IUE provided evidence for the onset of a wind in excess of several percent of the speed of light. During this phase, the far-ultraviolet spectrum of MWC 560 indicated the presence of intense ultraviolet continuum emission. However, the presence of metals such as iron and chromium in the expanding material produced strong absorptions, which indicated that the propagation of light emitted from an underlying nuclear core was impeded by the large optical thickness associated with the high-velocity expanding wind.

The large velocities associated with the wind in MWC 560 could be explained by a sustained thermonuclear runaway on the surface of the white dwarf, caused by deposition of matter from its companion, which resulted in the expulsion of material at very high velocities. The onset of the high-speed wind preceded a final ejection event in the system. This became evident by the transformation of the far-ultraviolet spectrum into one which closely resembles that of a classical nova in the early phase of shell ejection.

Thus, ultraviolet observations on MWC 560 may provide insight into the nature of symbiotic stars and the physical processes involved in the ejection of stellar material. For the first time, we have been fortunate to observe processes in an interacting binary preceding a major outburst. These IUE spectra will prove crucial for testing models that have been advanced to explain the evolution of symbiotic systems as interacting binaries.

Contact: A. G. Michalitsianos (Code 684)
(301) 286-6177

Sponsor: Office of Space Science and Applications

Dr. A. G. Michalitsianos has 14 years of service at Goddard. A physicist in the Laboratory for Astronomy and Solar Physics, he is interested particularly in the ultraviolet spectroscopy of interacting binary stars. Dr. Michalitsianos holds a BS in physics from the University of Arizona and a PhD in astrophysics from Cambridge University.

PARTICLE ACCELERATION AND TRANSPORT IN SOLAR FLARES

The ability to accelerate particles to high energies is a characteristic common to astrophysical plasmas at many sites throughout the universe, ranging from the Earth's magnetosphere, to solar flares, to pulsar magnetospheres, to supernova remnants, to radio galaxies. Understanding the acceleration processes which operate in these plasmas is a major objective of astrophysics.

Solar flares present a unique opportunity to further this objective, based on the wealth of diagnostic data that are available. Interactions between accelerated electrons and the ambient atoms result in hard X-ray and gamma-ray continuum emission. Interactions between accelerated ions and the ambient nuclei result in a variety of products, the most important being pions, neutrons, excited nuclei, and radioactive positron-emitting nuclei. The products of pion decay contribute to the gamma-ray continuum, while the de-excitation of various nuclei, the annihilation of positrons, and the capture of neutrons by hydrogen produce gamma-ray lines.

Solar flares have been observed at many wavelengths. They produce accelerated electrons and ions which are observed directly in interplanetary space. The scope of observations of solar flares is therefore quite large. In fact, only in solar flares is it possible to study simultaneously the acceleration of both electrons and ions.

Any study of acceleration in solar flares necessarily involves a study of particle transport as well, since it is in the transport of the particles that the diagnostic emissions are produced. We have developed a realistic solar flare magnetic-loop model in which particle acceleration and transport occurs. The loop consists of a semicircular coronal portion filled with low-density ionized gas and permeated by a constant magnetic field, and two straight portions which begin at the ends of the coronal segment at the transition region and extend into the chromosphere and photosphere.

The magnetic field and density in these two segments increase with increasing depth. Acceleration can occur in the ionized coronal segment, but not in the neutral gas beneath the transition region, whereas the bulk of the interactions will occur in the dense gas below the transition region, and not in the low-density gas in the

coronal portion. This loop, therefore, naturally is divided into an acceleration region and an interaction region.

We first employed this loop model in calculations of relativistic electron transport. In these calculations, we focus upon transport effects and assume that a spectrum of relativistic electrons is released impulsively in the coronal section of the loop. The initial spectrum then is allowed to evolve over time in a Monte Carlo simulation, in which we take into account energy losses, pitch-angle scattering by turbulence in the coronal region of the loop, and magnetic mirroring in the converging magnetic field below the transition region. We also calculate the time-dependent bremsstrahlung energy spectrum from the relativistic electrons.

The time-dependent gamma-ray bremsstrahlung emission from impulsive flares is highly peaked, increasing on a time scale of a couple of seconds and declining over a few to a few tens of seconds. Assuming that the electrons are released into the loop at the peak of the emission, we accurately can account for the subsequent decline of the emission with this transport model. However, probably the most important confirmation of this model is gamma-ray limb brightening. Magnetic mirroring below the transition region leads to interacting electron distributions in which there are more electrons moving in directions tangent to the photosphere than in directions away from it. Hence, there should be a preferential detection of gamma-ray emitting flares near the limb of the Sun. This phenomenon actually has been observed with the Gamma-Ray Spectrometer on the Solar Maximum Mission (SMM). To date, 15 solar flares with gamma-ray emission at energies greater than 10 MeV have been reported, with virtually all of the flares clustered near the limb of the Sun.

Having established a realistic transport model for solar flare particles, acceleration can be considered in more detail. We have investigated the stochastic acceleration of protons by either magnetosonic or Alfvén waves, both of which are capable of accelerating super-Alfvénic protons to relativistic energies. However, we find that magnetosonic waves are too inefficient, and that most of their energy is dissipated on electron heating. On the other hand, we find that Alfvén waves are very efficient. They are dissipated only by nonlinear Landau damping, which heats low-energy protons to super-Alfvénic energies, and by gyroresonant stochastic acceleration,



which then energizes them from super-Alfvénic to relativistic energies.

Using the same magnetic loop model as above, we investigated proton acceleration and transport in solar flares. We assumed that a spectrum of Alfvén waves was deposited impulsively in the coronal section of the loop by the primary energy-release mechanism, and that super-Alfvénic protons were present as a result of a preacceleration mechanism (e.g., nonlinear Landau damping). We took into account the quasilinear damping of the waves by the protons, their diffusion along the magnetic field lines by pitch-angle scattering, and their eventual interaction below the transition region. Once a large number of protons is above the acceleration threshold, nonlinear Landau damping can be neglected. This process, however, is essential in preaccelerating protons to energies above the threshold and will be included consistently in future work. The calculations were performed by solving numerically the coupled quasilinear equations describing the evolution of particles and waves.

The time profile of the nuclear line emission is similar to that of the gamma-ray bremsstrahlung, exhibiting a rapid rise and a somewhat more extended decline. Such a behavior is expected qualitatively from this proton acceleration model. Initially, when the energy density is high, protons are trapped diffusively in the corona and cannot interact, and the emission is thus a minimum. As the waves are damped, protons more easily can escape, and the emission increases. When the waves are dissipated almost completely, the emission reaches a maximum and then declines as protons stream relatively freely around the loop. Numerically, we found that an impulsive deposition of approximately 10 erg/cm^3 of Alfvén waves produced time profiles very similar to those observed.

The energy spectrum of the interacting particles can be determined by considering the ratio of the nuclear line fluence to the 2.223-MeV neutron capture fluence, since these emissions result from protons of different energies. We have not yet performed direct comparisons to the fluences, but find that we produce proton energy spectra similar to those known to account for this ratio. This acceleration model is thus quite successful in accounting for several observations from solar flares. Future work will involve modeling the other emissions resulting from energetic

ions as well, in addition to constructing a model for the acceleration of relativistic electrons.

Contact: James A. Miller (Code 665)
(301) 286-3642

Sponsor: NASA Headquarters Space Physics
Division

Dr. James A. Miller, a scientist in the Theory Office of the Laboratory for High-Energy Astrophysics, is employed by the Universities Space Research Association. He has worked at Goddard for 6 years. He received a BS from Gannon University and an MSc and a PhD from the University of Maryland at College Park.

ON THE CONTRAST AND STRUCTURE OF FACULAE

Faculae and sunspots are the only two active region features that blemish the photosphere of the Sun in continuum radiation (white light). As a consequence, they contribute significantly to variations in the solar constant. These energy variations are many magnitudes larger than those attributed to flares and coronal disturbances. The variability of the solar constant is considered to be one of the three leading causes for the present-day climate change (the other two being anthropogenic greenhouse gases and aerosols primarily of volcanic origin). Consequently, the behavior and structure of these features represent an important area of solar study.

These active-region features—sunspots and faculae—differ dramatically. Sunspots are large, localized, dark, easily discernible, and are seen clearest near disk center. Faculae, on the other hand, are small, bright objects, sprinkled over a wide area and seen mainly near the Sun's limbs as the features rotate across the solar disk. The structure of sunspots generally is agreed upon. These dark features are believed to be enormous wells penetrating hundreds of kilometers into the Sun's surface—some as large as the entire Earth. Locally, they inhibit the outflowing solar radiation by a significant factor, near 50 percent, leading to a reduced energy flow of roughly 10^{30} ergs/s. As mentioned, faculae do just the opposite; they emit more radiation. But there is no consensus on their structure; their structure and energetics are not understood. Whereas the blockage of

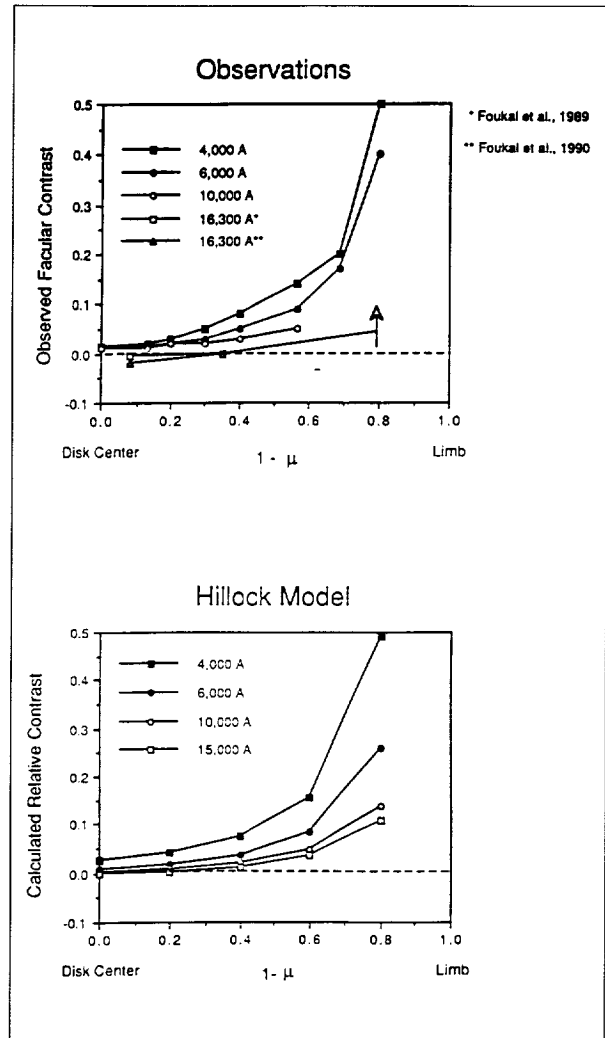
energy in sunspots is attributed to magnetic fields, faculae also have magnetic fields but are bright rather than dark. Where faculae previously had been modeled as wells similar to sunspots, we suggest that they actually may be hillocks. In fact, one of the famous, early astronomers, Sir William Herschel, referred to faculae as ridges.

Faculae virtually are unobservable at disk center. But as the Sun rotates, they show generally an increasingly brighter contrast on their journey toward the limb. Close to the limb, their contrast may decrease slightly because of obscuration effects from the surrounding photospheric gases; however, they still are significantly brighter than the limb-darkened gases.

Considering that the contrast behavior of faculae is almost the opposite to that of sunspots, we have suggested that the hillock geometry may do for faculae what the well geometry does for sunspots. We have developed a conical hillock model for comparison with the observations. In this model, all the photospheric isotherms and isobars were elevated vertically into a 150-km conical hillock shape, ignoring the presumed small temperature enhancement that must be associated with the expansion. This may be analogous to a pot of boiling water; the heating will not raise the temperature significantly but will simply distort the otherwise flat surface. In the solar photosphere, this geometry enhances the emission progressively as the facular hillock approaches the limb because its surface area increases. Moreover, the low contrast near disk center occurs naturally because the surface area seen from above is unchanged.

The contrast from this hillock model is shown in the lower panel of the first figure for a variety of wavelengths from the blue to the infrared and for different viewing angles on the solar disk. For comparison, the observed contrasts are shown in the upper panel of the first figure. The hillock model contrasts agree better with the general shape of the observed pattern than do the well model contrasts (not shown). Additionally, the model provides a positive contrast for the 4,000- to 10,000-Å wavelengths at disk center, and a negative contrast of -0.2 percent for the infrared wavelength of 15,000Å, in reasonable agreement with recently reported observations.

We adapted the one-dimensional envelope code of Endal and Twigg to model sunspot wells and facular hillocks. Downward and upward flows were considered



Observed facular contrasts using four different wavelengths from the blue to the infrared (upper panel). The two infrared curves shown are for the Foukal et al. findings from 1989 and 1990 since their central contrasts differ markedly from each other. Additionally, the value near the limb is described in their paper simply as "bright." The arrow on the right may indicate the uncertainties. (Lower panel) The hillock model contrasts are shown for similar wavelengths in the same format. The central contrast for the infrared wavelength is -0.2 percent, comparable to the Foukal et al. 1989 value of -0.3 to -0.4 percent.

to describe these features. We briefly discuss these results to show that the hillock geometry is not an unreasonable one for faculae.



Relating to standard envelope theory, the following equations are used:

$$\frac{\partial F^{rad}}{\partial r} + \frac{\partial(\rho C_p K S)}{\partial r} + Q_{eff} = 0$$

where

$$Q_{eff} = \rho C_p W S + \rho C_p V \frac{\partial T}{\partial x}$$

vertical horizontal
advection advection

where Q_{eff} represents a modification to standard envelope theory to account for advective energy transport. This allows us to investigate the effects of flow on the vertical distributions of temperature, pressure, density, and surface irradiance.

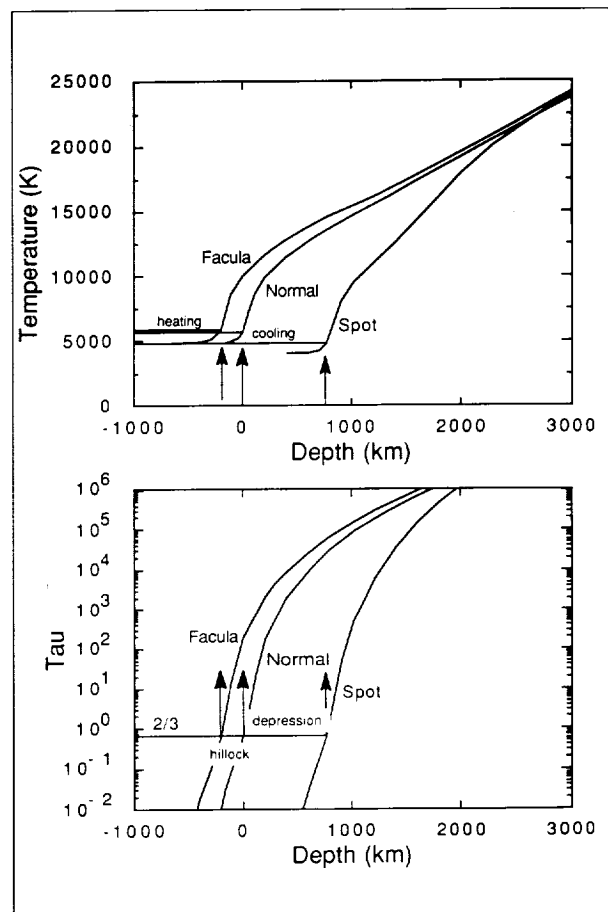
The one-dimensional envelope code solves the second-order energy equation and the first-order equation of vertical momentum balance (hydrostatic equilibrium). For the lower boundary conditions, we assume that the active region disturbance does not penetrate below a depth of 12,000 km. We provide magnitudes for the vertical and horizontal advectives to define Q_{eff} , and vary these rates until, for a given subsurface density, pressure, and temperature, the lower boundary condition is satisfied. The following photospheric boundary conditions are adopted for the normal spot and facular surface irradiance (L) and temperature (T) at $t=2/3$: $L_n=1.0$, $L_s=0.5$, $L_f=1.1$ (in units of the Sun's normal surface irradiance); $T_n=5,750$, $T_s=4,836$, and $T_f=5,897$ K, respectively. To satisfy these conditions, the flow velocities are near 50 m/s for downflow in the sunspot and near 20 m/s for upflow in the facula.

The second figure shows the model's computed temperature and optical depths for the normal envelope, sunspot, and facula, and we note the following features. First, near the photosphere ($t=2/3$), the three curves in each panel have similar shapes. They almost can be superimposed by simply shifting altitudes. The density structure shows similar behavior. This supports the view that the active region features can be approximated by altered geometrical structures.

Second, the sunspot cooling, together with hydrostatic equilibrium, provides for a reduced altitude (750 km) of the umbral photosphere ($t=2/3$), in accordance with the Wilson depression (about 500 km); and the temperature is reduced there by about 900 K. Third, the facular heating provides an uplifting of the surface (200 km), in accordance with the hillock geometry discussed

in this paper, and the temperature is enhanced by about 150 K. Because of buoyancy, the cooling and heating cause changes in the surface formation.

We note that the contrast model discussed earlier and the current envelope model are consistent with each other. The contrast modeling suggests a conical hillock with a base angle of 15° . From observations, the average diameter for faculae is 1,200 km. This provides an altitude for the tip of the faculae cone of 160 km, comparable to the 200 km obtained from the envelope model.



Temperature and optical depth for the Sun's normal upper convection zone and for a sunspot and a facula model. Cooling for the sunspot is achieved with a 50-m/s downflow located near 1,000-km depth. The models reach undisturbed conditions near 4,000-km depth, and the $\tau=1$ surface corresponds to the photosphere. At these locations, the change in photospheric height, and the effective temperature can be seen.

Our modeling efforts provide a unique view of faculae and sunspot structures. In this view, both features are controlled largely through the energetics of vast vertical flows along magnetic field lines within the Sun.

Contact: Kenneth H. Schatten (Code 914)
(301) 286-3831

Hans G. Mayr (Code 914)
(301) 286-7505

Dr. Kenneth H. Schatten, who received his PhD from the University of California at Berkeley, is a solar physicist with the Solar Radiation Office of the Laboratory for Atmospheres. Dr. Schatten has been with Goddard since 1969 and has received several awards for his scientific achievements.

Dr. Hans G. Mayr is an atmospheric scientist with the Dynamics Explorer and Pioneer Venus projects. Dr. Mayr, who holds a PhD from the University of Graz in Austria, has 21 years of experience with Goddard.

SHOCKS AND TWISTS IN THE SOLAR WIND

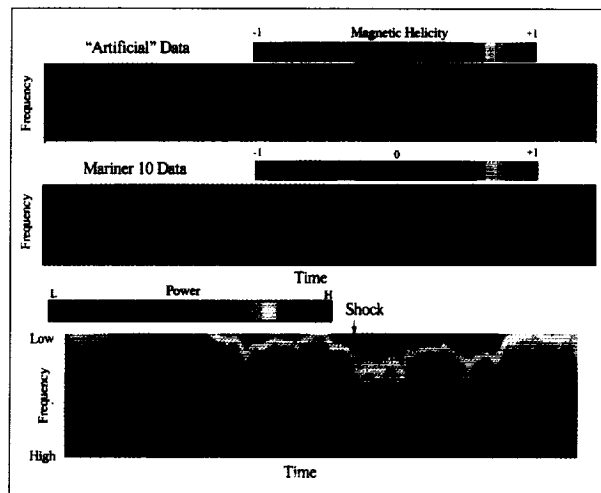
The Sun is a continuous source of ionized particles and magnetic fields that form a 400- to 800-km/s wind. Examined on large time scales, the solar wind consists of streams of faster and slower material that originate from distinctive regions on the solar surface. Because the Sun rotates, the pattern of the wind is like that of a lawn sprinkler, and thus the fast wind can overtake the slow wind, eventually forming very steep gradients in velocity, density, temperature, and magnetic field that are nearly discontinuous and directly analogous to the shock waves produced by rapidly moving objects in air. Transient events on the Sun also can lead to rapid ejecta that produce shocks at their leading edges. In addition to the large-scale structures and shocks, the solar wind contains continuously evolving turbulent fluctuations.

We have been studying both the properties of the turbulent fluctuations and how these are affected by the shocks passing through the medium. One aspect of the general turbulence recently studied is the spatial structure of the twists in the field, an idea quantified by what is termed magnetic helicity. Both the helicity structure of the interplanetary medium and the effects of shocks on turbulence may be studied usefully using a method rarely applied to magnetic field and plasma measurements in the

solar wind; namely, dynamic spectra that show the examined quantity as functions of both frequency and time.

Our group, working with other collaborators, had determined previously that the magnetic helicity of the solar wind seemed generally random as a function of the wave number, or spatial scale, of the fluctuations. This was taken to mean that the polarization of the broad-band turbulent fluctuations in the solar wind was random. We have tested this further by investigating the spatial structure of the helicity, and comparing it to that of fluctuations generated from artificial, randomly phased data that had nearly the same power spectrum for the magnetic field components and a field magnitude that was nearly constant, comparable to observations. The top two panels of the figure show the resulting images of helicity as functions of frequency and time for the solar wind and for artificial cases. Note that the solar-wind case shows larger regions of strong, coherent helicity, indicating that the random-phase model is not accurate.

Shocks in the interplanetary medium can influence the properties of the fluctuations. Not only the value of the density and other bulk quantities changes abruptly, but also the whole spectrum of fluctuations is increased in power, as shown in the bottom of the figure. When examined in further detail, however, we find that the major effects other than on the fluctuation level are confined to the shock region. For example, the relative



The top two panels show the magnetic helicity, or twists, of artificial and real data sets as a function of frequency and time. The bottom panel shows an example of the magnetic power versus frequency and time for a shock wave observed by the Voyager spacecraft.



importance of compressive fluctuations increases near the shock, and especially in front of it, but post-shock compressive fluctuations have nearly the same character as those well ahead of it. This is important for understanding the dynamical evolution of the interplanetary medium, especially in the outer heliosphere where much of the solar-wind material ultimately is shocked one or more times. While the shocks certainly heat the plasma, the incompressible fields may dominate the dynamics in terms of many other properties.

Contact: M. L. Goldstein (Code 692)
(301) 286-7828

D. A. Roberts (Code 692)
(301) 286-5606

A. F. Vinas (Code 692)
(301) 286-6221

Dr. M. L. Goldstein is a Co-Principal Investigator of the Goddard Space Physics Theory Program. His research interests during 19 years at Goddard have included the study of solar wind as a turbulent magnetohydrodynamic fluid, the stability of large-amplitude Alfvén waves, and the processes involved in producing solar and planetary radio phenomena. He holds an AB in physics from Columbia College in New York and a PhD in physics from the University of Maryland at College Park. He received a Goddard Special Achievement Award in 1975 and a NASA Exceptional Scientific Achievement Medal in 1991.

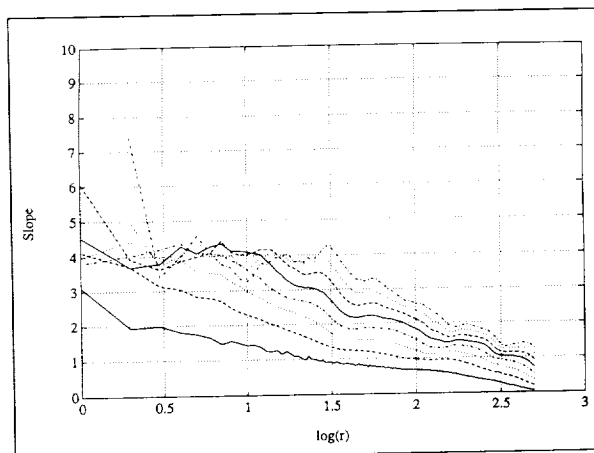
Dr. D. A. Roberts is a Co-Investigator on the Goddard Space Physics Theory Program with 5 years of experience at Goddard. His research focuses on interplanetary turbulence, solar wind acceleration, and low-dimensional descriptions of the magnetosphere. He received an SB in Earth and planetary sciences and a PhD in physics from the Massachusetts Institute of Technology.

Dr. A. F. Vinas is a Co-Investigator on the Goddard Space Physics Theory Program with 10 years of experience at Goddard. His research interests include fundamental plasma physics, solar wind plasma turbulence, analytical and numerical studies of plasma instabilities in the solar wind and magnetospheres, and the study of shock waves. He earned a BS and an MS in physics from the University of Puerto Rico, and a PhD in physics from the Massachusetts Institute of Technology.

CHAOS IN THE GEOSPACE ENVIRONMENT

The awesome splendor of the aurora borealis—the northern lights—is a phenomenon not soon forgotten once observed on a dark, clear winter night. Those who have seen the darting, roiling motions of the aurora can certainly appreciate that there could be chaotic aspects to the physical processes that give rise to those high-latitude displays. The aurorae are only a highly visible facet of the complex collection of physical processes that constitute the interaction of the Earth's magnetic field and particles with the fields and particles convected from the Sun by the solar wind. For example, the substorms that produce aurorae also produce enhancements of large-scale currents flowing from the Earth's magnetotail down through the ionosphere. We have studied several of the parameters that measure geomagnetic disturbances, such as the Auroral Electrojet (AL) index, which indicates the strength of some of the auroral currents. We are employing recent methods of analysis from dynamical systems theory to demonstrate and model the chaotic nature of the Earth's magnetosphere. These methods should help us to go beyond the limits of the conventionally applied power spectral- and linear-correlation analyses in understanding the geospace environment.

The dissipation inherent in physical systems such as the magnetosphere forces the system's phase-space volume to contract to a dynamical end-state called an attractor that may be described by fewer independent variables than the

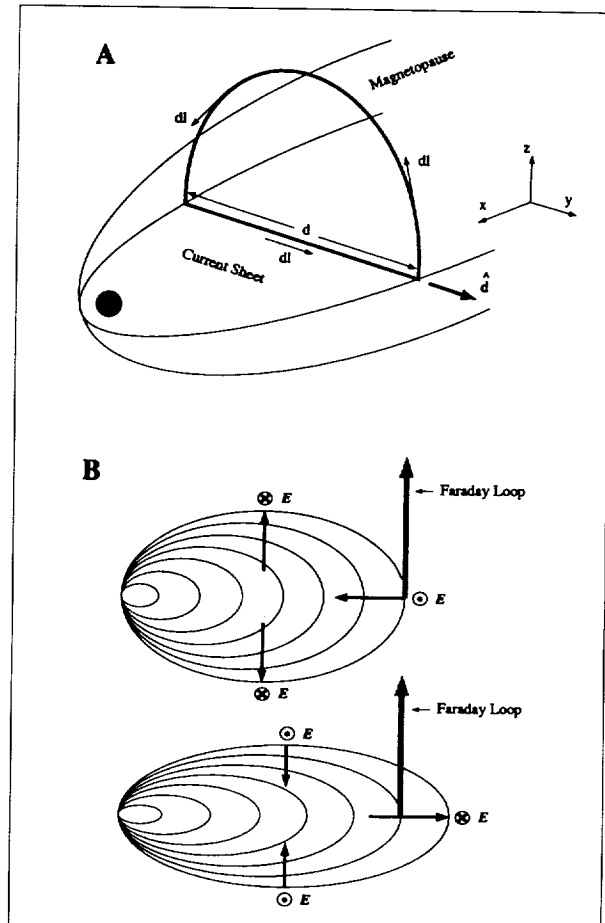


The logarithmic slope of the correlation function plotted versus the logarithm of the embedding dimension (r) for the geomagnetic parameter, AL. Each curve shows the slope variation for a different embedding dimension and an average asymptotic value near 4 is found.

original system. For example, a three-dimensional system might settle into a subset of a plane, in which case the attractor would be characterized by a dimension between 1 and 2. If the dimension is nonintegral, the attractor is fractal and called "strange." Generally, the time series for any variable associated with a system moving on a strange attractor appears random, but since it is actually deterministic it is called chaotic. The presence of an attractor for a system, whether strange or not, implies the possibility of a great simplification of the system's description. Since the magnetosphere intrinsically has a very large number of degrees of freedom, a low-dimensional attractor in this system could make the task of magnetosphere physicists much easier.

It has been found that the information about the dimensionality of an attractor for a physical system often may be recovered from a single time series. The one-dimensional data can be used to construct higher dimensional embedding spaces in which the attractor may be studied. In particular, we have used 40,000 points of AL data at 2.5-min resolution to find the dimension of the substorm attractor, as illustrated in the first figure. Each curve in the figure gives the results for different embedding dimensions (lower dimensions are at the bottom), and the flat regions in the slope-versus-distance curves yield the dimension. Once the dimension of the embedding space is high enough to embed the attractor, the attractor dimension (the slope) settles down to a value near 4. This implies the existence of an attractor, and that the dynamics of substorms may be described by as few as four variables.

The result just described gives us some confidence in attempting to construct low-dimensional models of geomagnetic activity. A nonlinear dynamical model of substorms developed recently by our group has its conceptual origin in an earlier dripping-faucet analogy. During the substorm expansion phase, a blob or bubble of magnetized plasma (a plasmoid) pinches off within the magnetotail and is carried away rapidly into the downstream solar wind. The magnetic field lines closer to the Earth snap back due to magnetic tension into a much more dipolar configuration. This magnetic rearrangement and its effects are thought to cause the auroral disturbances. In the dripping-faucet analogy, a droplet (plasmoid) is filled by a faucet (solar wind input) and pulled by gravity (field lines attached to the solar wind) while the water surface tension (tension in the Earth's field) resists droplet (plasmoid) formation.



(a) A Faraday loop passing across the equatorial plane of the Earth's magnetotail and then closing over the high-latitude tail surface. (b) Plasma sheet magnetic field lines shown in a meridional plane cut of a; field line oscillations lead to variations in cross-tail electric fields and to variations in the magnetic flux passing through the Faraday loop.

The water-drop analogy actually may be more profound than was assumed originally. Several researchers, including scientists at Goddard, have carried out extensive experimental and computational studies of the dripping faucet. They found that for low flow rates the faucet drips with a steady, clock-like pattern but for higher flow rates—while the drops may be separate and distinct—they fall in an irregular, chaotic pattern, strongly reminiscent of patterns in magnetospheric phenomena.

We are constructing a new magnetospheric response model based on the application of Faraday's law to a



closed loop encircling a cross section of the magnetotail, as shown in the second figure. This Faraday loop response model deals with global properties and evolution in the tail, and it is constructed from first principles. The model depends on the plasma physical and geometric state of the tail and governs the evolution of such measurable quantities as the magnetic flux in the tail, the diameter of the tail, the cross-tail electric field, and the cross-tail currents. This model, in its present, early state, is similar in many respects to the dripping-faucet analog model. Both are damped harmonic oscillators that are driven by a loading-unloading cycle; at the mathematical level, they differ only in details. The loop-model behavior, using model parameters and loading rates that are reasonable, compares well with our observational results, and indicates that chaotic dynamics may determine the time scales and patterns of the observed geomagnetic phenomena.

Contact: Daniel N. Baker (Code 690)
(301) 286-8112

D. Aaron Roberts (Code 690)
(301) 286-5606

Alex Klimas (Code 690)
(301) 286-3682

Dr. Daniel N. Baker is the Project Scientist for the Small Explorer (SMEX) Program and the Mission Scientist for the Solar, Anomalous, and Magnetospheric Particle Explorer (SAMPEX) project. He is Chief of the Laboratory for Extraterrestrial Physics. Dr. Baker, who has nearly 4 years of experience with Goddard, holds a BA, an MS, and a PhD from the University of Iowa.

Dr. D. Aaron Roberts, a scientist in the Interplanetary Physics Branch of the Laboratory for Extraterrestrial Physics, has devoted 5 years to the Space Physics Theory program and to analysis of Voyager data. He received a PhD from the Massachusetts Institute of Technology. His research interests include interplanetary turbulence and chaos in the magnetosphere.

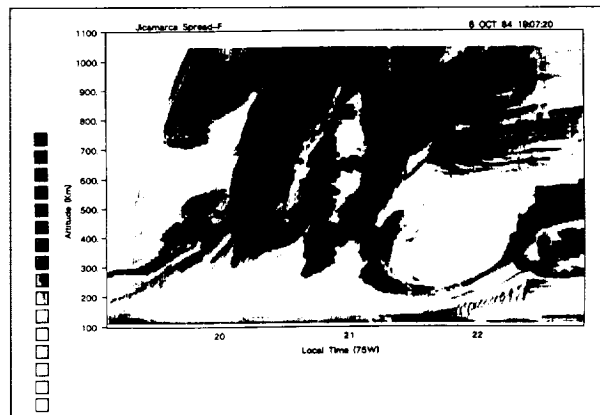
Dr. Alex Klimas, who has 16 years of service at Goddard, is Principal Investigator for the NASA Magnetospheric Physics Supporting Research and Technology Program and Principal Investigator for the NASA Space Physics Research and Analysis Support Program. Dr. Klimas, who also works in the Laboratory for Extraterrestrial Physics, earned a BS, an SM, and a PhD from the Massachusetts Institute of Technology.

ROCKET OBSERVATIONS OF SPREAD-F PLASMA TURBULENCE FROM KWAJALEIN ATOLL

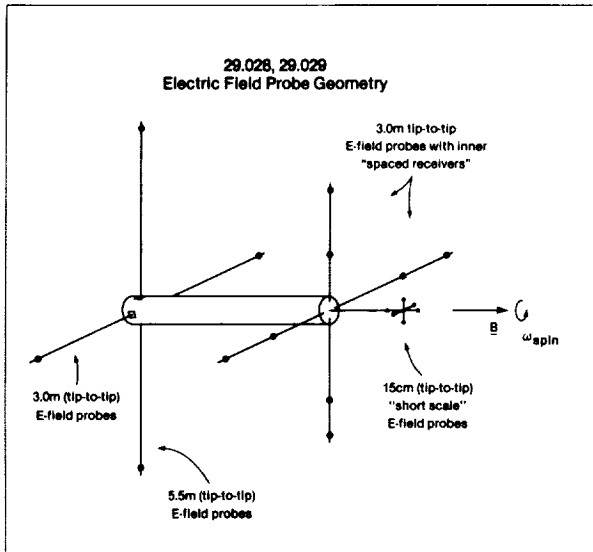
One of nature's most spectacular displays occurs in the ionosphere after sunset near the Earth's Equator. Although invisible to the eye, ground-based radars reveal that this region of space often erupts with puzzling planetary-scale, turbulent activity known as "Spread-F." An example of this phenomenon from the Jicamarca radar in Peru is shown in the first figure. In-situ probes have shown that turbulence such as this coexists with large-scale depletions, or "bubbles," in the ionosphere. These bubbles create plume-like trails of electric field and ion density fluctuations in space. Such irregularities are known to be highly disruptive to radio communications and satellite tracking operations.

Despite decades of research on Spread-F, several important aspects of this phenomenon still elude our understanding. In particular, these include the nature of direct-current (DC) and long-wavelength electric fields associated with Spread-F and its density depletions, as well as the detailed characteristics of the shorter scale turbulence: its wavelength, phase velocity, angular distribution, and power spectrum.

The San Marco D satellite, launched in 1988 into an equatorial orbit, included a very successful Goddard electric field experiment that addressed in particular the study of DC electric fields in plasma bubbles. To investigate the detailed wave properties and the changing characteristics of the Spread-F turbulence along a vertical trajectory, a rocket experiment was designed by



An example of Spread-F activity, as measured by the Jicamarca radar in Peru.



A rocket experiment developed by the Electrodynamicics Branch to study the Spread-F phenomena. The instrument studied the full-vector DC electric field and the electrostatic wavenumber, as well as the extremely short scale waves associated with Spread F.

Goddard's Electrodynamicics Branch, as shown in the second figure. Goddard's electric field experiment included multiple-length probes to measure the spatial attenuation of short-scale waves and interferometers to measure their wavelengths and phase velocities. The instruments thus are capable of observing both the full-vector DC electric field and the electrostatic wavenumber spectrum. In addition, an array of very short (15 cm) double probes were provided by co-investigators at Cornell University to study the extremely short scale waves. The payload instrument complement also included a plasma frequency probe to measure the plasma density profile, which provides direct evidence of the plasma bubbles or depletions, and a fixed-bias Langmuir probe to measure density fluctuations.

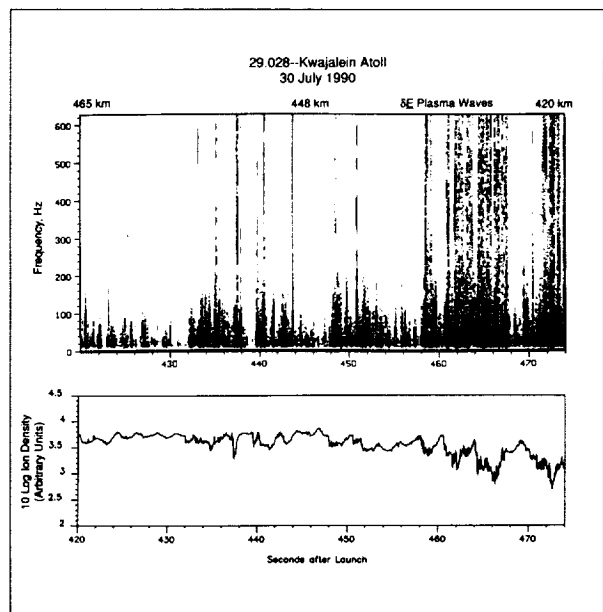
The rocket payload was prepared at NASA's Wallops Flight Facility along with its launch vehicle, a Terrier-Malemute rocket. An attitude control system developed at Wallops tilted the rocket on its side, so the spin axis was aligned along the magnetic field direction during the data-taking portion of the flight. This orientation facilitates measurements of the vector DC field and of the isotropy or anisotropy of the wave turbulence. The launch operations took place on the island of Roi-Namur,

which is part of Kwajalein Atoll, U.S. Marshall Islands, in the South Pacific.

The launch conditions were determined by monitoring the nighttime ionosphere with the UHF and VHF Altair radar at Roi-Namur. In addition, backscatter observations also were made with the Cornell University portable radar interferometer. Although Spread-F does not occur every night, it occurs most frequently (two to three times per week) at this longitude in the summer. (In fact, one key outstanding question is, Why does Spread-F occur only on some evenings?)

On the evening of July 29, 1990 (July 30, 1990 UT), well-developed Spread-F turbulence occurred along the flight azimuth over Kwajalein, as observed real-time in displays of Altair radar echoes. At this time, the rocket was fired along a northern trajectory achieving an apogee of 491 km. The payload pierced a number of plasma depletions on both its upleg and downleg traversals of the turbulent region. An electric-field spectrogram of a portion of the wave data is shown in the third figure, along with the simultaneously measured plasma density data.

The in-situ wave observations immediately confirmed the presence of significant wave turbulence in the same location as the plasma depletions. The observed modulation of the low-frequency electric field waves at twice the spin



An electric field spectrogram of a portion of the wave data collected by Goddard's rocket experiment over Kwajalein Atoll in July 1990.



rate showed that the broad-band turbulence is anisotropic at long- to medium-scale wavelengths (tens to hundreds of meters). These results bear directly on the Rayleigh-Taylor instability generation process. Furthermore, the electric-field wave spectra at times (but not always) were observed to extend to much higher frequencies on shorter scales (< 1 m). These short-scale waves, which are responsible for the UHF and VHF backscatter, may well represent direct evidence of the drift wave instability. The observed frequencies of the electric field spectra observed here extend well beyond those of any previously reported rocket-observed Spread-F turbulence. As the data analysis progresses, the multiple-baseline electric-field interferometer data is expected to yield the first rest-frame wavenumber spectrum of these waves and thus, will address several questions concerning the instability mechanism itself.

The electric-field data gathered on this rocket flight, in conjunction with the plasma density and radar observations, promise to further our understanding of Spread-F turbulence by a large degree.

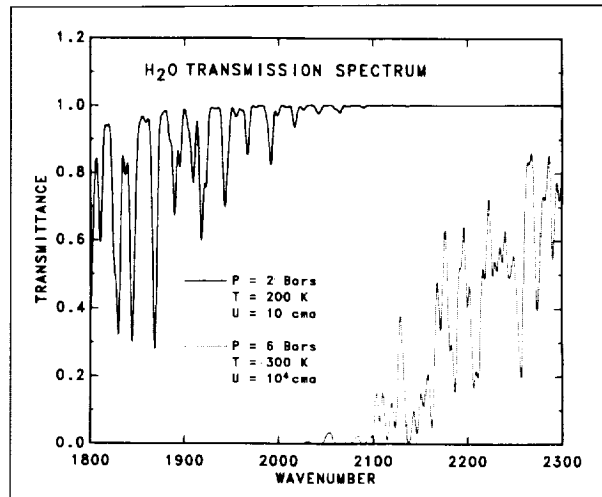
Contact: Robert F. Pfaff, Jr. (Code 696)
(301) 286-6328

Sponsor: Office of Space Science and Applications

Dr. Robert F. Pfaff, Jr., has nearly 6 years of experience in Goddard's Laboratory for Extraterrestrial Physics. He holds an AB from Brown University, a DES from the University of Paris, and a PhD from Cornell University. He was a Co-Investigator on the Polar Electric Field Instrument project. His research interests include electric-field instrumentation on rockets and satellites, as well as plasma wave instabilities and turbulence.

DETERMINATION OF THE WATER ABUNDANCE ON JUPITER

Clouds composed of NH_3 , NH_4SH , and H_2O are expected to form with increasing depth in the Jovian atmosphere. Previous determinations of the gas abundances in the Jovian atmosphere have revealed that carbon in the form of CH_4 and nitrogen in the form of NH_3 are enhanced by a factor of 1.5 to 2 relative to their solar abundances. However, previous determinations of the Jovian oxygen abundance, which should be in the fully reduced form of water, suggest a depletion by a factor



Effect of the water abundance on the peak emission level. The solid line shows the locations of the peak emission levels calculated for a two-times solar water abundance, saturated water profile, and no water cloud. The dotted line corresponds to a well-mixed water abundance of 3×10^{-5} and a saturated profile above the condensation level at 2.3 bars (but no water cloud). Gaseous and NH_3 cloud opacity have been included in the calculation of the peak emission level.

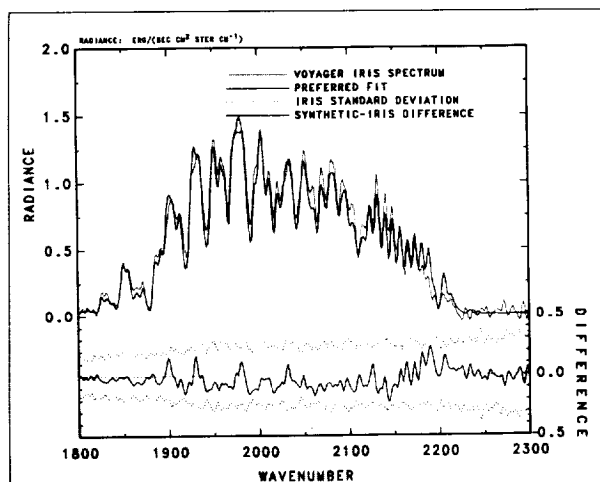
of approximately 50. If real, such a large depletion would have important consequences for models of the origin and evolution of the Jovian atmosphere and would be difficult to understand given the observed enhancements of the other elements.

Retrieving atmospheric concentrations of condensable species is complicated by the influence of atmospheric dynamics (convection), which can reduce the relative humidity above the condensation level (cloud base) to values well below saturation. Since water condenses in the Jovian atmosphere, the notion that an observed abundance reflects a depletion critically depends on the relative humidity profile and pressure level ascribed to retrieved abundance. For example, an abundance of 3×10^{-5} at 4 bars suggests a depletion of a factor of about 50, while the same abundance near 2 bars merely reflects saturated conditions. Complicating the retrieval process is the fact that water vapor is a dominant source of $5\text{-}\mu\text{m}$ gaseous opacity over a pressure range of nearly 5 bars.

The first figure compares the locations of peak emission levels for two different, well-mixed water abundances. In both cases, water is assumed to follow a saturated profile above the condensation level. For a two-times solar

abundance of water, 5- μm observations are limited by cloud and gas opacity to the region above the thermochemically predicted water cloud at 5 bars. Conversely, should water be depleted, observations in the 5- μm region would sound to greater depth due to the reduced water opacity.

The presence of multiple cloud layers in the Jovian atmosphere further complicates the retrieval. Previous analyses used a single, gray-absorbing cloud to model the extinction provided by the multiple cloud layers in the Jovian atmosphere. Since all of the thermochemically predicted condensates have particle single-scattering albedos near unity, the absorbing cloud approximation does not provide a reasonable representation of cloud extinction; multiple scattering effects are important. We use thermochemical equilibrium equations to determine the cloud base locations in a manner consistent with the retrieved gas abundances and thermal profile. Our radiative transfer model includes the effects of spectrally dependent anisotropic multiple scattering from the multiple cloud layers in the Jovian atmosphere. The spectral



Comparison of the average north equatorial belt Infrared Interferometric Spectrometer (IRIS) hot-spot spectrum (dotted line) to a synthetic spectrum calculated with a two-times solar abundance of water and a reduced relative humidity profile above the cloud (solid line). Optimum fit is obtained with the relative humidity decreasing from 100 percent at cloud base (4.9 bars) to 15 percent at 3 bars, then increasing to 100 percent at 1 bar above which the relative humidity remains constant. The optical depths of the NH_3 , NH_4SH , and H_2O clouds are 0.27, 0.02, and 4, respectively. This combination of parameters is our preferred fit to the entire IRIS spectrum for hot spots.

dependence of cloud extinction is included using Mie theory and the appropriate refractive indices for the cloud condensates. Line-by-line calculations are performed to model gaseous opacity.

Consistent with the findings of previous investigations, we find that a saturated water profile provides too much gaseous opacity in the 1900- to 2000- cm^{-1} region of the 5- μm spectrum. Nevertheless, additional opacity, provided by a water cloud near 5 bars, is required in the region near 2,130 cm^{-1} . The apparent discrepancy between the fact that a saturated vapor profile provides too much opacity in the 2- to 4-bar region and the need for a water cloud at depth, can be reconciled by decreased relative humidity above the water cloud as illustrated by the second figure. This points to the importance of dynamic drying of the vapor profile, as observed in the terrestrial atmosphere and identifies relative humidity as an important parameter to be retrieved together with cloud properties, temperature profile, and gas concentration.

Contact: Barbara E. Carlson (Code 940)
(212) 678-5538

Sponsor: Office of Space Science and Applications

Dr. Barbara E. Carlson, a scientist at the Goddard Institute for Space Studies for 4 years, specializes in radiative transfer in planetary atmospheres. She has a PhD from the State University of New York at Stony Brook.

REACTION RATE KINETICS OF $\text{H} + \text{GeH}_4$ AND THE IMPLICATION FOR MODELING GERMANE PHOTOCHEMISTRY IN THE ATMOSPHERES OF JUPITER AND SATURN

The possibility of detecting germane (GeH_4) in the reducing atmosphere of Jupiter was suggested in the early 1970s. Germane subsequently was identified as being present in Jupiter's atmosphere and has been observed recently in the atmosphere of Saturn. Of particular note is the conclusion that, based on the expected solar mixture of elements, GeH_4 is not the major chemical form of the total expected germanium in either planet. Thus, studies of germanium-containing molecules to determine their photochemistry and reactions which may either produce or remove GeH_4 are of interest. One such reaction to consider is that of GeH_4 with hydrogen atoms: $\text{H} + \text{GeH}_4$.



Previous studies of this reaction reported rate-constant results obtained only at 298 K. Due to the interest in germanium chemistry in the atmospheres of the giant planets, and in order to determine adequately the role of this reaction at temperatures more appropriate to those of the giant planets, we recently have undertaken a kinetic study of this reaction to measure, for the first time, its reaction-rate constant as a function of temperature. The laboratory method employed the direct technique of flash photolysis production of hydrogen atoms, followed by time-resolved resonance fluorescence detection and measurement of the H-atom decay signal based on reaction with GeH₄.

Results from the rate-constant data, measured over the temperature range 210 to 450 K, show the reaction of H + GeH₄ to have a positive dependence on temperature and to have a moderately rapid rate of reaction (approximately one in every 100 collisions leads to reaction) at temperatures appropriate to those of the atmospheres of Jupiter and Saturn.

The implication for modeling the germane photochemistry in the atmospheres of the giant planets derived from this kinetic study is that low-temperature data relevant for the atmospheric conditions are provided. This enables comparison of the reaction rate with the only other competitively feasible depletion process; namely, photolysis. These data are critical for valid interpretation and understanding of the observations of GeH₄ on Jupiter and Saturn because they impose some constraints on modeling the photolytic and chemical depletion of GeH₄ in the various regions of the atmospheres of these planets.

Contact: David F. Nava (Code 691)
(301) 286-5483

Walter A. Payne (Code 691)
(301) 286-6007

Louis J. Stief (Code 691)
(301) 286-7529

Sponsor: Office of Space Science and Applications

Dr. David F. Nava is an astrophysicist with the Laboratory for Extraterrestrial Physics. He is Co-Investigator for the Upper Atmosphere Research Program and for the Planetary Atmospheres Program, and he was Principal Investigator for NASA's Returned Lunar Sample Program. He also served on the editorial board of Chemical Geology. Dr. Nava, who received a PhD in chemistry from Arizona State University, has

worked at Goddard for 23 years and has received two NASA Special Achievement Awards and a NASA Exceptional Performance Award.

Dr. Walter A. Payne, an astrophysicist in the Astrochemistry Branch, is a Co-Investigator in the NASA Upper Atmosphere Research Program and the NASA Planetary Atmospheres Program. His professional interests include chemical kinetics, photochemistry of small molecules, and laser-induced fluorescence. Dr. Payne, who earned a PhD in physical chemistry from Howard University, has been at Goddard for 21 years.

Dr. Louis J. Stief, a Senior Scientist in the Laboratory for Extraterrestrial Physics, has worked at Goddard since 1969. His research focuses on atmospheric chemistry. He holds a BA in chemistry from La Salle University and a PhD in chemistry from The Catholic University of America. He received a Goddard Safety Award of Honor in 1990.

MAGNETIC FIELDS OF URANUS AND NEPTUNE

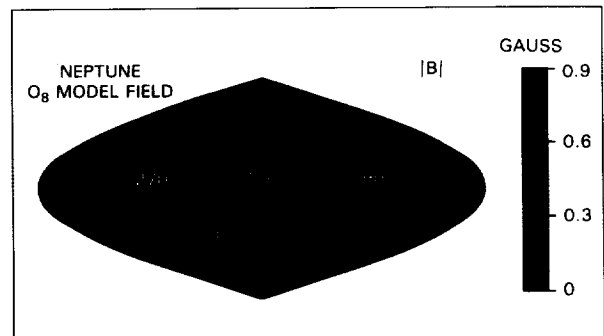
Voyager 2's remarkable journey through the Solar System provided close flybys of the twin giants—Uranus and Neptune—in January 1986 and August 1989. At both of these planets, Goddard-built magnetic-field sensors onboard Voyager revealed extraordinary magnetic field configurations. Uranus and Neptune have very complex magnetic field geometries, with magnetic poles at mid or low latitudes. In contrast, all of the other magnetic planets have relatively simple field geometries (dipolar), closely aligned with each planet's rotation axis. Research at Goddard in this area is directed toward: the development of modeling methods for the inversion of flyby observations; an understanding of the implications of the complex field geometry for charged-particle populations, magnetospheric processes and related phenomena; and a better understanding of the dynamo process of magnetic-field generation in planetary interiors.

Since Voyager's flyby trajectory brought the spacecraft much closer to Neptune than its predecessors, the rich complexity of the field is evidenced in the close-approach data as never before. Spherical harmonic modeling of the main field is approached by partial solution to the under-determined inverse problem (8th-order spherical harmonic model) using generalized inverse techniques.

Low-order dipole and quadrupole spherical harmonic coefficients are determined, or resolved, independently of the higher order terms; some with relatively large uncertainties. The model yields for Neptune a dipole of magnitude 0.14 G R_n^3 , tilted from the rotation axis by 47° towards 72° W longitude. By comparison, Uranus' dipole of magnitude 0.23 G R_n^3 is tilted by 59° toward 54° W longitude. All other planetary dipoles are tilted from the rotation axis by $< 15^\circ$ or so. The geometrical complexity of the field can be expressed in terms of the relative magnitude of the spherical harmonic coefficients by degree (for example, the ratio of quadrupole to dipole). Neptune's quadrupole is relatively large, equal to, or exceeding in magnitude the (surface) dipole field; for Uranus this ratio is comparable. Alternately, one can express this same complexity as a spatial offset of the dipole from the center of the planet. In these terms, both Uranus and Neptune dipoles are displaced by about one third to one half of a planet radius from the center.

The unusual magnetic field geometries of Uranus and Neptune can have dramatic effects on the magnetospheric population, dynamics, and related phenomena. The large dipole tilt, in concert with the planetary rotation, creates at Uranus a corkscrew magnetotail geometry, owing to that planet's large obliquity. At Neptune, a similar dipole tilt and rotation creates a magnetosphere with alternating pole-on and Earth-like geometry each rotation; that is, for part of a planetary rotation, the magnetic axis points into the solar wind (pole-on), unlike the terrestrial example. These planets provide extreme examples by which we may test our understanding of magnetospheric dynamics.

And at Uranus and Neptune, bright auroral phenomena will be observed along relatively large, low-latitude, distorted arcs. Particle precipitation may be expected to occur near any of several surface magnetic anomalies. Uranus and Neptune also have provided extreme examples—the first such examples—of planetary dynamos with widely separated magnetic and rotation axes. Prior to these encounters, the near-perfect alignment of magnetic and rotation axes observed for all of the magnetic planets was believed to be characteristic of the dynamo process. We now know it is not; the challenge of understanding why Uranus and Neptune are so different from their neighbors is perhaps the most fundamental question raised by the Voyager encounters.



Magnetic field intensity on the surface of Neptune, based on a low-order (octupole) approximation of the magnetic field derived from Voyager magnetic field observations. The blue regions depict areas of low surface magnetic field magnitude; red depicts high magnetic field regions. The major magnetic poles are seen at mid-latitude and near the equator.

Contact: J. E. P. Connerney (Code 695)
(301) 286-5884

M. H. Acuña (Code 695)
(301) 286-7258

Sponsor: Office of Space Science and Applications

Dr. J. E. P. Connerney is a physicist in the Laboratory for Extraterrestrial Physics with 10 years of service at Goddard. His primary interests are in instrumentation for magnetic field measurement and the study of the outer planets. Dr. Connerney is Co-Investigator on Voyagers 1 and 2, and he also is Co-Investigator on the Mars Observer. His work in modeling planetary magnetic fields and inverse theory was recognized in 1986 with the NASA Medal for Exceptional Scientific Achievement. He holds a BS and a PhD in applied and engineering physics from Cornell University.

Dr. M. H. Acuña is a U.S. Project Scientist for the International Solar Terrestrial Physics Program (ISTP), an international research effort by Japan, Europe, and the United States. He has worked at Goddard since 1969. His research focuses on experimental investigations of the magnetic fields and plasmas in the Solar System. Dr. Acuña is a Co-Investigator on Voyagers 1 and 2, and he is Principal Investigator for the Mars Observer Magnetic Field Investigation. He holds a BS and an MSEE from the University of Tucuman in Argentina and a PhD in space science and plasma physics from The Catholic University of America. He has received the Goddard Moe I.

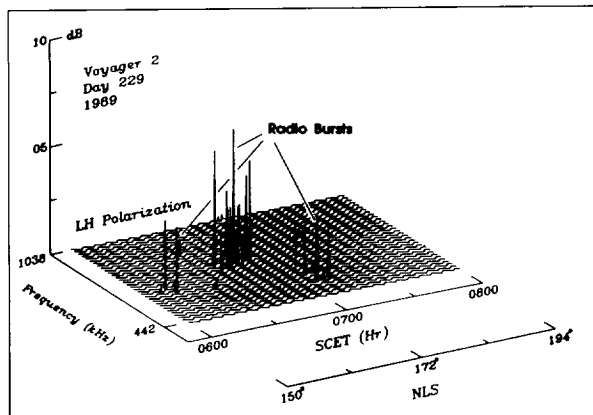


Schneebaum Memorial Award, the Medal for Exceptional Scientific Achievement, and the Exceptional Service Medal in recognition of his contributions to magnetometry and space research.

WHAT IS DRIVING THE NEPTUNE EMISSION?

The first evidence that Neptune had a magnetic field was revealed by Goddard scientists upon their discovery of low-frequency radio emissions emanating from the planet's magnetosphere. Eight days before closest approach, when Voyager 2 was still 11 million km from Neptune, bursty, narrow-band radio emissions were detected by the planetary radio astronomy experiment indicative of a planetary magnetic field strength of at least 0.35 gauss. During the next 8 days, as Voyager approached Neptune, the emission waxed and waned unpredictably. On some occasions, the radiated power exceeded 10^7 W; on other occasions, the emission went completely undetected for an entire planetary rotation.

On Earth, Jupiter, Saturn, and Uranus, major intensity fluctuations of the sort observed at Neptune are attributable either to the influence of satellite interactions with the planet's magnetosphere or to the influence of the solar wind. Specifically, variations in the solar wind plasma, that is, its density or speed, are often good predictors of radiated power as are some planetary satellites when they are at key locations in their orbits.



The plot shows the Neptune radio discovery on August 17, 1989. The emission is predominantly left-hand polarized. The event lasts about 1 hour and is restricted to frequencies between 500 kHz and 1 MHz. The Neptune longitude system (NLS) rotates with an intrinsic planetary rotation period of 16.11 hours.

At Neptune, none of the traditional explanations were capable of explaining the observed variations in radiated low-frequency power. Instead, recent evidence points toward an effective interaction between the interplanetary magnetic field (IMF) direction and the planet's magnetosphere. When the IMF direction is predominantly opposite Neptune's magnetic field direction where it meets the interplanetary medium, the emitted radio power is a maximum. This is evidence for the merging and reconnection of magnetic field lines between the IMF and Neptune's field and the subsequent transfer of energy into the radio source region. This kind of interaction is similar to that seen at the Earth when auroral substorms are observed.

Contact: Michael D. Desch (Code 695)
(301) 286-8222

Sponsor: Office of Space Science and Applications

Dr. Michael D. Desch is Co-Investigator on the planetary radio astronomy experiments on Voyagers 1 and 2 and the radio and plasma waves instruments on Ulysses. Dr. Desch, who has received the NASA Medal for Exceptional Scientific Achievement, has a PhD from the University of Florida. He specializes in the analysis of ground-based and spacecraft observations of magnetospheric phenomena. He has 11 years of service at Goddard.

SOURCE LOCATION OF NEPTUNE'S RADIO BURSTS: IMPLICATIONS FOR THE AURORAL ZONE

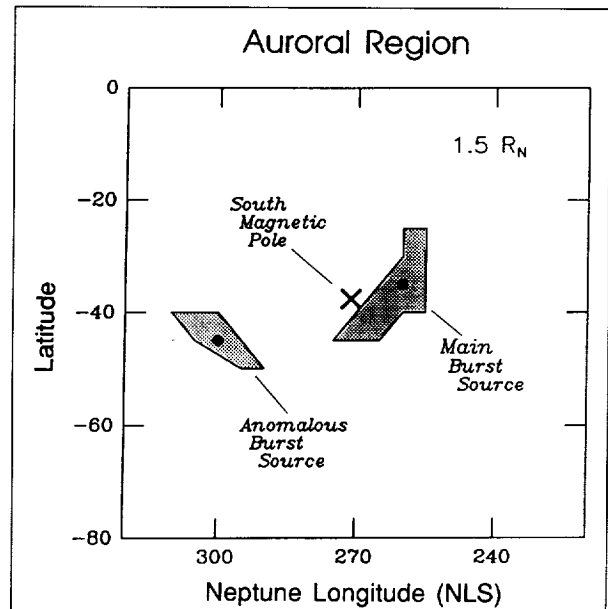
In August 1989, Voyager 2 made a close encounter with the planet Neptune. Onboard the spacecraft is the planetary radio astronomy (PRA) experiment, an instrument designed to detect nonthermal radio emissions from active regions within the planetary magnetospheres. During the inbound encounter with Neptune, the PRA receiver detected episodes of narrow-banded radio bursts between the frequencies of 400 and 1,300 kHz. These unusual bursts were first discovered by investigators at Goddard about 8 days prior to closest approach, with the strongest burst activity tending to reappear periodically at 16-hour intervals. This repetition is associated with the rotation of the planet and detailed statistical analysis of this repetition by investigators at Goddard has yielded a very accurate measurement of the planetary rotation period at 16.11 hours \pm 0.02 hour.

Burst activity at Neptune can be divided into two types. About 80 percent of the bursts belong to the main burst component detected between 550 and 1,326 kHz. However, the remaining activity belongs to a group of anomalous burst episodes detected at frequencies below 600 kHz. The truly unusual feature of the anomalous events is occurrence in planetary phase, which is shifted by about 100° in Neptune's longitude relative to the occurrences of the main burst component.

The PRA investigators at Goddard have devoted much of their post-encounter analysis to the localization of the burst radio source. Such localizations have proven invaluable for the identification of active regions within planetary magnetospheres. For example, at the Earth, radio location analysis has demonstrated that powerful kilometric radiation is emitted from the same active magnetic field lines associated with discrete auroral ultraviolet arcs. At Saturn, the derived location of intense kilometric emission corresponds almost exactly to the active auroral region observed in the ultraviolet. Thus, radio source localization allows investigators to obtain a picture of the active hot spots within a magnetosphere at kilometric and hectometric wavelengths that are directly comparable to those obtained at submillimeter wavelengths.

At Neptune, the localization analysis involved fitting the observations to sets of hollow, symmetric radiation cones. In general, the beaming pattern of most planetary radio emissions forms a conical shape, with the cone orientation defined by the magnetic field geometry. However, at Neptune, the magnetic field geometry is highly uncertain close to the planet where the radio source presumably lies. Hence, a magnetic-field-independent analysis, along with a field-dependent analysis, was performed yielding very similar results. The analyses indicate that the radio source location associated with the main and anomalous burst components lies in close proximity to the south magnetic pole, suggesting an auroral origin of the emissions similar to that observed at Earth and Saturn. Further, the sources' configuration about the pole suggests the presence of two active hot spots, nearly diametrically positioned on either side of the south magnetic pole.

An active south polar region suggested by kilometric wavelength observations is consistent with ultraviolet observations made by the Voyager 2 ultraviolet spectrometer, which indicate the presence of a large, extended bright region centered about 30° east of the pole.



The location of the main and anomalous radio burst sources. Their configuration suggests that there are two active hot spots located on either side of Neptune's south magnetic pole.

The relationship of the active auroral regions to the large-scale dynamic of the Neptunian magnetosphere will be an important focus for the PRA investigators at Goddard.

Contact: William M. Farrell (Code 695)
(301) 286-4446

Sponsor: Office of Space Science and Applications

Dr. William M. Farrell is involved in the analysis of Voyager radio astronomy data obtained at the Uranus and Neptune encounters. He was a NASA Graduate Research Fellow at the University of Iowa, where he received a PhD in physics. He has been at Goddard for about a year.

STRUCTURE AND DYNAMICS OF NEPTUNE'S ATMOSPHERE FROM VOYAGER IRIS MEASUREMENTS

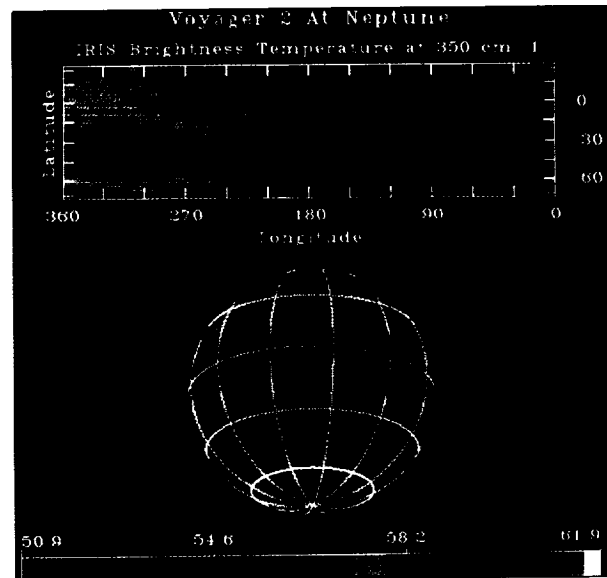
A major objective of the Voyager 2 Infrared Interferometric Spectrometer (IRIS) program is to characterize the thermal structure of the atmosphere of Neptune. Such a characterization can be used to constrain certain aspects of the dynamics and energetics of the atmosphere.



Data obtained from the IRIS experiment permit temperatures in the upper troposphere and lower stratosphere to be determined. For this purpose, measurements of the thermal emission within selected spectral intervals between 200 and 400 cm^{-1} are used. In this spectral region, the atmospheric opacity is dominated by collision-induced molecular hydrogen transitions, and the variation of this opacity with wavenumber permits information to be obtained from various atmospheric levels between approximately 30 and 1,000 mbar. Averages of several tens of spectra can be directly inverted to obtain temperature as a function of pressure level. Although the signal-to-noise ratio associated with individual spectra is inadequate to permit direct inversion, brightness temperatures within selected spectral intervals can be used as estimates of the average temperatures within discrete atmospheric layers. In establishing the behavior of the atmospheric temperature field, both approaches have been used.

The primary set of IRIS data used for diagnostic studies of atmospheric dynamics consists of a complete map of the planet between 20° N and 80° S. This mapping was accomplished by repeatedly scanning from north to south as the planet rotated beneath the spacecraft. The first figure shows a false-color representation of the brightness temperatures associated with a spectral interval centered at 350 cm^{-1} . Emission angle effects have been removed. Brightness temperatures in this spectral interval are representative of the mean atmospheric temperature in a layer between the 30- and 120-mbar levels. This layer is located near the tropopause or temperature minimum.

There are several features observed in this map which potentially provide information on the dynamical behavior of the atmosphere. The lowest temperatures are located at mid-southern latitudes while both the equator and pole are warmer. This behavior is qualitatively similar to that found on Uranus even though the two planets have quite different obliquities. The polar axis of Uranus lies essentially in its orbital plane while that of Neptune is inclined only about 26° from normal to its orbital plane. This indicates that the thermal structure is not controlled directly by the insolation. Significant redistribution of heat must occur within the atmosphere. The observed variation of temperature with latitude suggests that the meridional circulation in this portion of the atmosphere must consist of upwelling and adiabatic cooling at mid-latitudes with



Map of 350- cm^{-1} brightness temperatures obtained with the Voyager 2 IRIS experiment during the Neptune encounter. These measurements are representative of the mean atmospheric temperatures between 30 and 150 mbar. The data are shown for a cylindrical projection above and are projected onto a sphere below. The temperature scale in kelvins is shown at the bottom.

downward motion and associated compressional heating occurring at the equator and pole.

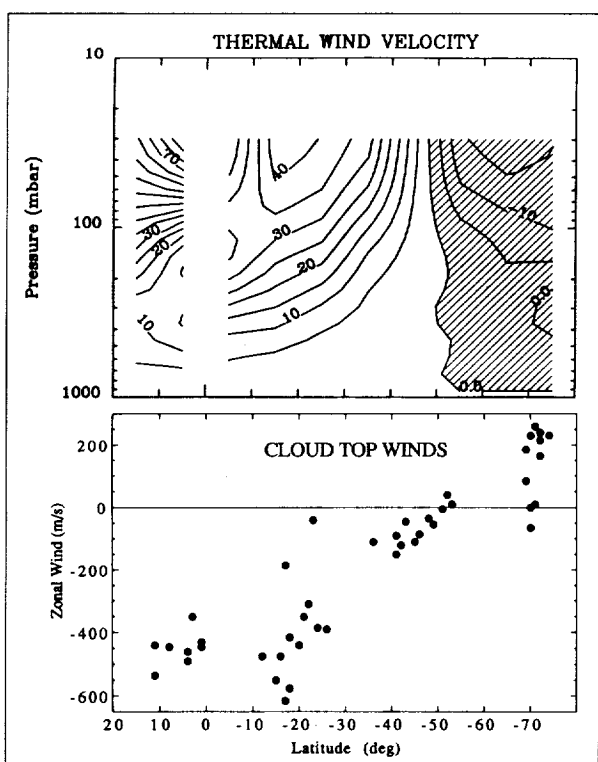
In addition to the large-scale variation of temperatures with latitude, substantial zonal structure also can be observed in the map. Part of this structure consists of wave-like patterns such as those observed between the equator and about 30° S. This structure may be associated with a large storm system, known as the Great Dark Spot, which is observed at about 20° S in visible images. The existence of observable variations of temperature with longitude suggests that wave activity may play a significant role in the dynamic meteorology of this portion of the atmosphere.

None of the features observed in the visible can be associated directly with an isolated feature in the infrared brightness temperature map. Even the intense cold spot centered at 40° S latitude does not appear to correlate with an observable cloud feature. This is in contrast to Voyager results obtained at Jupiter where features such as the Great Red Spot show prominently in maps of the tropopause temperature.

Information on the zonal (east-west) component of the wind can be obtained by considering the thermal structure

averaged over all longitudes. In this case, averaging of spectra in latitude bins results in adequate signal-to-noise ratios to obtain complete temperature profiles. These profiles were then used to construct a meridional cross section of temperature between 20° N and 80° S. This cross section was then used to calculate the thermal wind as a function of latitude and pressure level. The thermal wind is obtained from temperature gradients in latitude on constant pressure surfaces under the assumption that the horizontal pressure gradient is balanced by the Coriolis acceleration acting on the zonal flow. The wind speed obtained in this way is shown in the top panel of the second figure.

In calculating the thermal wind, the required lower boundary condition was taken as zero wind speed at 1,000 mbar. Thus, the wind speeds shown must be added to



Thermal winds (m/s) calculated from zonal mean temperatures obtained by inversion of IRIS data. Positive values indicate eastward winds. Thermal winds cannot be calculated near the equator where the Coriolis acceleration vanishes. (Lower panel) Wind speeds obtained from tracking cloud features observed in Voyager images. Note the anti-correlation between the thermal winds and the cloud-top winds.

those actually existing at the 1,000-mbar level. Positive values represent eastward winds while westward wind speeds are negative. The lower panel in the figure shows wind speeds obtained by the tracking of cloud features observed in visible images obtained with the Voyager cameras. The pressure levels associated with the cloud-top winds are not known with certainty, but presumably lie in the lower portion of the region to which the thermal winds pertain. The thermal winds can be seen to anti-correlate with the cloud-top winds, with both quantities changing sign near 50° S latitude. This behavior indicates that the wind speed must be decreasing with height at all latitudes, a phenomenon also observed on the other three giant planets. The decay of wind speed with height is observed to be quite slow, corresponding to a vertical scale of about 10 pressure scale heights. From this characteristic decay length, it is possible to infer that the frictional damping time scale is comparable to the radiative damping time scale of this portion of atmosphere. Since the radiative damping time is very long because of the low temperatures, this implies very weak momentum dissipation.

Contact: B. J. Conrath (Code 690)
(301) 286-6088
F. M. Flasar (Code 690)
(301) 286-3071
A. L. Weir (Code 690)
(301) 286-2863

Sponsor: Voyager Project, Office of Space Science and Applications

Dr. B. J. Conrath has 30 years of experience at Goddard. Since 1986, he has been Principal Investigator on the Voyager Infrared Spectroscopy Experiment, and he was Co-Investigator for the Nimbus 3 and 4 Infrared Spectroscopy Experiments, the Mariner 9 Infrared Spectroscopy Experiment, and the Voyager Infrared Spectroscopy Experiment from 1973 through 1986. He holds a PhD from the University of New Hampshire. His research interests include the structure and dynamics of planetary atmospheres. He was awarded the NASA Medal for Exceptional Scientific Achievement in 1981 and 1990.

Dr. F. M. Flasar works in the Laboratory for Extraterrestrial Physics. He is a Co-Investigator on the Voyager Infrared Spectroscopy Experiment and the Cassini Infrared Spectroscopy Experiment, as well as a team member on the Cassini Radio Subsystem Science



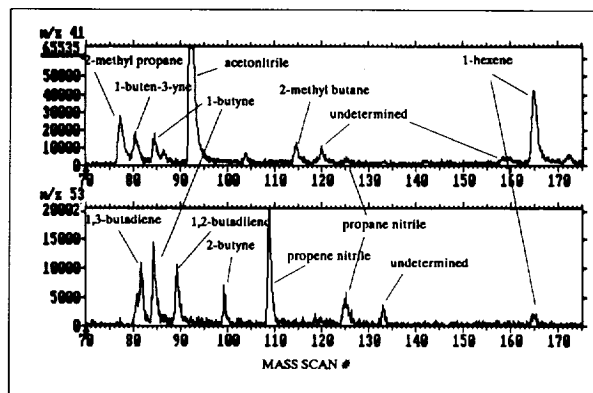
Experiment. His research focuses on the dynamics of planetary atmospheres. Dr. Flasar earned a PhD from the Massachusetts Institute of Technology. He has been at Goddard for 15 years.

Dr. A. L. Weir has been a National Research Council Resident Research Associate and has worked in the Planetary Systems Branch of the Laboratory for Extraterrestrial Physics for 1 year. He is an Associate on the Voyager Infrared Spectroscopy Experiment. He received a PhD from Cornell University.

LABORATORY SIMULATION OF COMPLEX CHEMISTRY IN TITAN'S ATMOSPHERE

The abundance of carbon in the form of methane in Titan's atmosphere ensures the occurrence of complex chemical reactions. A mixture of numerous saturated and unsaturated hydrocarbons as well as products of carbon/nitrogen chemistry such as nitriles and possibly amines, amino acids, and other compound classes are very likely generated in the atmosphere by reactions induced by photochemical processes, cosmic rays, lightning, Saturn's magnetospheric electrons and other energy sources. Goddard's Voyager IRIS experiment has, in fact, provided firm evidence for the presence of several hydrocarbon and nitrile species in Titan's atmosphere.

Laboratory simulations of these atmospheric processes are useful since they can point toward possible complex chemical reaction pathways which cannot be modeled accurately due to a lack of knowledge of the relevant rate constants. We have carried out spark discharge experiments in methane/nitrogen/argon mixtures and monitored the gaseous products with great sensitivity using a gas chromatograph/mass spectrometer (GC/MS). If most of the chemical species already detected at Titan are produced in these experiments, then there is a good possibility that some of the less abundant species produced in our simulations also may be present in Titan's atmosphere but below the sensitivity threshold of the IRIS experiment. These trace species and similar molecules from the same chemical groups would then be prime candidates for detection several years from now by instruments on the Cassini Orbiter and the Huygens Titan Probe.



A portion of the single ion chromatogram obtained by the Goddard GC/MS following a spark discharge experiment using a mixture of methane, nitrogen, and argon with relative abundances appropriate for Titan's atmosphere. The abundance of reaction products resulting from this simulation corresponds to minor species already detected in Titan's atmosphere.

The figure illustrates some of the raw data from our GC/MS experiment. Prior to introduction of the sample to the GC/MS, a series of high-voltage spark discharges were induced in a mixture of methane, nitrogen, and argon with relative abundances appropriate for Titan's atmosphere. The figure shows a portion of the single ion chromatogram for two mass values in the GC/MS experiment. Comparison of the entire mass spectrum at each peak with fragmentation patterns in a mass spectrometer database allows the identities of the molecules to be established. In the experiment, 20 product molecules were identified firmly, including several nitriles and many hydrocarbons. Several additional products whose mass spectra are not included in the database have not been identified yet. The relative abundance of several reaction products of these simulations corresponds to a surprising degree to minor species detected, to date, in Titan's atmosphere. A more detailed study has been initiated to establish the effect of parameters such as the rate of energy deposition and reactant partial pressures on the product distribution.

Contact: Paul Mahaffy (Code 915)
(301) 286-8184

Sponsor: Office of Space Science and Applications

Dr. Paul Mahaffy has conducted research in the Laboratory for Atmospheres at Goddard for 10 years. He is a team member for the Comet Rendezvous Asteroid

Flyby Mission's neutral gas and ion mass spectrometer and a team member for the Cassini Huygens Probe GCIMS. He holds a PhD from Iowa State University.

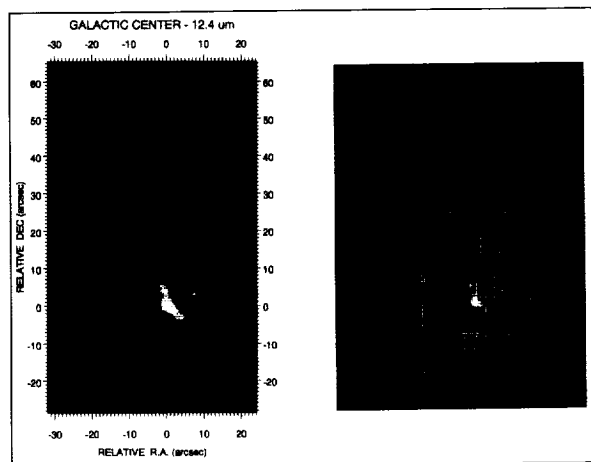
NEW ASTRONOMICAL IMAGES WITH A 5- TO 14-MICRON ARRAY CAMERA

A new infrared array camera system has been developed for high-background astronomical imaging at 5 to 14 microns. Photometry in the thermal infrared (about 10 microns) is dominated by the large background flux from the warm telescope, instrumentation, and the atmosphere. This background is about 10 times larger at 10 microns than it is at 2 microns, where much array astronomy is now being done. The problems of operating an array detector under these difficult conditions have discouraged most potential researchers.

The 58- by 62-pixel Goddard Infrared Array Camera now has completed seven observing runs at the 3.0-meter NASA/Infrared Telescope Facility and one run at the 4.0-meter United Kingdom Infrared Telescope (both located at Mauna Kea Observatory in Hawaii). All eight runs were successful, and the new results are the highest spatial resolution, most sensitive array images ever achieved at these wavelengths. The camera also was used in three unique experiments: the first 10-micron array imaging polarimetry observations, the first two-dimensional infrared speckle interferometry observations, and the first astronomical imaging at 20 microns using an array detector. The observing time required to obtain these data would have been prohibitive using conventional techniques.

Several astronomical research projects have been initiated with the camera, including studies of star formation in cool galactic clouds, the detailed morphology and energetics of the Galactic Center source complex, starburst processes in the nuclei of Seyfert galaxies and the most luminous Infrared Astronomical Satellite (IRAS) galaxies, two-dimensional infrared speckle interferometry of dust-embedded young stellar objects, and high-resolution global mapping of the atmospheric structure of the giant planets. Three achievements with the array camera will be discussed in detail in this report.

The array camera was designed and built in the Infrared Astrophysics Branch at Goddard, based on a 58- by 62-pixel hybrid Si:Ga (gallium-doped silicon)



A 12.4- μ m array camera image of the Galactic Center.

photoconductor array detector. The cryogenic optical system is diffraction-limited and typically produces 1.0 ± 0.1 arc-second stellar images (seeing- and tracking-limited) in long exposures on the telescope. Aberrations, field rotation and distortion (pincushion, etc.) are negligible.

Seeing-limited images of the central 16 arc-second (0.8 parsec) field of the Galactic Center obtained with the array camera at 4.8, 7.8, 8.7, 9.8, 11.6, and 12.4 microns have revealed new structural details in the infrared source complex on the 1-arc-second scale (see the first figure). The first image of large-scale emission structure over a mosaic of 4-by-6 array fields of view (60 by 90 arc seconds) also was made with 1 arc-second resolution at 12.4 microns, revealing a striking similarity between the warm dust distribution and the ionized gas emission shown by radio continuum interferometry. However, there are intriguing discrepancies between the positions of several of the bright source features. The most pronounced positional shift is seen at the positions of IRS 2 and nearby IRS 13. These two sources lie at the western edge of a 2-arc-second mini-cavity. The relative differences may be due to stellar wind which has depleted the dust particles close to the source of the outflow.

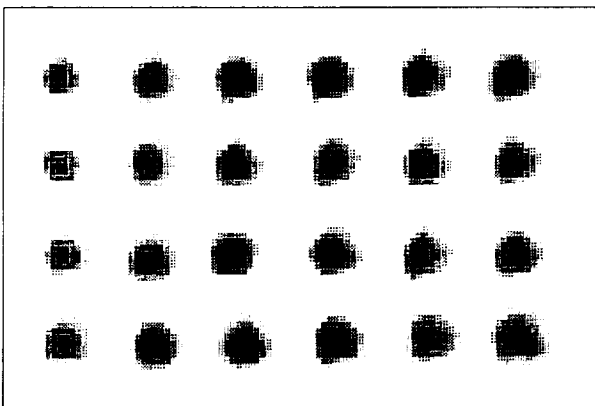
Color temperature distribution derived from the multi-color images suggests that sources of heating other than a central source at IRS 16/Sgr A* embedded along the ionized filaments in Sgr A West contribute to the heating of the intermixed dust, and that a combination of a central luminosity source and heating by embedded sources at



several of the bright peaks is responsible for the observed infrared and radio continuum emission.

The array camera also has been used to make the first two-dimensional infrared speckle interferometry observations (see the second figure). Short-exposure images of the dust-shrouded carbon star IRC+10216 at 5 microns resolve sub-arc-second source structure in the circumstellar shell on a scale smaller than the conventional limitations of atmospheric seeing and telescope aberrations. Fifty separate 5-mm short-exposure (1/30 sec) narrow-band (8 percent) images of IRC+10216 were taken as well as 50 images of reference star R Leo obtained under the same conditions. The pixel size is a 0.26 arc-second square, and the diffraction limit of the 3-m NASA Infrared Telescope Facility (IRTF) is 0.35 arc second at 5 microns. Seeing was excellent and differences between the images appear primarily as seeing-induced image wobble. In a conventional observation the diffraction-limited information would be blurred completely by atmospheric seeing effects.

The two sets of speckle images were processed using four techniques: centered direct sums (shift and add) of the images; two-dimensional speckle interferometry (power spectrum analysis); iterative deconvolution of one data set by the other; and Knox-Thompson speckle imaging processing. The spatial structure results obtained by all methods generally are consistent with a slightly asymmetric resolved source of average diameter of about 0.065 arc second. The Knox-Thompson speckle imaging reconstruction, the iterative deconvolution of IRC+10216 by R Leo, and the ratio of their power spectra all show a spatial asymmetry in IRC+10216. The apparent 5-mm



Individual short-exposure, narrow-band speckle interferometry observations of IRC+10216 taken at 5 μm in March 1988.

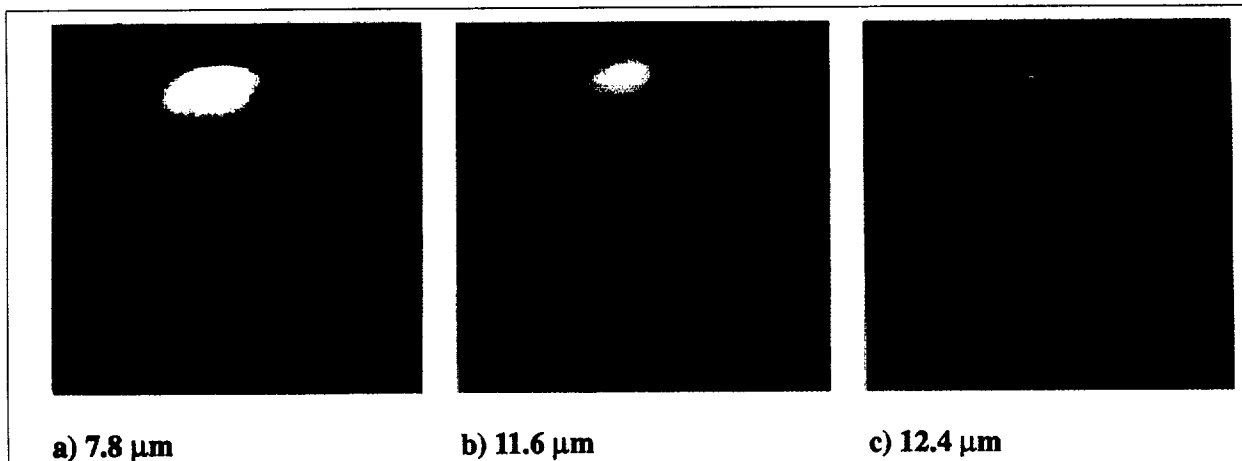
source asymmetry detected here is consistent with previous scanning results; however, the observed infrared fringe visibility of IRC+10216 is complex and time variable, and more extensive two-dimensional speckle observations on a larger telescope are planned.

Finally, new stratospheric infrared methane and ethane emission structure in the stratosphere of Saturn has been discovered at 7.8, 11.6, and 12.4 μm . The high spatial resolution global images show a variety of new features, including: a previously unknown narrow equatorial belt of enhanced 7.8- μm emission; a prominent, symmetrical north polar hot spot at all three wavelengths (which previously had not been imaged); and mid-latitude structure which is asymmetrically brightened at the east limb (see the third figure). The results confirm the polar brightening and reversal predicted by recent models for seasonal thermal variations of Saturn's stratosphere. The narrow equatorial belt of emission is about 10 to 30 percent brighter than the adjacent mid-latitude region. Corresponding but weaker equatorial emission is seen at 12.4 μm (C_2H_6) but is not detected unambiguously at 11.6 μm .

The common orientation and proximity of the inner edge of the ring, the ring shadow, and the narrow equatorial belt suggest a physical interdependence between Saturn's ring and the belt. An atmospheric current system (equatorial electrojet), convective transport of atmospheric gas along the sharp temperature discontinuity at the inner edge of the ring shadow, and infall of neutral material from the rings represent possible stimulating mechanisms for the observed features.

Other achievements with the array camera included:

- The first imaging polarimetry observations at thermal infrared wavelengths were carried out successfully on the Galactic Center Sgr A West complex at the United Kingdom Infrared Telescope (UKIRT). The image shows the magnetic field morphology, free of the confusion of the scattering component of polarization detected at near-infrared wavelengths.
- Seeing-limited array imaging at 12.4 μm of the Orion BN/KL infrared nebula has resolved a variety of luminous infrared sources, indicating that the luminosity of the region is not attributable to a single powerful object.
- New 12-micron array camera images of the well-known Trapezium star cluster, featureless in previous



(a, b, and c) a. A 7.8- μm image of the disk of Saturn. Saturn's ring system is not detected. b. An 11.6- μm image of the planet. The dark spots near the east limb result from localized array defects not affecting the rest of the image. c. The same image at 12.4 μm .

mapping observations, revealed complex structure, including a dramatic cavity-like, crescent-shaped shell surrounding the star Theta 1 D Orionis. This well-resolved dust shell provides a unique example for the study of evolving dust clouds associated with massive luminous stars and HII regions.

Contact: Daniel Y. Gezari (Code 685)
(301) 286-3432

Sponsor: NASA Headquarters, Astrophysics Division

Dr. Daniel Y. Gezari, an astrophysicist in the Laboratory for Astronomy and Solar Physics, has 15 years of experience at Goddard. He is Principal Investigator for the NASA Catalog of Infrared Observations and was Instrument Scientist for the Space Infrared Telescope Facility from 1984 to 1987. He holds an AB in physics from Cornell University, an MS in physics from New York University, and a PhD in astronomy from the State University of New York at Stony Brook. He received the NASA Medal for Exceptional Scientific Achievement in 1990 for his development of the Goddard Infrared Array Camera.

AN ALL-SKY MONITOR FOR A SOVIET HIGH-ENERGY ASTROPHYSICS OBSERVATORY

Astrophysics has benefited greatly from the ability to observe new celestial phenomena as quickly as possible after new objects become visible. This was well demonstrated with the discovery of a supernova in the

Large Magellanic Cloud in February 1987, when astronomers throughout the world were able to bring powerful telescopes to bear on the entire electromagnetic spectrum within a few days of the stellar explosion. In X-ray astronomy, this capability is no less important, and in some ways is even more so, since most of the X-ray binaries in our galaxy are transients, with outburst intervals ranging from months to many years. It is thus essential to have X-ray detectors that monitor the sky continuously on a time scale as short as hours to search for new or recurrent sources. These data can then be used as an alarm to alert observers using more powerful telescopes, and also to provide long-term records of the X-ray intensities of many sources. Such long-term light curves have provided sound evidence that the accretion disks and/or the companion stars in many X-ray binaries are precessing.

Typically, techniques for all-sky X-ray monitoring include pseudo-imaging devices (i.e., pin-hole cameras) with large fields of view or collimated detectors that scan over large regions of the sky. We have developed a pin-hole all-sky monitor capable of observing the entire sky all of the time. Recently, an opportunity arose to adapt this monitor system to the Soviet Spectrum X-Gamma mission scheduled for launch in 1994. This spacecraft will contain a very ambitious and powerful observatory with instruments for observing extreme-ultraviolet, X-ray, and gamma-ray sources.

The Monitoring X-ray Experiment (MOXE) is designed to monitor the entire sky in the X-ray range of 3 to 20 keV.

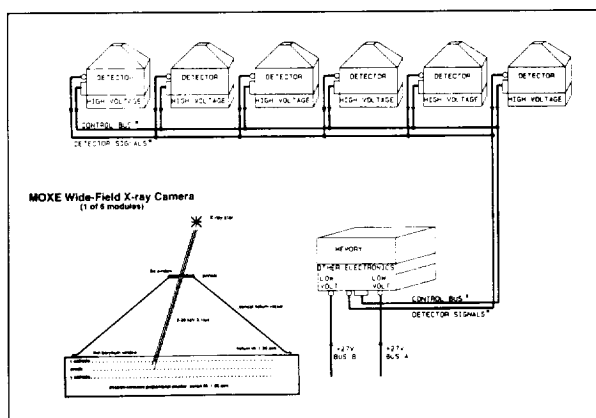


The experiment is a collaboration between the Los Alamos National Laboratory and the Laboratory for High-Energy Astrophysics at Goddard. The experiment consists of six single pin-hole X-ray cameras which use two-dimensional imaging proportional counters as the X-ray detectors. There also will be a command and data system and a large solid-state memory (about 1/2 Gbit) for storing data up to 32 hours. Since the X-ray sky has several dozen well-known X-ray sources that nearly always are bright, a star tracker or camera is not necessary, since these steady sources provide a celestial coordinate system with which to locate the new sources.

The MOXE is being designed, fabricated, calibrated, and tested through the joint efforts of a team of scientists and engineers located at several facilities throughout the United States and the Soviet Union.

Under contract to the Los Alamos National Laboratory, the Oak Ridge Detector Laboratory, Inc. (ORDELA), is furnishing the position-sensitive detectors based on modification of an already existing design. These detectors are approximately 32 cm on a side and will allow imaging resolution to better than 0.5 cm. ORDELA also will provide the voltage-sensitive preamplifiers and over-current detection and signaling.

Since the proportional counter is filled with xenon gas to a pressure of about one atmosphere, the force on the detector window (beryllium with a thickness of 75 microns) is over 2,000 pounds in space. Thus, a very strong window support structure must be fabricated that simultaneously provides maximum throughput of x rays to the detector volume. We have chosen to do this



The MOXE wide-field X-ray camera, designed to monitor the entire sky in the X-ray range 3 to 20 keV.

by transferring essentially all of that force to the pin-hole structure. The pin-hole dome will be filled with helium gas to a pressure equal to that of the counter gas (helium is transparent to x rays with energies above 3 keV). The force on the pin-hole window (2.5×0.625 cm of beryllium, 50 microns thick) is only about 4 pounds, and can be supported easily. An engineering model of this detector has been fabricated and tested successfully.

The high- and low-voltage power supplies are being provided by the engineering division of the Institute for Space Research located at Bishkek, USSR. The high-voltage power supplies are capable of 128 levels between 2,000 and 3,100 volts DC.

The memory module (ILMM) will have the capability of storing the MOXE 5-Kbps data stream for up to 32 hours. This is necessary since the 4-day orbit of Spectrum X-Gamma will only allow contact sessions with the ground at that interval.

The analog signal processing and the digital processing, the ground support equipment, and the system engineering are all responsibilities of Goddard. This is being accomplished in the Electronic Systems and Instrument Development Branches, with scientific guidance from the X-ray Astrophysics Branch.

The analog processing includes both position- and energy-determining circuitry for each of the six MOXE detectors. Several photon rate accumulators also are included. All data are presented in digital form to the digital processing system.

The digital processing is based on a dual microprocessor design that screens the data and places the acceptable events annotated with arrival times and detector identification into the ILMM. During contact sessions, the processor, observing the MIL-STD-1553 protocol, extracts the data from the ILMM and transmits it to the spacecraft for relay to the ground. In addition, it will gather housekeeping data for inclusion in the MOXE data stream and accept commands from the spacecraft for distribution within the MOXE.

The ground support equipment will be capable of simulating the spacecraft in all aspects. It will display the MOXE data in several formats, the most important of which is a histogram of x-y positions with energy as a parameter. It is anticipated that the same ground support equipment will be used postlaunch for quick-look data processing.

The instrument should provide the fluxes of more than 300 celestial X-ray sources per day, roughly equivalent to the number of sources in the entire Uhuru X-ray catalog.

Contact: Robert M. Joyce (Code 663)
(301) 286-5497

Richard L. Kelley (Code 666)
(301) 286-7266

Sponsor: NASA Headquarters, High-Energy
Astrophysics Branch

Mr. Robert M. Joyce has 25 years of experience at Goddard in the Laboratory for High-Energy Astrophysics. He has participated in research for numerous projects and missions, including HEAO, Pioneer, Helios, Voyager, and the Gamma Ray Observatory. He received a BS from the Capitol Institute of Technology.

Dr. Richard L. Kelley, a scientist in the X-ray Astrophysics Branch of the Laboratory for High-Energy Astrophysics, has been at Goddard for 7 years. His research interests focus on cryogenic detector development. He holds a PhD from the Massachusetts Institute of Technology.

THE GODDARD HIGH-RESOLUTION SPECTROGRAPH (GHRS)

The launch of HST opened a new era in space astrophysics. The HST is a long-term space observatory for astronomical imaging and spectroscopic observations from the ultraviolet through the infrared. The GHRS is central to HST's spectroscopic capabilities. It is the most versatile and highest resolution astronomical spectrograph ever orbited. The GHRS scientific instrument definition team, led by members of the Laboratory for Astronomy and Solar Physics (LASP), proposed and guided the development of the instrument.

The ultraviolet, below the atmospheric cutoff at 3,000 Å, is truly the Rosetta Stone for diagnosing the physical conditions of cosmic plasmas. Nearly all of the strong atomic and molecular lines lie in this part of the spectrum. Astronomical ultraviolet spectroscopy has a long history, beginning with sounding rocket flights in the 1960s and reaching a high state of sophistication with the IUE. With the GHRS, ultraviolet astronomical spectroscopy truly comes of age. The range of questions that can be addressed and the versatility of the analytic tools available

for the spectroscopic study of cosmic bodies are extended enormously by its sensitivity, flexibility, and resolution.

The GHRS is designed to operate solely in the vacuum ultraviolet, between 1,150 and 3,400 Å, with resolutions ranging from 2,000 to nearly 10^5 . A one-dimensional, photon-counting solid-state array—the digicon—serves as the detector, allowing for rapid data collection in as short as 50 ms. Unlike integrating imaging detectors, vidicons, CCDs, and the like, digicons have pulse-counting circuitry that provides anti-coincidence exclusion of cosmic ray-induced detector events, reducing noise and preventing spurious emission features from contaminating spectra. Low ($R=2,000$) and intermediate ($R=25,000$) spectra are obtained using first-order ruled gratings; the highest resolution ($R=90,000$) is achieved using echelles. A unique feature of the GHRS is its ability to perform Doppler compensation for spacecraft motion by magnetically steering the image of the spectrum across the diode array using flight software. Detector fixed-pattern noise is removed as well by offsetting the grating position several times in the course of a single observation, thereby shifting the spectrum over the diode array. Onboard wavelength calibration is provided by Pt-Ne lamps while absolute sensitivity is provided by astronomical sources.

The GHRS status (November 1990) is that all instrument functional capabilities have been tested, and the spectrograph is working flawlessly. The digicons are affected less by cosmic rays within the South Atlantic Anomaly than originally expected; this will allow a longer period of integration of bright targets than originally anticipated. Any image motion induced by the Earth's magnetic field is $< 1/4$ diode. The resolution through the large science aperture (2 arc seconds or 8 science diodes wide) was expected to be somewhat degraded by the spherical aberration of the HST optical telescope assembly. Observations show that the effect does not reduce the spectral resolution by more than a factor of three. Some additional resolution can be recovered via deconvolution.

Digicon photo-sensitivity is well within laboratory calibrations. There is no evidence of degraded ultraviolet performance by either the spectrograph or the telescope. Field mapping and target acquisition are working very well, even though they are somewhat more difficult than originally expected because of



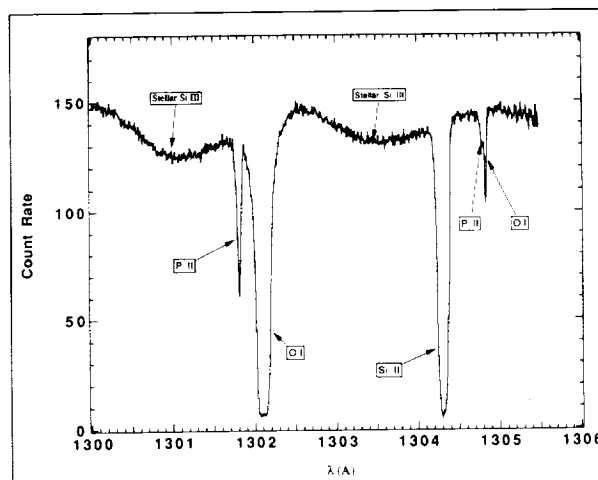
problems external to the spectrograph. All mechanical components are working superbly.

The GHRS is designed to study cosmic objects from Solar System bodies to quasars. To date, spectra have been obtained for a wide variety of objects. Low-resolution spectra have been obtained of stars in the Large Magellanic Cloud, the nearest galaxy to ours in the Local Group. Intermediate dispersion spectra have been obtained of Chi Lupi, a chemically peculiar, slowly rotating young binary star. Finally, high-resolution echelle spectra have been obtained of Xi Persei, a hot, massive, distant star in the next spiral arm within our galaxy. Xi Persei is both a bright light source for the study of the intervening interstellar medium and a mass-losing star in its own right.

The interstellar medium, the tenuous material out of which giant molecular clouds coalesce and the ultimate fuel for galactic star formation, is best revealed through absorption line studies in the ultraviolet. The density is sufficiently low that the atomic component of the medium resides almost completely within the ground state of the constituent ions, and the strongest absorption lines arising from this component are all found shortward of 3,000 Å. Typical densities are of order 0.01 to 10 cm^{-3} and temperatures range from 100 to 1000 K in the warm atomic clouds to greater than 10^6 K in the stellar wind- and supernova-shocked coronal gas. Typical velocities associated with the interstellar gas range from barely supersonic, only a few kilometers per second in the quiescent medium and in warm clouds, to hundreds of kilometers per second in the vicinity of strong stellar winds, stellar associations, and supernova remnants.

The figure shows a portion of a GHRS echelle spectrum of the O-type star Xi Persei. The broad stellar photospheric lines are seen underlying the absorption from interstellar atoms of ionized phosphorous and silicon and neutral oxygen. The O I feature at 1,304 Å is a complex blend of several clouds.

The GHRS has the capacity to resolve individual clouds to a velocity scale of about 1 km/s. With such high resolution, individual clouds can be isolated along any line of sight and the abundances of the elements, temperatures, and densities can be measured. A complete picture can be pieced together of the processes connected with elemental depletion onto dust grains, the solid phase of the interstellar medium, and the seed for the cold molecular clouds, and ultimately, for star



Interstellar lines in the spectrum of Xi Persei. The strongest feature is a blend of neutral oxygen at 1,302 Å, showing that there are several clouds of cold gas along the line of sight to the star. The effective resolution of this spectrum is about 90,000, or about 3 km/s. The stellar photospheric Si III lines clearly are seen as broad, shallow absorption features. The differences between the interstellar line profiles show that the singly ionized gas (P II, Si II) is more closely connected with Xi Persei than is the cooler atomic gas.

formation. It is possible to determine the turbulent motions within these clouds, to study the inhomogeneity of the medium on small spatial scales, and to see the connections between the gas and the stars and how the elements are incorporated into the medium and redistributed throughout the galaxy.

In addition, because of the repeated heating of the gas by star-produced shocks and radiation, the interstellar medium consists of many different phases completely out of thermal equilibrium with one another. One such phase, the million-degree coronal gas, was first discovered through ultraviolet observations with the Copernicus satellite nearly 2 decades ago and has been studied since using IUE. The details of the distribution of this material, its extent above the galactic plane, and its dynamics are major unanswered questions connected with galactic evolution. The coronal gas is presumed to be lofted into the outer galactic halo by heating from continual collision of supernova shocks with the interstellar matter in the plane and subsequent expansion of the gas. The GHRS has the sensitivity to probe these distant portions of the galactic system, and to study absorption against stars at very great distances

from the Sun and far from the symmetry plane of the spiral, in order to look at the energetic and mechanical processes connected with the gas. Only a few stars in the Magellanic Clouds, each giving information along only one line of sight, have been within reach of high-resolution IUE observations. The GHRS will be capable of observing hundreds of extragalactic sources with a resolution of better than 20 km/s. In the process, regions will be observed in the halo of the Magellanic Clouds as well, permitting a detailed comparison of the processes that structure the interstellar gas in three very different stellar systems.

The study of the galactic halo has broader implications for cosmology. The forest of absorption lines observed in the spectra of distant quasars is formed in the halos of intervening galaxies along the line of sight to the quasar. The study of the gas in our own halo will be important in the interpretation of the signature of galactic evolution preserved in the quasar absorption line forests.

Contact: Sara R. Heap (Code 681)
(301) 286-5359

Sponsor: Office of Space Science and Applications

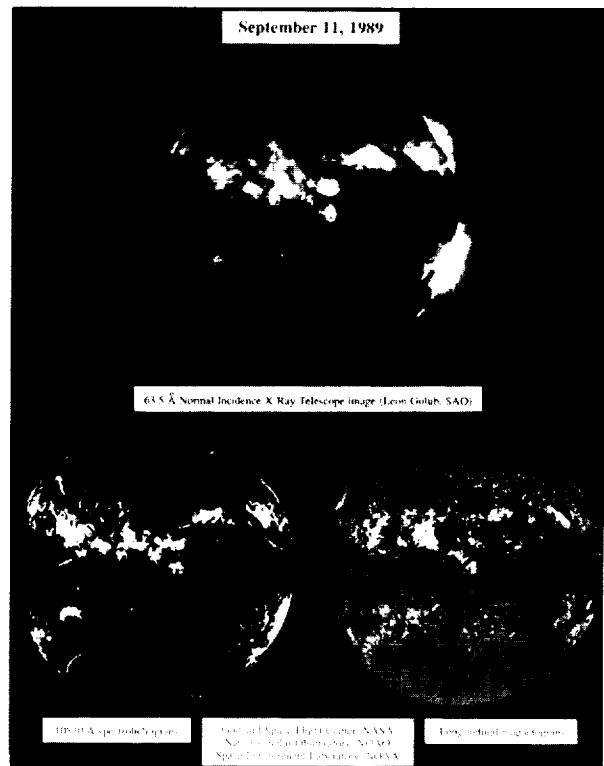
Dr. Sara R. Heap is Co-Principal Investigator for the HST GHRS. In this capacity, she plays a major scientific and technical leadership role within one of NASA's highest priority and most visible programs. She has 20 years of experience at Goddard, and previously served as Deputy Principal Investigator for the GHRS. She holds a BA in astronomy from Wellesley College, and an MA and a PhD in astronomy from the University of California at Los Angeles. She works in the Astronomy Branch of the Laboratory for Astronomy and Solar Physics.

HIGH-RESOLUTION MAGNETOGRAPH FOR THE SOUTHWEST SOLAR FACILITY

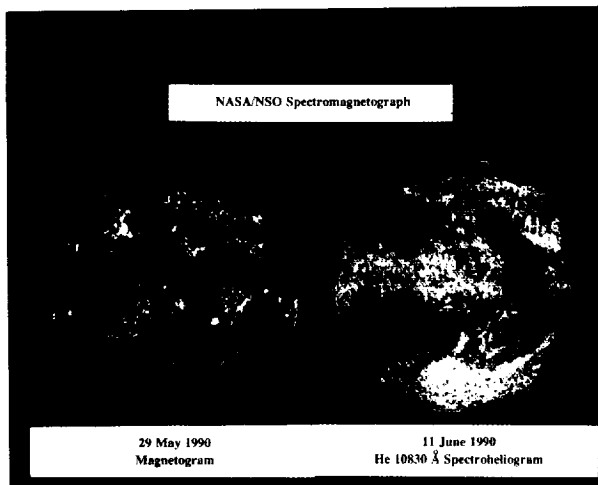
Goddard scientists in LASP help to operate, maintain, and improve the National Solar Observatory's (NSO) Kitt Peak Vacuum Telescope (KPVT) facility in Arizona. Two LASP scientists are stationed as long-term visitors at NSO/Tucson where they represent the Laboratory, assist in observation, instrument improvement, and data reduction and also conduct independent research programs. The Laboratory and NASA thereby gain full access to the facility's daily, high-resolution,

whole-Sun magnetograms, taken in a near-infrared line of neutral iron, and to spectroheliograms, taken in the 10,830-Å spectrum line of neutral helium.

The richness and utility of these data are well illustrated in the accompanying picture which makes plain the links between the magnetic loops and streamers in the solar corona seen in soft X-rays, the high chromospheric and coronal structures visible in He 10,830 Å, and the underlying photospheric magnetic fields, here portrayed as a gray-scale image with strong magnetic fields pointing toward and away from the observer appearing white and black, and magnetically neutral areas appearing gray. Such data are used extensively for operational planning and subsequent scientific interpretation of NASA flight mission and rocket experiments such as the Solar Maximum Mission, Ulysses, and LASP's Solar Extreme Ultraviolet Rocket Telescope and Spectrograph. For example, data taken during the sounding rocket flight of the Normal-Incidence X-ray Telescope (NIXT) are shown in the first figure. The daily magnetograms also are important components of the continuing effort to monitor and



A comparison of the ground-based data (lower panels) with the soft X-ray picture obtained during a sounding rocket flight.



Data from the new magnetograph showing active regions on the Sun near the maximum of solar activity.

understand the near-Earth space environment and the solar inputs to Earth.

An important new instrument—the NASA/NSO Spectromagnetograph—has been developed to operational status. This new facility will both replace and improve upon the aging existing instrumentation which has been in continuous service for over 15 years.

At the KPVT, a coelostat is mounted atop a 23-m tower to reduce distortions by ground-level turbulence, and focusing optics are housed in a vacuum tank to avoid image degradation by thermal convection inside the telescope. An electronically modulated half-wave retarder (Kerr Cell), a quarter waveplate, a linear polarizer, and broadband blocking filters admit spectrally isolated, alternating states of circularly polarized light to the entrance slit of a 10.7-m vertical Littrow spectrograph for Doppler-Zeeman analysis of appropriate spectral lines. In the current magnetograph, two 512-element linear detector arrays are placed at the exit plane of the spectrograph and are oriented perpendicular to its dispersion so that each pixel pair along a 512 arc-second column in the spatial dimension isolates two narrow bandpasses on either side of a spectrum line. Appropriate sums and differences of the paired readouts of the arrays at the two polarization states are computed in real time to yield velocity, total intensity, and longitudinal magnetic flux at each position along the entrance slit. Computerized scanning of the main image produces eventual digital raster images of the Sun with an effective pixel size of 1 by 1 arc-second as shown in the accompanying figure.

By contrast, the new Spectromagnetograph uses specially designed anamorphic transfer optics to re-image fully resolved solar spectra on a two-dimensional CCD detector. Under the control of an imaging workstation, commercial video processing boards digitize and accumulate the long-slit spectra in both states of circular polarization. The workstation is also the heart of the observer interface to the telescope and instrumentation. With the aid of software windows and real-time graphics, the observer controls most aspects of instrument set-up and data acquisition with a mouse and keyboard. A breadboard optical system is in place at one of the two spectrograph ports at the KPVT, and the instrument is fully capable of acquiring all the forms of data produced by the Diode Array Magnetograph, as shown by the two full-disk images in the second figure. A sturdier and more compact re-imaging system, optically identical with the breadboard layout, is being fabricated and will be installed in the near future. For the next few months, observations will be made with both the Diode Array Magnetograph and the Spectromagnetograph to insure the viability of the long-term record for scientific studies of the solar cycle.

In addition to replacing the current instrument, the Spectromagnetograph can record the full-line profiles in both states of polarization for limited spatial fields of view (e.g., solar active regions). Full analysis of these profiles substantially reduces spurious (and serious) crosstalk between magnetic fields, velocity fields, and the temperature-pressure structure of the solar atmosphere which contaminates the present observations because of their limited spectral sampling; moreover, thermodynamic information can be derived from the Spectromagnetograph profiles. Indeed, when the original design is fully implemented, an attached vector processor will reduce and analyze the resolved line profiles in cadence with the spatial scanning of the image. Thus, well-calibrated magnetic, velocity, and thermodynamic data will be produced in real time for all image formats and scientific analysis can proceed without cumbersome reduction procedures.

Both as a stand-alone facility and in cooperation with coordinated solar observing campaigns using both space-based and ground-based instrumentation, the Spectromagnetograph will be used to initiate new studies of the interaction of velocity and magnetic fields with the thermodynamic structure of the Sun from below the visible surface (through the techniques of helioseismology) to the outer layers of the atmosphere (through complementary

flight mission data). Simultaneous continuum and differential photometry of surface features associated with solar irradiance variations also can be made on a systematic, long-term basis, and rapid flare-associated phenomena can be studied with new confidence. The real-time position and width analysis of the line profiles will be a unique feature of the completed system with potential applicability to high-resolution, space-based imaging spectrometers where finite telemetry bandwidth demands all possible reduction of data volume without loss of information.

Contact: Harrison Jones (Code 682.2)
(301) 286-2865

Sponsor: Office of Space Science and Applications

Dr. Harrison Jones has been an astrophysicist in the Laboratory for Astronomy and Solar Physics since 1969. His research interests include the solar magnetic field, radiative transfer, and helioseismology. Dr. Jones holds a BS in astrophysics from the University of Rochester and a PhD in astrophysics from the University of Colorado.

A SOLAR INFRARED MAGNETOGRAPH

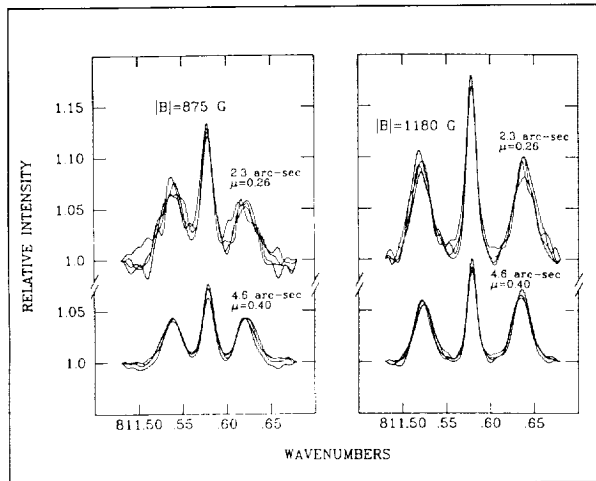
Magnetic fields on the Sun were first discovered by George Ellery Hale in the early years of this century. Hale used the Zeeman effect, wherein absorption lines in the visible region of the spectrum are split into several components by interaction between the absorbing atoms and the magnetic field near the solar surface. However, the interaction energy which causes the line splitting is a relatively small effect for field strengths found on the Sun. Consequently, the Zeeman splitting of visible spectral lines is a subtle effect in the solar spectrum.

To study solar magnetic fields, solar physicists have relied on the fact that the Zeeman effect also causes the split lines to have different polarizations. Solar magnetographs in common use today use rapid switching between orthogonal polarizations, so as to very sensitively infer the presence of a polarization signal on the portion of the Sun which is being observed. However, since the splitting of the spectral lines is incomplete, there is much overlap of orthogonal polarizations, and the measured net polarizations are often quite small. Moreover, in this so-called weak splitting regime, the measurements do not actually give the absolute strength of the field but more commonly yield quantities such as the line-of-sight component of the

magnetic flux. This is a problem for solar physicists who want to learn about the physical basis of phenomena such as solar flares, wherein magnetic energy is released by some as yet poorly understood process. To understand these mysterious processes, measurements of the full magnetic vector are required; i.e., both the field strength and its direction must be known over an entire solar active region. Using visible-region lines, such measurements have been notoriously difficult.

A new opportunity to improve greatly solar magnetic field measurements occurred in the early 1980s when mysterious emission lines were discovered in the solar spectrum, far out in the thermal infrared near 12- μm wavelength. These lines were quickly identified as being caused by nearly hydrogenic transitions in neutral magnesium, aluminum, and silicon. What is especially interesting about these emission lines is the fact that they show very large Zeeman splitting. Relative to the width of the lines, the Zeeman effect produces a splitting which is proportional to wavelength. The long wavelength of these infrared lines results in a Zeeman splitting which is nearly an order of magnitude greater than lines in the visible. Several examples of the well-resolved Zeeman splitting seen in solar magnetic regions are illustrated in the figure. Because of this enormous Zeeman splitting, these lines not only give a quantitatively more sensitive measurement of solar magnetic fields, but they also allow solar physicists to derive information about the magnetic field which cannot be obtained using traditional visible-region magnetographs. Why the lines are present in emission, instead of the usual absorption spectrum, remains unexplained. However, one possibility is that they are formed in the solar chromosphere at an altitude well above the visible photosphere. If so, they are even more important for magnetic field studies, because the characteristics of chromospheric fields are poorly understood and especially difficult to derive.

Very sensitive Zeeman lines have another important advantage: they often can show us the nature of very fine scale magnetic structures. Even when such structures are not spatially resolved, they often can be magnetically resolved; i.e., the nature of the small-scale structure can be apparent in the Zeeman pattern, even when the spatial resolution is only moderate. For this reason, infrared magnetic observations are highly complementary to high spatial resolution observations from space platforms, such as NASA's planned Orbiting Solar Laboratory. We therefore are developing an



Infrared emission lines in the spectrum of a sunspot penumbra, observed at two different locations from two differing angles. The sunspot magnetic field causes each line to appear as having three components. The separation of components increases in proportion to the magnetic field strength.

infrared vector magnetograph, using a high-resolution Fabry-Perot etalon and liquid helium-cooled infrared array detectors. This development presents special challenges. In the thermal infrared, telescope and optical components emit background radiation, which can overwhelm the solar emission line signal unless cold, narrow-band filters are used to limit the background. Moreover, such a magnetograph requires very high spectral resolution, and this never before has been accomplished in an instrument which uses thermal infrared array detectors. Nevertheless, it is likely that such an instrument can be constructed successfully, and it may serve as the prototype for a new generation of solar vector magnetographs.

Contact: Drake Deming (Code 693)
(301) 286-6519

Donald E. Jennings (Code 693)
(301) 286-7701

Sponsor: Office of Space Science and Applications

Dr. Drake Deming is Head of the Planetary Systems Branch of the Laboratory for Extraterrestrial Physics. He holds an AB in mathematics from the University of Chicago and a PhD in astronomy from the University of Illinois. He has 10 years of experience at Goddard.

Dr. Donald E. Jennings has 15 years of experience at Goddard in the Planetary Systems Branch of the Laboratory for Extraterrestrial Physics. His research focuses on planetary and solar astronomy. Dr. Jennings received a PhD in physics from the University of Tennessee.

MULTILAYER COATING ON HIGH-DENSITY TOROIDAL EXTREME-ULTRAVIOLET (EUV) GRATING

Multilayer coatings offer the potential for significantly enhancing the efficiency of optical components operating near normal incidence at extreme-ultraviolet (EUV) wavelengths, where all individual materials have very poor reflectance. This technology already has been demonstrated by several groups on mirrors that are either flat or gently curved, and even on gratings of low ruling density. Now, a 10-layer iridium-silicon multilayer has been applied to a flight-spare replica of the grating for a rocket experiment developed by Goddard's Solar Physics Branch. That instrument is the Solar EUV Rocket Telescope and Spectrograph (SERTS), which was designed to provide high spectral- and spatial-resolution observations of the solar corona at EUV wavelengths. This represents the first time that such a specialized coating has ever been attempted on a large format grating (95 by 88 mm) with high-density rulings (3,600 lines/mm). The coating was designed and applied by members of the Optics Branch at Goddard. The fact that the grating has a very delicate blaze on a replicated toroidal substrate made it even more challenging to produce the extremely high accuracies and uniformity necessary for a successful multilayer coating.

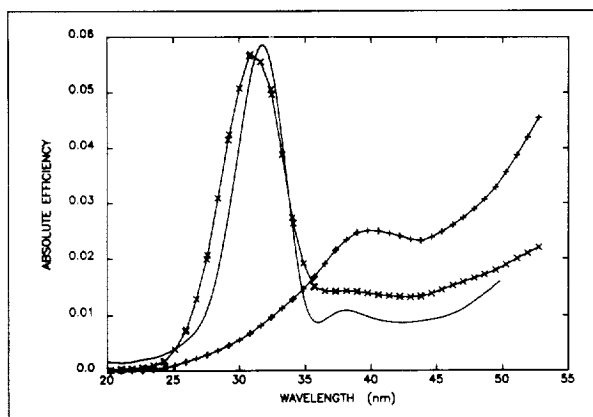
We have completed a series of measurements on this multilayer-coated grating at the SURF-II synchrotron facility of the National Institute of Standards and Technology (NIST), which demonstrate that the multilayer coating produced a peak absolute efficiency of 3.3 percent in first order at 31.1 nm, as shown in the first figure. This is the highest efficiency at the wavelength yet reported for a high-resolution grating operating at near-normal incidence. The greatest improvement occurred at 29.7 nm, where the grating's first-order efficiency increased from 0.30 percent to 2.8 percent, more than a factor of 9 above that of the standard gold coating. The multilayer coating provided some enhancement over the entire 10-nm band from 25 to 35 nm. In fact,

the measurements suggest that efficiency was even enhanced over the short wavelength band from 20 to 25 nm, although the individual values were so low that the resulting ratios are very uncertain there.

Using a constant normalization factor of 14 percent (presumably due in large part to the grating groove efficiency), the theoretically predicted reflectance curve for the multilayer agrees quite well with the measured performance, as also can be seen in the first figure. The multilayer grating efficiency does seem to peak at a wavelength about 0.5 nm less than that for the design curve, an amount which is roughly equivalent to uncertainties in the measurement's absolute wavelength scale. However, one definite difference is that the design's FWHM bandwidth of 4.5 nm is somewhat narrower than the actual measured value of 5.5 nm.

In any case, these bandwidths for multilayer-coated gratings are well matched to spectrographic instruments that use two-dimensional array detectors such as EUV-sensitive CCDs, whose active dimensions can be as large as 1 or 2 cm. With a number of pixels on the order of 1,000, such a system could provide high spectral resolution at EUV wavelengths over a bandpass of more than 40 nm with high sensitivity, if the multilayer coating itself did not degrade significantly the spectral performance of the toroidal grating.

To investigate that possibility, we also made before-and-after measurements of the multilayer grating's spectral



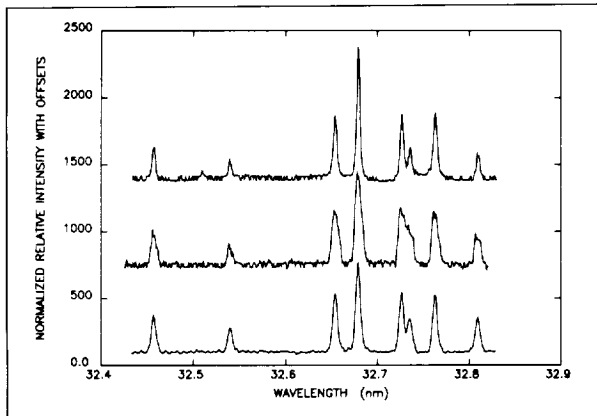
Absolute EUV efficiency of the SERTS test grating before (+) and after (x) multilayer coating. For comparison, the solid curve is the calculated theoretical reflectance of the design multilayer itself, scaled by a normalization factor of 0.14.

resolution in the SERTS Spectrograph Test Chamber at Goddard. This facility allows the spectrograph section of the SERTS rocket instrument itself to be attached to a vacuum system provided with a hollow cathode gas flow EUV light source. The light source uses a combination of helium and neon gases to produce a large number of spectral lines throughout the EUV wavelength range of interest. Since the spectrograph's entrance aperture, aluminum filter, toroidal grating, and film camera can all be flight units, this arrangement permits the final alignment and focus adjustments to be made on the SERTS optical components, as well as providing the pre- and post-flight instrumental performance parameters directly in the EUV wavelengths of interest.

For the tests described here, the original resolution measurements were made on the toroidal grating that was used in the two most recent flights of the SERTS rocket experiment, as a part of their pre- and post-flight calibrations. At that time, the grating selected for flight demonstrated a spectral resolution similar to its replica-mate. After the flight-spare grating was coated with the 10-layer Ir/Si multilayer, and after its EUV reflectance was remeasured at NIST, it was substituted for the SERTS-3 flight grating in the Spectrograph Test Chamber and tested for spectral resolution.

The resulting spectral traces over a number of EUV Ne II lines are shown in the second figure, which compares the resolution of the multilayer-coated grating with that of the gold-coated grating used in the SERTS-2 and SERTS-3 rocket flights. Clearly, the grating's excellent spectral imaging properties have not been degraded by the multilayer coating or by the process of applying it. The small difference in average line widths measured for the five strongest unblended lines seen in the figure (at 32.46, 32.65, 32.68, 32.76, and 32.81 nm) are well within the expected variations caused by errors in focusing or alignment, or caused by differences in the widths of the various slits used in the measurements.

In summary, the application of a multilayer coating to a large, high-density, aspheric diffraction grating replica has produced a significant enhancement in first-order efficiency over more than a 6-nm spectral band at wavelengths around 30 nm. This implies that a considerable improvement in throughput can be achieved in EUV instruments like SERTS that use gratings at normal incidence. The studies carried out to compare the



Microdensitometer traces of EUV Ne II spectra produced with a gold-coated grating (top and middle) and with a multilayer-coated grating (bottom). The top curve is from SERTS-2 pre-flight tests; the middle one is from SERTS-3 pre-flight tests.

spectral performance for the SERTS flight-spare grating after depositing the multilayer coating demonstrate that the grating suffered no loss in its excellent spectral resolution due to the coating process. These successful results have important implications for future instrument applications, such as for the Coronal Diagnostics Spectrometer on the Solar and Heliospheric Observatory (SOHO) mission and for the X-Ray EUV Imager experiment being considered for the Orbiting Solar Laboratory mission, both of which are based in part on the optical design of our SERTS rocket experiment. An investigation of the long-term stability of the new multilayer-coated grating is planned for the future.

We are now in the process of shipping the SERTS rocket experiment, including the multilayer-coated grating, for a scheduled flight in May 1991. This will be the first space flight of this grating.

Contact: Roger J. Thomas (Code 682.1)
(301) 286-7921

Sponsor: Office of Space Science and Applications

Dr. Roger J. Thomas has 20 years of experience at Goddard. He is an astrophysicist in the Solar Physics Branch of the Laboratory for Astronomy and Solar Physics. Dr. Thomas is a Co-Investigator on SERTS and on the X-ray EUV Imager, the Deputy Project Scientist for the Orbiting Solar Laboratory, a Co-Investigator for the Solar Ultraviolet Measurements of

Emitted Radiation project, and a Co-Investigator for the Coronal Diagnostic Spectrometer. He holds a BS in physics, an MS in astronomy, and a PhD in astronomy from the University of Michigan.

PHOTODISSOCIATION OF THE OH RADICAL

Gaseous free radicals, molecules that are very reactive and shortlived, play a prominent role in the chemistry of a comet's bright coma. Because the coma is composed of gas and possibly, small particles erupting from the nucleus, these free radicals reveal important information about molecules in the nucleus. Emission lines created by these free radicals are major features in the ultraviolet and visible spectra from comets. However, information on both the formation and destruction mechanisms of the free radical is required for detailed analysis of these spectral observations and for chemical modeling of the coma. Free radicals are assumed to break down through photodissociation.

Of the free radicals commonly found in the coma, such as OH, CN, and NH₂, vacuum ultraviolet absorption spectra have been measured only for OH. The hydroxyl (OH) radical is one of the most predominant molecules observed in the coma. It is long-lived and is the major product of water dissociation in comets. With this in mind, a laboratory study has been initiated to quantify the amount of OH dissociation that occurs and the rate of dissociation.

Since high concentrations of the OH radical (approximately 10¹² to 10¹³ molecules per cm³) are required for the experiments, the radicals are generated in a recently constructed fast-flow system by the chemical reaction: H + NO₂ → OH + NO. The radicals are dissociated by the 157-nm output of an excimer laser to yield atomic oxygen and hydrogen. The hydrogen atoms are monitored by atomic-resonance fluorescence, and the OH radicals, by laser-induced fluorescence.

H atoms from the photodissociation of OH have been observed; several calibration methods were used to quantify this process by determining the amount of OH that was dissociated by light. Gas-phase actinometry with nitrous oxide (N₂O) is being used to calibrate the light absorption of 157 nm. The quantum yield, which is a relative measurement of the amount of dissociation

to light absorption, was measured to be 1.10 ± 0.28 . When the quantum yield is compared with the absorption spectrum, the two studies are in good agreement. The OH experiment may be used as a test case for other radicals, in particular, NH_2 . This process could lead to information about the presence of ammonia in the coma, as a source of NH_2 .

Contact: Regina J. Cody (Code 691)
(301) 286-3782

John E. Allen, Jr. (Code 691)
(301) 286-5896

Carol Moralejo (Code 691)
(301) 286-3783

Sponsor: Office of Planetary Atmospheres

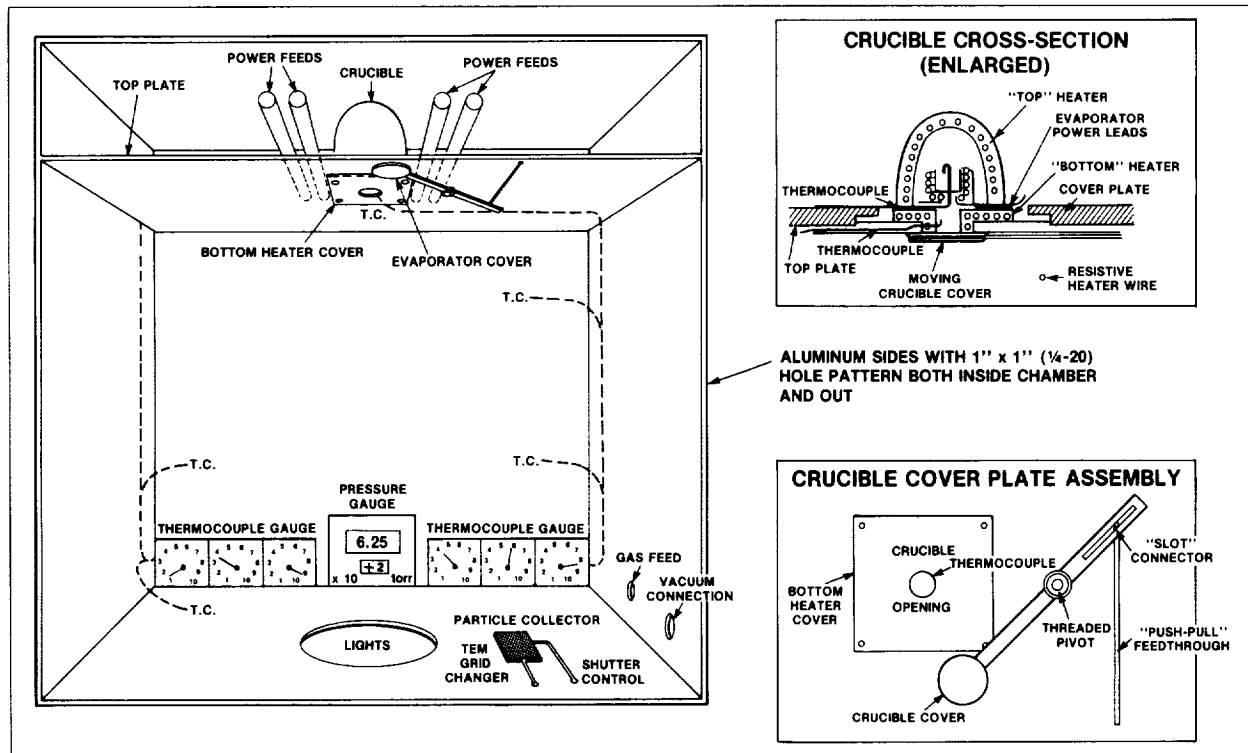
Dr. Regina J. Cody has 17 years of experience at Goddard. She currently works in the Astrochemistry Branch of the Laboratory for Extraterrestrial Physics. Dr. Cody holds a BS in chemistry from West Liberty State College in West Virginia and a PhD in physical chemistry from the University of Pittsburgh.

Dr. John E. Allen, Jr. also works in the Laboratory for Extraterrestrial Physics. A Goddard scientist for 12 years, he received a BS and an MS in applied physics and a PhD in physics from the University of Florida.

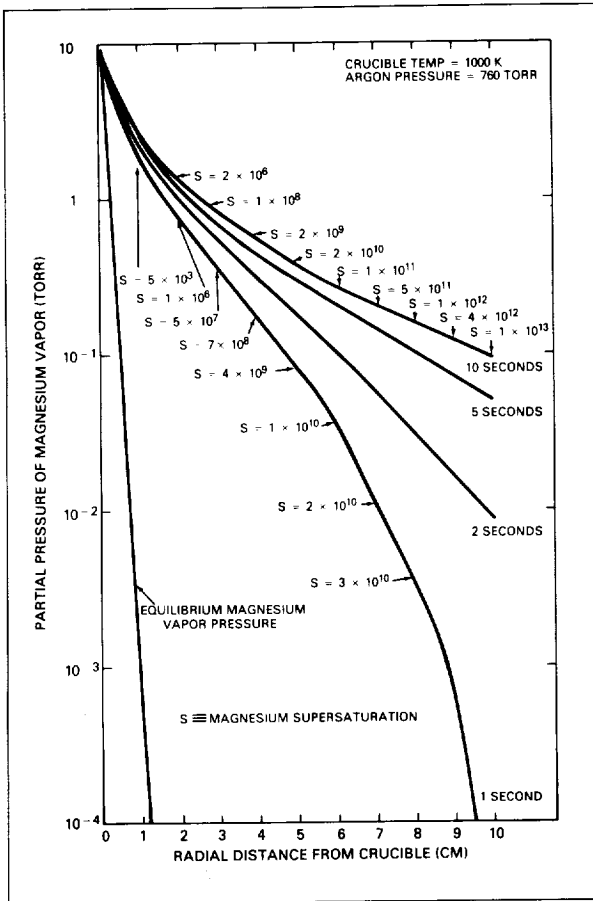
Dr. Carol Moralejo, who has been at Goddard nearly 2 years, has a BED in education from McGill University in Canada, a BSc, and a PhD in chemistry from Concordia University in Canada. She is at Goddard as a National Research Council Resident Research Associate.

MICROGRAVITY NUCLEATION EXPERIMENTS ON THE KC-135 REDUCED GRAVITY RESEARCH AIRCRAFT

The study of the formation and interaction of very fine grained refractory particulates is important for a variety of reasons, in fields as diverse as volcanology, meteorology, astrophysics, planetary science, and the politics of nuclear arms control. Although the nucleation of several refractory systems has been studied to some extent in terrestrial laboratories, accurate studies of the interaction between very fine grained particulates are hampered greatly by particle-settling effects. The



Schematic diagram of the Microgravity Nucleation Chamber.



Calculated values of the partial pressure of magnesium vapor and supersaturation as a function of time and distance from the crucible along the axis of the experimental system.

microgravity environment of the Space Station will enable the study of particle interactions during much longer time periods than are possible on Earth. This should allow the accurate measurement of interparticle sticking coefficients and the determination of the morphology, cohesiveness, and surface properties of the resulting aggregates for a wide variety of particle compositions.

Uniform quiescent suspensions of monodisperse particles (10 to 50 nm in diameter) in low-pressure gas are difficult, if not impossible, to achieve by the injection or resuspension of previously characterized particulates. Yet such well-characterized suspensions are an ideal starting point for many of the more interesting particle-interaction experiments envisioned for the Space Station. We have shown that it is possible to produce such suspensions by the direct condensation of refractory vapors under controlled conditions in a microgravity environment. The

studies necessary to predict both the size distribution and characteristics of the particles produced by such a method of necessity also yield high-quality data on the vapor phase nucleation of refractory materials.

Few laboratory studies of the nucleation of refractory materials have been published, and none of the published studies are consistent with classical nucleation theory. A major source of uncertainty in many of these studies is the degree to which thermally driven convection has influenced the measured experimental parameters such as the partial pressure of the metal vapor or the temperature in the region of nucleation. Convective instabilities make well-controlled vapor phase nucleation studies of very refractory materials such as carbon, silicon carbide, or aluminum oxide almost impossible to perform at 1 g.

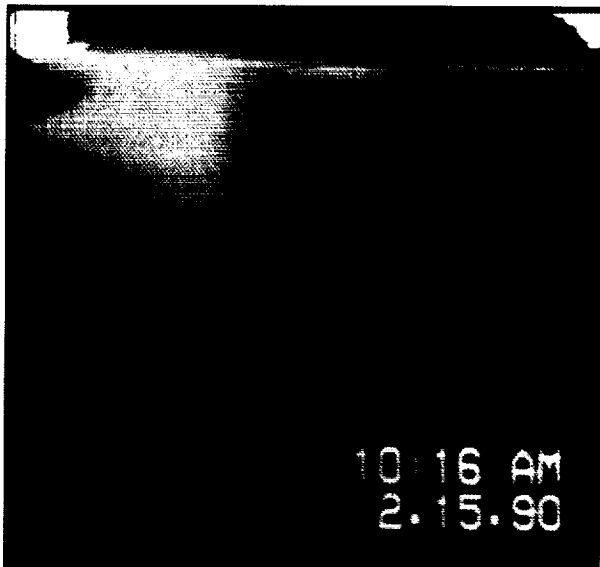
The primary scientific objective of our research during the next several years is to obtain data on the conditions under which refractory particles nucleate from vapor. In addition to a determination of the pressure and temperature at which condensation occurs we also wish to determine the morphology, composition, and crystal structure of the particulates as a function of our experimental parameters. The primary engineering goal of our proposed research is to build a system capable of producing a predictable, monodisperse, homogeneous suspension of well-characterized refractory particles which will be used as the starting point for various particle-interaction experiments to be performed aboard both the Space Station and the Space Shuttle. Both objectives can be met by a judicious combination of laboratory experiments on the ground and aboard NASA's KC-135 experimental research aircraft.

The KC-135 is a modified version of the Boeing 707 and on a typical mission, flies a series of 30 to 40 parabolic trajectories between the altitudes of 24,000 to 34,000 feet over the Gulf of Mexico. For a period of approximately 25 seconds during each parabolic maneuver, experiments can be performed in zero gravity. On February 14, 15, and 16, 1990, we flew our microgravity nucleation experiment through a total of 90 parabolas and obtained data on the vapor phase nucleation of magnesium metal in argon over the temperature range 800 to 1,150 K. A schematic drawing of the experimental apparatus is shown in the first figure.

In this apparatus, a very steep temperature gradient is established between the hot crucible and the cool walls of the chamber. Once zero gravity is achieved, a shutter

opens and magnesium vapor from the crucible begins to diffuse into the chamber. The second figure illustrates the high degree of supersaturation which can be attained in the vapor as the magnesium diffuses down the temperature gradient away from the crucible. At some value of temperature and supersaturation, magnesium vapor overcomes the barrier to nucleation and forms smoke particles approximately 10 to 20 nm in diameter. These particles are detected by using a video camera to monitor radiation scattered by the smoke from a rapidly scanned laser beam which forms a very well defined plane along the temperature gradient.

The third figure is one video frame from our recent KC-135 campaign which illustrates two points. First, the nucleation front (the inner boundary of the smoke cloud) is quite distinct. Since we know the temperature gradient in the system and the time at which this frame was obtained we can calculate the conditions under which nucleation occurred. We are now in the process of analyzing the nucleation data which we recently obtained. Second, the cloud of smoke particles is free from large-scale convective cells. In fact, the smoke cloud is extremely uniform and tends to expand into the chamber at a steady rate, possibly in response to the thermal gradient. Such a cloud would be an ideal subject for studies of particle coagulation if a longer time period was available



One frame from our video camera taken approximately 5 seconds after achieving zero-g which shows the crucible opening (top), the nucleation front, and previously condensed magnesium smoke slowly expanding away from the crucible.

than is possible on the KC-135. These experiments will be possible in the Gas-Grain Simulation Facility on Space Station Freedom. For the near term, we will continue to use flight opportunities on the KC-135 to collect data on the nucleation of a variety of refractory materials and to characterize the behavior and properties of the condensates in preparation for an opportunity to carry out particle coagulation experiments in space.

Contact: J. A. Nuth (Code 691)
(301) 286-9467

F. Ferguson (Code 691)
(301) 286-2133

L. Lilleht (Code 691)
(301) 286-2133

J. E. Allen (Code 691)
(301) 286-5896

Sponsor: NASA Headquarters, Solar System
Exploration Division

Dr. J. A. Nuth is the Head of the Astrochemistry Branch in the Laboratory for Extraterrestrial Physics and has been working at Goddard for 16 years. He earned a BS in both astronomy and chemistry, an MS in geochemistry, and a PhD in chemistry from the University of Maryland. Dr. Nuth is an expert in nucleation processes and high-temperature chemistry.

Mr. F. Ferguson is a NASA Graduate Student Researcher in the Chemical Engineering Department at the University of Virginia. He has been working at Goddard since 1988. Mr. Ferguson has a BS and an MS in chemical engineering from the University of Virginia. He is quickly becoming an expert on microgravity nucleation processes.

Dr. L. Lilleht is an Associate Professor of Chemical Engineering at the University of Virginia who has collaborated with members of the Astrochemistry Branch since 1983. He has a BS in chemical engineering from the University of Delaware, an MS in chemical engineering from Princeton University, and a PhD in chemical engineering from the University of Illinois. Dr. Lilleht is an expert in heat and mass transfer processes.

Dr. J. E. Allen has been a member of the Astrochemistry Branch since 1984 and employed as an astrophysicist at Goddard since 1978. He has a BS and an MS in physics and a PhD in applied physics from the University of Florida. Dr. Allen is an expert in lasers and optics.

Earth Sciences





As we prepare for Mission to Planet Earth, a 15-year coordinated effort to study and understand the intricate interrelationships that contribute to global change, our scientists are developing effective strategies of coordinated measurements and observations. They are utilizing these measurements and observations for the development and application of predictive Earth system models.

EARTH SCIENCES

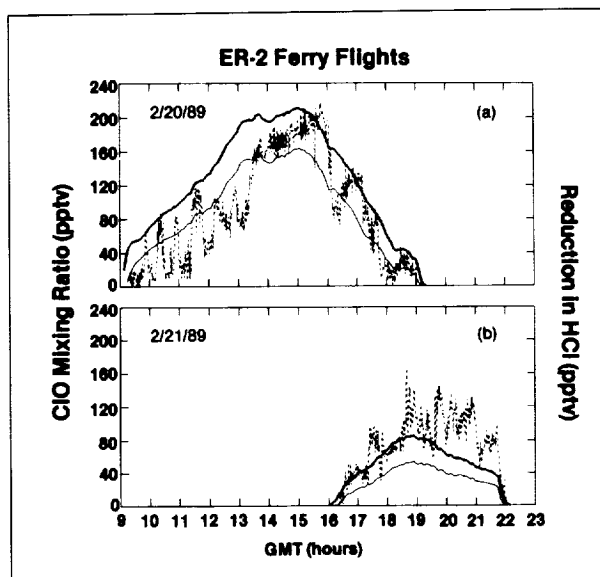
HETEROGENEOUS REACTIONS IN THE NORTHERN POLAR VORTEX AND THEIR EFFECT ON MIDDLE LATITUDE CHEMISTRY

In the early 1970s, there was concern that continued release of man-made fluorocarbons, inert compounds which are broken down by photolysis in the stratosphere, would lead to an increase in chlorine-catalyzed ozone loss and a gradual thinning of the ozone layer which protects the surface of the Earth from ultraviolet radiation. The impact of ozone was expected to be gradual because most of the chlorine released from the fluorocarbons would form long-lived reservoir species HCl and ClONO₂. The dramatic springtime thinning of the ozone layer over Antarctica (the ozone hole) was not predicted by any model and clearly was not the result of normal gas-phase photochemical reactions. Observations made by the National Ozone Expeditions and the Airborne Antarctic Ozone Experiment established that heterogeneous chemical reactions, which take place on the surface of polar stratospheric cloud particles (PSCs), both release active chlorine from the reservoir species and sequester odd nitrogen species in the reservoir HNO₃, which results in rapid ozone loss.

Although PSCs are not observed as frequently in the Northern Hemisphere winter polar vortex as they are in the colder Southern Hemisphere vortex, and a dramatic Northern Hemisphere springtime ozone loss is not observed, the reported trend in Northern Hemisphere ozone loss is larger than expected during winter months. Aircraft measurements, made during the Airborne Arctic Stratospheric Expedition (AASE) in 1989, indicate that heterogeneous reactions in the Northern Hemisphere are converting the HCl reservoir to reactive chlorine. Because of limited spatial coverage, the aircraft campaign cannot indicate the hemispheric impact of the heterogeneous chemical reactions.

We have addressed this question with a three-dimensional chemistry and transport model. This model, which uses winds from a data assimilation procedure for transport, has been validated by the good comparisons of the evolution of calculated ozone fields with satellite measurements for 1979 and 1989. Model output also has shown features of the aircraft measurements from the AASE period. Because the model transport compares well with data, we feel that it is a good tool to extrapolate the local AASE measurements to a hemispheric domain.

◆ *The GSFC Space Geodesy Branch's GEM-T3 gravity model, complete to degree and order 50, uses tracking data from 31 satellites; altimetry data from the Geosat, Seasat, and Geos-3 satellites; and surface gravity normal equations from Ohio State University. Anomalies are computed with respect to a reference of the rate of acceleration due to gravity. Negative values imply a gravity or mass deficit; positive values indicate a gravity or mass surplus.*



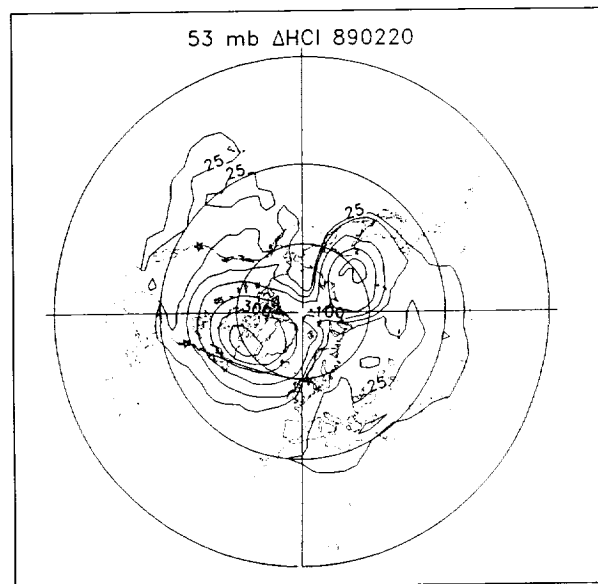
ER-2 measurements of CIO (dashed lines), for the 2/20/89 flight from Stavanger, Norway, to Wallops Island, Virginia (a), and for the 2/21/89 flight from Wallops Island to Moffett Field, California (b), are compared with model values of potentially reactive chlorine (bold lines). The difference in HCl is due to heterogeneous processing.

We defined two HCl experiments. In the first, the continuity equation for HCl is calculated normal gas-phase photochemical production and loss. In the second, an additional loss for HCl, which represents heterogeneous processes, is included whenever the temperature reaches the low values required for the appearance of polar stratospheric clouds. The difference between these two runs is potentially reactive chlorine. The simulation began on December 28, 1988. By late January 1989, the amount of potentially reactive chlorine was significant over the entire polar area.

Many factors have an impact on the partitioning of this free chlorine, including the concentrations of odd nitrogen species which affect the formation of ClONO₂ and the history of isolation of a parcel. This makes direct comparison of measurements for polar flights with the model difficult. However, measurements of CIO also were made on the transit flights of the ER-2 from Moffett Field in California to Wallops Island in Virginia on December 28, 1988, and from Stavanger, Norway, to Moffett Field via Wallops Island on February 20 and 21, 1989. These measurements were made between late morning and afternoon. The

February CIO measurements were enhanced relative to the December 28 measurements; this enhancement is not explained by the seasonal difference.

The February CIO measurements are compared with the amount of potentially active chlorine calculated from the model along the aircraft flight track in the first figure. The qualitative behavior of the CIO closely tracks the behavior of the potentially reactive chlorine from the model. A polar plot of the chlorine from the model for February 20 indicates that the large amount of chlorine encountered by the aircraft is confined to two longitude intervals, as the second figure demonstrates. For the latitude band between 46° and 62° North, concentrations of potentially reactive chlorine as large as 100 parts per trillion, which are seen on the aircraft track, appear for less than 20 percent of the band. This suggests that elevated values of CIO would not be observed generally at middle latitudes. By March, photochemical reactions led to reformation of reservoir species and a decrease in the CIO enhancement. Therefore, by the time the CIO formed in the polar vortex could be mixed more generally into the hemisphere, the



The difference in HCl due to heterogeneous processing of potentially reactive chlorine for 2/20/89 is given for the Northern Hemisphere. The stars indicate the locations of Stavanger, Wallops Island, and Moffett Field. The flight track from Stavanger to Wallops Island is indicated on the figure. The model shows that values of potentially reactive chlorine as high as 200 pptv on the aircraft flight track are found only in a small part of the Northern Hemisphere.



photochemical recovery will have mitigated its effect. These calculations show that the impact of heterogeneous processes acting on the surfaces of PSCs in polar night on middle-latitude ozone is limited by both the geographical extent and the duration of perturbed air.

Contact: Anne R. Douglass (Code 916)
(301) 286-2337

Richard B. Rood (Code 916)
(301) 286-8203

Sponsor: NASA Headquarters, Biogeochemistry and Geophysics Program

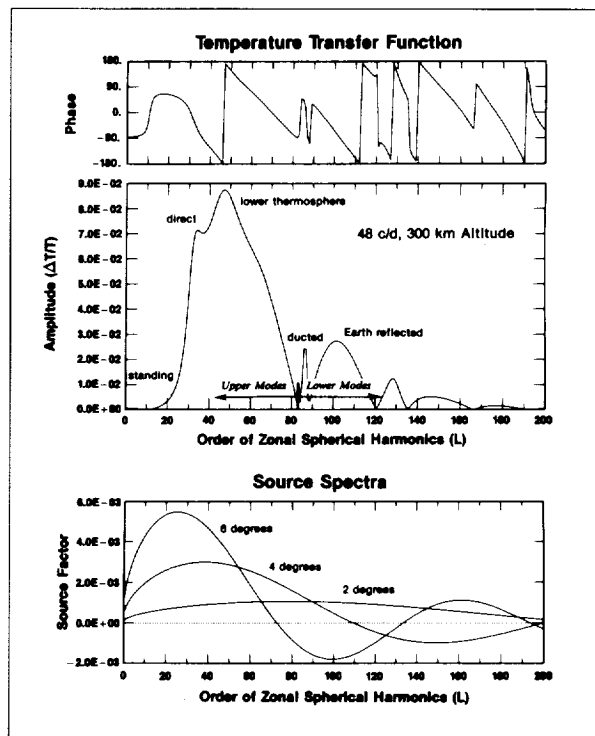
Dr. Anne R. Douglass, who has worked for Goddard for more than 9 years, is interested in development and interpretation of two- and three-dimensional photochemical models of the stratosphere. She holds a BA from Trinity College, an MS from the University of Minnesota, and a PhD from Iowa State University.

Dr. Richard B. Rood received a BS from the University of North Carolina at Chapel Hill and an MS and a PhD from Florida State University. During more than 8 years of atmospheric research at Goddard, he has received the Laboratory for Atmospheres Support Award, the NASA Quality Increase Award, and the NASA Performance Award.

TRANSFER FUNCTION MODEL FOR THERMOSPHERIC GRAVITY WAVES

The atmosphere responds to impulsive perturbations in two ways. Low-frequency oscillations are transmitted as gravity waves, gravity being the restoring force. High-frequency oscillations are transmitted as compressional sound waves. Unlike sound waves, gravity waves can propagate large distances. They are observed readily with satellites and ground-based instruments.

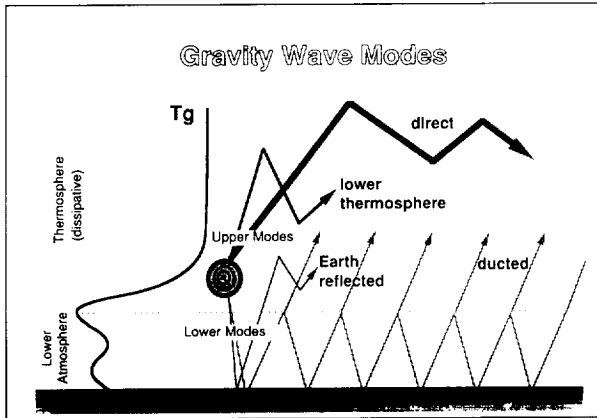
Thermospheric gravity waves have been divided into two categories: large- and medium-scale perturbations. Large-scale waves (1,000-4,000 km) have high propagation velocities (500-1,000 m/s). There is convincing evidence that large-scale waves are generated in the auroral zone by particle precipitation and electric fields. Medium-scale waves have shorter wavelengths (100-400 km) and much smaller propagation velocities (100-250 m/s). Excitation near the ground by lightning, high-speed shear flows, or orographic modulation of wind fields have



Computer amplitude and phase for the temperature transfer function at 300 km, plotted versus the order of zonal spherical harmonics or (horizontal) wave number, L . The excitation source is due to Joule heating which peaks at 130 km. The chosen frequency is 48 cycles per day, corresponding to a period of 0.5 hour. In the lower panel, spectra are shown for source pixels 2, 4, and 6 degrees wide.

been suggested and confirmed in some cases. There is evidence from the Dynamics Explorer and ground-based measurements that these waves also are generated in the auroral zones.

Different theoretical models have been developed to describe gravity waves. On one end are fully analytical models which make use of a dispersion relationship, without relating the waves to their excitation. On the other end are fully numerical Thermospheric General Circulation Models (TGCMs). The Transfer Function Model (TFM) discussed here is between these two approaches. It is less restrictive than the analytical approach, relating the global propagation of the gravity waves to their excitation. Unlike TGCMs, the TFM is simplified by the linear approximation, allowing the model to be very fast computationally without being limited in the spatial and temporal resolutions. The TFM also describes wave



Schematic illustration of wave modes identified with the transfer function model.

propagation through the lower atmosphere. Although the model was developed originally to understand the Dynamics Explorer measurements, it also has been used to interpret ground-based observations. The model also was applied to interpret the Pioneer spacecraft measurements in the thermosphere of Venus.

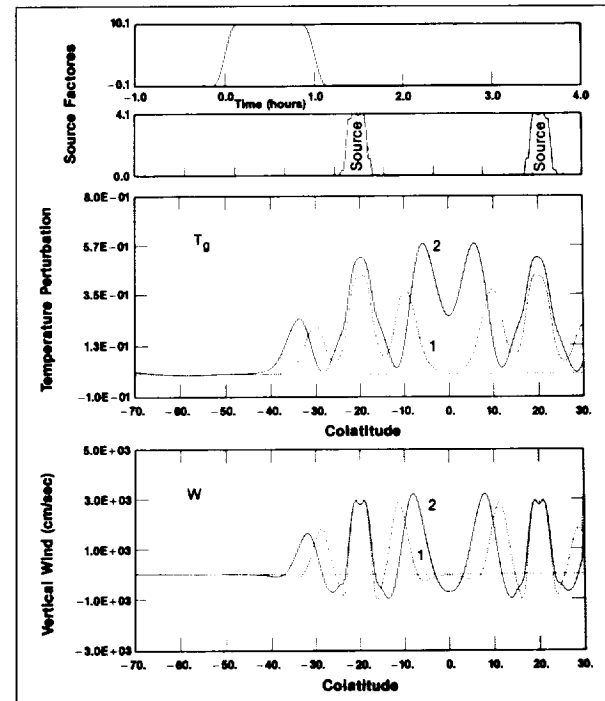
The TFM describes the horizontal variations of the variables in an expansion of spherical harmonics and the time dependencies in terms of Fourier components. Solutions of the reduced differential equations for energy, mass, and momentum conservation are time-consuming but need to be done only once. Such a solution represents the height variations in amplitude and phase of the transfer function (TF) shown in the upper panel of the first figure. For a chosen frequency, the TF describes the atmospheric response to a source which is uniform in the wave number L and can be viewed as the efficacy for exciting atmospheric perturbations.

The TF exhibits structure with amplitude maxima and rapid-phase variations characteristic of resonances that are the signatures of certain gravity wave modes. The first resonance describes a wave propagating near the speed of sound (about 700 m/s) and is called the direct wave. The second resonance is created by the wave that propagates obliquely up from the lower thermosphere, with a horizontal propagation velocity of about 390 m/s.

The narrow resonance maximum at $L=85$ is near the lower cut-off for propagating gravity waves in the lower atmosphere and extends all the way down to the ground. This feature is the signature of a wave that

propagates in a duct formed by the Earth's surface and the mesopause temperature minimum. The horizontal propagation velocity is about 270 m/s, near the speed of sound for the lower atmosphere. At higher wave numbers, the broad-amplitude maxima horizontal phase velocities are less than 230 m/s.

Two classes of gravity waves are identified: those affected mainly by the propagation properties of the thermosphere or upper atmosphere (upper modes) and by the lower atmosphere (lower modes). The wavelengths of the upper modes are much larger than those of the lower modes, and their propagation velocities differ accordingly. However, the two classes of waves also have much in common. In each case, there are long- and short-wavelength components. The direct wave propagates quasi-horizontally like a surface wave and makes up the long-wavelength component of the upper modes. The ducted wave makes up the long-wavelength component of the lower modes. Waves originating in the lower thermosphere make up the short wavelengths of the upper modes. Waves reflected from the Earth's surface make up the short wavelengths of the lower modes.



Using a Fourier transform, an impulsive perturbation of 2-hour duration is simulated. The excitation is attributable to a ring source in the auroral zone



These gravity wave modes are illustrated schematically in the second figure.

In the third figure, the application of this model is illustrated with the simulation of an impulsive perturbation that took only a few minutes of computer time. A ring source is chosen at 20° colatitude, 500 km wide. It is turned on abruptly (rising to a maximum in 10 minutes) and turned off after 1 hour. The upper panels show the time history and geometry of the source. In the lower panel, snapshots of the computed variations in temperature and vertical velocity are presented at 24 and 36 minutes after the source is turned on. Out of the source region, one perturbation propagates toward the Equator, while a second one propagates toward the pole (the center of the ring source) where convergence or wave focusing leads to amplification. The vertical velocity and temperature perturbation are in phase inside the source regions; but away from the source, the vertical velocity trails the temperature perturbation. The computed perturbations closely resemble observations from DE-2 on Day 363 in 1981, orbit 2195, except that the vertical velocities are smaller than those observed.

Contact: Hans G. Mayr (Code 914)
(301) 286-7505

Isadore Harris (Code 914)
(301) 286-8560

W. Dean Pesnell (Code 914)
(301) 286-6291

Sponsor: Office of Space Science and Applications,
Space Physics Division

Dr. Hans G. Mayr is an interdisciplinary scientist on the Dynamics Explorer project. He holds a PhD degree from the University of Graz in Austria and has 23 years of service with Goddard. He has received the Goddard Exceptional Performance Award and the NASA Exceptional Achievement Medal.

Dr. Isadore Harris, who received a PhD from Northwestern University, is a planetary astronomer with 32 years of service at Goddard.

Dr. W. Dean Pesnell is a physicist with the Applied Research Corporation. He earned a PhD at the University of Florida.

HEAT FLUXES AND ROLL CIRCULATIONS OVER THE WESTERN GULF STREAM DURING AN INTENSE COLD AIR OUTBREAK

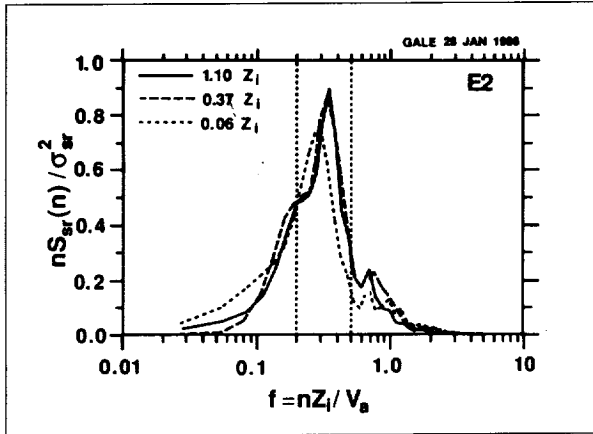
Cold air outbreaks are important climatological events for the atmosphere and ocean. The maximum net annual heat losses from both the north Atlantic and the north Pacific Oceans to the atmosphere occur over the warm western boundary currents. Net heat loss is maximized during cold air outbreaks, due to large sea-air temperature and humidity differences coupled with strong offshore winds. It has been suggested that heat (sensible and latent) transfer from the warm western oceans during cold air outbreaks plays a distinct role in the Northern Hemisphere winter circulations.

As this synoptic-scale disturbance forces the dry and cold continental air mass to flow over a much warmer sea surface, upward fluxes of sensible heat and moisture dramatically increase. The enhanced fluxes cause the convective Marine Atmospheric Boundary Layer (MABL) to grow, warm, and moisten downstream, which then produces clouds within the MABL. During cold air outbreaks over the warm ocean, satellite images generally show the widespread existence of cloud streets (two-dimensional horizontal roll vortices) in the near-shore areas and mesoscale cellular convection in the downstream areas. The cloud streets and mesoscale

GOES VISIBLE 28 JANUARY 1986 1800 GMT



The GOES visible image, NCAR Electra (E1, E2, E3, and E4) and King Air (K1 and K2) aircraft crosswind stack locations, and the western and eastern Gulf Stream fronts for the GALE January 28, 1986 case. The symbol "CE" indicates the cold eddy of ocean currents.

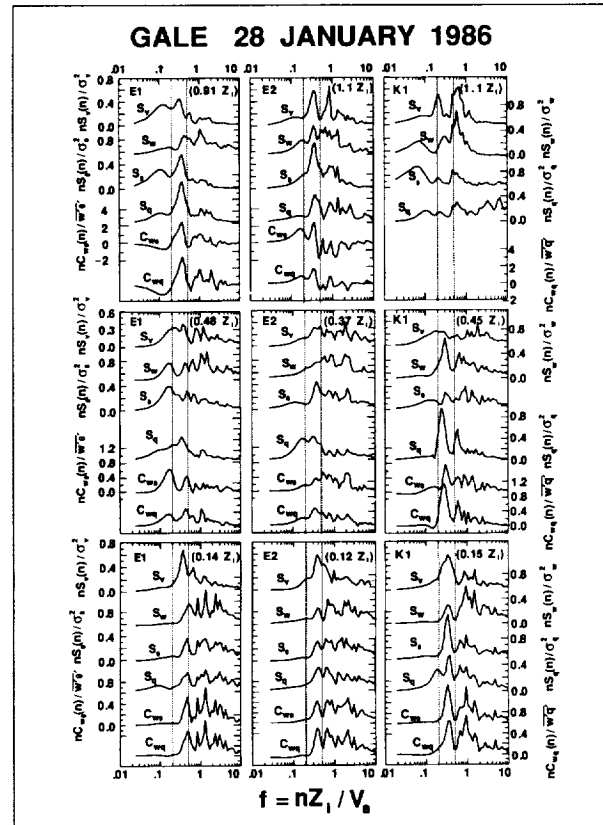


Spectra of solar radiation (S_{sr}), normalized by variances (σ_{sr}^2), for E2. The solid curve indicates reflected solar radiation near the cloud top, and the dashed curves indicate the downward solar radiation of the subcloud layer. The parameter n is the frequency, V_a , the true air speed, and Z_i , the inversion base height. The dashed lines at $f=0.2$ and 0.5 indicate the roll frequency band.

cellular convection are important connections between air-sea interactions and the transfer of energy and momentum through the MABL. The research on the roles of cloud streets and mesoscale cellular convection in the MABL dynamics and the mechanisms responsible for the mesoscale convection organizations is very important. The knowledge may help to develop important climatic indices from space-measured parameters.

An intense cold air outbreak, with the sea surface temperature warmer than the 70-m-level air temperature by approximately 19 °C to 24 °C, occurred offshore of the Carolinas in the Genesis of Atlantic Lows Experiment (GALE) area on January 28, 1986. The first figure shows the Geostationary Operational Environmental Satellite (GOES) visible image, the National Center for Atmospheric Research (NCAR) Electra (E1, E2, E3, and E4) and King Air (K1 and K2) aircraft crosswind stack locations, and the western and eastern Gulf Stream fronts for this case. The GOES visible image shows that cloud streets, with axes nearly parallel to the mean MABL wind directions, prevail over the Gulf Stream. The purpose of this article is to study the turbulence structure in the MABL for this case and the significance of roll vortices to heat fluxes.

The vertical organization of roll circulations in the MABL has been studied in terms of the spectra of solar radiation (S_{sr}), crosswind velocity (S_v), vertical velocity (S_w),



Spectra of crosswind velocity (S_v), vertical velocity (S_w), potential temperature (S_θ), and humidity (S_q); cospectra of temperature (C_w) and humidity fluxes (C_{wq}) for the upper, middle, and lower MABL at E1, E2, and K12. Spectra are normalized by variances, and cospectra by covariances (covariances are positive except for W at $0.9 Z$ of E1, and wq at $1.1 Z$, of E2). Flight levels are indicated in parentheses.

potential temperature (S_θ), and humidity (S_q), and of the cospectra of temperature (C_w), and humidity fluxes (C_{wq}). The second figure shows variance-normalized S_{sr} for E2. The third figure shows variance-normalized S_v , S_w , S_θ , and S_q , and covariance-normalized C_w and C_{wq} for the upper, middle, and lower MABL at E1, E2, and K1. The results suggest that cloud streets (roll vortices) are vertically organized convection in the MABL having the same roll scale for both the cloud layer and subcloud layer, and that the roll spacing is about three times the MABL depth. The roll circulations contribute significantly to the sensible heat and moisture fluxes.

For the lower half of the MABL, the contributions to the upward fluxes of sensible heat and moisture mainly come



from the roll-frequency (RF, $f=0.2-0.5$) and medium-frequency (MF, $f=0.5-5$) bands. The RF band contains roll vortices; the MF band contains the dominant convective thermals in both the unstable surface and mixed layers. The results also suggest the importance of roll vortices in transporting sensible heat and moisture increases higher in the atmosphere and that these transports near Z_i are carried out primarily by roll circulations in the roll vortex regime. These results are in good agreement with previous studies.

Near the MABL top, roll circulations are highly organized with strong signals. For the clear thermal-street region (E1), the updraft branches of roll circulations transport wetter and cooler air upward, while the downdraft branches transport the entrained drier and warmer air downward. Thus, roll circulations transfer sensible heat downward ($C_{w\theta} < 0$) and moisture upward ($C_{wq} > 0$). This negative $C_{w\theta}$ suggests that roll vortices consume turbulent kinetic energy while increasing potential energy through entrainment and penetration near Z_i of the clear thermal-street region. On the other hand, near Z_i of the cloud-street region (E2), the updraft branches of roll circulations transport wetter and cooler air upward, while the downdraft branches not only transport entrained drier and warmer air downward in the dry region, but also transport the wettest and coolest air (caused by the evaporative cooling of cloud droplets) downward in clouds, which are near the edges of the dry downdrafts. Therefore, the evaporative cooling-influenced roll circulations transfer sensible heat upward ($C_{w\theta} > 0$) and moisture downward ($C_{wq} < 0$). This positive $C_{w\theta}$ suggests a cloud-top entrainment instability due to roll-scale evaporative cooling, which can generate turbulent kinetic energy and enhance entrainment near the cloud top. At E2, the dominant scales are consistent among clouds, roll vortices, and cloud-top entrainment instability due to evaporative cooling, suggesting that the roll-scale evaporative cooling might help maintain cloud streets at E2 rather than stratocumulus or any other cloud types. Other cold air outbreak cases measured during GALE will be analyzed to validate the findings.

Contact: Shu-Hsien Chou (Code 912)
(301) 286-2935

Sponsor: Global-Scale Atmospheric Processes
Research Program

Dr. Shu-Hsien Chou studies air-sea interactions and boundary-layer dynamics during cold air outbreaks to

improve understanding of the roles of cloud streets and mesoscale cellular convection in boundary-layer dynamics and to develop remote-sensing techniques for ocean-air heat fluxes. Dr. Chou has been working in this area since she joined Goddard in 1980. She holds a PhD in meteorology from New York University.

DIABATIC INITIALIZATION IN THE GODDARD LABORATORY FOR ATMOSPHERES (GLA) DATA ASSIMILATION SYSTEM

The objective analysis and assimilation of observed meteorological variables such as wind, mass, and moisture provide a gridded initial condition for atmospheric model integration. However, the relationship between these objectively analyzed fields does not correspond necessarily to a particular model balance, so that substantial non-meteorological noise may be produced during model integration. The goal of an initialization procedure is to modify the analyzed fields such that the model balance is achieved in the initial condition.

Diabatic dynamical adjustment currently is being examined for purposes of initialization in the Goddard Laboratory for Atmospheres (GLA) Data Assimilation System. This initialization procedure is a generalization of an earlier dynamical adjustment scheme. Here, this scheme is extended to include diabatic processes.

The dynamical adjustment begins with 3 hours of backward adiabatic model integration. The model employed here is a new, 17-layer version of the fourth-order GLA General Circulation Model (GCM). Adiabatic backward integration is followed by 3 hours of forward diabatic integration using the full forecast model, including all physical parameterizations. A high-frequency filter, the Euler-backward scheme, is used throughout the entire forward and backward integration to eliminate non-meteorological noise. After initialization is completed, the subsequent 6-hour forecast, which computes the next step for the data assimilation procedure, proceeds smoothly and continuously from initial time.

The most important result of the procedure is a practical elimination of the initial imbalance in precipitation and evaporation fields (the spin-up effect), from the very beginning of the forecast calculation that is essential for a successful data assimilation procedure. Only two 6-hour

assimilation cycles—or 12 hours of data assimilation with the initialization procedure—are necessary to achieve a global balance of precipitation and evaporation.

Contact: Michael S. Fox-Rabinovitz (Code 911)
(301) 286-7438

Brian D. Gross (Code 911)
(301) 286-3314

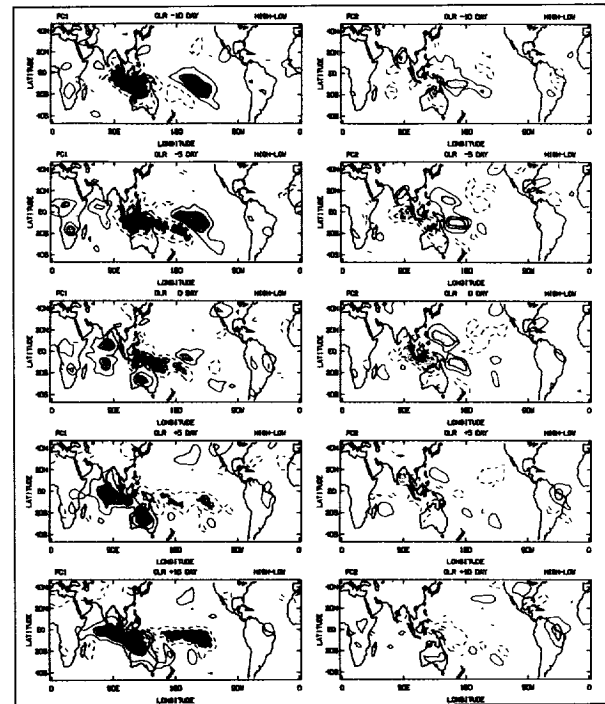
Sponsor: Office of Space Science and Applications

Dr. Michael S. Fox-Rabinovitz is Senior Research Scientist with the Universities Space Research Association at the GLA. During his 3 years at Goddard, he has been responsible for the development of atmospheric GCMs and initialization techniques for the 4-D Earth Observing System (EOS) Data Assimilation System and other EOS-oriented studies. Dr. Fox-Rabinovitz holds an MS in fluid dynamics from Moscow State University and a PhD in meteorology from the World Meteorological Center in Moscow.

Dr. Brian D. Gross is a National Research Council Resident Research Associate in the GLA. He received his PhD in atmospheric science from the University of Colorado. Dr. Gross, who has been at Goddard for 2 years, currently is working on initialization techniques for the GLA Data Assimilation System.

GLOBAL-SCALE CIRCULATION ANOMALIES AND TROPICAL-EXTRATROPICAL INTERACTIONS

Studies of climate changes are concerned typically with identifying potential anomalous forcing of the atmosphere on interannual and longer time scales and with understanding the sensitivity and feedback of the atmosphere to these changes in forcings. Examples include studies of the influence of unusually warm sea surface temperatures associated with El Niño and (on longer time scales) studies of the impact of potential anthropogenic increases in carbon dioxide. On the other hand, in addition to the seasonal cycle, the atmosphere is known to have a great deal of variability within a season, typically as great or greater than the longer term climate changes one wishes to detect. This variability often is termed natural variability because much of it is believed to arise primarily through processes internal to the atmosphere.



OLR anomalies computed as the difference between the high and low composites with lags of -10 days to +10 days associated with the first (left panel) and the second (right panel) zonal wind empirical orthogonal functions. Contour interval is 10.0 W/m^2 . Zero contours are omitted. Negative values have dashed contours. Values greater than 20.0 W/m^2 appear in blue, and values $< -20.0 \text{ W/m}^2$ appear in red.

Examples of these processes include various instability mechanisms associated with the mean atmospheric state, the excitation of normal modes of the atmosphere, and multi-equilibrium states in which the nonlinear properties of the equations governing the atmosphere are important.

The present study is devoted to obtaining a better understanding of this so-called natural variability on time scales longer than 1 week and less than a season. We concentrate on this part of the intraseasonal spectrum because it is perhaps the most poorly understood part of the intraseasonal spectrum and also because most state-of-the-art general circulation and climate models underestimate this variability (typically by a factor of one-half). Clearly, GCMs which poorly simulate this variability cannot be used legitimately to detect climate change. The current focus of this study is on tropical/extratropical interactions, planetary wave propagation, and the role of



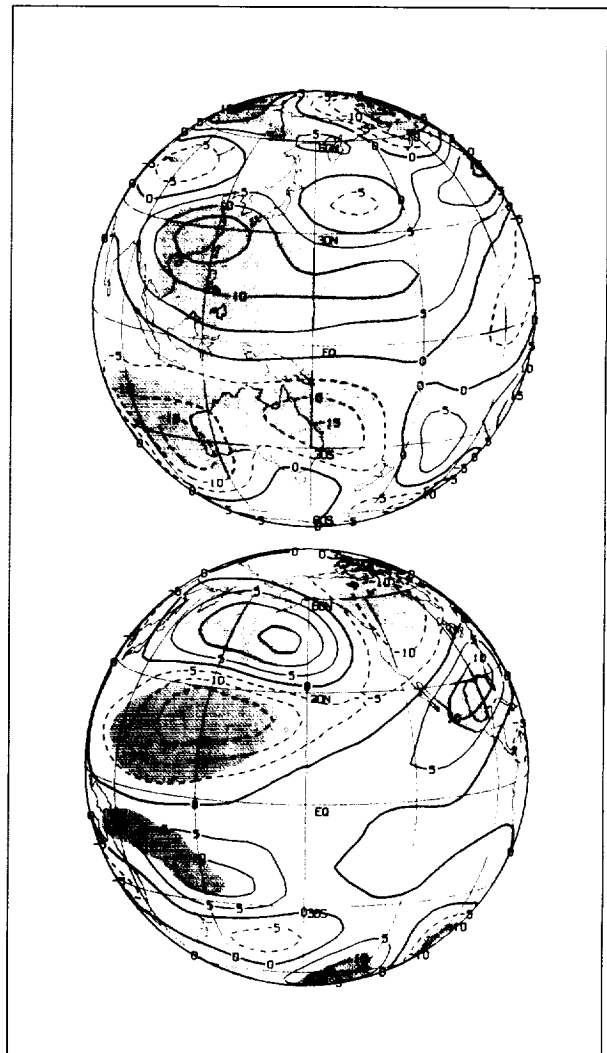
barotropically unstable modes in the Pacific sector during boreal winter.

In the tropics, the Madden-Julian oscillation is the dominant intraseasonal signal. This mode is characterized in the velocity potential field as an eastward-propagating, global-wave-number-one pattern, with a period ranging between about 40 and 60 days. Its signature also can be seen clearly in the anomalous outgoing longwave radiation (OLR) field in the regions of Indonesia and the western tropical Pacific. The left panel of the first figure shows an example of the average signature of this oscillation as it goes through a half cycle based on a compositing technique. This compositing technique uses as an index the extreme values of the dominant upper tropospheric zonal wind oscillation based on an empirical orthogonal function analysis in the Pacific sector. The negative values of OLR indicate regions of anomalous convective heating while the positive values indicate regions of weaker-than-average heating. Changing the sign of the anomaly pattern produces the other half of the cycle. The influence of this anomalous heating on the atmosphere is shown in the upper panel of the second figure. This response, also determined from the compositing technique, is dominated in the upper troposphere by a pair of anomalous anti-cyclones straddling the Equator over Indonesia and the western Pacific. This response corresponds to the heating field implied by the OLR pattern at Day 0 in the left panel of the first figure. The pattern with the opposite sign corresponds to a pair of anomalous cyclones.

The signature of these changes in the wind field is an oscillation in the strength of the tropical easterlies and more subtle changes in the shape and intensity of the east Asian jet. These changes in the wind field have a profound impact on the propagation of waves toward the Equator emanating from the region of the Tibetan Plateau. During the phase of weak easterlies, the waves propagate strongly into the tropics and some reflection occurs back toward the middle latitudes, which affects the circulation over western North America. On the other hand, the phase of strong easterlies shows little propagation toward the Equator and has the signature of a trapped response.

The lower panel in the second figure shows the anomalous composite atmospheric circulation based on the second most variable upper tropospheric zonal wind fluctuation in the Pacific sector. This pattern shows two wave trains apparently emanating from the central tropical Pacific.

The OLR pattern associated with this mode is shown in the right panel of the first figure. This anomalous circulation pattern again corresponds to Day 0 of the OLR pattern. The sign of the OLR pattern and the fact that the largest amplitude in the OLR occurs 5 days prior to the maximum atmospheric response is consistent with the interpretation that these circulation anomalies are forced by the anomalous tropical heating. However, an energetic analysis of this circulation anomaly suggests that, in the



The 200-mb stream function anomalies computed as the difference between the high and low composites associated with the first (upper panel) and second (lower panel) zonal wind empirical orthogonal functions. Contour interval is $5.0 \times 10^6 \text{ m}^2/\text{s}$. The colored regions indicate anomalies significant at the 99-percent level.

Northern Hemisphere, much of the energy of this mode is gained through barotropic exchanges with the mean east Asian jet. The response in the Northern Hemisphere thus appears to be that of a tropically forced mode initiating and/or phase-locking with a middle-latitude mode associated with a barotropically unstable east Asian jet.

The primary implications for modeling the general circulation are that an improper simulation of the Madden-Julian oscillation will affect adversely not only the tropical circulation but also the variability in middle latitudes and that it is necessary to simulate the mean atmospheric state very well in order to obtain a proper simulation of low-frequency variability. The latter arises, for example, from the dependence of wave propagation characteristics and barotropic instability conditions on the second derivatives of the mean zonal wind.

Contact: Siegfried Schubert (Code 911)
(301) 286-3441

Chung-Kyu Park (Code 911)
(301) 286-8695

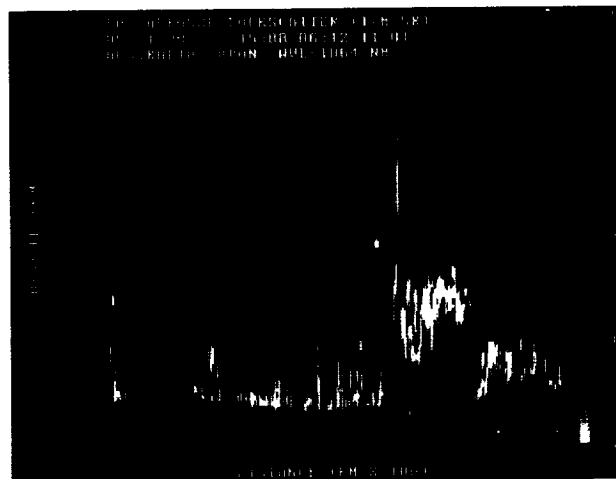
Sponsor: Climate and Global-Scale Atmospheric
Processes Program

Dr. Siegfried Schubert works in the Global Modeling and Simulation Branch of the GLA. His main interests during more than 7 years at Goddard have been GCM and observational diagnostic studies with an emphasis on low-frequency variability and predictability. He received a PhD in meteorology from the University of Wisconsin.

Dr. Chung-Kyu Park is an employee of Centel Federal Service Corporation with 4 years of service with the GSFC Global Modeling and Simulation Branch. He holds a PhD from the University of Missouri. Dr. Park's interests include climate dynamics associated with the interaction between the tropical circulation and extratropical waves and the low-frequency variability of the atmosphere.

GLOBAL BACKSCATTER EXPERIMENT (GLOBE)

The Global Backscatter Experiment (GLOBE) was intended to provide data on prevailing values of atmospheric backscatter cross section. The primary intent was predicting the performance of space-borne lidar systems, most notably the Laser Atmospheric Wind Sounder



Data from the NASA DC-8 acquired by visible and near-infrared lidar on a flight from Darwin, Australia, to Tokyo, Japan. The atmospheric cross-section shows aerosol concentration changes over four orders of magnitude as a function of height and latitude.

(LAWS) for EOS. A second and related goal was to understand the source and characteristics of atmospheric aerosol particles. For remote ocean locations, and the Southern Hemisphere in general, a significant lack of knowledge exists.

The major components of the experiment were flight surveys throughout the Pacific region by the NASA DC-8 aircraft. A Goddard lidar system was operated on the missions to obtain aerosol backscatter cross section at the fundamental and doubled Nd:YAG laser wavelengths of 1.064 μm and 0.532 μm and, in addition, at a wavelength of 1.54 μm which was generated by Raman shifted-down conversion of the 1.064- μm radiation. The system was the first operational lidar in the 1.5- μm wavelength region.

Advantages of 1.5- μm lidar are eye-safe operation and increased sensitivity to aerosol characteristics. An important factor of the visible/near-infrared backscatter measurements is accurate calibration. A new scattering cross-section calibration technique based on hard-target laser measurements was developed for the experiment.

The GLOBE flights were carried out in November 1989 and May-June 1990. Examples of aerosol backscatter cross-section measurements are shown in the figure. The figure depicts the aerosol cross section at 1.064 μm that was obtained on a flight from Australia to Japan on



May 31, 1990. The figure also depicts features that were characteristic of the aerosol distribution over the Pacific. In general there are three vertical regions which may be defined: the mixed-boundary layer, a cloud-pumped layer, and the free troposphere. Aerosol scattering varies by more than four orders of magnitude, and cross sections in the mixed-boundary and cloud-pumped layers typically are several orders of magnitude above that for the free troposphere. The upper troposphere generally is very free of aerosol scattering. However, areas of increased aerosol concentration are found. In the figure, an aerosol plume in the upper troposphere is apparent with increasing extent and concentration at more northern latitudes. The plume is most probably associated with the Asian land mass.

Contact: James Spinhirne (Code 917)
(301) 286-9099

Sponsor: Office of Atmospheric Dynamics and
Radiation

Dr. James Spinhirne holds a PhD in atmospheric science from the University of Arizona. He has been at Goddard for 12 years.

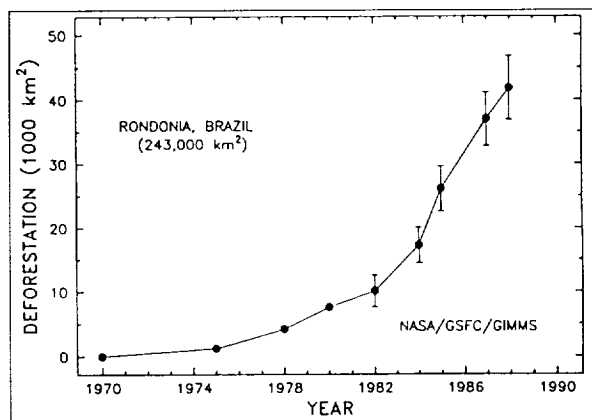
REMOTE SENSING OF AEROSOL AND TRACE GAS EMISSIONS FROM BIOMASS BURNING IN BRAZIL

Growing populations in Africa and South America have cultivated more and more land during the last decade, cutting and burning the forests. Biomass burning in the tropics has expanded drastically as a result of this controlled and uncontrolled deforestation. These fires release trace gases and particulates into the atmosphere. It is important to understand the process because burning forests are a major source of atmospheric trace gases and their atmospheric variations. These trace gases, along with carbon dioxide, produce the greenhouse effect and affect the chemistry of the troposphere.

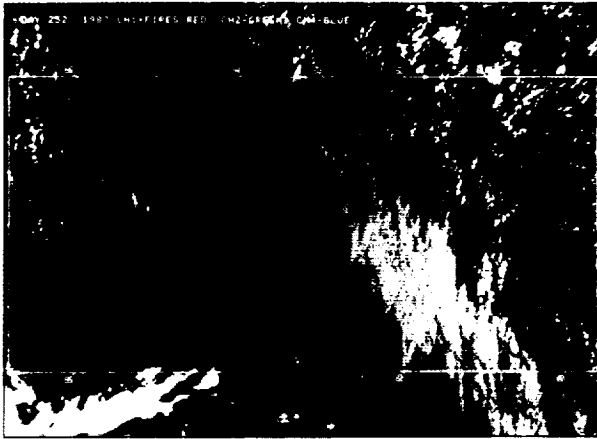
Biomass burning in the tropics is of particular interest because of the large extent of forest clearing and agricultural burning. Estimates based on satellite imagery show 200,000 km² of scorched land in Brazil alone. Intense ultraviolet radiation in the tropics enhances atmospheric chemical reactions, while the impact of aerosols on climate is increased as more solar radiation is reflected back to space.

To understand the role the burning process plays in the creation of trace gases, it is important to study smoke particles released by the fires. Knowledge of the optical characteristics of smoke particles is important for two reasons. First of all, there exists an important relationship between trace gases and smoke particles. Smoke particles are one of the emission products from biomass burning. Since they are formed through incomplete combustion, as are trace gases emitted from biomass burning, their relative abundance is proportional to the abundance of trace gases. As a result, remote sensing of smoke particles can be used to assess the magnitude of trace gas emissions from biomass burning associated with deforestation in the tropics. These remote sensing methods rely on optical characteristics of the smoke particles derived from ground-based and airborne measurements as well as on analysis of satellite imagery. The determination of the amount of trace gases released is based on measurements of the ratios of trace-gas-to-particulate emission rates. Until this work, there were no measurements of the optical characteristics of smoke particles emitted in the tropics. To use smoke particles as a tracer of these emissions it was necessary to establish the particle mean size and the resulting relationship between the smoke particles' mass and their effect on the outgoing radiation.

Second, smoke particles have an impact on atmospheric composition and energy balance. Particles emitted from biomass burning may affect the radiation budget and boundary layer meteorology by reflecting sunlight to space and by absorbing solar radiation. Smoke particles also are a major source of cloud condensation nuclei. Therefore, an increase in the aerosol concentration from



Rate of deforestation in the state of Rondonia, Brazil.



False-color composite showing the fires and smoke of biomass burning in Rondonia, Brazil. The image was generated from Advanced Very High Resolution Radiometer (AVHRR) channels 1 through 4. Fires are shown in red, vegetation in dark green, smoke in yellow, thick clouds in white, and thin, high clouds in blue. The latitude and longitude lines are indicated. The image shows some 1,500 fires. As a result, heavy smoke covers approximately 50,000 km².

smoke particles may cause an increase in the reflectance of thin-to-moderate clouds and a decrease in the reflectance of thick clouds. The aerosol effect for most clouds is dominated by an increase in cloud albedo. It has been suggested that the net cooling effect from increases in aerosol concentrations can be as strong as the heating effect from the increase of global carbon dioxide and other trace gases and thus acts in the opposite direction. The net effect of increased concentration of aerosols and trace gases on the Earth's energy budget therefore is not obvious.

Sunphotometry has been a useful tool to measure optical properties of aerosols for many years; however, until this past decade when tropical biomass burning became a significant issue in the research community, few researchers studied the optical properties of smoke with Sunphotometry. In this article, ground-based and airborne measurements of the smoke particles' optical properties are reported.

Measuring the optical properties of smoke emissions from biomass burning in Brazil required a multi-temporal and multi-elevational approach to characterize smoke aerosol background conditions, fresh smoke from the

flaming phase, aged smoke from flaming, fresh smoke from the smoldering phase, and a mixture of all of these. Sunphotometers were used at ground level and in the Brazilian Space Agency aircraft on September 3, 4, and 6 in 1989, during prescribed fire events near Alta Floresta, Matto Grosso, in Brazil. Ground observations of mixed smoke, representing background conditions, were made in the mornings before the fires were started. Plume observations were made from flaming and smoldering conditions, and in the case of the flaming source, observations from 10 m, 500 m, 1 km, and 10 km from the source allowed evaluation of the effects of short-term aging on the aerosols.

Carbon monoxide samples were taken during the smoldering and background profiles. The emissions of particulates and carbon monoxide are correlated highly at ground levels; however, different dispersion rates and atmospheric lifetimes caused by very different mass and physical properties make it difficult to know how well they correlate in a large convective laboratory such as the Amazon Basin. The background extinction coefficient profile at 450 nm was plotted against the carbon monoxide profile. Both demonstrate an exponential decrease in value with elevation over nearly an order of magnitude of change for each variable. The smoldering profile also demonstrated a high degree of similarity, although the correspondence was not as good as with the background profile. These data suggest that remote sensing of the optical properties of aerosols is potentially a good estimator of carbon monoxide emissions under these two conditions.

Spectral measurements from the ground and from aircraft of the smoke aerosol optical thickness indicate large Ångstrom coefficients of $\alpha=2.1-2.5$ except for the upper troposphere (above 3.5 km), as measured from the aircraft and during morning conditions where the measured smoke was emitted at least 1 day earlier ($\alpha=0-1.5$). These results are in agreement with measurements conducted in North America from aircraft and with lidar backscattering in Brazil. Assuming a log-normal distribution of the smoke particles, with σ in the range 0.3-0.9 μm , the effective radius R_{eff} for the plume is in the range 0.10-0.18 μm for fresh smoke, 0.10-0.13 μm for smoldering, and 0.2-0.4 μm for background aged smoke. For the whole atmospheric mixed layer, far away from the plume, the effective radius is 0.16, 0.20, and 0.22 μm , respectively.



Other measurements of the tropical smoke aerosol optical characteristics were reported for several biomass fires and smoke conditions, as a function of time and height in the atmosphere. Analysis of the upward radiance indicated that perhaps the width of the smoke particle size distribution is much narrower than reported from fires in North America. A strong correlation was found between the aerosol particle profile and the carbon monoxide profile. This high correlation indicates that smoke particulates can be a good tracer for emission of trace gases from biomass burning in the tropics. Further investigations also are required to characterize the plume aerosols, taking better account of background conditions. A more complete trace gas and particulate profile is required for specific burning conditions to compare with Sun-photometer data profiles. Without this, remote sensing of biomass emission will remain only an educated guess.

Contact: Brent Holben (Code 923)
(301) 286-2975

Yoram Kaufman (Code 913)
(301) 286-4866

Didier Tanré (Code 923)
(301) 286-4007

Sponsor: The Global Inventory Monitoring and
Modeling Studies/Biospheric Sciences
Branch

Mr. Brent Holben has 13 years of service at Goddard. He holds a BS in agronomy from the University of Idaho and an MS in watershed sciences from Colorado State University. He works in the Biospheric Sciences Branch on various issues relating to atmospheric scattering of shortwave radiation and remote sensing of global-scale terrestrial and atmospheric processes.

Dr. Yoram Kaufman has worked at Goddard for 10 years. He received his BSc and his MSc in physics from the Israel Institute of Technology and his PhD in atmospheric physics from Tel Aviv University.

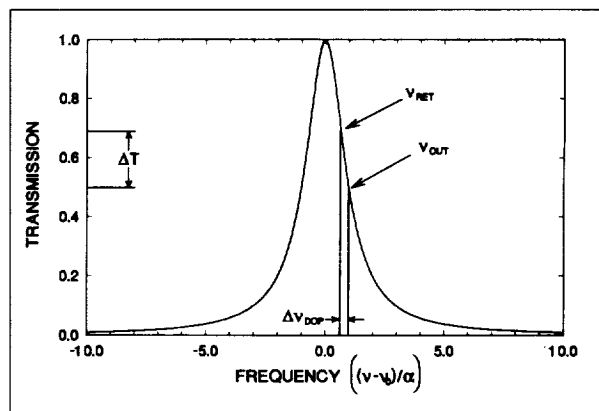
Dr. Didier Tanré earned a BS, an MS, and a PhD from the University of Lille in France. He also is interested in remote sensing of global-scale terrestrial and atmospheric processes. He has worked at Goddard in the Biospheric Sciences Branch for 2 years, and is a National Research Council Senior Research Associate.

NEW DOPPLER LIDAR METHODS FOR ATMOSPHERIC WIND MEASUREMENTS—THE EDGE TECHNIQUE

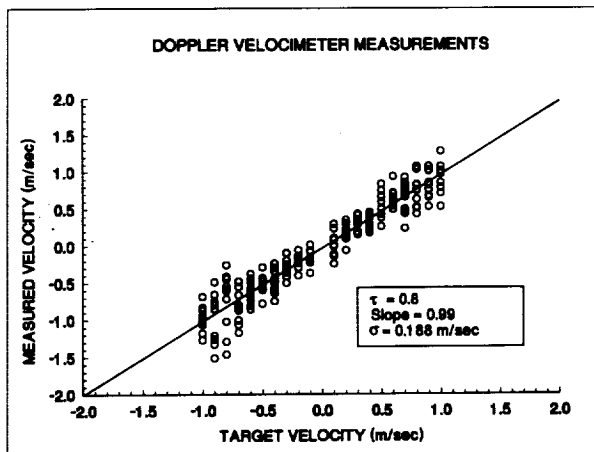
We have developed the edge technique, a powerful new method for the detection and measurement of small frequency shifts. It can be used with a lidar to obtain range-resolved measurements of the wind in the atmosphere with high accuracy and high vertical resolution. The technique can be used with a broad range of wavelengths.

Our primary interest is in using the edge technique with a lidar system to measure wind velocity remotely. Recent studies indicate that a global determination of the tropospheric wind field to accuracies of 1 m/sec to 5 m/sec is the single, most important measurement for numerical weather forecasting. This measurement could be carried out with a space-borne lidar system sensing the Doppler shift of a laser signal backscattered from the atmosphere. In addition, high spatial and temporal resolution ground- and aircraft-based wind measurements are important for the observation and forecasting of phenomena such as wind shear, microbursts, and severe storm outbreaks.

In the edge technique, the laser frequency is located on the edge of the spectral response function of a high-resolution filter, as the first figure shows. Due to the steep slope of the edge, very small frequency shifts produce large changes in filter transmission. The Doppler shift due to atmospheric motion is determined from a differential measurement of the frequency of the outgoing laser beam and the laser return backscattered from the atmosphere.



The edge technique for measuring small Doppler shifts using a laser located on the edge of the spectral response function of a high-resolution filter.



The velocity of a laboratory target measured with the edge technique compared with the actual target velocity.

The use of a differential technique to measure the Doppler shift renders the measurements insensitive to laser frequency jitter and drift. The frequency measurement accuracy that can be achieved is on the order of 100 times better than the spectral bandwidth of the measurement. Theory shows the edge measurement also is insensitive to the spectral width of the laser, provided the width is smaller than the characteristic width of the edge filter. The relatively broad laser spectral width that can be used with the edge technique permits a proportionately shorter (100 times) transfer-limited temporal pulse width and a corresponding improvement in vertical resolution. Also, for the edge technique, the optical requirements for a large-diameter telescope are hundreds of times diffraction-limited, whereas a heterodyne system requires diffraction-limited operation. In the visible and near-infrared wavelengths, a lidar system using the edge technique would obtain orders-of-magnitude larger signals than in the thermal-infrared. For a system working at ultraviolet wavelengths, the Rayleigh backscatter would provide an even larger signal.

We recently have performed laboratory experiments which demonstrate many of these characteristics. In particular, the high sensitivity and accuracy of the edge technique and the insensitivity of the differential measurement to frequency jitter and drift have been verified.

The velocity of the laboratory target measured with the edge technique is compared with the actual velocity of the target in the second figure. The measurements were made with a laser located on the edge of a high-resolution etalon

fringe. The accuracy achieved (0.19 m/s) corresponds to a Doppler shift 1/100th of the spectral bandwidth used.

Contact: C. Laurence Korb (Code 917)
(301) 286-6233

Bruce M. Gentry (Code 917)
(301) 286-6842

Sponsor: NASA Headquarters, Radiation Dynamics and Hydrology Branch

Dr. C. Laurence Korb is a Senior Scientist in the GLA. Since joining NASA 18 years ago, he developed and served as Project Scientist for the Skylab Multispectral Scanner Program and as Principal Investigator for the Differential Correlation Radiometer Experiment, the Ultra High Resolution Laboratory, the Pressure and Temperature Lidar Program, the Laser Atmospheric Sensing Experiment, and the Doppler Lidar Wind Program. He received his PhD in physics from Florida State University in 1967.

Mr. Bruce M. Gentry received a BS in physics from the University of Santa Clara. Since 1978, his research at Goddard has included high-resolution spectroscopy, passive remote sensing, and lidar. He developed the High-Resolution Cooled Optics Spectrometer, the Tunable Diode Laser Spectrometer, and numerous experimental spectroscopic studies with those instruments. He currently is developing a Doppler Wind Lidar using the edge technique.

INTERNATIONAL SATELLITE CLOUD CLIMATOLOGY PROJECT (ISCCP) CLOUD CLIMATOLOGY COMPLETE THROUGH 4 YEARS

The International Satellite Cloud Climatology Project (ISCCP) of the World Climate Research Program has been collecting data since July 1983 and plans to continue through 1995. The first 5 years of satellite image data and the first 4 years of the cloud climatology have been archived. Global coverage of the Earth by the combination of meteorological satellites is providing an unprecedentedly detailed view of clouds and their variations on time scales from 3 hours to several years, and spatial scales from 30 km to planetary.

ISCCP has provided key lessons for the kind of multiple dataset processing system that must be developed for

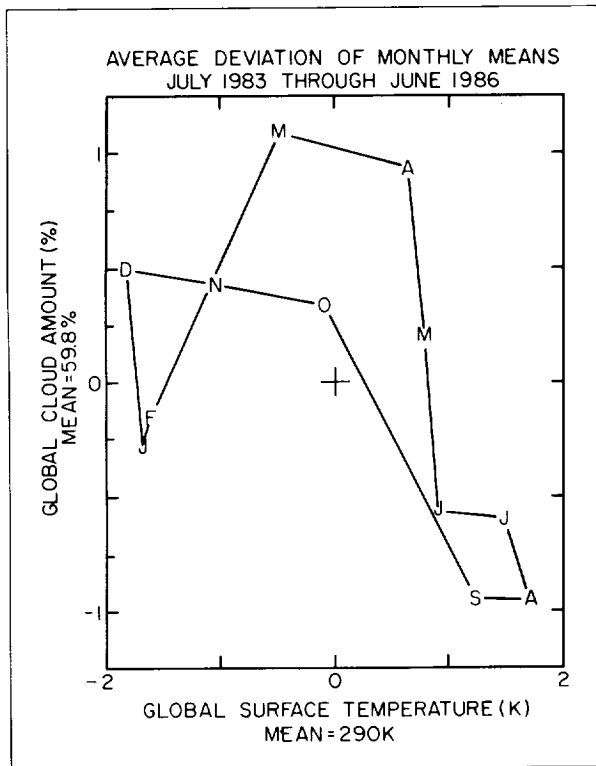


EOS. ISCCP also has illustrated the difficulties associated with maintaining accurate, well-documented instrument calibration information.

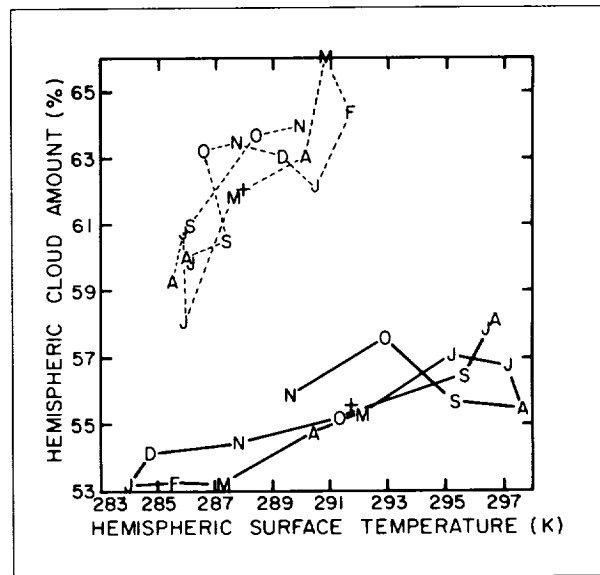
This comprehensive perspective on cloud behavior has revealed the complexity of the effects that clouds can have on climate, but also has provided the quantitative measurements needed to develop models of this phenomenon. The complexity can be illustrated in two ways. The first figure shows the average seasonal cycle of global mean cloud amount versus global mean surface temperature, revealing a semi-annual cycle in cloud amount. The second figure shows that this semi-annual cycle is caused by the summation of two hemispheric cycles that have different amplitudes and phases. However, the seasonal variations of hemispheric mean cloudiness actually are dominated by changes in the tropics, while the seasonal variations of hemispheric mean surface temperature are dominated by changes at high latitudes. Hence, the

seasonal variation of cloudiness is not linked simply to that of surface temperature, nor does it provide a simple, linear radiative feedback on the seasonal temperature variations. The point is reinforced by the complex distribution of cloud properties suggested by the zonal mean values shown in the third figure.

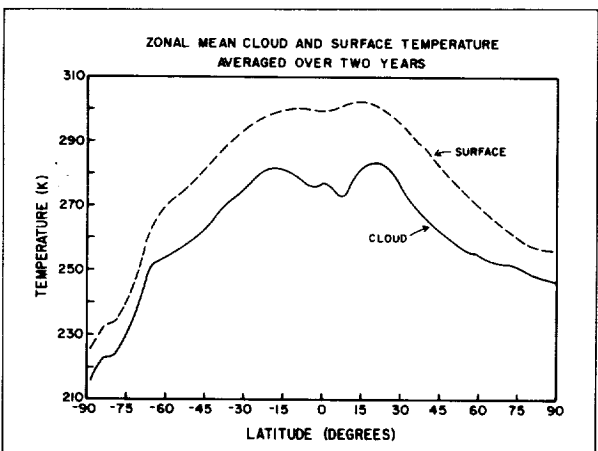
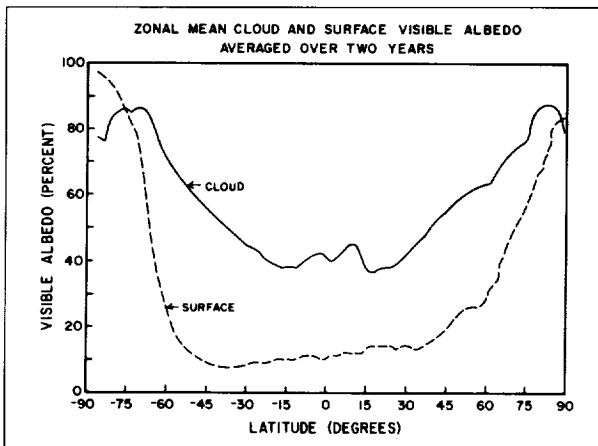
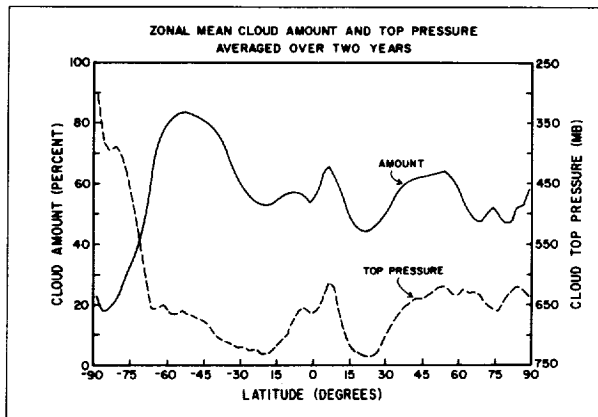
Climate GCMs now can be held to this standard: they must portray accurately both the distribution of mean cloud properties and the diurnal, synoptic, and seasonal variations that occur. Moreover, the occasional occurrences of El Niño can be studied to see whether the models correctly represent the cloud changes associated with transient climate perturbations. Key features of clouds are that they are generally higher in altitude and optically thicker over land than over ocean; however, ocean areas are most frequently overcast and cloudier overall than land areas. Tropical cloudiness, rather than being composed primarily of deep convective clouds, is a roughly equal mixture of convective towers, mesoscale anvils, and cirrus, as well as shallow, boundary-layer convection. In general, higher latitude clouds are optically thicker but with lower tops than tropical clouds; their properties vary over a wide range, because they are a mixture of several types of clouds.



Deviations of global monthly mean cloud amount and surface temperature from their annual means averaged over 3 years from July 1983 through June 1986. The mean values of cloud amount and surface temperature are shown on the axes. Letters indicate months of the year.



Variations of hemispheric monthly mean cloud amount and surface temperature for the period from July 1983 through November 1984. Northern Hemisphere values are shown by the solid line, and Southern Hemisphere values are indicated by the crosses.



Zonal, annual mean cloud and surface properties averaged over the period from July 1983 through June 1985 as a function of latitude. The top panel shows the cloud amount and cloud-top pressure, the middle panel shows cloud and surface visible albedos, and the lower panel shows the cloud and surface temperatures.

Contact: William B. Rossow (Code 940)
(212) 678-5567

Sponsor: Earth Sciences Directorate

Dr. William B. Rossow heads the ISCCP Global Processing Center and serves on NASA planetary and Earth sciences projects. During his 12 years at Goddard, Dr. Rossow has served on the First ISCCP Regional Experiment team, the Orbiter Cloud Photopolarimeter team for the Pioneer mission, the Photopolarimeter Radiometer team for Galileo, and the Earth Observing Scanning Polarimeter team for EOS. He holds a BA in physics and mathematics from Hanover College and an MS in physics and a PhD in astronomy from Cornell University.

EFFECT OF CLOUD WATER VARIATIONS ON GLOBAL CLIMATE MODEL (GCM) CLOUD FEEDBACK

Predictions of the climatic response to increasing trace gas concentrations are limited severely by uncertainties in cloud feedback. Most GCMs suggest a positive cloud feedback associated with decreasing cloud cover and increasing cloud height as our climate warms. However, this tendency is produced by simple cloud parameterization schemes which do not include a separate budget for condensed water. Clouds form and dissipate in a single model timestep, and their optical properties usually are prescribed. A recent doubled-carbon-dioxide experiment conducted by the British Meteorological Office (UKMO) with a cloud water budget, different properties for liquid and ice particles, and interactive optical thickness produced a climate sensitivity of only 1.9 °C, as compared with the 5.2-°C sensitivity of the same GCM with diagnostic clouds which depend only on relative humidity.

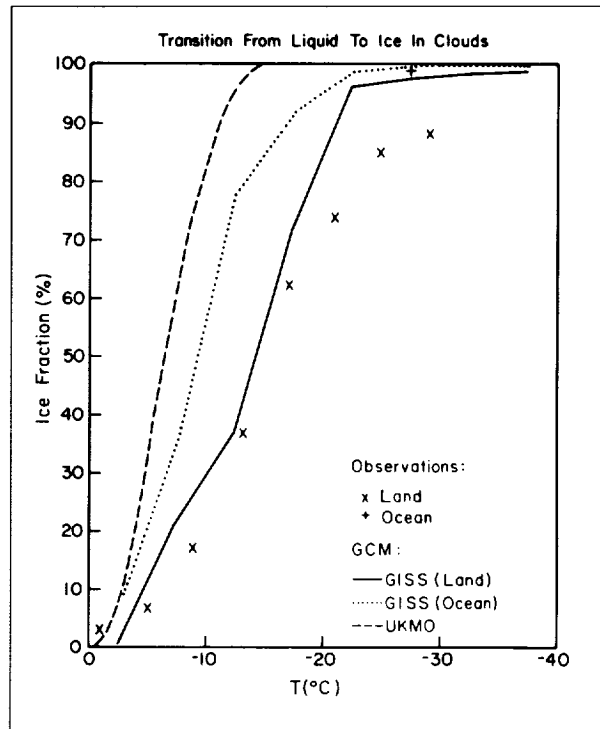
Goddard Institute for Space Studies (GISS) scientists have recently implemented a cloud water budget parameterization in the GISS GCM. The scheme has some characteristics in common with the UKMO GCM, but includes more realistic liquid and ice properties and several physical processes absent from the latter model. For example, the scheme incorporates condensed water from the cirrus anvils of deep cumulus clouds into the budget. The Bergeron-Findeisen process of diffusional growth of ice crystals in a mixed-phase cloud with supercooled liquid water is represented. Cloud particle



effective radius increases with cloud water content consistent with an assumption of constant droplet number density. Cloud microphysical properties are different for maritime and continental clouds, reflecting differences in cloud condensation nucleus populations. In seasonal cycle simulations, the model reproduces the general increase of cloud liquid water with latitude observed by the Scanning Multichannel Microwave Radiometer (SMMR) without producing the excessive liquid water content at high latitudes that plagues some GCMs. The GCM also is consistent with the Earth Radiation Budget Experiment-derived temperature dependence of longwave radiation-trapping over the oceans, despite the large uncertainties in the microphysical properties of cirrus clouds.

To test the model's climate feedback the GCM has been subjected to uniform positive and negative 2 °C sea surface temperature (SST) perturbations in perpetual-July mode with fixed sea ice. The resulting climate sensitivity can be estimated as the change in SST divided by the change in net radiative flux at the top of the atmosphere. Cloud feedback can be isolated by comparing the global climate sensitivity to that for clear regions only. The new GCM's global sensitivity is $0.8\text{ }^{\circ}\text{C} \times \text{m}^2/\text{W}$, which tentatively suggests a response to doubled carbon dioxide of approximately 3 °C. The ratio of total-to-clear sky sensitivity is 1.3, implying a near-neutral but slightly positive cloud feedback. By comparison, the standard Model II GISS GCM has a sensitivity of $1.2\text{ }^{\circ}\text{C} \times \text{m}^2/\text{W}$ to the same SST perturbation, a 4.2 °C sensitivity to doubled carbon dioxide, and a global sensitivity 2.4 times its clear-sky value. Thus, the behavior of the new model appears to be intermediate between that of the UKMO GCM (strong negative cloud feedback) and GISS Model II (strong positive cloud feedback).

The accompanying figure illustrates one reason for the difference between the UKMO model and the new GISS GCM. In both models, ice clouds, which have large particles and small mean water contents, have shorter lifetimes (fastest conversion to precipitation) than do liquid clouds. Thus, at altitudes at which ice clouds in the current climate give way to liquid clouds in the warmer climate, time-averaged cloud cover increases. In the UKMO GCM, the transition from liquid to ice occurs between 0 °C and -15 °C, at low and middle altitudes where increased cloud cover is a negative cloud feedback. As can be seen in the figure, however, aircraft and SMMR observations suggest that considerable liquid water exists



Fraction of ice in clouds as a function of temperature, comparing aircraft observations over land, SMMR observations over ocean, the GISS GCM, and the UKMO GCM.

down to -30 °C, where the greenhouse effect of clouds is appreciable. The GISS model provides a better match to the observations; the result being a more neutral cloud feedback.

The optical-thickness feedback also is quite different in the two models. Cloud water content in the UKMO GCM increases at a rate of 9.6 percent per degree Celsius—twice as large as that inferred from aircraft observations over the Soviet Union. However, analysis of global ISCCP data by GISS scientists reveals that over much of the globe, and especially over the oceans, optical thickness (and therefore cloud water content) decreases with temperature instead, implying a more neutral or even positive cloud optical-thickness feedback. The new GISS GCM qualitatively reproduces the ISCCP results.

The new GCM's lower climate sensitivity relative to that of GISS Model II is largely attributable to the model's different treatment of optical thickness. In Model II, optical thickness is prescribed to decrease with altitude, so the shift to higher clouds in the warmer climate decreases the total optical thickness. This makes clouds in the warmer

climate more transmissive in the infrared, but it also causes the absorbed solar flux to increase dramatically. The latter effect dominates, increasing the positive feedback beyond that caused by decreasing cloud cover alone. In the new version of the GCM, the cloud cover decrease is smaller, and the cloud optical-thickness change is more neutral. Thus, the infrared cloud-height feedback is larger but the solar optical-thickness feedback is almost zero, resulting in a lower overall climate sensitivity.

Contact: Anthony D. Del Genio (Code 940)
(212) 678-5588

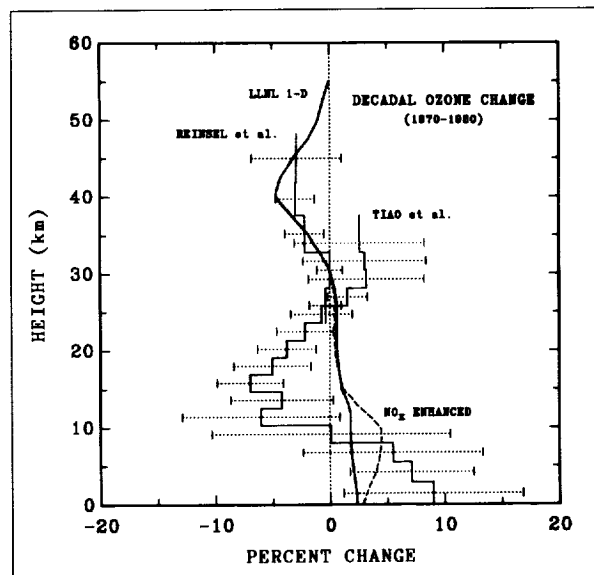
Sponsor: Earth Sciences Directorate

Dr. Anthony D. Del Genio, a physical scientist with GISS, is Coordinator of the GISS/Columbia Atmospheric and Planetary Science Program. Dr. Del Genio specializes in comparative dynamics of planetary atmospheres and in cumulus and large-scale cloud parameterization, and his professional interests include the modeling of superrotation on slowly rotating planets and the role of moist convection in tropical dynamics. Dr. Del Genio earned his PhD at the University of California at Los Angeles, and he has served with Goddard for 12 years. He is a recipient of the NASA Special Achievement Award.

RADIATIVE FORCING OF CLIMATE CHANGES IN THE VERTICAL DISTRIBUTION OF OZONE

Continued increases of atmospheric trace gases such as CO₂, CH₄, N₂O, and various chlorofluorocarbons (CFCs) due to human activity are adding steadily to the greenhouse effect. Ozone, too, is a significant atmospheric greenhouse gas, but it is more complex than the others because ozone is the major source of atmospheric heating, and, because of its strong ultraviolet and visible absorption, abundance changes of ozone directly impact the stratospheric temperature profile. The atmospheric distribution of ozone is affected strongly by photochemical interactions with other trace gases, particularly the CFCs. Also, the natural variability of ozone is large, both geographically and seasonally, which makes long-term trends in the distribution of ozone difficult to measure.

An added complexity is the dependence of the radiative forcing on the pressure level of the ozone change. For

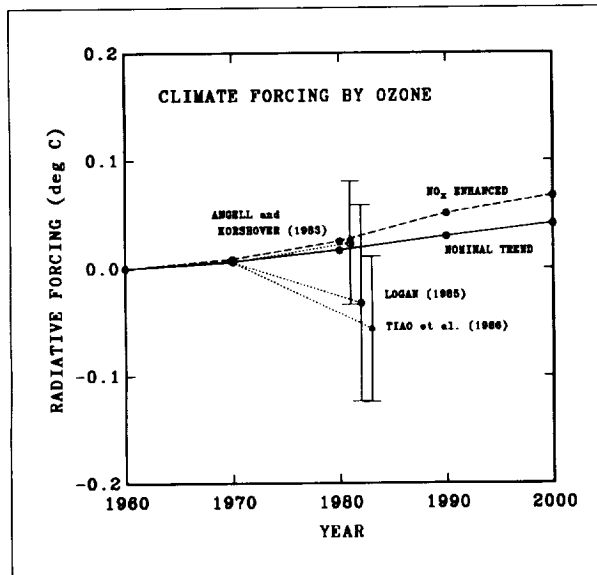


Computed and observed rates of change in ozone distribution during the 1970s. The solid and dashed lines give the global average vertical ozone change obtained from one-dimensional photochemical modeling for current trend and NO_x-enhanced trace gas scenarios, respectively. The histogrammed curves (with observational uncertainties) show the observed trend in ozone distribution over the northern mid-latitudes from ozonesonde data and Umkehr measurements.

example, ozone added to the stratosphere above about 30 km produces surface cooling because the added ozone effectively robs the troposphere and surface of solar energy that otherwise would warm the ground. On the other hand, ozone added near ground level has little or no effect on the surface temperature. On a per-molecule basis, ozone changes near the tropopause are the most effective in influencing the surface temperature; here, the low temperature of the ozone enables efficient trapping of thermal radiation emitted from the ground, with a 1-Dobson Unit increment of ozone producing 0.06 W/m² (or 0.018 °C) of greenhouse warming.

So far, marginally reliable trends of ozone distribution have been determined since about 1970 for the northern mid-latitudes from ozonesonde measurements. Calibration problems and sparse spatial coverage are the major sources of uncertainty.

Nevertheless, the available measurements summarized in the first figure show near-surface ozone to be increasing by about 1 percent each year (and producing a



Radiative forcing of global and regional surface temperature due to changes in vertical ozone distribution. The solid and dashed lines depict the global warming expected for the 1-D photochemical models shown in the first figure in response to current trace gas increases. The dotted lines (with estimated uncertainties) show the regional forcing of the surface temperatures over the northern mid-latitudes based on the observed distribution trends previously reported.

small greenhouse warming contribution). CFC-induced ozone decreases of about 0.5 percent each year near 40-km altitude also produce a small warming contribution. However, because of their greater sensitivity, ozone decreases in the upper troposphere and lower stratosphere, between 10 and 20 km, dominate the column-integrated radiative forcing.

The best determined ozone trends, taken at face value, imply regional surface cooling by -0.04 °C per decade over northern mid-latitudes. Compared to the 0.067 -°C warming contributed by carbon dioxide over the same time period, the radiative forcing by changes in the vertical distribution of ozone is clearly an important factor in assessing potential contributors to climate change.

One-dimensional photochemical modeling can reproduce the observed ozone decrease in the middle stratosphere due to CFCs, and two-dimensional models also can reproduce the upper troposphere and lower stratosphere decreases at high latitudes. However, the photochemical models predict ozone

increases at low latitudes which would produce a globally integrated warming trend as indicated in both figures, but which at present, cannot be confirmed by available measurements.

The lack of ozonesonde measurements from tropical latitudes of sufficient quality and time span precludes determination of climate forcing by trace gas-induced ozone changes on a global scale, and thus also precludes verification of the photochemical model predictions of greenhouse warming on global average. SAGE II measurements, which sample the upper tropospheric and lower stratospheric ozone, appear promising but have not yet accumulated measurements over a sufficiently long time span to determine a trend in long-term ozone distribution.

Contact: Andrew A. Lacis (Code 940)
(212) 678-5595

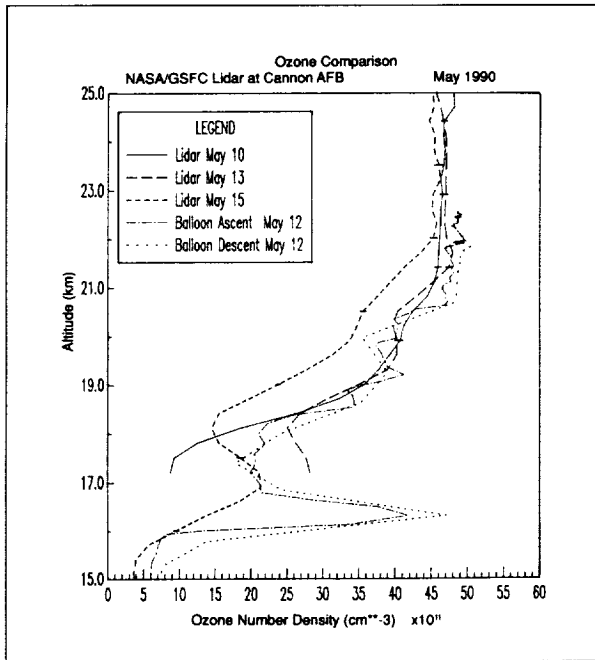
Sponsor: Earth Sciences Directorate

Dr. Andrew A. Lacis is a physical scientist with more than 10 years experience with Goddard. He holds a PhD from the University of Iowa and is involved in radiative transfer and climate modeling at GISS.

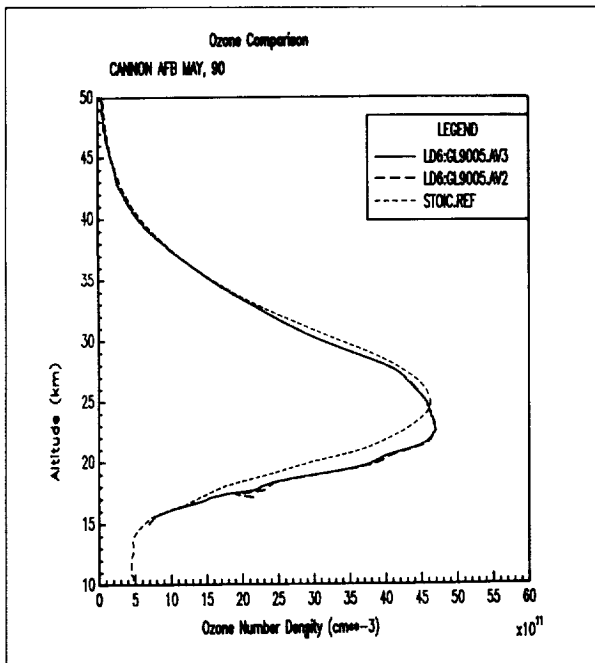
LIDAR MEASUREMENTS OF TEMPERATURE AND OZONE

The Goddard Stratospheric Ozone Lidar Trailer Experiment was deployed at Cannon Air Force Base in Clovis, New Mexico, in the spring of 1990, and made measurements of ozone and temperature in conjunction with a NASA-sponsored balloon launch from Fort Sumner, New Mexico, approximately 60 miles west of the lidar location. The balloon package contained several ozone-measuring instruments, including an ultraviolet-absorption instrument.

The Goddard lidar is a differential-absorption lidar which transmits two wavelengths, one which is absorbed strongly by ozone and one which is absorbed only weakly. The weakly absorbed wavelength serves as an atmospheric reference, and ozone can be extracted from the difference between the two lidar returns. The reference wavelength also can be used to determine temperature between altitudes of 30 and 70 km. The lidar is installed in a trailer and has been designed to be a transfer calibration standard for the



Comparison of ozone measurements by balloon launch and NASA Goddard lidar at Cannon Air Force Base for May 10, 13, and 15, 1990.



Average of all data collected at Cannon Air Force Base compared with the reference profile used in the Stratospheric Ozone Intercomparison campaign for July 1989.

international Network for Detection of Stratospheric Change (NDSC).

During the New Mexico campaign, data were taken over a period of 6 weeks. The balloon package was launched but experienced a balloon failure near 75,000 ft. An ozone profile was retrieved from both ascent to and descent from 23 km. This provided some overlap with the lidar profiles which typically began at 17 km. The balloon detected a very narrow layer of high-concentration ozone at about 16 km which is just noticeable in the lidar data from the evening after the balloon launch. The next data were taken 3 days after the balloon flight, because of bad weather. After the flight, the lidar data acquisition software was modified to collect data down to 15 km. The first figure shows the lidar data from May 10, 13, and 15, along with the balloon ascent and descent profiles. It can be seen that the extended lidar profile on the 15th still detects a layer which has moved slightly higher but still appears to have maintained the width over the 3 days. We have not yet been able to explain satisfactorily the layer or its stability, but meteorological data still is being analyzed.

The second figure shows an average of all the data collected at Cannon AFB compared with the reference profile used in the Stratospheric Ozone Intercomparison campaign for July 1989. There are seasonal differences noted, particularly at and below the ozone maximum.

Since this campaign, the lidar has been undergoing major modifications to improve the signal-to-noise ratio and to expand the altitude range for ozone determination. The modifications were to be completed in the fall of 1990, and a series of instrumental tests were scheduled for Table Mountain, California, in February 1991.

Contact: Thomas J. McGee (Code 917)
(301) 286-5645

Sponsor: Upper Atmosphere Research Program

Dr. Thomas J. McGee currently is the Principal Investigator of the ground-based ozone lidar program. He is building a Temperature and Aerosol Lidar for inclusion in the NDSC. A member of the Optical Society of America, Dr. McGee has 10 years of experience at Goddard. He received a PhD in physical chemistry from the University of Notre Dame.

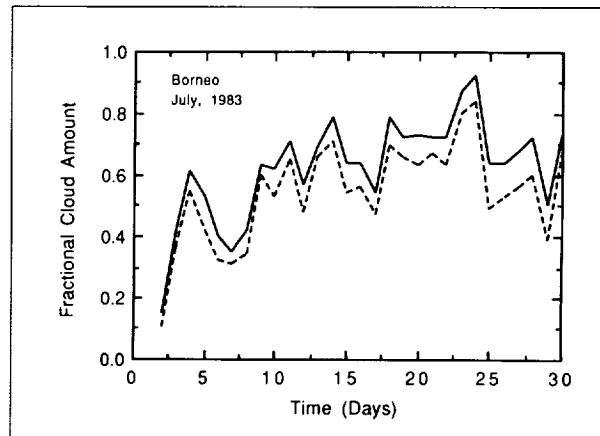


THE DERIVATION OF CLOUD PARAMETERS FROM SATELLITE-MEASURED RADIANCES FOR USE IN SURFACE RADIATION CALCULATIONS

Heat and momentum exchanges between the atmosphere and the Earth's surface are important mechanisms in forming atmospheric and oceanic motions. Information on the distribution of these exchanges is, however, rather poor because of large spatial and temporal variations and inadequate surface observations. Ideally, the large-scale spatial and temporal distributions of surface radiation budgets can be derived best by coupling a theoretical radiative transfer model to satellite retrievals of atmospheric and surface properties. The accuracy of surface radiation calculations depends heavily upon the information on the atmospheric, cloud, and surface parameters. Among these parameters, clouds are the most important, yet least understood.

A method has been developed for deriving cloud optical thickness, amount, and height from satellite-measured radiances for use in surface radiation calculations. The method of cloud retrieval is to specify subjectively a cloud reflectivity threshold for identifying satellite pixels which are likely to be filled totally with clouds. Area-averaged values for cloud parameters are derived from the reflectivities of these cloudy pixels and from the satellite-measured radiances in the visible and infrared (IR) window channels. Because the cloud reflectivity threshold is specified empirically, errors in the derived cloud parameters are expected. Theoretical radiative transfer calculations show, however, that if the derived cloud parameters are consistent with the radiation at the top of the atmosphere, they can be used for accurate surface radiation calculations. Errors arising from the uncertainties in cloud amount, height, and optical thickness offset each other to a large extent.

The cloud retrieval scheme is applied to the ISCCP Geostationary Meteorological Satellite B3 radiances for the western tropical and subtropical Pacific regions. Mean cloud amount, optical thickness, and height are computed for 2.5° by 2.5° latitude-longitude regions. Using a radiative transfer model, surface solar and IR fluxes are computed from the derived cloud parameters and the National Meteorological Center analyses of atmospheric and surface temperature and humidity fields. Two cloud reflectivity thresholds, 0.3 and 0.4, are used. The daily mean fractional cloud cover derived using the two cloud

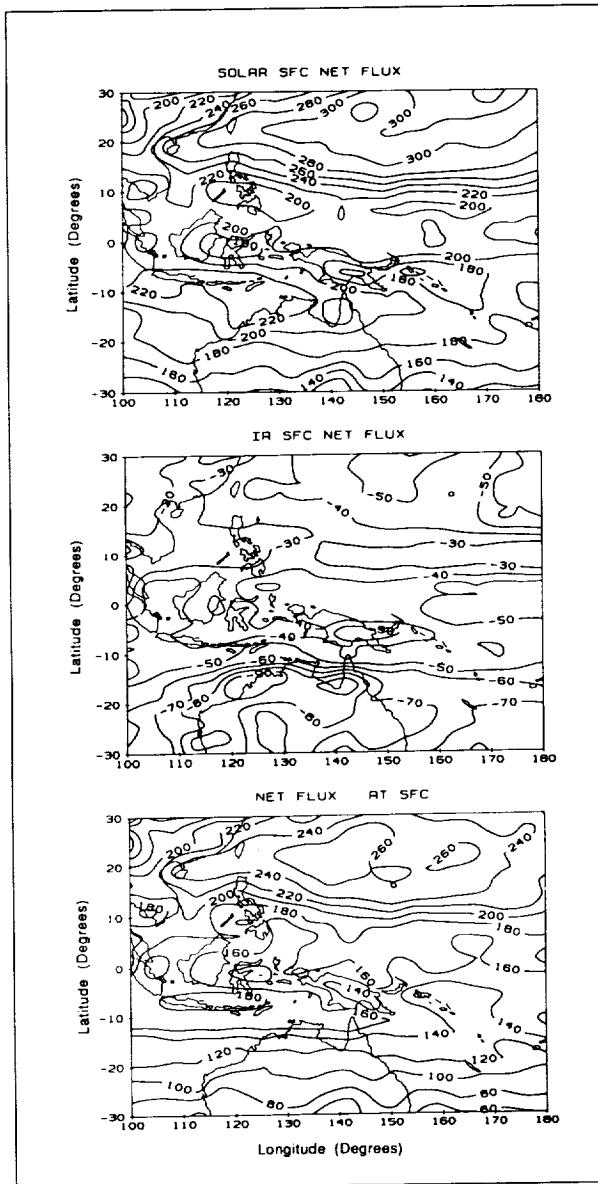


The daily fractional cloud amount derived for the Borneo area (0° - 2.5° N latitude, 110° - 112.5° E longitude) for July 1983. The solid and dashed curves are for cloud thresholds of 0.3 and 0.4, respectively.

thresholds is shown in the first figure for a region in western Borneo (0° - 2.5° North, 110° - 112° East) for the month of July in 1983. Except for the first few days of the month, this region is rather cloudy, with a cloud amount of 0.5-0.9. The monthly mean cloud amounts are 0.62 and 0.54, respectively, for the cloud thresholds of 0.3 and 0.4. The inferred cloud parameters are sensitive to the cloud threshold, but the surface radiation is rather insensitive. Over a broad area in the region from 30° South to 30° North and from 100° to 180° East, the difference between the monthly net surface fluxes for the two cloud thresholds is $< 2 \text{ W/m}^2$.

Monthly mean radiative fluxes are computed for the tropical and subtropical regions between 100° and 180° East. The second figure shows the distribution of the computed net downward surface fluxes for the solar radiation (top panel), the IR radiation (middle panel), and the total radiation (bottom panel) using a cloud threshold of 0.4. The distribution of surface solar radiation follows closely the distribution of the IR brightness temperature measured by the satellite. The two rows of minimum solar radiation correspond to the two rows of cloud clusters in the Intertropical Convergence Zone (ITCZ). The maximum in the Northern Hemisphere subtropical region corresponds to the region of minimum cloudiness.

On the other hand, the distribution of surface IR radiation does not correspond so well to the distribution of brightness temperature. The downward surface IR radiation is small in dry atmospheres and large in humid atmospheres.



Distributions of the computed net downward solar flux (top panel), to the net downward IR flux (middle panel), and the total net downward flux (bottom panel) for the Borneo area (0° - 2.5° N latitude, 110° - 112.5° E longitude) for July 1983. The units of flux are W/m^2 .

The minimum net downward (or equivalently maximum net upward) surface IR radiation for Australia is attributable to the dry atmosphere and the high daytime desert temperature. Because the magnitude of the downward IR radiation is comparable to that of the upward IR radiation, the net surface IR radiation is a factor

of 2-6 smaller than the net surface solar radiation. Accordingly, the distribution of net surface radiation (bottom panel) follows that of solar radiation.

The total net surface radiative heating increases from approximately $100 W/m^2$ in the Southern Hemisphere subtropical region to approximately $160 W/m^2$ in the equatorial region. It reaches a maximum of $260 W/m^2$ in the Northern Hemisphere subtropical region. For a mixed ocean layer 60 meters deep, a surface heating of $100 W/m^2$ lasting for 1 month will cause an increase of $1^{\circ}C$ in water temperature. The spatial distribution of surface radiative heating as shown in the figure has a significant implication for the oceanic and atmospheric circulations.

Surface solar radiation has been derived empirically by a number of investigators from the satellite radiation measurements using linear regressions. Results of this study also show a linear relationship between the solar fluxes at the surface and at the top of the atmosphere. It is found that the relationship is dependent strongly upon the solar zenith angle. With a given amount of solar flux at the top of the atmosphere, differences in the daily surface solar fluxes could be greater than $30 W/m^2$ for latitude zones 20° apart in the tropical and subtropical regions. The humidity difference in a latitude zone causes the data points to scatter but is not great enough to alter the linear relationship. Surface reflectivity has an insignificant effect on the relationship. The linear relationships derived for various climatic regimes can be used to compute the surface solar fluxes from the satellite-derived fluxes at the top of the atmosphere.

The inferred cloud heights are sensitive to the cloud threshold. Vertical distributions of solar heating and thermal cooling in the atmosphere change accordingly. Although the total atmospheric cooling (thermal cooling minus solar heating) changes only slightly, the peak of the cooling profile shifts upward with clouds as the cloud threshold increases. The shift in the vertical distribution of heating/cooling in the atmosphere could have a significant implication for the large-scale atmospheric circulations.

Contact: Ming-Dah Chou (Code 913)
(301) 286-4012

Sponsor: NASA Headquarters Climate Program

Dr. Ming-Dah Chou, who holds a PhD in meteorology from New York University, develops radiative transfer



models for atmospheric heating/cooling calculations and studies the effect of radiative forcing on climate. Dr. Chou, who has 11 years of experience at Goddard, received the Goddard Exceptional Performance Award in 1981.

TROPICAL RAINFALL AND GLOBAL CHANGE

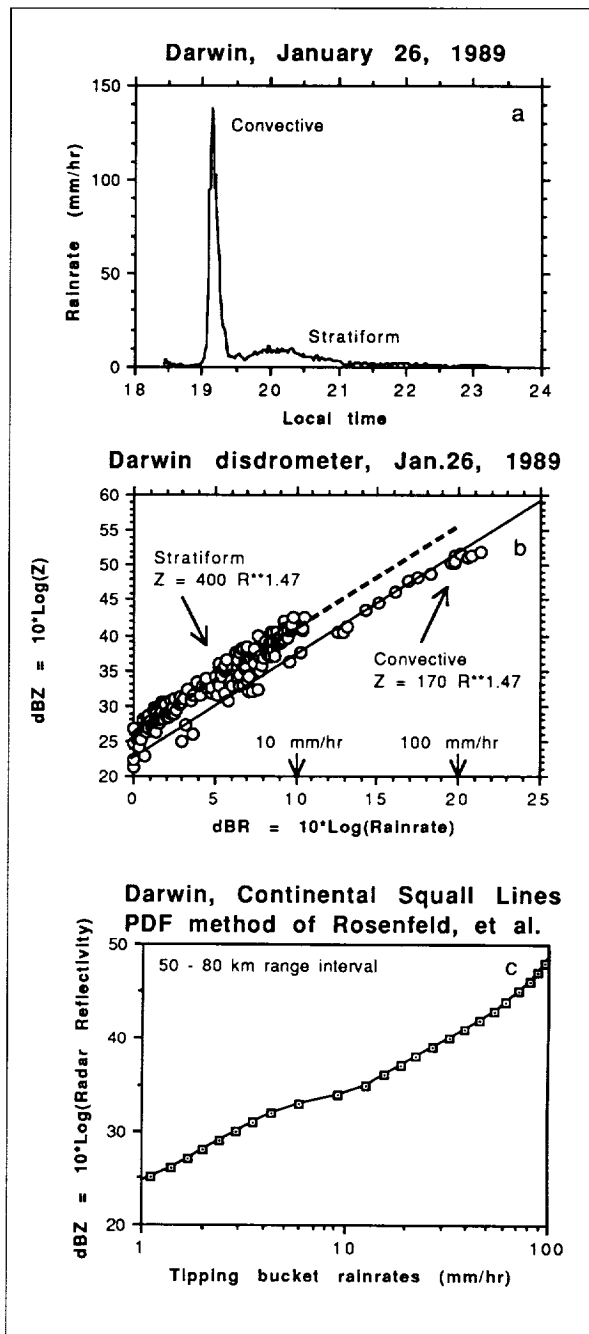
A primary driving force of atmospheric circulation patterns is latent heat released during the formation of tropical rain. Accurate measurements of shifting tropical rainfall patterns are required to improve global circulation models and their forecasts of worldwide weather and climatic conditions, including assessments of global change.

Space-borne and ground-based meteorological radars will comprise the backbone of future tropical rain observing systems being designed to monitor rainfall variability. Calibration of satellite radars over ground-based radar validation sites in the major tropical rainfall regimes will allow accurate satellite rain rate retrievals over remote tropical oceans and jungles.

Field studies currently are underway to develop knowledge of tropical rain rate characteristics and to establish methodologies ensuring satellite and ground-truth rain rates with the highest possible accuracy. Validation sites have been established in Florida, Northern Australia, Kwajalein Atoll and Thailand under the Ground Truth Program of the Tropical Rainfall Measuring Mission (TRMM). These sites are equipped with digitized radars, rain gauges of various types, and in some cases, raindrop disdrometers. Additional sites are planned.

The top graph of the figure shows a time series of rain rate in Darwin, Australia, during the passage of a tropical squall line, with its leading edge of heavy, convective rain and large trailing area of light, stratiform rain. Such squall lines are often several hundred kilometers long and are among the mesoscale convective systems that account for much of the rainfall and latent heat release in the tropics. Accurate measurement of these distant rainfall regimes by radar requires knowledge of the appropriate radar reflectivity rain rate (Z-R) relation.

The radar measurement of rain rate, accomplished by observation of backscattered microwave radiation, is, under



Convective stratiform rain regimes of tropical squall lines in Darwin, Australia: (a) a 6-hour series of rain rates observed during a squall line passage; (b) radar reflectivity versus rain rate for the time series above, as calculated from raindrop size distribution observations, in a log-log coordinate; and (c) effective Z-R relation for Darwin squall lines from radar and tipping bucket rain gauge observations.

ideal conditions, dependent only on the size of distribution of raindrops. The middle graph of the figure shows calculated radar reflectivity and rain rate from raindrop size observations during the event shown in the top graph. The convective and stratiform portions of the storm are separated clearly into two distinct linear families in the log-log plot, indicating separate power law Z-R relations.

A recent, independent study of Ze-R relations from radar and rain rate observations in Darwin corroborates the stratiform-versus-convective result shown in the middle graph. Ze refers to the reflectivity actually observed by an operational radar. The bottom graph shows matched percentiles of rain rate, from tipping bucket gauges, versus radar reflectivity, for continental squall-line cases during the 1987-1988 rainy season.

Note that a straight fit to the data points having rain rates < 10 mm/hr in the bottom graph would be parallel to, but offset from, a straight-line fit to the data points having rain rates greater than 10 mm/hr. This shift in Ze-R relations between the convective and stratiform portions of Darwin squall lines is the same as shown for Ze-R relations by the disdrometer data in the middle graph during the following rainy season, except for effects due to the radar beam-width.

Radar measurement of tropical rain will be improved for future satellite radar missions and ground-truth validation sites by these and further studies of tropical rain characteristics currently in progress.

Contact: David A. Short (Code 913)
(301) 286-7048

Otto W. Thiele (Code 910)
(301) 286-9006

Daniel Rosenfeld
Hebrew University

Sponsor: Office of Space Science and Applications

Dr. David A. Short, a research meteorologist with 11 years of service at Goddard, holds a PhD in meteorology from Texas A&M University. Dr. Short recently completed a 1-year research fellowship in Japan and has been active in the TRMM, a joint U.S.-Japan project, since 1985.

Mr. Otto W. Thiele, a senior research meteorologist with 24 years of service at Goddard, received his formal meteorological education at the University of

Texas. Mr. Thiele is a co-originator of the initial TRMM space flight proposal and organizer of the TRMM Global Validation Program.

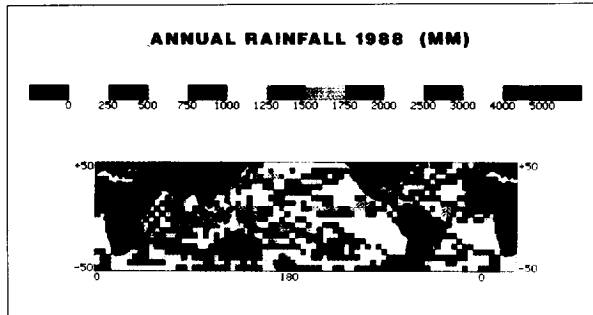
Dr. Daniel Rosenfeld holds a PhD in atmospheric sciences from the Hebrew University of Jerusalem, Israel, where he is now Lecturer and Head of the Laboratory for Rain and Cloud Physics. Dr. Rosenfeld, an internationally recognized expert in the fields of radar meteorology, cloud seeding, and cloud physics, is also a member of the TRMM Science Team.

MONTHLY OCEANIC RAINFALL INDICES FROM SPECIAL SENSOR MICROWAVE/IMAGER (SSM/I) DATA

Accurate measurements of global precipitation are vital to the advancement of our knowledge of the dynamics of the atmosphere and oceans. The rapidly varying spatial and temporal distribution of precipitation poses a great challenge to meteorologists to estimate the time/area average rainfall over the globe. The network of rain gauges over land is mostly inadequate, and in oceanic regions the network of rain gauges is almost nonexistent. Satellite-borne sensor systems which can cover a large area in a short time are ideal for the study of precipitation.

The Special Sensor Microwave/Imager (SSM/I) is a four-frequency (19.35, 22.235, 37 and 85.5 GHz) microwave radiometer on board the Sun-synchronous Defense Meteorological Satellite Program (DMSP) satellite. The instrument scans a swath of approximately 1,400 km with a constant look angle of approximately 53 degrees on the Earth's surface. The spatial resolution varies from 69 by 43 km at 19.35 GHz to 15 by 13 km at 85.5 GHz. The SSM/I measures radiation in both horizontal and vertical polarizations at all frequencies except 22.235 GHz where it measures only the vertically polarized component. The first copy of this instrument was launched in June 1987, and, since it is an operational instrument, one or more copies can be expected to be operating in orbit nearly all the time for the foreseeable future.

Rainfall estimation techniques using passive microwave data have been developed using Nimbus-5 Electrically Scanned Microwave Radiometer (ESMR) data. The microwave brightness temperature as observed from a space-borne sensor is dependent upon the radiation emission from the Earth's surface and modified by the



A map of the amount of annual rainfall, as measured by the SSM/I. The range varies from 100 to 4,000 mm/yr.

intervening atmosphere. Hydrometeors are the main sources of absorption and scattering of microwave radiation in the atmosphere. Over oceans, the microwave radiation at 19.35 GHz can be related to the rain intensity over the dynamic range of 2-2.5 mm/hr from first principles with only a few approximations. The histogram approach is based on the observation that rain rate can be modeled in statistics by a mixed distribution. The mixed distribution consists of a discrete probability of no rain at zero rain rate and a log-normal distribution for the raining part. Hence, the parameters of the rain rate probability distribution function (pdf) can be related to the temperature histogram.

Twenty months of SSM/I data have been processed into monthly histogram and rain totals. An annual rainfall map is shown in the first figure. The range varies from 100 to 4,000 mm/yr. From these data, one can see a general suggestion that the rain totals are greater by about 20 percent for the morning passes than for the evening passes. The lack of ground truth over oceanic regions makes verification of the results difficult. A comparison with the climatology data sets shows the monthly mean rain estimated using the pdf method generally gave lower values. This is probably because of the inhomogeneity within the field of view of the microwave sensor and the non-linearity of the rain rate/brightness temperature relationship. For beam widths the size of the SSM/I, the bias factor is about 1.8 based on the Global Atlantic Tropical Experiment data. With the correction, the retrieved precipitation values compared well with the climate data sets.

This method of studying precipitation using passive microwave radiances may be used to provide global precipitation estimates.

Contact: Alfred Chang (Code 974)
(301) 286-8997

Sponsor: Office of Space Science and Applications

Dr. Alfred Chang has 16 years of experience at Goddard. Previous experience in the Laboratory for Hydrospheric Processes includes work on the ESMR and SMMR for Nimbus 5, 6 and 7. His interests include radiative transfer calculations and microwave interactions with precipitation, snow, soil, and vegetation. Dr. Chang holds an MS and a PhD in physics from the University of Maryland.

THE IMPACT OF SEVERE STORMS ON SATELLITE RADAR ALTIMETER MEASUREMENTS

The water content of the atmosphere has a strong effect on active radar signatures. The intensity of this effect varies with radar frequency. Radar backscatter from liquid water is used in the development of sensors for the measurement of precipitation. Ground-based and airborne measurements of precipitation are now commonplace, and a program is underway to build a rain radar for TRMM.

The rain signal causes noise in radar altimeters that are used to map the sea surface topography. Radar altimeters are built to penetrate the moist atmosphere to the sea surface. Consequently, frequencies are used which are less sensitive to atmospheric moisture. However, in the presence of rain, the signal is attenuated, and, in the case of intense rain, the signal is reflected by the rain. Between 1985 and 1989, the U.S. Navy successfully operated the GEOSAT altimeter satellites to measure the ocean surface. We have used the observations from this system to explore the impact of rain on radar signals.

The accompanying figure shows the impact of a severe rain squall on the GEOSAT altimeter signal. Hurricane Gilbert passed through the Caribbean in the fall of 1988. On September 12, it moved over the island of Jamaica, causing billions of dollars in damage. At the same time, the GEOSAT altimeter flew over the southeast wall of the storm.

The picture in the upper left-hand corner of the figure shows the cloud cover generated by the storm as seen in the infrared from a National Oceanic and Atmospheric Administration (NOAA) polar orbiting satellite. The eye

of the hurricane is over the eastern region of Jamaica. A broad red band is shown extending from the top to the bottom of the inset figure. This band follows the path of the satellite from north to south. The dark red line on the right side of the band is the actual ground track of GEOSAT. The width of the band at any point is related to the power in the radar return signal. A wide band indicates strong return, whereas a narrow band indicates an attenuated signal. Note how the signal becomes attenuated and eventually is cut off as the altimeter passes over the southeast side of the hurricane.

The three-dimensional plot beneath the infrared image is a display of the variation in the returned radar as a function of time. The narrow axis which projects into the page is the time in nanoseconds, or gate, in which

the return signal is captured. On GEOSAT there were 64 return gates to capture the reflected radar pulse. Each profile along this axis is called a waveform of the return power. These waveforms have been averaged over about 100 radar pulses every 0.1 second. The vertical axis is the strength of the return power (normalized by the total returned power). The long axis is a time line in seconds of the ground track. This ground track is the same as shown in the inset infrared image. The right side of the time line corresponds to the red band at the top of the infrared image and the left side of the time line corresponds to the bottom portion of the red band, just below the gap near the eye of the hurricane.

Before the altimeter reaches the hurricane, the returned waveforms are fairly consistent in shape, except over the



The impact of Hurricane Gilbert on the radar signal from the U.S. Navy's GEOSAT altimeter satellite. The inset figure shows a composite of an infrared image of Hurricane Gilbert as it crosses Jamaica and, in red, the GEOSAT altimeter returned power. The three-dimensional plot displays the variations in the returned power along the red line.



two islands in the Bahamas which cause small gaps in the measurements. This is because the sea surface is relatively flat. As the altimeter begins to fly over the hurricane, the waveform begins to vary. Some of this is caused by an increase in surface wave heights in the northeast quadrant of the hurricane. Surface wave height can be measured by the rate of return power (large waves cause the power to be distributed through more gates). The most dramatic variation in the waveforms occurs when the radar goes over an intense rain squall in the southeast sector of the hurricane (aircraft radar showed rain rates in excess of 5 cm per hour). The waveform becomes homogeneous through the receiver gates just before the radar loses signal lock, which causes the gap in the data.

The analysis of the radar from Hurricane Gilbert shows that the signal is disturbed by intense precipitation. The specular reflection is damaged leading to a variation in the waveform, and the return power is strongly attenuated. Both of these factors increase with the intensity of the rain. Using a threshold of attenuation as an indicator of rain, we have mapped the rainy regions of the world's oceans during 1987 from the GEOSAT altimeter data.

We have constructed seasonally averaged global maps of the rainy areas. The Intertropical Convergence Zone is delineated clearly in these maps, and the seasonal movement of this region can be identified. Similarly, the South Pacific Convergence Zone and mid-latitude rain belts are delineated. Our maps show more active precipitation in mid-latitude regions during the summer months. This is because they identify only regions of rain produced by convective activity.

Contact: Chester J. Koblinsky (Code 926)
(301) 286-2880

Edward J. Walsh (Code 972)
(303) 320-6357

Prabhakara Cuddapah (Code 913)
(301) 286-5390

This work was done in collaboration with Dr. Len Fedor of the NOAA Environmental Research Laboratories.

Sponsor: Office of Space Science and Applications

Dr. Chester J. Koblinsky, who has been at Goddard for 7 years, was awarded the NASA Medal for Exceptional Scientific Achievement in 1990 for his work on the scientific applications of satellite radar altimeter

measurements. He received his PhD in physical oceanography from Oregon State University.

Dr. Edward J. Walsh works in the Observational Science Branch, where he is involved in the design and verification of airborne and satellite radar systems. Dr. Walsh has been at Goddard for 10 years and with NASA for 23 years. He earned his PhD in electrical engineering from Northeastern University.

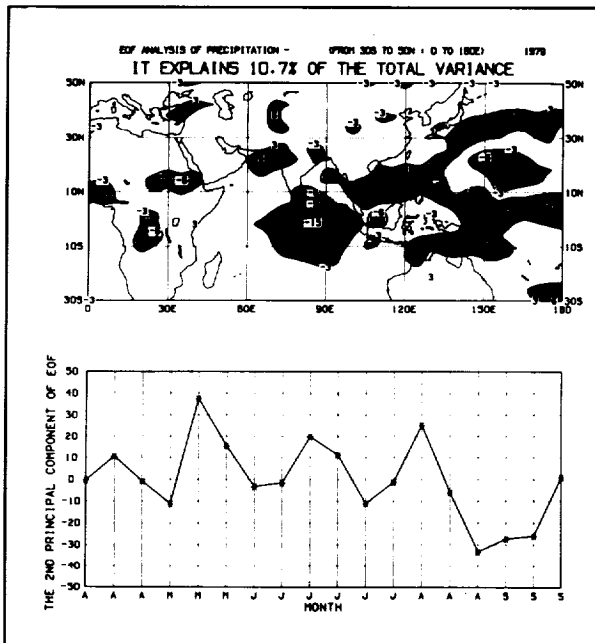
Dr. Prabhakara Cuddapah is a member of the Climate and Radiation Branch, where he has been involved with precipitation studies. He has been at Goddard for 24 years. He holds a PhD in meteorology from New York University.

PRECIPITATION ESTIMATES DERIVED FROM SATELLITE DATA

Precipitation is produced from clouds; therefore, cloud physical and geophysical parameters have been used to estimate mean precipitation over a time period. To estimate precipitation from all types of clouds and over all regions of the globe, an algorithm which makes use of the cloud-top altitude, cloud amount, and cloud emissivity has been developed.

One parameter affected by all three of these cloud parameters is the cloud radiative forcing at the top of the Earth-atmosphere system. However, not all clouds produce rain and not all rain reaches the ground. Another parameter, which is an estimate of ground heating, is used to take this fact into account. The precipitation-estimate algorithm depends on both of these parameters: the cloud radiative forcing and the ground-heating effect. Both of them can be derived from difference fields of OLR. Therefore, the precipitation-estimate algorithm is referred to as the difference fields of OLR.

Currently, there is no reliable global precipitation measurement over the oceans. To check the consistency among passive remote-sensing techniques, especially over tropical oceans, algorithms have been developed from visible radiometry which make use of information on cloud optical thickness and from microwave radiometry which make use of information on cloud hydrometeors. In the tropics, the correlation coefficient between the precipitation estimates derived from difference fields of OLR (infrared radiometry) and precipitation estimates derived from microwave radiometry is 0.844. The correlation

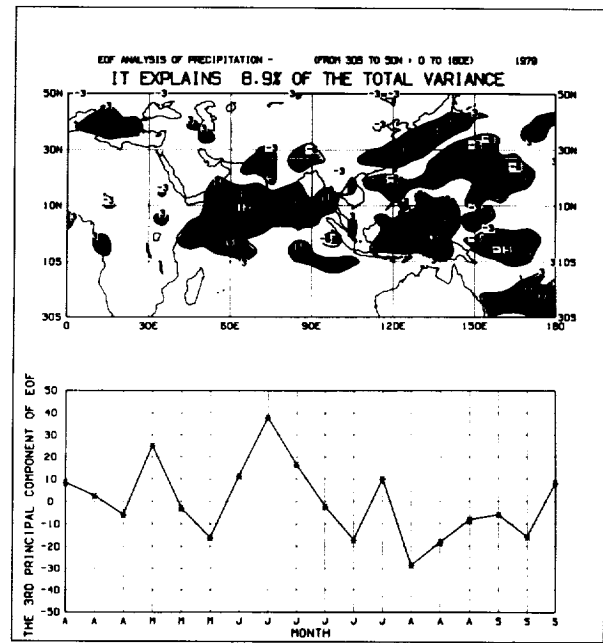


The second EOF and its practical component over a region from 30°S to 50°N latitude and 0° to 180°E longitude during the northern summer season.

coefficient is 0.877 between the infrared radiometry and visible radiometry during the day. The correlation coefficient between the precipitation estimates and rainfall derived from rain gauge data over the land is 0.799 when the number of rain gauge reports is greater than 10 in a 4° by 5° latitude-longitude grid box.

Global 10-day mean and monthly mean precipitation has been derived for the first Global Atmosphere Research Program (GARP) global experiment year. The seasonal and intraseasonal variations of atmospheric circulation patterns have been studied using the mean precipitation estimates. The derived precipitation estimates show all the known characteristics of the climatological global precipitation variations such as those associated with the seasonal cycle and the 30- to 60-day oscillations.

A regional analysis using the derived precipitation estimates and in-situ rainfall data also was carried out over the East Asian monsoon region and adjacent regions. It was found that the regional precipitation fluctuation over East Asia is connected with the precipitation fluctuations in the equatorial regions to 10° S latitude. Many of the precipitation features over East Asia, such as the intraseasonal oscillations, appear to have their origins in the near-equatorial regions. Empirical orthogonal function



The third EOF and its principal component over a region from 30°S to 50°N latitude and 0° to 180°E longitude during the northern summer season.

(EOF) analyses performed on the derived-precipitation estimates show that the 30- to 60-day oscillations are very pronounced over the global tropics and extratropics, especially during the northern summer season.

For purposes of illustration, the first and second figures show the second and third EOFs and their principal components over a region from 30° South to 50° N latitude and 0° to 180° E longitude. The 30- to 60-day oscillations, the monsoon trough, and the May-yu trough are well revealed in the figures. The results demonstrate the potential uses of these global precipitation-estimate techniques for climate studies, validation of GCMs, and GCM data assimilation.

Contact: Man-Li C. Wu (Code 911)
(301) 286-4087

Sponsor: NASA Headquarters, Office of Space
Science and Applications

Dr. Man-Li C. Wu is a Principal Investigator for cloud physical parameter retrievals using visible, thermal, infrared, and microwave radiometries. Her research interests during her 12 years at Goddard have included estimating precipitation from satellite data and studying the seasonal to interannual variability of climate associated with rainfall. She holds a PhD from the University of Chicago.



AIRBORNE LIDAR DETECTION OF SUBSURFACE OCEANIC SCATTERING LAYERS

The U.S. National Academy of Sciences has listed the study of biogeochemical cycles from space as a high-priority task in the study of global change. One biological variable that can be observed is the concentration of chlorophyll in the world oceans. The Airborne Oceanographic Lidar (AOL) instrument can observe the vertical distribution of ocean constituents and water optical properties. This makes it possible to complement satellite observations of ocean color by depth-resolved observations of pigments and particles. This will enhance the quality of estimates of total chlorophyll pigments as observed from satellites. The airborne lidar technology used by the AOL has been described in previous reports; here I will report on observations made at night during a flight across coastal waters, the waters on the continental shelf and slope, the Gulf Stream, and over the Sargasso Sea. The absence of sunlight makes it possible to observe the scatterers in the water in more detail. The scatterers include inorganic particles, organic debris, and to a significant extent in the upper layers of the ocean, organisms such as algae, microorganisms and larger phytoplankton up to the size of shrimp and fish.

The airborne lidar observations that I report here were obtained from the NASA P-3 aircraft in early June 1986, as a cooperative effort between NASA and the Naval Ocean Systems Center. The Laser used was a frequency doubled Nd:YAG (532 nm) laser that produced a 5-ns pulse (measured at half maximum pulse amplitude). The AOL and data system was as described in earlier publications. We also launched airborne expendable bathythermographs (AXBTs) to obtain the vertical temperature profiles of the upper layers of the ocean. This made it possible to relate phytoplankton density to water layers, since specific plankton populations tend to confine themselves to certain water layers.

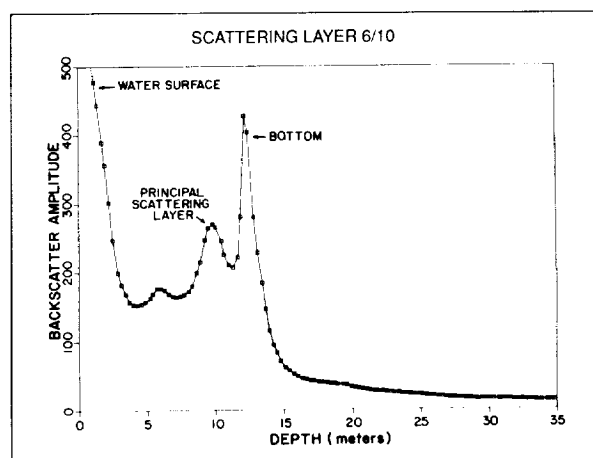
The results are illustrated in two figures. The first figure shows a typical return wave form near the coasts, where the bottom is close enough to the sea surface to give a clear reflection of the laser pulse. The spike near 12 m is the bottom reflection, the maximum near 10-m depth is due to in-water scatterers, and the water surface reflection is very strong, as one would expect. The width of the return from the scattering layer shows the

scatterers to be distributed over a range of depth, while the bottom return is very sharp.

If one now takes a typical return from clear water, as it is found in the Sargasso Sea east of the Gulf Stream, and subtracts it from each return pulse, one gets a "residual signal" that emphasizes the difference between clear water returns and scattering from plankton and sediments. The second figure shows the intensity of scattering in terms of gray scales, black being zero and white being very high intensity in the residual signal. The upper panel starts east of the Gulf Stream in the Sargasso Sea. The ticks along the horizontal scale are approximately 6 km apart. The track shows that in the Sargasso Sea, there is little residual scattering at any depth. In the second panel, as the track extends towards the northwest through the Gulf Stream, the slope water, and the continental shelf towards Assateague Island, one sees a scattering layer in the Gulf Stream and the slope water. Near the shelf break, the scattering intensity increases significantly.

In the third panel, the horizontal scale has changed to the tick marks being 1 km apart. Note how the bottom comes into view near 5 km from the left edge of the panel, then one sees the shoal as a bump on the bottom. The shoal seems to generate a wake in the form of a turbidity plume that extends towards shore. This plume may well be the wake of the shoal in a current; possibly a tidal current. The highest intensity in the plume occurs 7 km from the shoal.

Since there is no ship in the area to establish "sea truth" by taking water samples and analyzing them, we have to



A typical waveform from the inner portion of the flight line for data collected in an area of the Atlantic Ocean southeast of Wallops Island, Virginia.



A series of density plots of the residual waveform data from a flight over the Atlantic Ocean southeast of Wallops Island, Virginia. The observations were acquired over a number of differing water masses, including near-coastal, shelf, slope, and Sargasso Sea water.

speculate about the kind of scatterers present. We suggest that the scattering layers observed in the slope waters near the Gulf Stream and on the outer continental shelf are due to elevated phytoplankton concentrations. By contrast, the plume at the shoal and in the wake of the shoal is likely due to entrained sediments stirred up from the bottom.

Our observations illustrate the feasibility of laser sounding of the upper ocean to measure concentrations of scatterers, and, when verified further by "sea truth data" from ships, the possibility of measuring plankton concentrations. Chlorophyll can be observed by the fluorescence induced by the laser light, as has been demonstrated and reported in numerous publications. The added capability to look at the layered structure of scattering matter extends our observational capability in a significant manner.

Contact: Frank E. Hoge (Code 972)
(804) 824-3411

Sponsor: NASA Headquarters, Ocean
Processes Branch

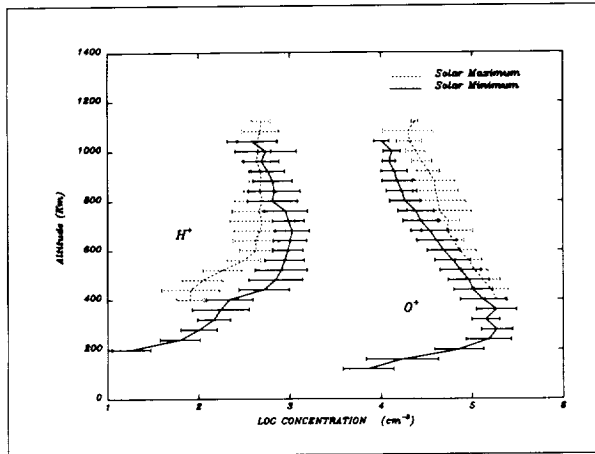
Dr. Frank E. Hoge, who has 24 years of service at Goddard, currently works in the Laboratory for Hydrospheric Processes. He has worked with the AOL program since 1975. He received an MS and PhD from West Virginia University.

POLAR CAP F REGION ION COMPOSITION—THE MEASUREMENTS

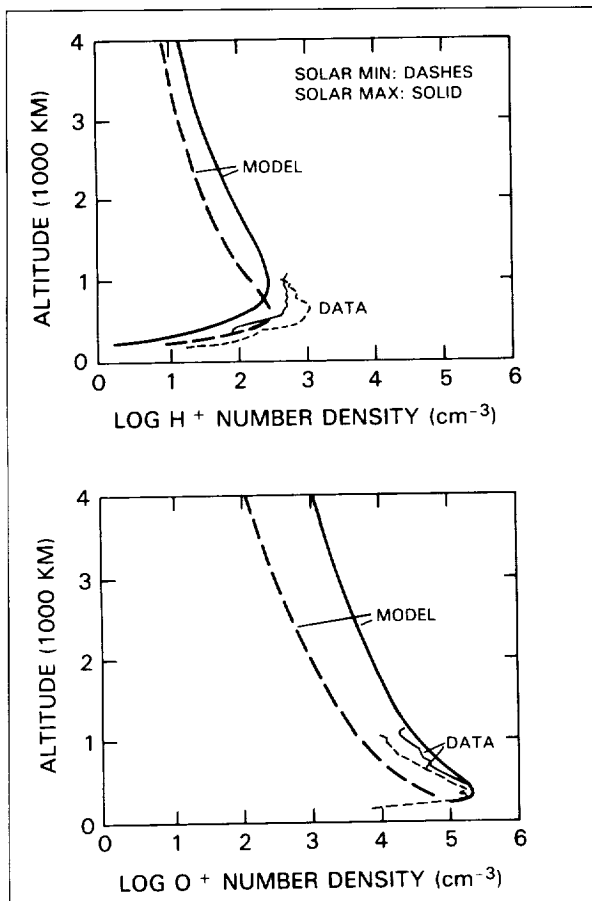
Theoretical modeling of the distribution of the thermal plasma ionosphere over the Earth's polar cap has far outstripped published data in predicting the controlling factors of the ion distributions in the polar regions. This is particularly true in regard to studies of the polar wind evolution in the topside F regions. (The polar wind refers to the upward acceleration of the light ions H^+ and He^+ in the midst of the dominant heavy ion O^+ ; the flow velocity of the light ions becomes supersonic.) Quantitative theoretical studies of the polar wind began with its conception by Banks and Holzer in 1968. This was followed by scores of further detailed theoretical studies of its spatial and temporal variations, up to the most recent computations of Cannatta and Gombosi in 1989, who predicted solar minimum and maximum differences.

In contrast to the proliferation of theoretical model studies there have been only three papers published which used direct measurements to offer evidence for the presence of the polar wind in the topside F-region. No previous studies have attempted to explore the details of the polar wind development using in-situ measurements. We have focused our attention on measurements in the topside ionosphere by using satellite ion composition and plasma temperature observations to describe solar maximum-minimum differences in the altitude distributions of the thermal ions O^+ and H^+ in the F region dayside polar cap. We studied the summer noontime region, modeled in detail using a steady-state polar wind model by Cannatta and Gombosi in 1989. The vertical distributions of the light ion concentrations relative to those of the oxygen ions are related directly to the vertical flow velocities. Hence, given measurements of the ion distributions, the flow profiles can be determined. In the theoretical models, both parameters are derived simultaneously from assumed high-altitude and low-altitude boundary conditions.

All available, computer-readable, thermal ion composition measurements from Earth-orbiting satellites have been put into a common computer file format for easy manipulation. The ion measurements obtained under solar maximum conditions at polar cap latitudes within a 6-hour, magnetic, local-time window about noon in the summer were culled from this data set for comparison to similar data for a solar minimum period. The results show distinctive solar-cycle variations in the topside F region altitude concentrations that reflect changes in the polar



The altitude distribution of the average ion concentrations in 40-km-altitude windows for two extremes of the solar cycle.



A comparison of the average observations to those theoretically modeled in the polar wind study of Cannatta and Gombosi.

wind source region. The first figure depicts the altitude distribution of the average concentrations in 40-km-altitude windows for these two extremes of the solar cycle. A comparison of the average observations to those theoretically modeled in the polar wind study of Cannatta and Gombosi are shown in the second figure. There are significant differences in the measured and theoretical values. It has been determined that the differences result from a strong dependence of the distributions on solar activity. Although both the model and data correspond to solar maximum and minimum activity conditions, they correspond to slightly different F10.7 values—enough of a difference to account for the discrepancy between the data and modeled values.

Contact: Joseph M. Grebowsky (Code 914)
(301) 286-6853

Walter R. Hoegy (Code 914)
(301) 286-3837

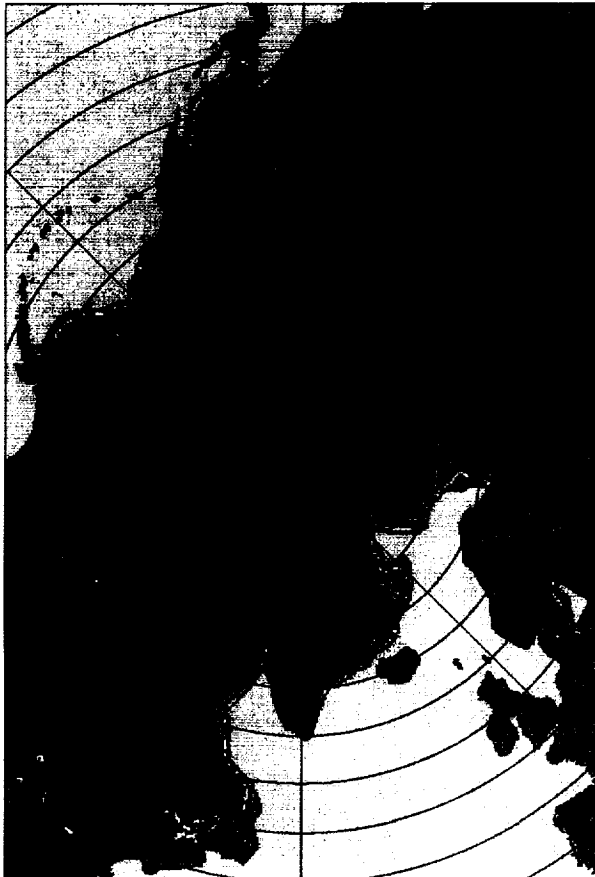
Sponsor: NASA Space Physics Division

Dr. Joseph M. Grebowsky has worked at Goddard for 23 years. He currently conducts research on low-energy plasmas in planetary ionospheres within the Planetary Atmospheres Branch. He holds a BS from Manhattan College and an MS and a PhD from Pennsylvania State University.

Dr. Walter R. Hoegy has spent 22 years at Goddard, after 2 years at the National Institute of Standards and Technology. His research interests focus on planetary ionospheres and solar-terrestrial relations in the planetary atmosphere. He is developing a new instrument to measure the solar flux on future aeronomy missions. He holds a BSE, an MS, and a PhD from the University of Michigan.

ARCTIC AND ANTARCTIC SEA ICE, 1978-1987: SATELLITE PASSIVE MICROWAVE OBSERVATIONS AND ANALYSIS

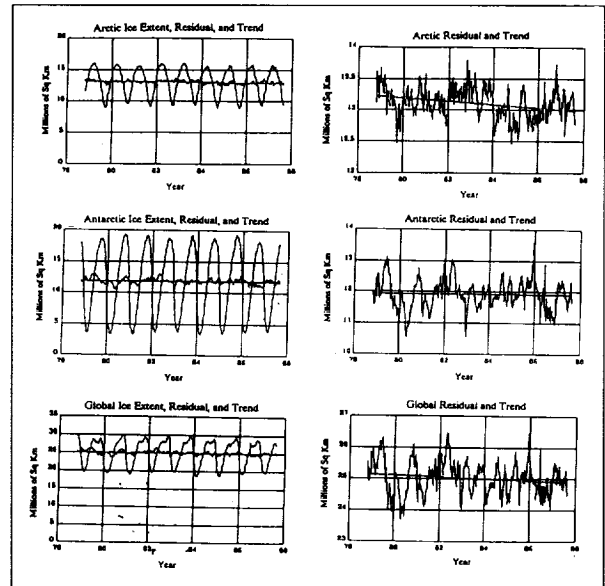
An atlas of sea ice coverage in the Arctic and Antarctic as observed with the Nimbus-7 SMMR is in its final stages of preparation. This book extends to a total of 15 years the satellite passive microwave record of global sea ice coverage begun with the 4-year record presented in its companion volumes, *Antarctic Sea Ice 1973-1976: Satellite Passive Microwave Observations* (Zwally et al.,



Monthly averaged sea ice concentrations in the Arctic for February 1979. Open ocean is shown in light blue. Ice concentrations of 96 to 100 percent are shown in purple. The color contours are in ice concentration steps of 4 percent.

1983) and *Arctic Sea Ice, 1973-1976: Satellite Passive Microwave Observations* (Parkinson et al., 1987), in keeping with the importance of sea ice as a component in the global climate system. In the earlier atlases, a single-channel instrument, the ESMR, was used.

The sea ice information presented in the new volume reflects a distinct advance over the information presented in the earlier atlases in that the SMMR is a multispectral, dual-polarization microwave imager. The multichannel SMMR data permit the elimination of ice temperature and type variations in the calculation of ice concentrations. This, in turn, has permitted more accurate determination of sea ice and the distinction between first-year and multiyear sea ice. For this reason, it is possible to present improved estimates of the open water within ice margins. An example of the monthly-averaged sea ice

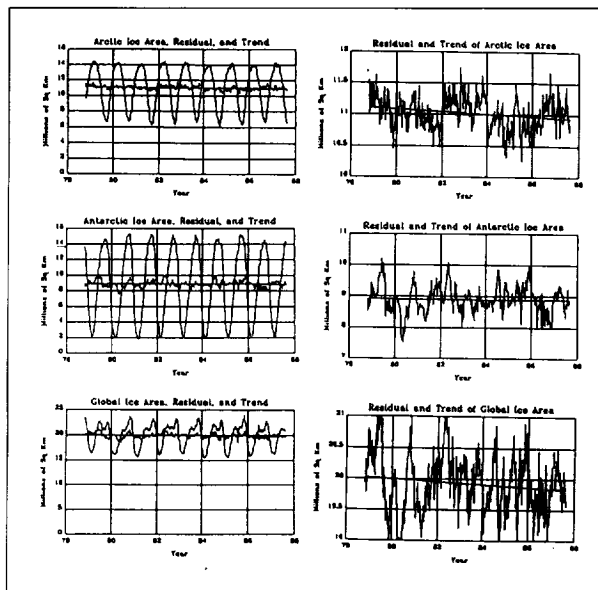


Arctic, Antarctic, and Global Sea Ice extents, their residuals after removal of the seasonal cycle, and their trends. The residuals and trends are shown on an expanded time scale on the right to emphasize the trends.

concentration maps that are part of the atlas is shown in the first figure.

The amplitudes of the seasonal oscillations in the sea ice extents (areas enclosed by the ice margins) of the Arctic and Antarctic given here are about the same as those in the ESMR atlases. The sum of the hemispheric sea ice extents, the global extent, also has an appreciable amplitude in its seasonal oscillation, varying from its minimum of about $20 \times 10^6 \text{ km}^2$ to a maximum of $30 \times 10^6 \text{ km}^2$. In view of the fact that a significant portion of the Earth's oceans is covered by sea ice, this suggests that average global oceanic insolation has an appreciable seasonal variation in spite of the out-of-phase characteristic of the boreal and austral seasons.

The integrated Arctic and Antarctic sea ice areas and extents presented here do not exhibit any monotonic trends in their extrema. The maxima in the global extents, however, do give a visual impression of a 9-year decline. Statistical analysis of the entire dataset suggests that there is a statistically significant downward trend of 2.1 percent during 8.8 years in the Arctic sea ice areas and extents, but none in the Antarctic. This differing behavior in the two hemispheres may have important implications for global ocean circulation. While the SMMR record is too short to



Arctic, Antarctic, and Global Sea Ice areas, their residuals after removal of the seasonal cycle, and their trends. The residuals and trends are shown on an expanded scale on the right to emphasize the trends.

define a climatic trend, it is an important baseline for comparison with future microwave observations.

In addition to the atlas, the SMMR polar data are due to be archived on CD-ROMs. To this end, a sampler disk has been produced and distributed to the user community for comments and for selection of a preferred format prior to issuing a full dataset.

Contact: Per Gloersen (Code 971)
(301) 286-6362

Donald J. Cavalieri (Code 971)
(301) 286-2444

Josefino C. Comiso (Code 971)
(301) 286-9135

Claire L. Parkinson (Code 971)
(301) 286-6507

H. Jay Zwally (Code 971)
(301) 286-8239

William J. Campbell
U.S. Geological Survey

Sponsor: Oceans and Ice Branch

Dr. Per Gloersen is a physicist with 21 years of service at Goddard. He currently works as a senior scientist in the Oceans and Ice Branch of the Laboratory for Hydrospheric Processes. His project experience includes work on Nimbus 5, 6, and 7, as well as Seasat. Dr. Gloersen holds an MA and a PhD in physics from The Johns Hopkins University.

Dr. Donald J. Cavalieri, a physical scientist at Goddard for 11 years, works in the Oceans and Ice Branch at the Goddard Laboratory for Hydrospheric Processes. His research focuses on the development of techniques for using passive microwave satellite observations and on the application of those techniques to the study of sea ice and its interactions with the atmosphere and oceans. He received a PhD from New York University.

Dr. Josefino C. Comiso was the Chief Scientist of the 1987 Arctic Aircraft/Submarine Sea Experiment. During his 11 years at Goddard, his research interests have included polar oceanography and biology, as well as sea ice and snow studies. He earned a PhD in physics at the University of California at Los Angeles.

Dr. Claire L. Parkinson's 12 years of research at Goddard have included various sea ice and climate studies, including coauthoring atlases of Arctic and Antarctic sea ice and a textbook on general circulation modeling of the atmosphere, oceans, and ice. She also has written a book on the history of science. Dr. Parkinson works in the Oceans and Ice Branch of the Laboratory for Hydrospheric Processes. She holds a BA from Wellesley College and an MA and a PhD from Ohio State University.

Dr. H. Jay Zwally is a research scientist involved with observing and modeling the variability of polar sea ice and continental ice sheets. He received a PhD in physics from the University of Maryland. During his 17 years at Goddard, Dr. Zwally has received the NASA Group Achievement Award for his contribution as an author of the Antarctic Sea Ice Atlas and the Goddard Exceptional Performance Award for his leadership in establishing a recognized cryospheric research program.

Dr. William J. Campbell is a scientist in the Water Resources Division of the U.S. Geological Survey. He received a BS in physics from the University of Alaska and an MS and a PhD from the University of Washington. His interests include sea ice physics, oceanography, and microwave remote sensing.

THE BOTSWANA WATER AND ENERGY BALANCE FIELD EXPERIMENT

The Botswana water and energy balance experiment originally was conceived as a 3-year study of the moisture and energy exchanges in a semi-arid savanna environment. The study was to complement concurrent similar investigations being conducted in other ecosystems. The Botswana study was partitioned into two phases:

- A retrospective phase which would analyze various aspects of approximately 10 years (1979-1988) of satellite, climatic, and ground data, and
- A 6-week field experiment during which intensive measurements of atmospheric, surface, and subsurface parameters would be made.

The overall purpose of the study was to examine the simultaneous integrated use of different portions of the electromagnetic spectrum as gathered by satellites to determine and monitor the physical and hydrologic status of the Earth's surface.

Although the basic theory of the physical processes leading to remotely sensed signatures on a local scale is fairly well understood, the application to large, inhomogeneous pixels is not straightforward. Most energy balance models have been tested and calibrated predominantly using point-of-local-ground observations. Little is known about the influence of spatial (within pixel) variability of surface characteristics on model performance and its

consequences for the inverse problems. Therefore, application of remotely sensed signatures to infer physical hydrological information at pixel scale requires fundamental solutions to the problems of pixel-scale parameterization and model calibration. In summary, the study established several specific objectives to help answer these problems of scaling. These objectives are:

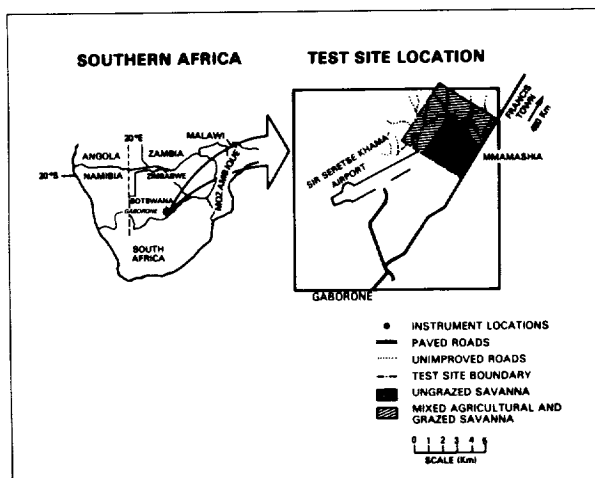
- To determine the influence of pixel surface inhomogeneity on the satellite signal.
- To establish the parameterization of surface physical properties at satellite scales.
- To explain the influence of surface inhomogeneity on the performance of water and energy balance models.
- To accomplish the scaling of point measurements to pixel- and regional-scale processes.
- To understand the implications of these questions for the inverse problem; i.e., the extraction of information on the physical status of the Earth's surface from remotely sensed measurements.

The acquisition of adequate ground data reflecting the spatial variability of surface physical and meteorological data was a necessity for the study. The key to the field experiment was a multilevel approach, whereby measurements by various similar sensors were made at several altitudes and resolutions.

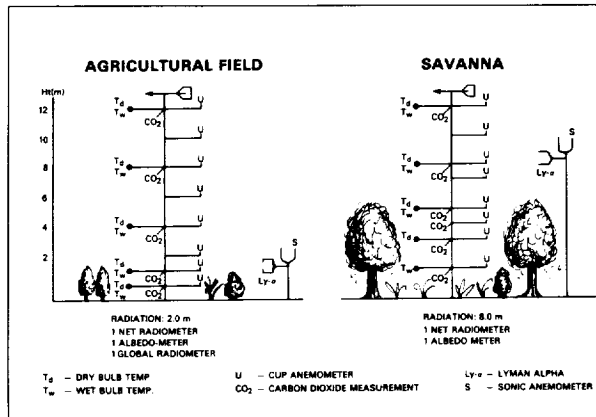
The field experiment was conducted in 1989 from January to March in South Central Botswana. Data collection was performed at two adjacent sites of contrasting surface character. Instruments were localized in an ungrazed natural savanna and in a cultivated field of both mixed agricultural and grazed area. Together, these two locations were representative of the majority of land surfaces common to this type of ecosystem.

The following types of measurements were made at each site:

- Flux measurements of sensible and latent heat were made by both eddy correlation and the profile method. Standard measurements of temperature, vapor pressure, air speed, and global and net radiation were made. CO₂ profiles were measured alternately at the two sites.
- Surface temperatures were measured continuously by thermal-infrared radiometers from a 6-m height,



Map depicting the relative location of the study area for the Botswana field experiment.



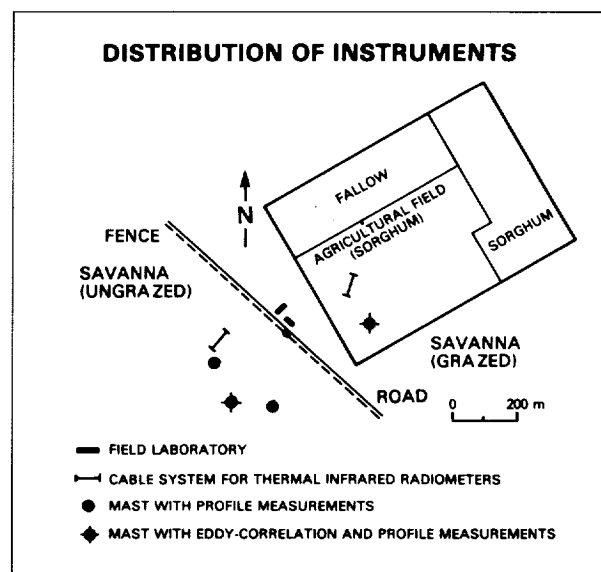
Basic setup of meteorological instruments.

along two 30-m cable systems, one in the savanna and one in the agricultural field. Each cable system contained two radiometers with 4-degree and 15-degree fields of view (FOV). A typical example of surface temperature scanning for the agricultural field and the savanna is shown in the fifth figure. Surface temperature also was measured with the same instrument (15-degree FOV) mounted on a light aircraft. During six NOAA passovers, a 5-by-5 km area was covered by 20 flight lines 250 m apart, also covering the thermal-infrared cable systems.

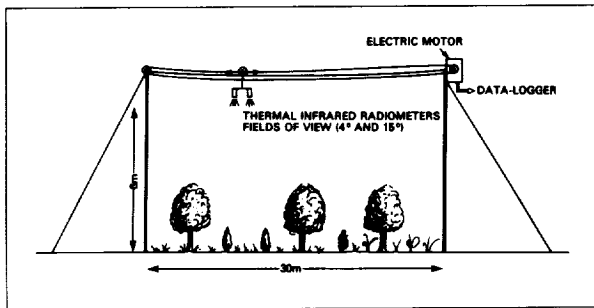
- Soil temperatures were measured at eight vertical profiles (five depths) under the thermal-infrared cable systems.
- Soil moisture was measured in three ways: volumetrically, by neutron probe, and by using gypsum blocks. About 60 neutron access tubes were spread over the experimental site and along the thermal-infrared cable systems and measured weekly. Surface moisture to 10 cm was measured volumetrically twice weekly at all neutron tube locations and daily along the cable systems. The gypsum blocks were installed in four vertical profiles (five depths) along the cable systems and monitored every 15 minutes.
- The intensive study site at Mmamashia was classified into homogeneous vegetation units using 1:50,000 panchromatic, stereo aerial photographs, and field observations. Typical samples of the major units were described quantitatively in vertical strata consisting of herbs, shrubs, and larger trees. Grass samples and individual shrubs and

trees were harvested to determine leaf dry weight. Leaf area was measured in subsamples and used to calculate the relationship of leaf area and dry weight. From these observations, the leaf area index (LAI) will be calculated for each vertical stratum of the vegetation units. The vertical and horizontal distributions of LAI and green leaf biomass will be derived for the 5-km study site from these data.

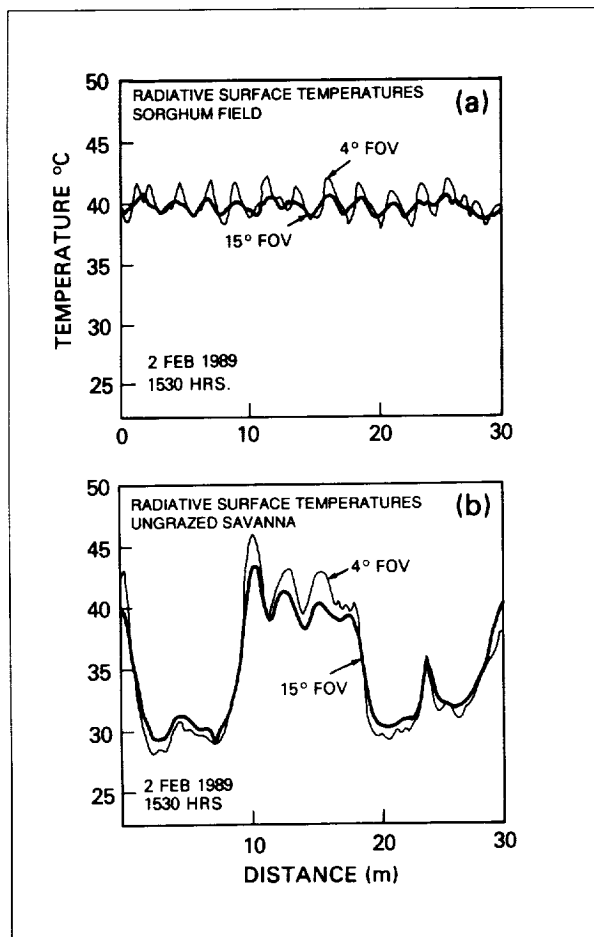
- During the field campaign, the following satellite data were acquired: NOAA-AVHRR (LAC-data) at 0220 and 1420 local standard time (LST) (NOAA-11) and at 0720 and 1920 LST (NOAA-10); METEOSAT, every hour; Landsat/TM, two images, at the beginning and end of the field campaign; and Satellite Pour L'Observation de la Terre (SPOT), two images, at the beginning and end of the field campaign.
- The reflections in the red and near-infrared bands also were measured by an aircraft-mounted radiometer. These measurements were made by an Integrated Camera and Radiometer system (ICAR). The ICAR consists of a computer-operated optical camera and a red and near-infrared radiometer having exactly the same footprint as the camera. In addition, a thermal-infrared radiometer of the same type used on the cable system was mounted on the ICAR, having a fixed footprint within the footprint of the optical camera.



Map depicting the relative instrument locations within the Botswana study site.



Thermal infrared cable system for measuring radiative surface temperature.



Typical patterns of a radiative surface temperatures measured in (a) the agricultural field, and (b) the ungrazed savanna.

The radiometer system was mounted on a Cessna-206 aircraft. The 5- by 5-km intensive study area was traversed with 20 5-km flight lines, spaced at intervals of 250 m. The photograph scale was 1:4,300 on the film

which can be projected to 1:400 with good resolution. Complete photographic coverage (1200 exposures) was obtained once, with a slight along-track overlap and 100 m between the lines. Individual FOVs were 100 by 50 m. Flights were made on five occasions to coincide with near-nadir NOAA-11 satellite overpasses. Complete radiometer and radiative surface temperature datasets were obtained on each flight.

- Atmospheric soundings of air temperature and relative humidity were performed daily from Gaborone International Airport, 7 km from the field site.
- Stomatal resistance was measured as an internal resistance for small samples of cover types and branches of different tree species. This was done by a bulk stomatal resistance chamber.
- Surface emissivity was measured frequently for different surface types (bare and vegetation-covered) using an emissivity box.

The Botswana Water and Surface Energy Balance Research Program is a cooperative research activity of the Free University of Amsterdam, the Hydrological Sciences Branch of NASA, and the Meteorological Services of Botswana. Other participants are the Earth Resources Branch of NASA, the Department of Physics and Meteorology of the Agricultural University of Wageningen and the Remote Sensing Unit of the United Nations Food Agricultural Organization in Rome.

Contact: Manfred Owe (Code 974)
(301) 286-5173

Sponsor: Land Processes Branch, Free University of Amsterdam

Dr. Manfred Owe has 10 years of service at Goddard. He works in the Hydrological Sciences Branch of the Laboratory for Hydrospheric Processes. He earned his PhD in soil science from the State University of New York at Syracuse.

OCEAN WIND WAVE MODELING

Wind waves at the ocean form the direct link between the atmosphere and oceanic boundary layers. Historically, wind waves have been investigated to obtain design conditions for coastal and offshore structures and to assess safety at sea. After some theoretical work in the

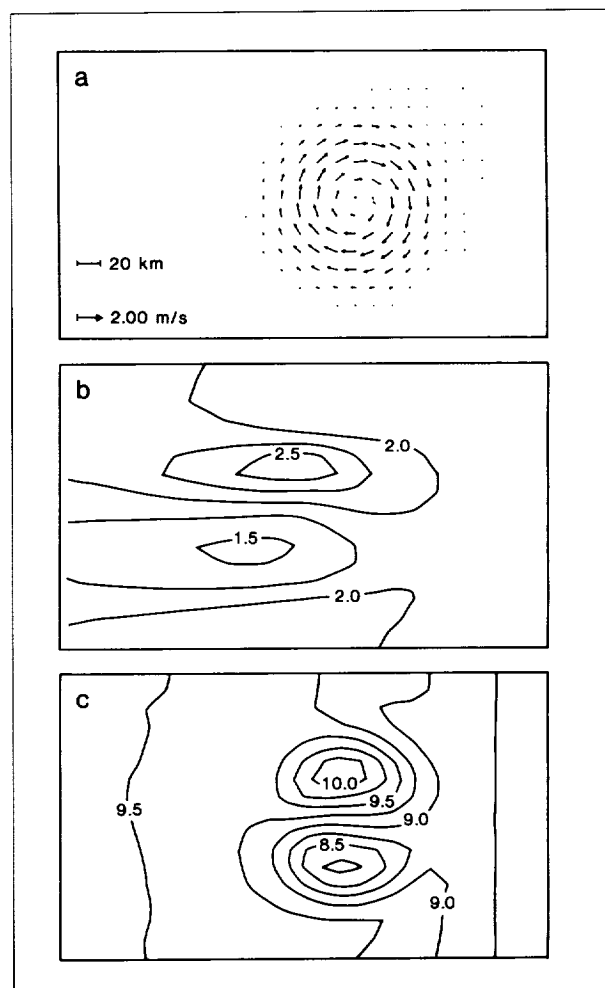


early 19th century, wind-wave research for practical conditions started in World War II in preparation for the amphibious operations of D-day. In both theoretical and numerical models, the ocean, ocean wind waves, and the atmospheric boundary layer usually are treated as separate systems. However, the necessity to treat the ocean-atmosphere boundary as an integral system becomes more and more apparent, as we seek to increase our knowledge of the relevant physics and to improve prediction models.

For a detailed investigation of boundary processes at the ocean surface, a wave model is required which is based on first principles as presently known. At NASA, two such models are available; the first is the wave model (WAM) developed by the international wave modeling community. This model includes the kinematics of wave propagation in deep and shallow water and the dynamics of wave growth (due to wind), wave energy dissipation (due to wave breaking and bottom friction) and nonlinear resonant wave-wave interactions. The second is the Wavewatch model, developed at Delft University of Technology in the Netherlands. In addition to the physics of the WAM model, this model incorporates effects of ocean currents on wind waves. This model provides all information needed to estimate the effects of ocean waves on ocean currents, although this information has not yet been implemented in ocean current or tidal models. Wavewatch is undergoing further development at NASA, and is intended as a tool for the investigation of the physics of wind waves and of interactions between wind waves and the atmospheric (and oceanic) boundary layers.

The first project for which Wavewatch will be used at NASA is the Sea Wave Dynamics Experiment (SWADE) project. For this project, extensive wave measurements will be performed off the East Coast between Cape Hatteras and Cape Cod. This area includes part of the Gulf Stream, and it is likely that several warm core rings will pass close to the main measurement arrays. Wavewatch will be used to estimate the effects of the Gulf Stream on waves at the measurement sites and in the analysis of the data. Furthermore, model results and data will be used to assess effects of currents on wind waves in practical conditions. This is particularly interesting, because wave-current interactions usually are considered for academic interest only, neglecting processes of generation and dissipation (i.e., kinematics only).

In preparation for SWADE, calculations have been made for some simple-but-realistic wave conditions over a warm core ring. In the figure, the current-induced modulations of wave heights are shown both for swell in a calm situation and for wind sea in a storm situation. Swells consist of waves of moderate steepness, the energy of which is confined to narrow bands in both frequency and direction. Wind seas are steeper and much more broad-banded. The figures show a significant effect of currents on wave heights in and beyond the ring.



Waves propagating over a Gulf Stream ring: current vectors (a) and isolines of significant wave heights (b and c); mean wave and wind directions from right to left). Panel b shows model results for a swell with a mean period of 14 seconds with no wind. Panel c shows results for a wind sea with a similar period, with a wind speed of 20 m/s.

Furthermore, the effects of currents on swell and wind sea are clearly different. In the wind sea case, the dynamic interactions between currents, waves, and wind prove to result in interactions significantly different from those obtained with conventional (kinematics only) approaches. Finally, the calculations show variations in energy fluxes from atmosphere to waves and from waves to surface turbulence and currents across a warm-core ring of roughly a factor of two. This implies that momentum and mass fluxes through the ocean surface also may vary significantly across the ring, suggesting that the effects of interactions between ocean currents, waves, and the atmospheric boundary potentially are significant.

Future research on wave modeling is intended to focus on several goals:

- To increase our knowledge on the dynamical processes governing wave growth and decay. In particular, wave breaking seems to be understood poorly.
- To investigate the interactions between waves, currents, and the atmospheric boundary layer. An integral approach is expected to increase our knowledge of the physics of mass, momentum, and heat fluxes throughout the ocean surface. This knowledge will help to improve the separate models and might result in integrated modeling of the combined boundary layers (including waves).
- To assimilate data in wave models. Because local wave fields contain information on winds over large areas, assimilation of data on a limited number of locations potentially can be used to give a full, two-dimensional estimate of errors in surface winds. This is confirmed by initial data assimilation experiments in Great Britain, the Netherlands, and Germany.

The first two research topics will be assessed in SWADE, whereas the last topic shows interesting prospects for EOS.

Contact: Hendrik L. Tolman (Code 911)
(301) 286-5796

Dean G. Duffy (Code 911)
(301) 286-9543

Sponsor: Air-Sea Interaction Program

Dr. Hendrik L. Tolman has completed his first year at Goddard as a National Research Council Resident Research

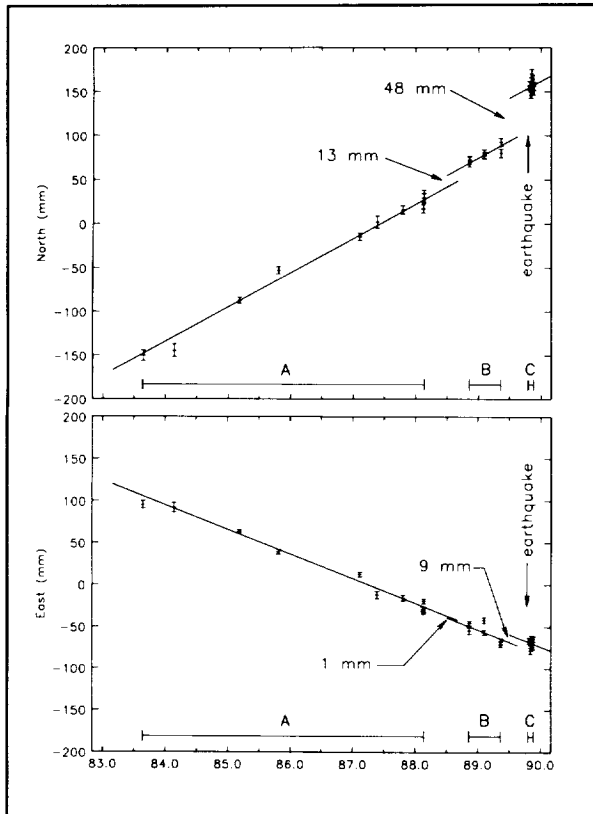
Associate. Since 1985, his research has focused on wave-current interaction modeling. His interests include wind waves and ocean-wave and atmosphere-wave interactions. He earned his MS and his PhD in civil engineering from Delft University of Technology in the Netherlands.

Dr. Dean G. Duffy works in Goddard's Laboratory for Atmospheres. He has completed 11 years of service at Goddard; in 1985 he received the Outstanding Scientific Achievement Award for his work. His research interests include dynamical meteorology, applied math, and numerical weather prediction and modeling. He holds a BS from Case Institute of Technology and an ScD from the Massachusetts Institute of Technology.

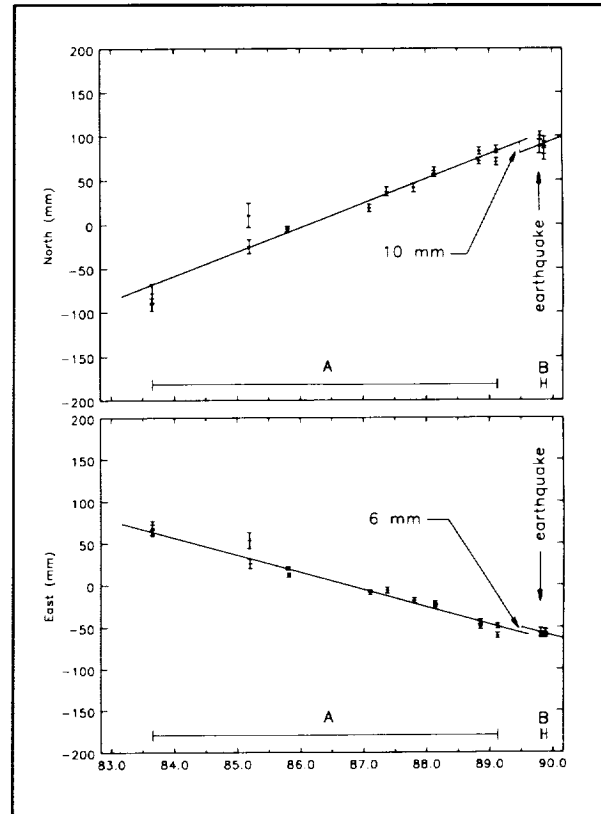
RECENT APPLICATIONS OF SPACE GEODESY

Two space geodetic techniques have a proven capability to provide subcentimeter relative positioning capability over baselines of several thousand kilometers—Satellite Laser Ranging (SLR) and Very Long Baseline Interferometry (VLBI). In the SLR technique, ultrashort laser pulses are reflected off specially designed geodetic satellites. The returning pulse is recorded by sensitive detectors and the roundtrip transit time is measured using precise time interval counters with precisions measured in trillionths of a second. The precise range data from a global network of stations is used collectively to define the orbit of the geodetic satellite from which the relative positions of the individual stations can be inferred. In the VLBI technique, signals from radio stars, or quasars, located billions of light-years from Earth are collected simultaneously by large radio telescopes, recorded, and accurately time-tagged by hydrogen masers at the participating sites. The observed delay between the arrival times of the signals provides a measure of the inter-site baseline component along the quasar line-of-sight. In spite of vastly different error sources, recent comparisons of the two space geodetic techniques show agreement at the 1- to 2-cm level for sites where both system types are present.

The SLR and VLBI technologies first were developed in the 1960s and applied to the accurate measurement of long baselines in the 1970s. In 1979, NASA Headquarters created the Crustal Dynamics Project (CDP) at Goddard and charged it with the further development of space



North and east positions of Fort Ord as functions of time in years. An arbitrary offset has been subtracted from each point to center the plot. The error bars are one-sigma formal standard errors. Intervals A, B, and C show the data from the old Fort Ord site, the new Fort Ord site (established following the destruction of the first monument) prior to the earthquake, and the new Fort Ord site after the earthquake, respectively. The first break is the estimated error in the survey tie between the old and new Fort Ord sites. The second break is the displacement of the new Fort Ord site during the coseismic time interval.

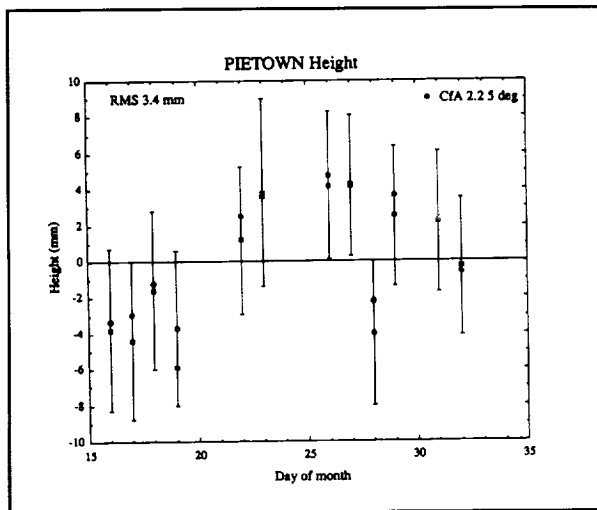


North and east positions of the Presidio as functions of time in years. An offset value has been subtracted from each point to center the plot. The error bars are one-sigma formal errors. There is one break in the line corresponding to the displacement in the coseismic time interval.

geodetic techniques and their operational use in the accurate measurement of contemporary tectonic plate motion and regional crustal deformation. During the past decade, the CDP and its international partners have provided a database which includes: the time-varying positions for hundreds of global sites accurate at the centimeter level; tectonic plate velocities and baseline rates accurate to a few millimeters per year; and Earth-orientation data accurate at the milliarc-second level.

At 5:04 p.m. on Tuesday, October 17, 1989, the San Francisco area was shaken by a magnitude 7.1 earthquake with

an epicenter located at Loma Prieta, near Santa Cruz. CDP, in cooperation with NOAA, responded within days of the emergency by sending two mobile VLBI units (MV-2 and MV-3) and one mobile SLR (TLRS-4) system into the region. The mobile VLBI units occupied sites at Fort Ord (near Monterey), Presidio (in San Francisco), and Point Reyes on the California coast. Operating in parallel with permanent VLBI sites in California and elsewhere in North America, the mobile units accurately measured the crustal displacements resulting from the largest earthquake to hit the contiguous United States since the beginning of the project. When compared to measurements taken prior to the earthquake, the postquake VLBI measurements showed that the Fort Ord site was displaced 49 mm (plus or minus 4 mm) at an azimuth of 11 degrees (plus or minus 4 degrees) and that the Presidio site was displaced 12 mm (plus or minus



The vertical height of the Pietown VLBI site as determined by 12 separate VLBI sessions over a 16-day period in October and November, 1989. A constant offset has been subtracted from each point to center the plot. The squares represent the solutions with the full constellation of quasars while the points marked CFA 2.2 represent the solutions where sources subject to the greatest atmospheric delay have been deleted.

5 mm at an azimuth of 148 degrees (plus or minus 13 degrees). No anomalous changes were observed at Point Reyes, at the mobile laser/fixed VLBI site at Mojave, or at the VLBI and SLR base stations located relatively far from the epicenter. In addition to providing important constraints to theoretical seismological models describing the event, these measurements established updated and accurate fiducial controls in support of parallel interagency measurement campaigns which used highly portable Global Positioning System geodetic receivers.

During fiscal year 1990, the CDP also moved beyond its traditional geodynamics role and began laying the groundwork for an important future role in the determination of mean sea level in support of the government-wide Global Change Program. Microwave altimeters onboard future oceanographic satellites—including the European ERS-1 and Topex/Poseidon missions—will determine the instantaneous height of the satellite above the ocean surface. The satellites will be tracked with centimeter-level accuracy by NASA's ground-based SLR network. The precise ground positions, as determined by SLR in a terrestrial reference frame with an origin at the Earth's center-of-mass, combined with centimeter-accuracy

range measurements to the satellite yield a precise orbit in the same reference frame. When combined with the microwave altimeter data, the precise orbit permits the determination of mean sea level relative to the center of the Earth. Furthermore, the global monitoring of SLR and VLBI site positions (especially in the vertical) permits differentiation between apparent sea level changes, caused by vertical movement of the Earth's crust, and actual sea level changes, caused, for example by the melting of the polar ice caps.

In an attempt to assess the present capabilities of VLBI to determine vertical height, several North American stations participated in a special experiment during fiscal year 1990. The vertical height of a site interior to the grid at Pietown, New Mexico, was determined in 12 separate sessions during a 16-day period. The one-sigma precision of 3.4 mm was the best ever obtained.

Since the absolute accuracy of space geodetic techniques currently is limited to the centimeter level by uncertainties in the atmospheric propagation path delay, a great deal of research and development effort has been expended in reducing these errors. A dual-frequency SLR system, operating at wavelengths of 532 nm and 355 nm, recently has been established at the 1.2-Meter Telescope Facility at Goddard. Using ultrashort pulse lasers and picosecond-resolution streak cameras, the system will determine the atmospheric path delay to the satellite by measuring the differential time of flight between the two wavelengths. The system will be used initially to test various atmospheric models, currently used in the global network of single-wavelength SLR systems, which use surface measurements of meteorological parameters as input. Later, it will be integrated fully into the ranging receiver to provide range measurements with an estimated absolute accuracy of 3 mm. A parallel research effort in VLBI is investigating atmospheric model parameter-estimation techniques sometimes in conjunction with collocated vapor radiometers designed to measure the wet component of atmospheric delay.

Contact: John J. Degnan (Code 901)
(301) 286-8470

Sponsor: Office of Space Science and Applications

Dr. John J. Degnan is Deputy Manager of the CDP and a member of the Geoscience Laser Ranging System Engineering Team. During his 26 years at Goddard, he has published extensively on lasers and their applications in



the fields of ranging, communications, remote sensing, and medicine. Dr. Degnan received his PhD in physics from the University of Maryland.

GEODYNAMIC EFFECTS OF ATMOSPHERIC VARIATION

The atmosphere is constantly in motion. As a result, it produces two types of geodynamic effects that can be detected by means of modern space geodetic techniques. Studies now have been conducted using global meteorological data to compute these effects as a function of time and to compare them with geodetic observations.

The first effect under consideration is in the Earth's rotation. Under the assumption that the net angular momentum of the solid Earth-atmosphere system is constant, any variation in the atmospheric angular momentum (AAM) will be reflected in the rotation of the solid Earth. Modern measurements of the Earth's rotational variations using SLR and VLBI have achieved great accuracies in both the length of day (LOD) and the polar motion. The LOD represents the axial component of the solid Earth's rotation around the rotation axis, whereas the polar motion represents the two equatorial components of the rotation in terms of the tilt in the rotation axis relative to the solid Earth.

The axial component of AAM long has been recognized as the primary cause of LOD variations for periods shorter than a few years. Using modern global meteorological data from the European Centre for Medium-Range Weather Forecasts (ECMWF) for the period 1980-1988, researchers now have investigated the forcing exerted on the polar motion by the equatorial components of AAM. The Earth's polar motion is a quasi-periodic, quasi-circular motion of the rotation axis around some mean position in the vicinity of the North Pole. It has two major components: the annual wobble and the 14-month Chandler wobble. The study has shown that AAM is indeed responsible for most of the observed annual wobble, as the first figure demonstrates.

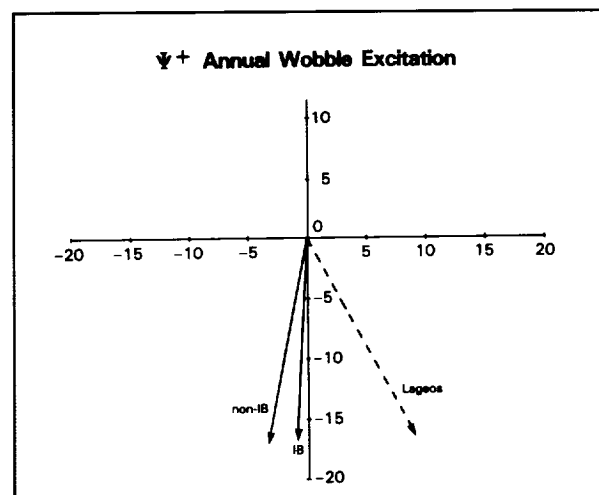
Two ideal cases of ocean response are considered: with and without the inverted-barometer effect; the difference is only moderate for the annual wobble excitation. The inverted-barometer hypothesis assumes that the ocean level responds to the overlying atmosphere pressure in an isostatic manner. A relatively small, but still significant

discrepancy is found between the computed and the observed excitations. This discrepancy is presumably the result of other geophysical phenomena that exert seasonal forcing on the polar motion, such as the continental water mass redistribution and ocean circulations.

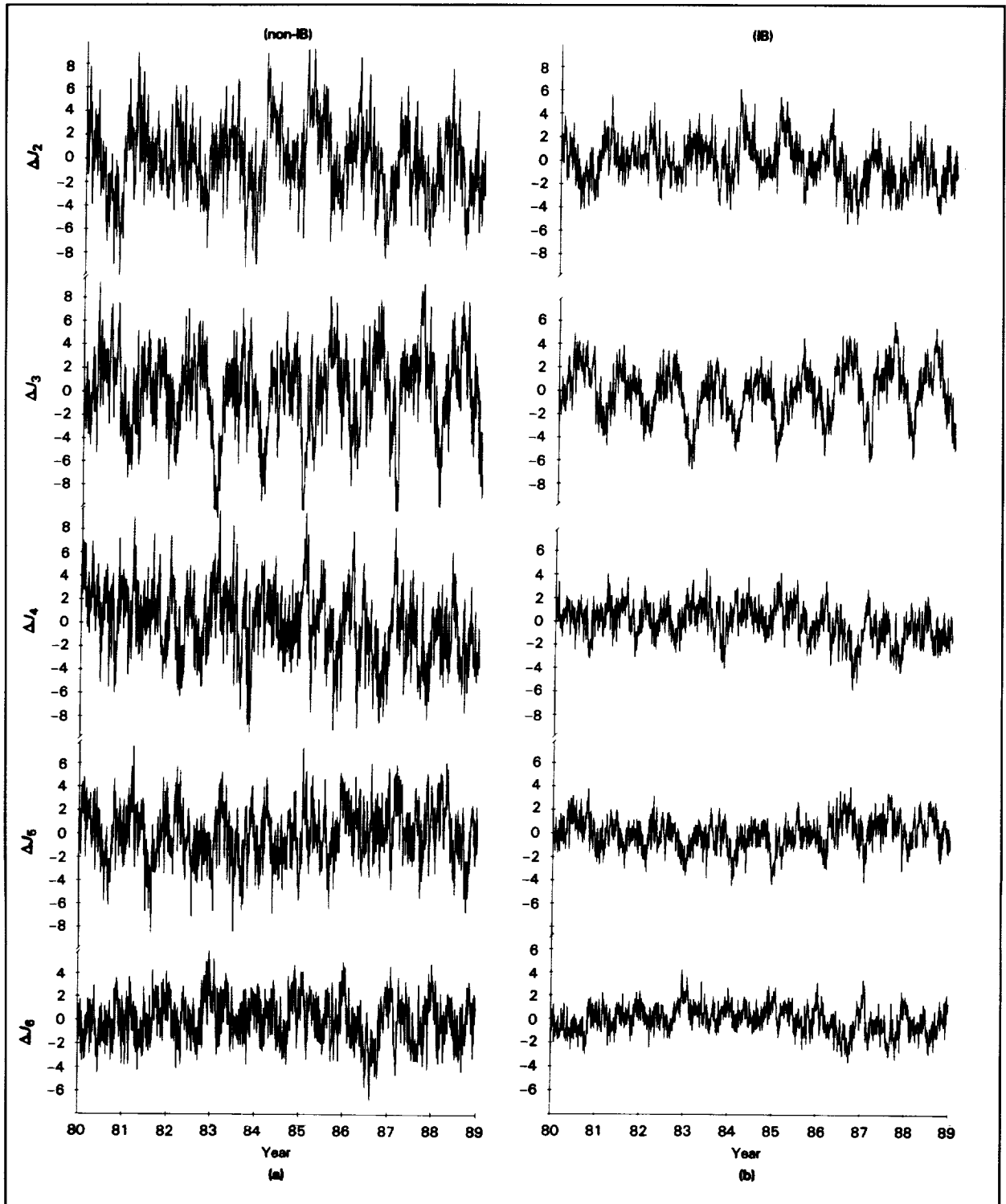
The atmospheric forcing of the Chandler wobble is less certain because its study is more prone to data noise. Thus, the extent to which AAM is responsible for the excitation of the Chandler wobble is difficult to determine. Still, researchers have found definite correlation between equatorial AAM and the observed Chandler excitation, with statistical confidence well over 99.9 percent.

The second geodynamic effect of the atmosphere mass movement is in the Earth's external gravitational field, U . Any such movement will be felt by orbiting satellites as gravitational perturbations, according to Newton's gravitational law. Traditionally, this gravitational perturbation has not been modeled; this presumably has led to misfits in the satellite orbits, resulting in biases in the determination of U .

Thus, in a first phase of an investigation to model properly this perturbation, researchers used the same ECMWF data as above and computed the atmospheric influences on the low-degree zonal harmonic coefficients of U ; again, with and without the oceanic inverted-barometer effect, as is shown in the second figure. These estimates



The prograde component of the atmospheric excitation of the annual wobble, 1980-1988, with and without the inverted-barometer (IB) effect. The vector pointing is with respect to January 1. The dashed vector is that observed from the Lageos laser-ranging data for the same period.



The temporal variations of the Earth's low-degree gravitational coefficients ($J_x, x=2^6$, in units of 10^{-10}) caused by atmospheric mass redistributions for 1980-1988: (a) for the case without the IB effect, and (b) for the case with the IB effect.



have been compared with the observations from geodetic satellites; the amplitudes are found to be comparable whereas the phases differ considerably. The latter, again, indicates the influences of other seasonal mass redistribution phenomena such as continental water redistribution and solar tidal deformations in the Earth and in the ocean.

Contact: Benjamin Fong Chao (Code 921)
(301) 286-6120

Sponsor: NASA Crustal Dynamics Project

Dr. Benjamin Fong Chao works in the Laboratory for Terrestrial Physics. His research interests during his 10 years at Goddard have included global geodynamics, as well as Earth's rotational and gravitational variations. He holds a BS in physics from National Taiwan University and a PhD in Earth sciences from the Scripps Institute of Oceanography at the University of California, San Diego.

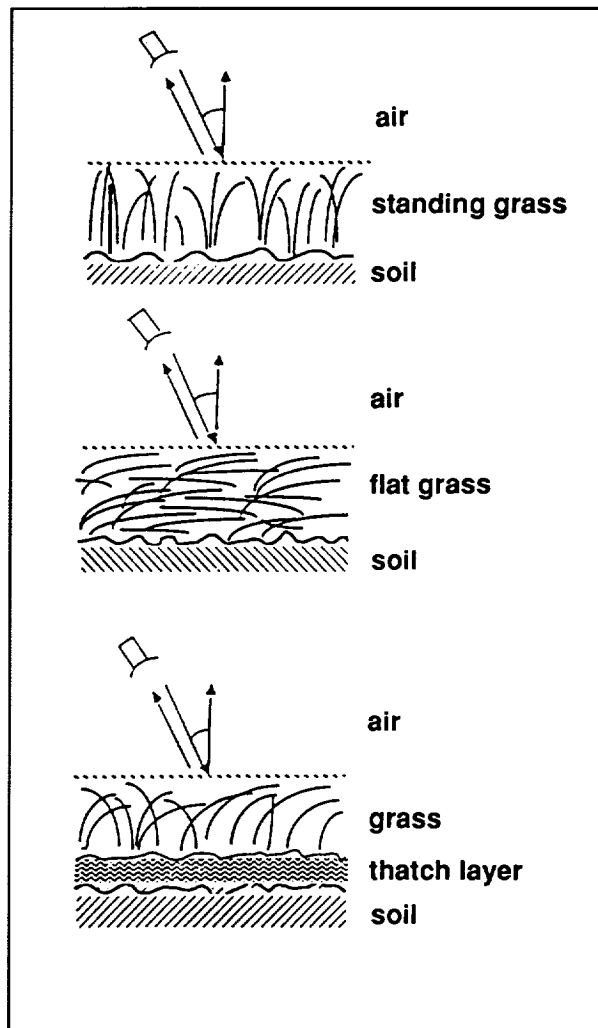
ACTIVE AND PASSIVE MICROWAVE MODELING OF GRASSLANDS

Grasslands are one of the most prominent ecosystems on Earth. Nearly one-third of the United States and 17 percent of the Earth's surface are covered by grasslands. To monitor a grassland's temporal and biophysical changes, remote-sensing instruments may be used to obtain low-cost, repeatable, and nondestructive information. It has been shown that controlled fires prior to the growing season have increased the grass yield up to 200 percent. This is an important issue when monitoring grass areas and detecting boundaries of induced fire regions.

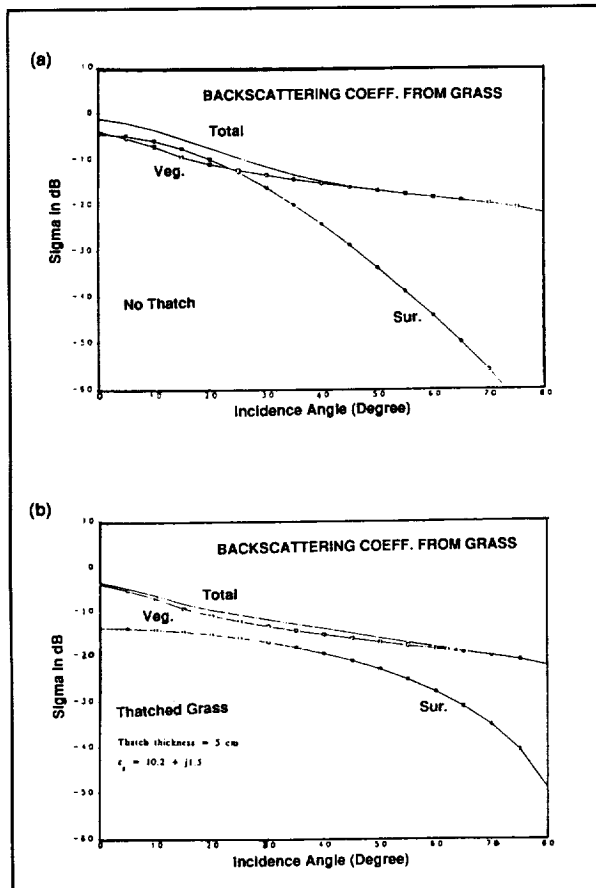
Research to date has shown a strong correlation between the remotely sensed data (both active and passive) and the surface soil moisture and canopy structure variations due to burn treatment. Burning grasslands is a common practice for range management to remove the dead vegetation of previous seasons. In unburned regions, the dead vegetation builds up a layer of thatch 2 to 5 cm thick. When this layer is wet it masks the underlying soil and reduces both active and passive sensors' sensitivity to soil moisture. These observations have been supported by radar and radiometer data collected over tall grass prairies in Kansas. To retrieve soil moisture information in view of the above-mentioned difficulties, a model for the grass

canopy has been developed. The following is a synoptic review of the model.

In this model, the grass canopy has been treated as a collection of randomly oriented, elongated elliptical discs over an irregular (rough) surface. The distorted Born approximation is used to calculate the backscattering coefficient from a nonuniform distribution of grass blades. Two particular features of this model which are unique for grass canopies are the variations of canopy structure and the presence of the thatch or detritus layer. The structure of the canopy varies depending upon the height of the grass. When the grass is short, it has one structure (standing blades); as the grass grows, the blades



Variations of canopy structure: standing grass, flat grass, and grass over a thatch layer.



Backscattering coefficients from grass with and without a thatch layer.

bend and lodge, thus creating another structure. On the other hand, the dead vegetation of previous years decays and builds up a layer of spongy material with an effective dielectric constant. The two features correspond to two treatments of burned and unburned grass canopies, respectively.

For active remote sensing, both copolarized and cross-polarized backscattering coefficients are computed, and their dependencies on the soil moisture, surface roughness, vegetation density, and the dielectric constant of the thatch layer have been studied.

For passive remote sensing, the above model has been used in conjunction with Peake formulation, based on energy conservation and reciprocity, to calculate the emissivity or the brightness temperature from the canopy. Moreover, it also is assumed that the canopy, air, and ground are all in thermodynamic equilibrium.

The model treats the structural variations by taking into account size distributions and non-uniform orientation of standing and lodging grass blades. Averaging over the orientation is performed by introducing distribution functions both in azimuth and inclination angles. The distribution functions can be determined by measuring angles of blades in sample regions in the canopy during the field measurements.

The figures illustrate the model and preliminary results worked out for a grass canopy at HH polarization and 5-GHz, C-band frequency. In the second figure, when there is no thatch the backscattering coefficient is highly dependent on the return from the soil surface, particularly at 0- to 20-degree incident angles. When the thatch layer, as a highly absorbing material, is present, the return from the soil surface reduces more than 5 dB in near-nadir incident angles.

Currently, data obtained over Konza prairie grass is being processed to verify the model and consequently infer soil moisture information. L-band radiometer data and L-band and C-band synthetic aperture radar data are the primary sources of data in this study.

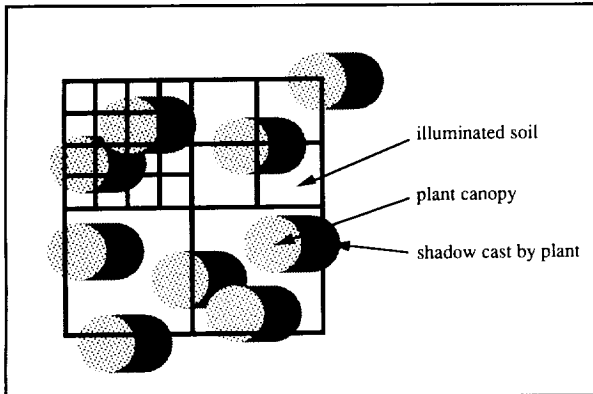
Contact: Sasan S. Saatchi (Code 974)
(301) 286-4840

Sponsor: NASA Headquarters, Office of Ecosystem Dynamics and Biogeochemical Cycles

Dr. Sasan S. Saatchi participated in this work as a National Research Council Resident Research Associate in the Hydrological Sciences Branch of the Laboratory for Hydrospheric Processes. He has 4 years of service with Goddard. He holds a PhD in electrical engineering from George Washington University. His research interests focus on modeling vegetation canopies for microwave remote-sensing applications. He is currently employed at the Jet Propulsion Laboratory in Pasadena, California.

SUBPIXEL PARAMETERIZATION OF FRACTIONAL VEGETATION DISTRIBUTION

The physically based parameterization of spatially variable vegetation using satellite imagery is an unsolved problem in global-scale hydroclimatology studies. One critical issue is the characterization of fractional, or subpixel, plant cover in natural and agricultural environments. In many semivegetated areas, plant cover varies randomly at characteristic length scales of



Nadir view of schematic scene of randomly located plants. The parameterization problem consists, in part, of determining the functional relation among subpixel cover types, plant geometry, and solar angle in relation to plant distribution and pixel size.

several meters, which are much smaller than pixel sizes of current or future (e.g., EOS) satellite sensors (several tens of meters). Soil background reflectance also varies over a wide range of length scales, from meters to several thousands of meters. Since satellite observations integrate the reflectance of all elements within the pixel, techniques are required to disaggregate the subpixel soil and vegetation components through physically based parameterizations.

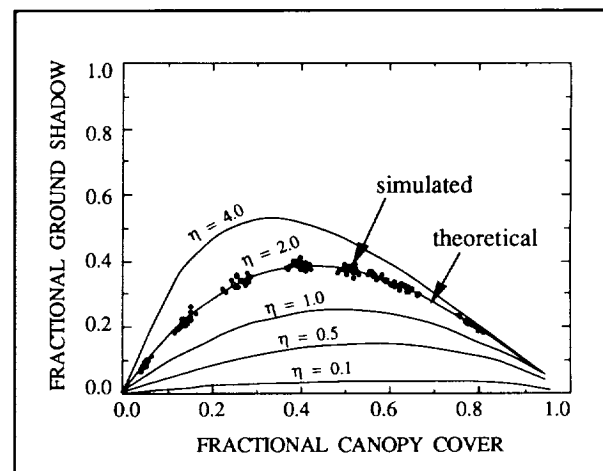
Recent studies have examined the above problem using a stochastic-geometric modeling approach in conjunction with visible/near-infrared imagery. The problem is illustrated in the schematic scene of randomly located plants shown in the first figure. The scene contains three cover types: plant canopy, illuminated soil, and

shadowed soil. Superimposed on the scene are pixels of different sizes. It is noted that the smallest pixels can contain a wide variety of combinations of the three cover types. Some small pixels, in fact, contain pure canopy, shadow, or illuminated soil. However, as the pixels become larger and larger, that variability diminishes as a functional or singular relation develops among scene properties. The parameterization problem thus can be defined partly as determining the functional relations among the different fractional cover types in terms of plant geometry and solar angle for different plant densities, distributions, and pixel sizes. Although the problem is defined above in terms of subpixel parameterization of imagery, it equally is applicable to subgrid or subregional parameterization in the context of large-scale hydrologic and climatologic models.

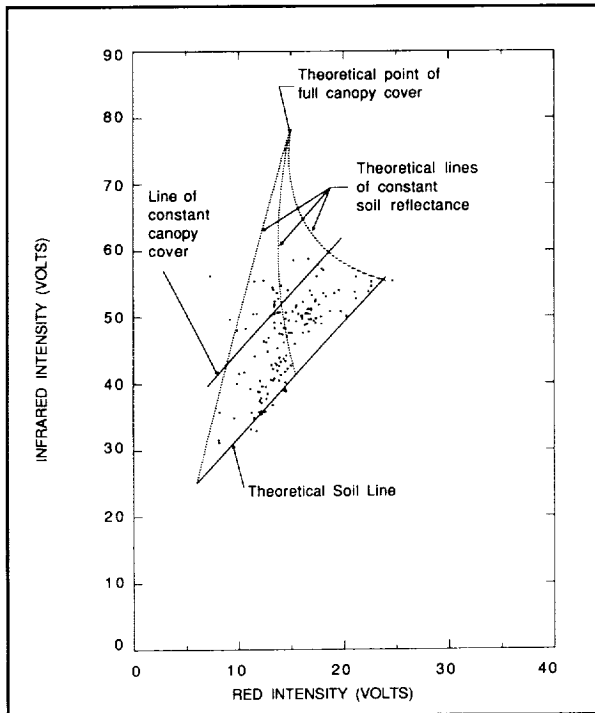
Subpixel parameterizations have been developed for the specific case of Poisson-distributed plants and for several agricultural geometries (e.g., row crops) using a stochastic-geometric modeling approach. The results for the Poisson case, displayed in the second figure, indicate a general set of curves relating the amount of subpixel ground shadow to the amount of subpixel canopy cover. The results are presented in terms of a nondimensional similarity parameter, η , defined as the ratio of the mean shadow cast by a single tree, A_s , to the mean vertically projected area of an individual plant canopy, A_t , or $\eta = A_s/A_t$.

Similarity of Canopy Geometry		
Canopy Shape	Geometric Similarity Parameter	Solar-Geometric Similarity Parameter $\eta = A_s/A_t$
i) Circular Cylinders	$b = D/H$	$4 \tan \theta$ πb
ii) Square Cylinders	$b = D/H$	$\frac{\tan \theta}{\pi}$
iii) Cone	$\phi = \tan^{-1}(D/H)$	$(\cot \chi - \pi/2 + \chi)/\pi$
iv) Sphere	none	$\tan \theta \sin \theta$

where
 D = mean canopy width
 H = mean canopy height
 θ = solar zenith angle
 $\chi = \sin^{-1}(\tan \phi / \tan \theta)$



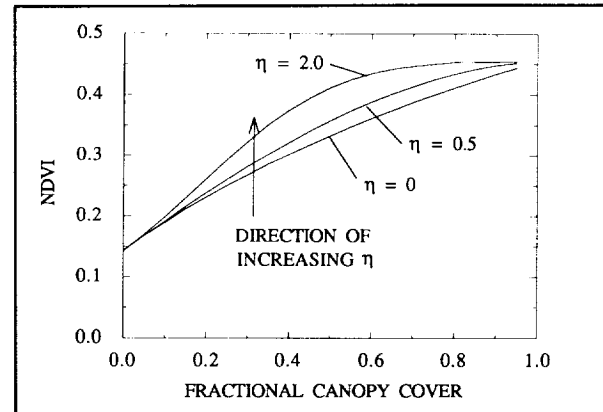
Theoretical generalized curves of fractional ground shadow versus total fractional canopy cover for any Poisson-distributed plant for η ranging from 0.1 to 4.0. Curves are applicable for $S > 10$. For $\eta = 2.0$, pixels from Monte Carlo simulations also are plotted for $S = 450$ and indicate favorable comparison to the theoretical line.



Interpretation of red/near-infrared scattergram, using method-of-moments and stochastic-geometric modeling, of aerial imagery over a vegetated landscape predominantly containing juniper trees.

Large η represents large zenith angles or plants with large shadows (tall, bulky plants), while small η represents low Sun zenith angles or plants with small shadows (thin, flat plants). The similarity parameter for different geometric shapes is provided in the first table.

Monte Carlo simulations indicate that there is a lower bound scaling limit to the validity of the parameterization. That is, the functional relation among cover types exists only if the size of the pixel is sufficiently large compared to the subpixel components. To quantify that limit, a Sampling Scale Ratio criterion is defined, $S = A_p / \eta A_s$, where A_p is the area of the pixel. The simulations indicate that for S greater than 10, the theoretical Poisson parameterizations are valid. The results of one such simulation ($\eta = 2.0$ and $S = 450$) also are plotted on the second figure, indicating excellent agreement with the analytical result. Preliminary field tests over a semi-arid region in Arizona containing predominantly juniper trees also indicate good agreement and that further research is warranted.



Comparison of NDVI versus subpixel canopy cover for several values of the nondimensional similarity parameter, η , using typical, constant plant and soil reflectances.

The above subpixel parameterization was incorporated into a physically based algorithm that estimates subpixel fractional vegetation cover, on a pixel-by-pixel basis, using only multispectral imagery. The overall approach applies the method of moments to a stochastic-geometric model of canopy-soil reflectance, and one set of red/near-infrared imagery without ground truth. The method involves the derivation of conditional reflectance moments (mean, variance, spectral covariance, and spatial covariance) for subsets of pixels possessing similar attributes (e.g., constant fractional canopy) that can be identified through their common orientation in the red/infrared scattergram. Application of the technique to aerial imagery over the juniper area yields the theoretical interpretation of the red/near-infrared scattergram shown in the third figure. The results provide preliminary evidence of the feasibility of this approach.

As a second application of the subpixel parameterization, the sensitivity of the Normalized Difference Vegetation Index (NDVI) to variability in landscape properties was investigated. It was shown analytically that, within the context of the stochastic-geometric model, NDVI is a nonsingular function of fractional canopy amount due to differences in soil albedo, pixel size, solar angle and ground shadow. For example, a comparison of NDVI versus fractional canopy cover for various values of η using typical constant plant and soil component reflectances is shown in the fourth figure. The results indicate that a physically based understanding of the structure of the landscape components is essential for accurate interpretation of remotely sensed images.



Contact: Michael F. Jasinski (Code 974)
(301) 286-7099

Sponsor: NASA Headquarters, Hydrological Sciences
Branch

Dr. Michael F. Jasinski joined the Hydrological Sciences Branch in October 1989 after completing his ScD in hydrology at the Massachusetts Institute of Technology. His principal interest is in the parameterization of large-scale hydrology. He also holds a BS and an MS in civil and environmental engineering from Cornell University.

A MODEL OF A VEGETATED LAND SURFACE FOR USE IN STUDIES OF LONG-TERM CLIMATE VARIABILITY

The extent to which the Earth's land surface affects climate is largely unknown. Although it is possible, for example, that reduced evaporation in a region suffering drought can prolong the drought or that shifted circulation patterns associated with tropical deforestation can alter climate on a global scale, it also is possible that land processes are of minor importance—compared to ocean forcing, for instance—in determining climate patterns. The immediate goal of our project is to quantify the effect of the land surface on climate variability through decadal numerical simulations with a state-of-the-art atmospheric GCM coupled to a sophisticated land surface model (LSM). A long-term goal is to connect the coupled land-atmosphere model to a full-ocean model for studies of the complete Earth system.

Since the GCM to be used has been developed already, recent efforts have focused on developing the appropriate LSM. We have required that it account explicitly for the critical effects of vegetation on the surface energy balance and that it be computationally efficient enough for the lengthy proposed simulations. A working version is now complete. The land surface in a single GCM grid square, which may span 100,000 km², is modeled as a mosaic of several tiles of varying sizes, with each tile representing one of several basic vegetation types. Existing vegetation maps, for example, might indicate that a particular grid square should be divided into two tiles, with grassland in one and broadleaf deciduous trees in the other. (Bare soil is considered as a separate vegetation type.) Each tile interacts independently with the GCM's atmosphere.

In the current version of the LSM, the surface energy balance equations at a single tile are based on those of SiB, a well-established, physically based land surface vegetation model that already has been tested extensively in GCMs. We thereby take advantage of the considerable research that went into characterizing SiB's vegetation types. Off-line tests demonstrate that for the case of a uniform vegetation cover, our model and SiB respond to atmospheric forcing in essentially the same way, in spite of our numerous model simplifications.

Our LSM, however, differs conceptually from SiB in its treatment of subgrid vegetation distributions. SiB assumes a homogeneous mixture of vegetation in a grid square and allows the separate types to interact when surface latent and sensible heat fluxes are computed. As a result, SiB is relatively computationally expensive. The computations are simplified greatly with the mosaic approach. Although neither approach is conceptually superior, mathematical analysis and some off-line simulations demonstrate that under many conditions, the two approaches similarly partition the incoming radiative energy into outgoing radiative and turbulent fluxes.

The decadal climate simulations are next on the agenda. The anticipated increased understanding of natural climate variability should aid in establishing criteria for identifying anthropogenic climate change.

Contact: Randal Koster (Code 974)
(301) 286-7061

Max Suarez (Code 911)
(301) 286-7373

Sponsor: NASA Headquarters Modeling, Data, and
Information Systems Program Office

Dr. Randal Koster, a Goddard employee for 3 years, works in the Hydrological Sciences Branch of the Laboratory for Hydrospheric Processes. His studies focus on land surface modeling and water vapor transport in GCMs. He received a BS from the California Institute of Technology, and an MS and a PhD from the Massachusetts Institute of Technology.

Dr. Max Suarez works in the Global Modeling and Simulation Branch of the GLA. His main interests are in climate modeling and studies of the atmospheric circulation. He holds a BS from the University of Florida and a PhD from Princeton University.

Flight Projects





In the Flight Projects Directorate, research and technology developments reach fruition as they are translated into successful flight projects and NASA missions.

FLIGHT PROJECTS

GAMMA RAY OBSERVATORY (GRO)

The Gamma Ray Observatory was launched from the Kennedy Space Center aboard the Space Shuttle Atlantis earlier this spring. In the last year there was extensive testing of the communications, command, and data retrieval systems. The support operations staff was trained. The instrument teams completed their preparations for operations and have turned their attention to the challenging task of scientific analysis. The anticipation of the rewards of the observational phase after 13 years of development and testing of hardware has generated a new wave of enthusiasm by the scientific teams.

The first phase of the GRO mission, lasting about 15 months, will be devoted to a full-sky survey by the two wide-field instruments, covering the energy range from 1 MeV to 30 GeV with more than a factor of 10 improvement in sensitivity over previous observations. The low-energy instrument will concentrate on individual objects during this phase while the gamma-ray burst experiment will monitor the unocculted sky continuously with unprecedented sensitivity and good spectral capability. Combined, these observations will cover the range of energies from 50 keV to 30 GeV.

A strong guest investigator program has been implemented. The first-phase activity will emphasize correlated observations at other wavelengths and theoretical analysis to enhance interpretations, but also will provide limited data opportunities with two of the four GRO instruments. To support guest investigator activities, a GRO Science Support Center has been established at Goddard.

The combination of GRO observations and correlated observations of the first phase will provide a quantum leap in our knowledge of the gamma-ray sky, now rather incomplete in coverage in both spatial and spectral dimensions. The second phase and beyond will be characterized by increased opportunities for participation by the broader scientific community.

The launch of GRO underscores the continuing resurgence of space astrophysics with unprecedented observing capability over the full range of wavelengths. When combined with the phenomenal developments in computing and networking capabilities and analysis techniques, the scientific return will revolutionize our understanding of the astrophysical universe.

GRO will bring to these studies the most direct means of studying nuclear processes and the major transfers of energy taking place in the cosmos. Supernovae and active

◆ *ONBOARD VIEW—Backdropped against clouds over water, the Gamma Ray Observatory (GRO) is still in the grasp of Atlantis' remote manipulator system (RMS).*

galaxies, pulsars and quasars, black holes and neutron stars are the dramatic types of objects which often can be studied most directly by means of gamma-ray observations. Considering the large improvement in observing capability possible with GRO, the expectations are very high for both anticipated and unanticipated improvements in our knowledge of the explosive and dynamic universe in which we reside.

Contact: Donald A. Kniffen (Code 662)
(301) 286-6617

Sponsor: Office of Space Science and Applications,
Astrophysics Division

Dr. Donald A. Kniffen is an astrophysicist in the Gamma Ray Astrophysics Branch, the GRO Project Scientist, and a Co-Investigator on one of the GRO instruments. Dr. Kniffen was one of the pioneers of gamma-ray astronomy beginning with balloon-borne experiments in the 1960s and continuing with the first successful high-energy spark chamber gamma-ray telescope flown on the second Small Astronomy Satellite. Dr. Kniffen holds a BS from Louisiana State University, an MA from Washington University in St. Louis, and a PhD from The Catholic University of America in Washington, D.C. He has 30 years of experience at Goddard.

GAMMA RAY OBSERVATORY (GRO) SCIENCE SUPPORT CENTER

The four instruments on the GRO satellite will investigate gamma-ray emissions from diffuse components as well as persistent and transient gamma-ray phenomena from compact objects. The combined spectral coverage of the four instruments ranges from about 50 keV to 30 GeV.

The GRO Science Support Center has been established at Goddard to facilitate a strong guest investigator program. The support center is a self-contained entity within the Laboratory for High-Energy Astrophysics. A GRO Fellowship program has been approved which also will be administered through the support center. It is projected that approximately five fellowships will be granted per year. The support center currently has a support staff of 10, including 7 astrophysicists. Four of these scientists are GRO instrument specialists who will support guest investigator research at the following principal investigator sites: Goddard and

Marshall Space Flight Centers, the University of New Hampshire, and the Naval Research Laboratory.

It is expected that participation by the general astrophysics community in the GRO observing program will enhance greatly the degree and quality of results forthcoming from this second Great Observatory. For the first phase of the guest investigator program, 43 U.S. proposals and 10 foreign proposals were approved. Approximately 20 of these proposals involve data analysis from two of the GRO instruments, the Burst and Transient Source Experiment (BATSE) and the Oriented Scintillation Spectrometer Experiment (OSSE).

During the first phase, the data reduction and analysis software packages will be finalized. Using the principal investigator data analysis systems, the support center will develop a comprehensive, integrated package for remote accessing of the data from all four instruments. The support center also will make available interfaces with other data analysis systems. In conjunction with the High-Energy Astrophysics Science Archive Research Center (HEASARC) at Goddard, the support center will archive all GRO data products for general user access, using resources within the National Space Science Data Center (NSSDC). The HEASARC and GRO support center also will collaborate in the development of multiple-wavelength analysis tools.

The near-term computing configuration within the support center includes several VMS- and UNIX-based workstations at Goddard, as well as workstations at the principal investigator sites. This environment is dedicated to supporting guest investigator observations and analysis and to developing further the necessary tools to this end. User participation in this process is encouraged.

Contacts: Donald A. Kniffen (Code 662)
(301) 286-6617

Jay P. Norris (Code 668)
(301) 286-3367

Sponsor: Office of Space Science and Applications,
Astrophysics Division

Dr. Donald A. Kniffen is an astrophysicist in the Gamma Ray Astrophysics Branch, the GRO Project Scientist, and a Co-Investigator on one of the GRO instruments. Dr. Kniffen was one of the pioneers of gamma-ray astronomy beginning with balloon-borne experiments in the 1960s



and continuing with the first successful high-energy spark chamber gamma-ray telescope flown on the second Small Astronomy Satellite. Dr. Kniffen holds a BS from Louisiana State University, an MA from Washington University in St. Louis, and a PhD from The Catholic University of America in Washington, D.C. He has 30 years of experience at Goddard.

Dr. Jay P. Norris is an astrophysicist in the HEASARC, Office of Guest Investigator Programs. His scientific career has spanned branches of high-energy astrophysics in which he has pursued development of cosmic-ray, gamma-ray, and X-ray instrumentation; studies of fast transients in gamma-ray astronomy; and analysis of X-ray observations of compact objects. He recently returned to Goddard after 7 years with the Space Science Division at the Naval Research Laboratory.

HIGH-ENERGY GAMMA-RAY ASTRONOMY ON THE GAMMA RAY OBSERVATORY (GRO) AND BEYOND

The GRO has four instruments which cover the gamma-ray spectrum from 0.2 MeV to 30 GeV. The upper end of this range, 20 MeV to 30 GeV, will be viewed by the Energetic Gamma Ray Experiment Telescope (EGRET). The EGRET instrument consists of four main systems. These are the anti-coincidence system, the electron/positron track imaging system, the time-of-flight/coincidence system, and the energy calorimeter. The EGRET track imaging system consists of a set of 36 orthogonal wire spark chambers with digitized read-out.

The improvements in effective area and angular resolution will allow EGRET to survey the entire sky with an area, solid angle, and efficiency factor more than 10 times that of previous satellite gamma-ray telescopes and will provide detailed maps of the full-sky gamma-ray emission. From these maps, astronomers can extract information about the locations, intensities, and spectra of a variety of compact objects (pulsars, neutron stars), extended objects (molecular clouds, galactic arm structure), and extragalactic objects (other active and normal galaxies, and quasars).

To advance gamma-ray astronomy beyond EGRET will require a future-generation gamma-ray telescope. The scientific purpose of such an instrument will be to provide detailed observations of gamma-ray sources using the

EGRET full-sky results as a guide. Clearly, increased sensitivity and angular resolution will be needed, but background noise from the instrument must be minimized. Increased sensitivity can be achieved by using large detectors with several square meters of active area. To improve the angular resolution approaching the pair production kinematic limit will require improvements in spatial resolution to about 0.1 mm, as well as reduction of the effects of Coulomb scattering before the direction of the electron pair has been measured. Additional criteria for the design of such an instrument also may involve optimization for higher energies (100 MeV to 100 GeV), reduced solid angle (point source instrument), and increased live-time (reduced event processing time).

As has been realized for a long time, these design goals can be achieved using large-area (2 m by 2 m) drift chambers. While drift chambers have been used in particle accelerators for many years, the power required by the high-speed amplifiers and discriminators has prevented the viable use of large-area chambers in space. Within a Supporting Research and Technology (SRT) research program, an amplifier and discriminator have been designed which consume 25 mW and 65 mW at 8 V, respectively, using high-speed bipolar transistors. These designs have been implemented using surface mount technology. Drift chambers offer another advantage for the construction of a high-energy gamma-ray telescope. Xenon gas can be used for the drift gas and, at a pressure of 2 to 3 atmospheres if 2- to 4-m depth is used, can double as the pair production medium. This eliminates the need for large-area thin metal foils, which are difficult to fabricate. This also allows several measurements to be made of the electron/positron track directions before Coulomb scattering begins to dominate over the initial uncertainty imposed by the pair production kinematics. Good spatial resolution also is needed to achieve angular resolution near the kinematic limit. The drift velocity of electrons in pure xenon is 1 to 2 mm/ μ s for moderate values of electric field and pressure. The addition of a cooling gas, such as carbon dioxide at about 1 percent, will increase the drift velocity to about 10 to 15 mm/ μ s. This is needed to reduce the memory time of the drift chamber and hence, the number of potentially confusing cosmic rays which also would be detected along with the gamma rays. This moderately slow drift velocity reduces the timing resolution corresponding to a 0.1-mm spatial resolution.

While these improvements affect mainly the track imaging system, all the systems of a gamma-ray telescope of

2 m by 2 m by 2-4 m will require innovative designs and careful optimization. For example, the anti-coincidence and the time-of-flight coincidence systems, in particular, will require a sophisticated design with interactive computer processing to screen out potentially confusing cosmic rays while maximizing the instrument live-time.

Currently, work is progressing on several engineering prototype drift chambers. A complete gamma-ray telescope with sixteen 1/2-m by 1/2-m drift chambers will be ready soon for testing at an accelerator. Larger 1/2-m by 2-m drift chambers are being designed to simulate the electrical and mechanical properties of 2-m by 2-m drift chambers.

Contact: Carl E. Fichtel (Code 660)
(301) 286-6281

Stanley D. Hunter (Code 662)
(301) 286-7280

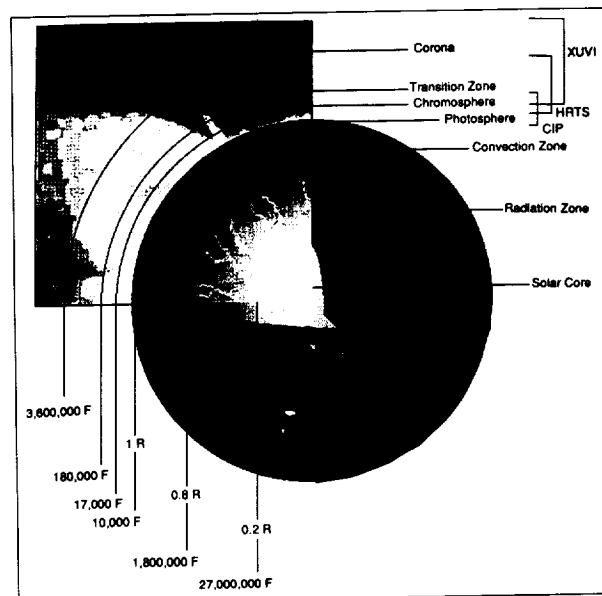
Sponsor: Office of Space Science and Applications and Supporting Research and Technology Program

Dr. Carl E. Fichtel is Chief Scientist at the Laboratory for High-Energy Astrophysics, Acting Head of the Gamma Ray Astrophysics Branch, and a Senior Goddard Fellow. He has more than 150 publications in solar particle physics, cosmic rays, and gamma-ray astrophysics. Among other awards, he has received the John C. Lindsay Memorial Award and the NASA Exceptional Scientific Achievement Medal. He holds a PhD from Washington University in St. Louis.

Dr. Stanley D. Hunter, Co-Investigator on EGRET, earned his PhD at Louisiana State University. During his 5 years at Goddard, he has played a major role in the EGRET hardware development and is developing a new gamma-ray telescope while also pursuing molecular cloud and cosmic-ray studies. Dr. Hunter has won a Special Achievement Award and a Certificate for Outstanding Achievement.

HIGH-RESOLUTION, COORDINATED SOLAR OBSERVATIONS BY THE ORBITING SOLAR LABORATORY (OSL)

The Orbiting Solar Laboratory (OSL) mission is designed to achieve a major advance in solar physics through high-resolution, coordinated observations of solar



The OSL science goals. The OSL is designed to make high-resolution, coordinated observations of solar hydrodynamic and magneto-hydrodynamic phenomena over a wide spectral range and extended periods of time.

hydrodynamic and magneto-hydrodynamic phenomena over a wide spectral range and extended periods of time.

The OSL science payload consists of the Coordinated Instrument Package (CIP) to observe the photosphere and the chromosphere, the X-ray Ultraviolet Imager (XUVI) to observe the corona, and the High-Resolution Telescope and Spectrograph (HRTS) to observe the transition zone between the chromosphere and the corona. The CIP is the focal plane instrument package of a 1-m aperture, diffraction-limited, on-axis Gregorian telescope, while the HRTS and the XUVI have their own built-in telescopes. A finder telescope provides full-disk images of the Sun for solar activity monitoring and identification of observation targets.

The CIP design has evolved during the past decade. It consists of two filtergraphs—a tunable filtergraph (TF) and a photometric filtergraph (PF)—and the Kiepenheuer Institut Solar Spectrograph (KISS). The TF is a narrow-band birefringent tunable filter system (4600-6700 Å) created for intensity, velocity, and magnetic field measurements of the plasma; the PF is a broad-band system (2200-6600 Å) designed for measurements of the temperature and density distributions of the plasma. Each filtergraph is equipped with a filter wheel for wavelength selection, a high-resolution charge-coupled device (CCD) camera of



0.08-arc-second pixel, 80 by 80-arc-second field of view (FOV), and a background CCD camera of 160 by 160-arc-second FOV. The KISS is an echelle spectrograph (2700-9000 Å) with a 0.1 by 80-arc-second entrance slit. As the slit is stepped across its 160-arc-second range, plasma properties are measured along the instantaneous position of the slit within the FOV of the filtergraphs. Aluminized slit jaws reflect the image surrounding the slit into a CCD camera to allow precise determination of the slit position relative to other CIP focal planes.

The Phase-B study of the KISS was completed by Dornier in May 1990. A modular design was developed to facilitate its integration into the CIP.

The Spacelab-2 HRTS design is adapted to the OSL mission mainly by replacing the film cameras with CCD detectors, adding an image motion compensation system (IMC), and incorporating long-life upgrades. A 30-cm Gregorian telescope feeds a focal plane package that consists of a stigmatic tandem Wadsworth slit spectrograph (1200-1700 Å), supported by an ultraviolet slit display and a visible-light slit display. As the spectrograph entrance slit is moved across the solar image at the Gregorian focus in a step-and-stare manner, data necessary to assemble two-dimensional images of the solar disk are collected by a multi-detector mosaic CCD camera. Each of the two slit display systems is equipped with a single-detector CCD camera. Except for the visible-slit CCD detector, all HRTS CCD detectors need to be coated with ultraviolet-sensitive phosphor for wavelength conversion from the ultraviolet to the visible.

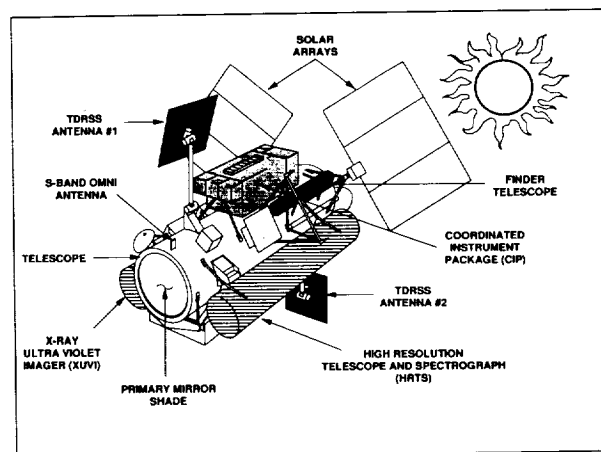
The XUVI Phase-A study is underway and will be completed this year. The current XUVI design concept uses the technology of multilayer coatings applied to the thin-film filter technology to provide the required narrow-band normal incidence optical systems for extreme ultraviolet wavelengths (45-355 Å). Two sets of imaging instruments observe the corona with different angular resolutions and magnifications; one set consists of two full-disk imagers with 2.3-arc-second pixels to study coronal transients and flares, and to identify observation targets for the two 0.25-arc-second pixel, high-resolution imagers (HRI). Within each imager, four optical channels are clustered around a single, intensified focal plane detector that sequentially views the four images selected by a rotary shutter/channel selector; the wavelength of each channel is determined by the blocking filter and the multilayer coating prescription of the mirrors.

The OSL will be launched by a Delta II launch vehicle into a 510- to 900-km polar Sun-synchronous orbit with continuous solar viewing for extended periods each year for a minimum of 3 years.

The Tracking and Data Relay Satellite System (TDRSS) will be used for communication with the ground and for tracking. The OSL instruments will have a total science data output of 20 Mbps during real-time observations. For the rest of the day, science data will be collected at 2 Mbps through continuous store-and-playback operations. Science data will flow from the instruments to the OSL Science Data Operation Center (SDOC) at Goddard in a standardized and highly automated manner, using multi-mission data transport and acquisition facilities.

During real-time observations, scientists will be able to control the observations from the SDOC. Near-real-time, quick-look, high-resolution instrument data and a continuous stream of full-disk images from the finder telescopes will be available at the SDOC. Command checking at the Payload Operations Control Center (POCC) will be automated to minimize delays.

The Attitude Control System points the OSL at any point within 18 arc-minutes of the Sun center to 9-arc-second accuracy and tracks the average solar rotation. The three OSL instruments are equipped with their own IMCs to reduce image jitter. The HRTS IMC is a limb tracker; the IMCs of the CIP and XUVI are feature trackers, which



OSL Pre-Phase-B configuration. The OSL payload consists of the CIP, which will observe the photosphere and the chromosphere; the XUVI, which will observe the corona; and the HRTS, which will observe the transition zone between the chromosphere and the corona.

compare the current picture with a stored reference picture of the same solar region to generate error signals for correction. The CIP IMC is designed to achieve 0.02-arc-second image stability in 20 seconds.

For the purpose of coordinated observations, adjustable mounts are provided for the HRTS and the XUVI for FOV adjustments to achieve coalignment with the CIP FOV and among themselves. Spectrograph slits of the CIP and the HRTS will be coaligned to within approximately 10 arc-minutes. The visible-light slit jaw system of the CIP, the visible-light slit display of the HRTS, and the visible transmitting filters in the HRIs of the XUVI provide the common wavelength reference necessary for coregistering simultaneous observation data sets from all OSL instruments.

After an initial observation period dedicated to the principal investigators and their co-investigators, the OSL will be operated as a facility like the International Ultraviolet Explorer to serve the entire solar physics community. Full facility and personnel support will be provided at the SDOC for any guest observers and guest investigators whose observation/investigation proposals have been selected.

The OSL is the prime candidate for a fiscal year 1992 new start. Selection is underway for two Phase-B contractors to undertake definition studies in 1991 for the spacecraft and the 1-m telescope. This will be followed by selection of a Phase-C/D contractor to provide the spacecraft and the telescope, and to integrate the three instrument packages.

Contact: Roger A. Mattson (Code 460)
(301) 286-7751/5024

Sponsor: Office of Space Science and Applications

Mr. Roger A. Mattson, Project Manager for OSL and the Cosmic Background Explorer Mission (COBE), has worked at Goddard for 26 years. Mr. Mattson, who holds a BS in chemical engineering, was Project Manager for the first successfully launched, commercially developed upper stage and the first NASA employee to attend the National War College.

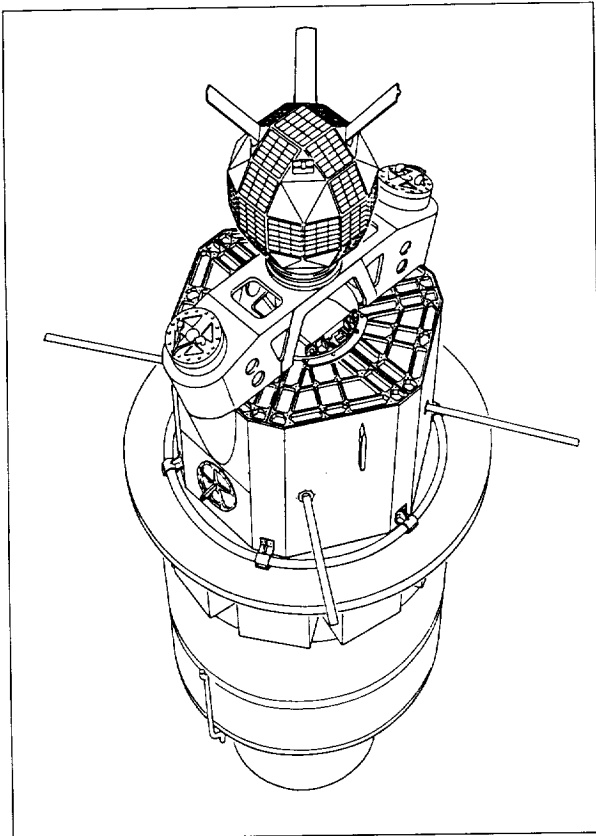
PEGSAT—THE FIRST PEGASUS PAYLOAD

Pegsat, the first satellite carried into orbit by the new Pegasus launch vehicle, was designed, built, and supported operationally by the Goddard Special Payloads

Division under a joint agreement between the Defense Advanced Research Projects Agency (DARPA) and Goddard. Its purpose was threefold: to support instrumentation to measure the launch environment; to support and eject into orbit a Navy Small Experiment Communications Satellite (SECS); and to support two barium-release experiments to study the Earth's magnetic and electric fields.

Pegsat was conceived, designed, built, tested, and ready at the launch site for flight in less than 1 year. Pegsat was launched successfully on April 5, 1990 and placed in a 270-by-370 nmi near-polar orbit. Excellent data were received from the environment measurement system. The SECS was deployed and operated successfully. Both chemical canisters were activated successfully over Northern Canada during the latter part of April, providing the science team with excellent observations of the barium cloud as far south as Texas. Pegsat was operating 5 months after launch and has not experienced any failures. The batteries-only power system should provide adequate power for several more months of operation. Engineering data still is being obtained which will be useful in the design of future spacecraft.

Several factors made it possible to accomplish this task in such a short time. Most important, the personnel responsible for development and implementation of the project were experienced, hands-on engineers, and their number was kept to a minimum. Although Pegsat was the first satellite developed by the Special Payloads Division, the key engineers and technicians had extensive experience in sounding rocket and Shuttle payload development and operations. Management was by technically cognizant engineers using a combination of participatory and autocratic management styles. Key decisions within a discipline (e.g., structure, time management, etc.) were made by the lead engineer/manager while interdisciplinary problems were worked out and scheduling was coordinated by the lead engineers and technicians on an informal basis. Outside contacts and coordination with other groups were managed by one person—the project manager. Other factors allowing the rapid and successful accomplishment of this task were the adaptation and use of available components, as well as consideration during the early design phase of assembly processes, qualification testing, and field support procedures based on available facilities, tooling, and manpower capabilities and availability.



Pegsat, the first satellite carried into orbit by the new Pegasus launch vehicle, was launched successfully on April 5, 1990. It was designed, built, and supported operationally by Goddard.

The Pegasus structure was required to support several heavy components in addition to housing and supporting the flight environment instrumentation and spacecraft subsystems. These components were the SECS and associated eject mechanism weighing approximately 150 lb, two chemical release canisters weighing 46 lb each, the 50-lb silver/zinc battery, and the 14-lb lead/acid battery. The primary structure is of semi-monocoque construction consisting of machined magnesium bulkhead segments and sheet aluminum shear webs, a central cylinder, and bent-up stiffeners fastened together primarily with squeezed rivets and a small number of blind rivets. Although purposely designed with a high degree of conservatism to allow start of fabrication prior to final determination of detailed subsystem support requirements and loading, the primary structure accounted for less than 10 percent of the total weight with no element stresses higher than 10 ksi (approximately 25 to

35 percent ultimate strength) based on finite element analysis. Two identical structures were built to allow concurrent testing and flight build up. This was fortuitous in that when the launch vehicle developer, Orbital Sciences Corporation, decided to do a series of inert flights with the B-52 prior to the actual launch, the Engineering Test Unit (ETU) was available. Mechanical assembly of both structures was done in-house.

For the inert flights, the ETU was attached to the inert Pegasus vehicle, which was suspended from the B-52 carrier aircraft. Data were transferred to a tape recorder on board the aircraft, which collected data during taxi, takeoff, flight maneuvers, and flight buffeting. Data also were recorded during landing with the inert vehicle and would have been recorded with the flight vehicle if the mission had been aborted. Data obtained during the powered flight of Pegasus with Pegasus was transmitted via an S-band telemetry system. During flight, measurements were made of acceleration and loads including shock, acoustics, random vibration, sustained periodic vibrations, pressure profile, and temperatures inside the payload fairing. The transducers used to make these measurements were ones left over from previous projects and were used since they met the requirements. There was insufficient time and money to acquire new ones.

Two telemetry systems were used to conduct the Pegasus mission. TM-1 was configured to provide maximum frequency response from the environment experienced by the payload during aircraft roll, takeoff, prelaunch, and launch phases of the Pegasus vehicle. The high-speed data portion (prelaunch) of the mission used the B-52 onboard tape recorder for data recovery.

During the launch and orbital insertion phases, data was transmitted by an S-band transmitter which was multiplexed into the Pegasus vehicle antenna system. The transmitter was manufactured in 1975 for use in the NASA Sounding Rocket Program. TM-2 is for on-orbit measurements, housekeeping data, pyro signal monitoring, and aspect information from the three-axis magnetometer. The transmitter was designed and built in-house at Goddard as part of the Interplanetary Monitoring Platform (IMP) Satellite Project during 1968-69. Using 20-year-old drawings from the IMP project, new antennas were built and installed in the Pegasus spacecraft. The antenna system is a basic, four-element turnstile array. Use of the VHF frequency required a deployed antenna length greater than that allowed by the Pegasus fairing. For

simplicity, the antenna elements were required to be folded manually for flight and to erect themselves unassisted once in orbit. The material used for the individual elements was obtained from a standard roll-up 0.75-in steel carpenter's rule. It provided the flexibility and deployed rigidity necessary for the antenna system at a minimum cost. The elements were bent under the Pegasus nose fairing, and, after deployment, the antenna elements automatically extended to their full length.

The spacecraft was equipped with redundant command receiver and decoder systems to provide for ground control. The receivers were used originally for the sounding rocket Skylab calibration rocket (CAL/ROC) Program in the early 1970s. The command antenna system used four surface-mounted quadraloop elements that were designed and built by the Physical Science Laboratory of New Mexico State University originally for use on sounding rocket payloads. The elements used on Pegasus were flown previously on a sounding rocket mission which was recovered by parachute.

Power is provided by a battery configured from eighteen LR-40 silver/zinc cells manufactured by Yardney Electric Corporation. A small Gates lead/acid battery was included in the spacecraft to provide backup power in the event that low temperatures were encountered unexpectedly. Based on the planned mission operations and the power consumption of the various subsystems, it was determined that the LR-40 battery could provide in excess of 90-day mission power requirements. Solar cells and rechargeable batteries were not used because of inadequate lead times and the fact that the first chemical release would probably coat the solar cells, rendering them ineffective for further mission use.

A power conservation system turns the command receiver on one orbit prior to the release pass opportunity and turns it off after a release pass. Since the orbital period is approximately 95 minutes, the command receiver requires power for only slightly more than 3 hours. This is repeated once every 24 hours.

Once the command receiver is turned on, the spacecraft can be commanded on for mission operations and status monitoring. Also, another timer in Pegasus automatically turns the system off after approximately 10 minutes. This precludes leaving the spacecraft in the "on" state. A backup timer, called a watchdog timer, was incorporated to provide a means of resynchronizing the power saver clock

if necessary. The watchdog timer, is reset every time the spacecraft is contacted from the ground station. If the spacecraft is not contacted in a 24-hour period, the watchdog timer turns the command receiver on until the ground station can contact the spacecraft and resynchronize the power saver clock.

The Pegasus on-orbit operations were supported by two tracking ground stations: a prime station located at Churchill, Canada and a backup station at Goddard. The prime station at Churchill was supported by the Wallops Flight Facility. It consisted of a fully equipped trailer with all of the equipment necessary for VHF telemetry acquisition, processing, and recording. It also provided programmed tracking as well as the command and encoding system for spacecraft control.

The backup station at Goddard was assembled using readily available commercial components, many of which are used by amateur radio enthusiasts. The 550-MHz command transmitter was borrowed from the NASA Sounding Rocket Program. The station is still operating.

Contact: B.R. Pincus (Code 740.2)
(301) 286-5874

J.E. Pownell (Code 743.1)
(301) 286-5091

J.J. Rast (Code 740.2)
(301) 286-5321

Sponsor: Office of Space Science and Applications
and DARPA

Mr. B.R. Pincus is Head of the Systems Development Office of the Special Payloads Division and is Pegasus Project Manager. He has worked for Goddard since 1962 and has supported a variety of aerospace programs including sounding rockets, Spartan, Get Away Specials, and Shuttle-related missions. He holds a BS in electrical engineering from the Georgia Institute of Technology.

Mr. J.E. Pownell is Head of the Payload Design Section in the Special Payloads Division. He holds a BS degree in electrical engineering from the University of West Virginia and has worked for NASA for 28 years. He was responsible for the Pegasus spacecraft electrical systems as well as the command and data acquisition systems.

Mr. J.J. Rast is a staff engineer in the Systems Development Office of the Special Payloads Division and was responsible



for the Pegasus structure and mechanical system. Prior to this, he had been Head of the Application and Development Section (formerly Structures and Mechanisms Section) since its inception in 1970. He holds a BS in aeronautical engineering from the University of Maryland.

EARTH OBSERVING SYSTEM (EOS)

The Earth Observing System (EOS) is to be the centerpiece of NASA's "Mission to Planet Earth." NASA plans to launch a total of six major Earth-looking scientific observatories starting in 1998, and these observatories are to be accompanied by still other observatories provided by the European Space Agency. Once the program is fully under way, there will be two NASA observatories and one each from Europe and Japan, all in orbit at the same time. The goal is to provide a minimum of 10 years of simultaneous, continuous Earth observations.

The NASA observatories will be placed in Sun-synchronous polar orbits at 705 km and will have 1:30 p.m. (EST) equatorial crossing times. There are to be two series of NASA observatories with three platforms in each series. The A series instrumentation will focus primarily on measurements designed to enhance our understanding of Earth's climate and hydrologic systems and ecosystem dynamics, whereas instrumentation in the B series will focus primarily on upper atmospheric and solid-Earth processes. Platforms in either series will be launched at 5-year intervals, the first platform in the A series being followed 2 1/2 years later by the first platform in the B series.

As the instruments and the platforms to carry them are being developed, a major EOS Data and Information System (EOSDIS) is being developed to provide access to the data from the instruments and to the scientific results of research using these data. EOSDIS will serve both flight operations and science data requirements. EOSDIS will provide for planning, scheduling, command, and control of both the overall mission and the individual EOS instruments, and it will provide for the production of standard and specialized data products. Also provided will be computational facilities for support of research, data archival and distribution, and communications.

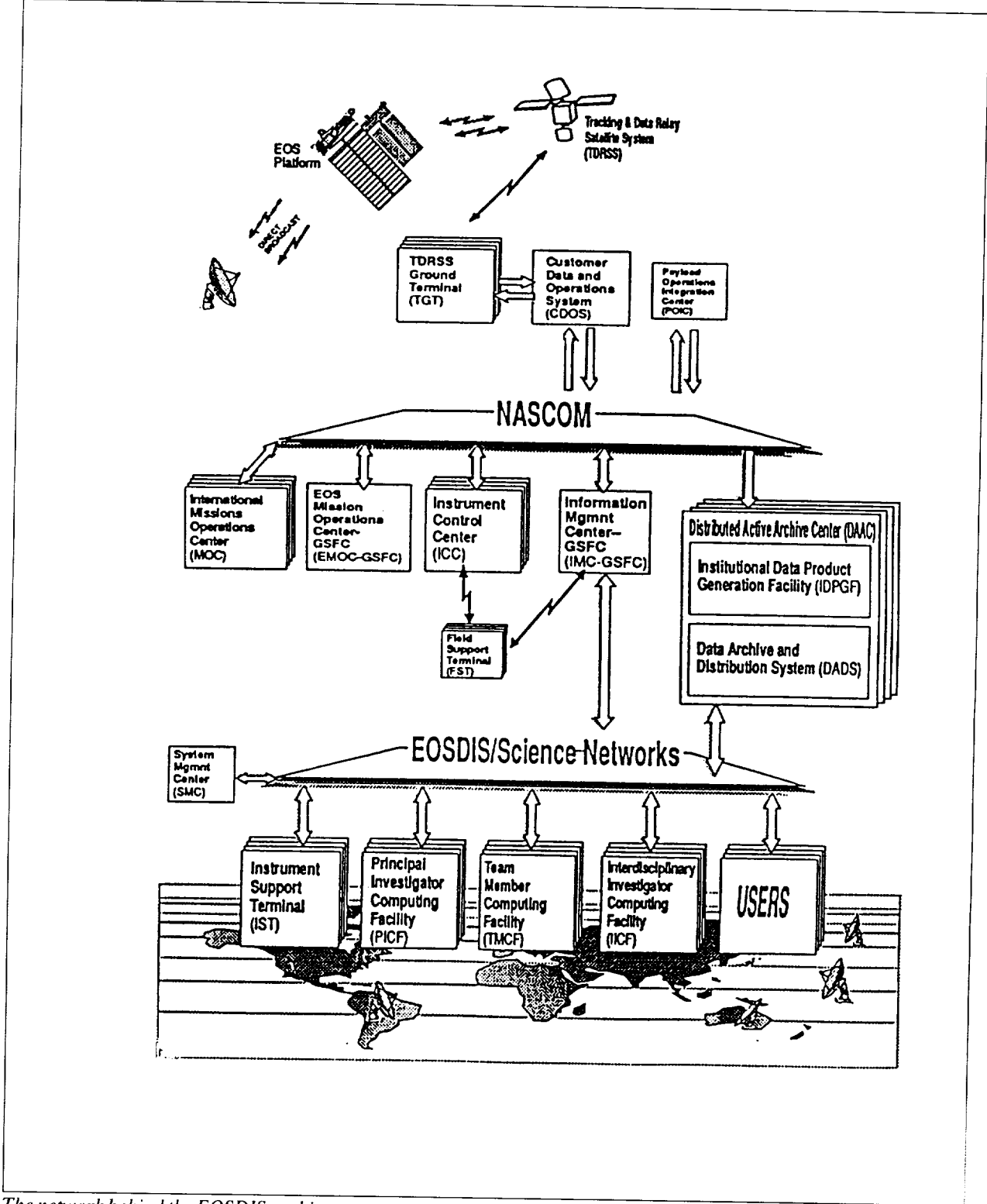
EOSDIS will be the most complex and advanced information system ever developed to meet scientific research needs. It will deal with an enormous data volume of 50,000 terabytes and have an extremely high data processing rate (up to 50 Mbps of raw telemetry input and 500 Mbps output of a great variety of high-level geophysical data products), which will require considerable processing to achieve. EOSDIS is to be developed in a flexible, evolutionary way. The first step, the establishment of EOSDIS Version 0, takes advantage of data processing capabilities at various U.S. centers, which have holdings of large-scale, moderate-volume, long-term geophysical data sets.

These centers have been designated Distributed Active Archive Centers (DAACs). They are located at Goddard, Langley Research Center, Marshall Space Flight Center, the Jet Propulsion Laboratory, the Earth Resources Observation Systems (EROS) Data Center in Sioux Falls, South Dakota, the National Snow and Ice Data Center in Boulder, Colorado, and the Alaska Synthetic Aperture Radar Facility in Fairbanks, Alaska. The plan is to develop commonality among the data systems at the DAACs to provide a unified Earth system view to the multiplicity of users who will represent a variety of scientific disciplines.

The experience gained with the multiple data systems' users will be the basis for the evolution of user-sensitive requirements for EOSDIS. Also, at the DAACs, it will be possible to test technologies relevant to EOSDIS. Product generation service, in which algorithms supplied by instrument scientists can be used to provide higher level output products to users, will be initiated at the DAACs, and electronic networking among scientists' computing facilities will be substantial. A schematic of the ultimate EOSDIS is shown in the accompanying figure.

The overall goal of EOS is to advance scientific understanding of the entire Earth system on a global scale through developing a deeper understanding of the components of that system, the interactions among the components, and the changes taking place in the system. Three mission objectives have been defined for EOS:

- To create an integrated scientific observing system that will enable multidisciplinary study of the Earth's critical, life-enabling, interrelated processes involving the atmosphere, the oceans, the land surface, and the solid Earth.



The network behind the EOSDIS architecture.



- To develop a comprehensive data and information system including a data retrieval and processing system to serve the needs of scientists performing an integrated multidisciplinary study of Earth.
- To acquire and assemble a global data base emphasizing remote-sensing measurements over a decade or more to enable definitive and conclusive studies of various aspects of Earth system science.

In pursuit of the third objective (developing a 15-year global data base), EOS is to make measurements related to the global distribution of energy input to and output from the Earth; atmospheric structure, composition, and dynamics from the ground to the mesopause; the physical and biological structure, composition, and dynamics of the land surface; key characteristics of the Earth's biogeochemical cycles; physical and biological characteristics of the oceans; characteristics and distribution of land and sea ice; the distribution of worldwide precipitation; and the dynamic motions of the Earth as a whole, including tectonic plate motions.

There have been three approaches to providing the instruments needed to carry out the EOS objectives. Six major instruments, designated as U.S. research facility instruments, are being developed by the NASA centers. Twenty-four other candidate instruments have been selected for consideration for flight through the NASA Announcement of Opportunity (AO) process. Those finally selected will be developed under the leadership of principal investigators from universities, industry, and government. In addition, there are mission-unique instruments—the Wide-band Data Collection System and a data communications package—supporting communications requirements.

A major step toward ensuring in-depth analyses of the data that will flow from the many instruments has been the selection, also through the AO process, of 28 interdisciplinary investigations. The interdisciplinary investigations will perform modeling studies in various areas that may be grouped into hydrological-system studies, climatological-process studies, biogeochemical-cycles studies, and geophysical-process studies. (Geophysical-process studies include atmospheric, oceanic, and solid-Earth studies.)

The NASA observatories, including both platforms and instruments, and the EOSDIS are being managed by Goddard. The six designated U.S. research facility instruments are the Moderate-Resolution Imaging Spectrometer (MODIS), the High-Resolution Imaging Spectrometer (HIRIS), the

Geoscience Laser Ranging System (GLRS), the Laser Atmospheric Wind Sounder (LAWS), the Atmospheric Infrared Sounder (AIRS), and a radar altimeter.

There are two versions of MODIS: MODIS-Tilt, primarily for ocean applications, measures biological and physical processes when off-nadir pointing is desired to avoid sunglint; and MODIS-Nadir, primarily for land applications, has greater spatial resolution and is used when off-nadir pointing is not required.

HIRIS serves as a very high resolution companion to MODIS. GLRS studies the Earth's crustal movements using arrays of retroreflective targets and performs high-resolution, precision profiling of ice sheets and of land and cloud-top surfaces. LAWS uses Doppler lidar to perform direct tropospheric wind measurements. AIRS, working in conjunction with the Advanced Microwave Sounding Unit, measures atmospheric temperature and moisture. Finally, the radar altimeter measures sea-surface elevation.

EOS will advance every aspect of the study of Earth from space, including all of the traditional disciplines which make up Earth science. EOS will extend and build upon the Upper Atmosphere Research Satellite (UARS) and Ocean Topography Experiment programs by providing long-term continuity in measuring stratospheric composition and ocean circulation. It will improve meteorological observations to help extend the range of long-term forecasts. It will enhance measurements for biological oceanography and increase our ability to measure biogeochemical and hydrological processes on the land surface, particularly at large scales, and our ability to determine motions at the edges of tectonic plates.

EOS is a cooperative international effort. NASA's contribution will be complemented by contributions from the European Space Agency and the Japanese National Space Development Agency. The Europeans and the Japanese will provide additional polar orbiting observatories and scientific instruments. Some U.S. instruments will fly on the platforms of the international partners, and some of their instruments will fly on the U.S. platforms. EOS scientific data will be made available to researchers from all the partners.

Contact: Jeff Dozier (Code 900)
(301) 286-8228

Jeremiah J. Madden (Code 420)
(301) 286-3249

Sponsor: Office of Space Science and Applications

Dr. Jeff Dozier is completing his first year at Goddard as a visiting scientist on the EOS Project. He is a professor of geography at the University of California, Santa Barbara. He holds a BA in geography from the California State University, Hayward, and an MS and PhD from the University of Michigan.

Mr. Jeremiah J. Madden is Acting Associate Director of Flight Projects for the EOS Project at Goddard. He is responsible for project management and technical direction for EOS. Prior to his EOS appointment, Mr. Madden served as Project Manager for the GRO Project. He has been at Goddard 32 years. He received his BE in mathematics from Duquesne University and his MA in engineering administration from George Washington University. He received the NASA/Goddard Performance Management and Recognition System Award in 1986 and 1987.

VERSION 0 OF THE EARTH OBSERVING SYSTEM (EOS) DATA AND INFORMATION SYSTEM (EOSDIS)

The goals of EOSDIS are to support the planning and execution of EOS data acquisition and to provide the Earth-science-related research community with easy and reliable access to the full suite of EOS data from the NASA instruments on U.S. and international platforms. EOSDIS will be distributed among seven DAACs where data products are generated, stored, and distributed. The development and implementation of EOSDIS will be evolutionary, with extensive involvement by the scientific users in all phases including the definition study, data analysis, system specification and design, and integration and testing. The evolutionary development concept is a step-by-step process that will allow the gradual transition from the existing Earth-science-related data and information systems to the full-scale EOSDIS configuration. Two independent Phase-B studies of EOSDIS were conducted between January 1989 and April 1990. The requirements, architecture, design concepts, and development approach have undergone considerable scrutiny during this period by the EOS science community represented by the EOSDIS Science Advisory Panel. The procurement process is underway for the design and implementation phase of the EOSDIS Core System (ECS).

While the procurement is in progress, some pathfinder/prototyping activities can start immediately and help guide the Phase-C/D contractor's development. An

effort called Version 0 (V0) will be starting immediately to establish working prototypes of EOSDIS science data processing, archiving, and distributing functionalities. DAAC personnel will participate in a joint V0 system engineering effort and also will implement DAAC-unique functions at their facilities. Also, an information system will be prototyped at Goddard.

The primary goal of EOSDIS V0 is to establish working prototypes of EOSDIS science data processing, archiving, and distributing functionality. The EOSDIS V0 project will consolidate present applicable capabilities, build new capabilities where needed, develop experience with data services that are needed most urgently at the DAACs, and build working relationships among DAACs that will be critical when EOSDIS becomes fully operational. More specifically, the EOSDIS V0 project will:

- Enhance near-term scientific productivity through improved access to current data and the production and use of new data sets derived from currently available and newly acquired data. This will include some support for the EOS Programs Office-funded development of pathfinder data sets—existing moderate-volume, long-term data sets which must be processed into community consensus data products.
- Integrate and evolve current information management capabilities (Pilot Land Data System, NASA Climate Data System, NASA Ocean Data System, etc.) to establish integrated Earth-science information systems as a step towards supporting an interdisciplinary view of EOSDIS. The result of this should be a unified Earth sciences view for users. However, in so doing, it is essential to provide at least the present level of service with no interruption or degradation to the users of the respective data systems at the DAACs.
- Take near-term actions to improve the infrastructure for collaborative, distributed research, including initiating a Global Change Master Directory and interoperable catalog system; adopting initial standards, protocols, and guidelines; and expanding the exchange of data and the connectedness of the Earth-science community.
- Build an enhanced experience base at the DAACs that will influence directly the progressive implementation of EOSDIS by the Phase-C/D contractor. Such experience with the multiple data systems' users will help evolve user-sensitive requirements.



V0 will be based primarily on existing data systems at the DAACs with augmentations to hardware and software occurring to improve the Earth-system view and to ensure that EOSDIS functionalities are demonstrated at each of the DAACs. These functionalities will vary in degree. The information management functionality will be substantial, while the product generation and data archive and distribution functionalities will be limited. During the V0 time frame, though not supported by the V0 EOSDIS project, there will be substantial Science Computing Facility (SCF) capabilities provided to the investigators by the EOS program. The V0 EOSDIS project will enhance networking capabilities among the DAACs and between DAACs and select SCFs. Some capacity will be provided at the DAACs to support initial testing of algorithms developed by the scientists at their SCFs.

Contact: H.K. Ramapriyan (Code 423)
(301) 286-9496

G.R. McConaughy (Code 423)
(301) 286-7741

T.D. Taylor (Code 423)
(301) 286-5520

Sponsor: EOS Project

Dr. H.K. Ramapriyan has worked at Goddard for 12 years. In addition to EOSDIS, Dr. Ramapriyan has worked on Landsat, Shuttle Imaging Radar-B, the Land Analysis System, Pilot Land Data System, and Nimbus 7. Dr. Ramapriyan holds a BE and an ME from the Indian Institute of Science and a PhD from the University of Minnesota.

Ms. G.R. McConaughy has completed 1 year at Goddard in the EOS Ground Systems and Operations Project. She also has worked on the Pilot Land Data System, the NASA Master Directory, Landsat, and Nimbus projects. She holds a BS in mathematics from Allegheny College.

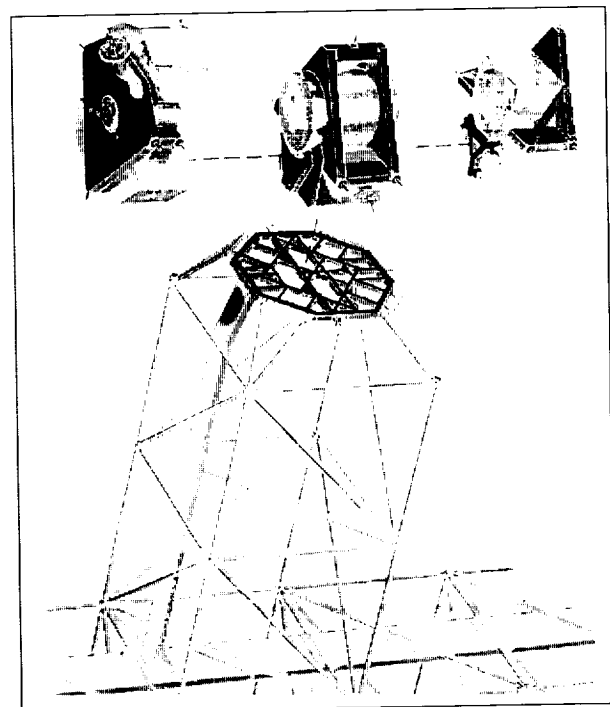
Mr. T.D. Taylor has worked at Goddard for more than 28 years. He holds a BE in electrical engineering from the University of Florida and an MS from George Washington University. He has received the Award of Merit, the Outstanding Service Award, and the Special Act or Service Award for his work on projects including the International Ultraviolet Explorer and the Upper Atmosphere Research Satellite.

ASTROMAG

Astromag is a superconducting magnet facility designed for placement on Space Station Freedom. It will produce a high-intensity magnetic field in space to support high-energy particle physics and space physics experiments. Astromag instruments will address issues now of central importance to the investigation of cosmic rays: the origin and evolution of matter in the galaxy; the search for antimatter and dark matter of cosmological significance; and the origin and acceleration of relativistic particles in the galaxy.

The heart of the central facility is the superconducting magnet and its cryogenic system. The magnet and cryogenic system consist of two superconducting coils, a superfluid helium storage tank, and a circulation system, as well as various valves, and plumbing and instrumentation. A vacuum vessel houses all other components. Latching mechanisms allow the exchange of instruments in orbit without bringing the facility back to Earth.

The assembly and servicing capabilities of the Space Station make it possible to develop Astromag as a facility in



An artist's rendering of Astromag, a superconducting facility designed for placement on Space Station Freedom.

which, after a few years of observations, scientific instruments can be exchanged, and new experiments can be carried out. Astromag allows two experiments to be performed simultaneously and is expected to operate for 3 to 4 years without return to Earth for refurbishment.

Astromag's primary scientific goal is the study of cosmic rays—a suprathermal gas of energetic charged particles still of unknown origin—which pervades the galaxy. Some small fraction of this material is believed to come from space beyond the galaxy. Cosmic rays provide a unique sample of matter from far outside the Solar System and an important means of studying the dynamics and evolution of the galaxy.

Study of the origin, acceleration, and propagation of cosmic rays is certain to yield important new understanding of the phenomenon of relativistic plasmas in space. The small fraction of particles from outside the galaxy will be searched for antiparticles, direct evidence for the existence of stars and galaxies made of antimatter. Such a discovery would have profound cosmological implications.

Astromag will be capable of measuring high-energy nuclei and electrons in cosmic rays with precision and sensitivity between 10 and 1,000 times that of previous experiments in particle astrophysics. Such studies will extend our knowledge of these rare particles to much higher energies where predictions of different theoretical models involving high-energy phenomena in our galaxy clearly can be tested.

NASA, through its AO process, selected three experiments for definition and development:

- Large Isotope Spectrometer for Astromag (LISA). The principal investigator is Dr. J.F. Ormes, of Goddard.
- Measurements of cosmic rays including antiprotons, antinuclei, and a search for primordial antimatter (WIZARD). The principal investigator is Dr. R.L. Golden, of the Particle Astrophysics Laboratory at New Mexico State University.
- Spectra, Composition, and Interactions of Nuclei above 10 TeV (SCIN). The principal investigator is Dr. T.A. Parnell, Marshall Space Flight Center.

The basic Astromag concept shown in the figure and summarized in the table consists of three components: the Astromag Core Facility, two in-orbit replaceable

Astromag System Parameters		
Magnet	Field Intensity	7.0T
	Stored Energy	11.0MJ
	Decay Rate	1 percent per year at 4° K
	Size	1.7 m diam. (650kg)
Cryostat	Working Fluid	Liquid Helium
	Life time	3 to 4 years
	Tank capacity	3,500 liters
	Size	2.1 m diam. 2.6 m long (1,350 kg)
Utilities	Power	2-3 kW
	Data	150 kbps
	Command	1 kbps
Size	Core Facility	4.4 m diam. 2.7 m long 4,000 kg total
	Experiments:	
	LISA	4.4 m diam. 2.0 m long 2,400 kg
	WIZARD	4.4 m diam. 2.0 m long 3,400 kg
	SCIN	4.4 m diam. 2.2 m long 1,500 kg
	Outrigger	5 m x 5 m x 10 m high

experiments, and the Space Station Freedom support elements (a zenith-oriented outrigger extension, attached-payload accommodations equipment, and the full complement of assembly and servicing equipment). The support elements, which provide the structural, power, data, and command interfaces between Astromag and the Space Station Freedom, will be installed prior to the launch of Astromag and the first set of experiments.

Astromag is an international project being developed jointly by Agenzia Spaziale Italiana (ASI) and NASA. Astromag and the three selected experiments currently are undergoing definition (Phase-B) studies as the next step leading toward a launch prior to the year 2000.



Contact: George Anikis (Code 410)
(301) 286-8416

Sponsor: Office of Space Science and Applications,
Flight Systems Division and Space Physics
Division

Mr. George Anikis is the Deputy Project Manager for Astromag. Currently serving on the Explorer and Attached Payloads Project, he has worked at Goddard for 12 years. Prior to Astromag, Mr. Anikis also worked on the Orbiting Geophysical Observatories, the Orbiting Solar Observatories, the Meteorological Sounding Rocket Program, and the Far Ultraviolet Spectroscopic Explorer. He holds a BES in electrical engineering from The Johns Hopkins University.

EXPENDABLE EXPLORER SPACECRAFT (EES)

The Goddard Advanced Missions and Analysis Office initiated a study for performing Explorer Missions from 1999 to 2007 using a generic Expendable Explorer Spacecraft (EES). The EES will provide a medium-cost capability with which science missions from various disciplines can be carried out during a 10-year period, using a medium expendable launch vehicle. The study was conducted without any specific science payload designated; however, payload proposals submitted in response to the 1986 NASA Dear Colleague Letter for potential Explorer missions were used as the guideline for the EES requirements. For these science requirements, strawman spacecraft were considered to establish a basis for developing cost and technical parameters for the EES program. Spacecraft configurations were studied for science payloads flying in five different orbits as follows:

- Low-Altitude, 28.7 deg, 600-km altitude, circular.
- Polar, 600-km altitude, circular.
- Sun-synchronous, 98.7 deg, 833-km altitude, circular.
- Geosynchronous, 28.7 deg, 35,786-km altitude, circular.
- Molniya, 63.4 deg, 12-hour elliptical.

The major guidelines for this study effort were:

- Utilize the Delta-II launch capability.

- Design the spacecraft to fit within the 10-ft-diameter Delta fairing.
- Exclude Shuttle serviceability.
- Constrain the total average cost for five spacecraft to \$50 million each, not including scientific instruments, launch vehicles, and operations costs.
- Use new technology, if cost effective and available by 1995.
- Provide a spacecraft design for a 3-year orbital life.

The EES spacecraft was designed to provide a platform from which a variety of Explorer-class scientific instruments can operate in orbits that are defined generally by the capabilities of the launch vehicle. The EES spacecraft program is planned as a series of five missions managed by a single prime/mission integration contractor. The thrust of the EES program is to provide as much commonality of hardware, software, procedures, and documentation as possible across the five missions to reduce cost, risk, and time-to-launch. The EES is based on existing technology, or technology expected to mature by 1995 that will yield high performance for lower cost and lower weight. Emerging technologies of interest include: the integrated circuits for advanced command/telemetry/ data storage systems; GaAs solar cells; improvements in battery cells (such as super NiCd); and CCDs for star track detectors.

The spacecraft design shown in the table is based on a modular approach to attaching an instrument package to a simple electrical and mechanical interface. In this sense, the interface is very similar to the Multimission Modular Spacecraft (MMS) currently being used for the Explorer Platform Project. However, the EES is not designed to be Shuttle-launched or serviced in orbit and does not have the attendant costs associated with man-rated spaceflight.

The spacecraft design is a versatile configuration which allows parallel build-up and integration of hardware. It makes use of several features from both the Scout-class Small Explorer (SMEX) spacecraft and the MMS-Explorer Platform. By combining elements from both of these programs, using a single, prime contract and a streamlined management approach, the EES program will provide a robust Explorer program in the 1999-2007 era.

Spacecraft Performance Requirements		
Item	Baseline Performance	Enhanced Performance
1. Attitude Control	0.1 arc deg pointing	1 arc sec pointing (celestial)
2. Power	1000 watt load bus, 200 sq. ft. solar array (silicon), single drive, NiCd batteries	1000 watt load bus, 200 sq. ft. solar array (GaAs), single or multiple drive, super NiCd batteries
3. Command & Data	MIL-STD-1773 data bus, 1 MHz clock rate, 1 Gbit data storage, 100-200 Kbps avg. on data bus, 1.25 Mbps burst data	Same, 3 Gbit data storage
4. RF Communications	TDRS Omni (1 Kbps RT) Omni/Gnd (1.25 Mbps dump)	TDRS Omni (1 Kbps Rt) TDRS Hi Gain gimballed (1.25 Mbps dump)
5. Propulsion	Geosync bi-prop (no ACS or orbit maintenance, except Molniya)	Hydrazine ACS and orbit maintenance for LEO and Molniya, GEO bi-prop
6. Thermal Control	MLI Blankets, Tapes and Paint	Louvers MLI blankets, Tape and Paint, Heat Pipes
7. Structure	Aluminum conventional construction, honeycomb panels	Same
8. Mechanisms	Solar array deployment, Solar array drive	Antenna gimbals, solar array deployment, solar array drive

The candidate spacecraft configurations considered were spinning spacecraft with body-mounted solar cells, dual spin spacecraft, gravity gradient stabilized spacecraft, and three-axis stabilized spacecraft with celestial or nadir pointing. The gravity gradient mode was discarded because of its poor performance from an attitude-control point of view. The spinners are low-cost spacecraft candidates, but generally do not meet many science requirements. Therefore, the baseline is a three-axis stabi-

lized design with capability for variations in subsystem capabilities.

Transmitting science data directly to a single ground antenna, using omni spacecraft antennas, provides a significant cost savings in the baseline design. While this limits the amount of stored data that can be transmitted to the ground, the cost of a high-gain TDRSS antenna is not included for those missions that do not require a large amount of data. The use of TDRSS high-gain antennas is considered to be an enhancement to the baseline spacecraft.

The EES is a multimission program with many options in spacecraft structure design and in subsystem implementation. This flexibility allows for a lower cost program. Commonality of hardware through phased procurements and selected mass buys is recommended. A single, prime contractor should be used to ensure the commonality of design, hardware procurement, and integration processes.

Contact: James E. Phenix (Code 402)
(301) 286-9409

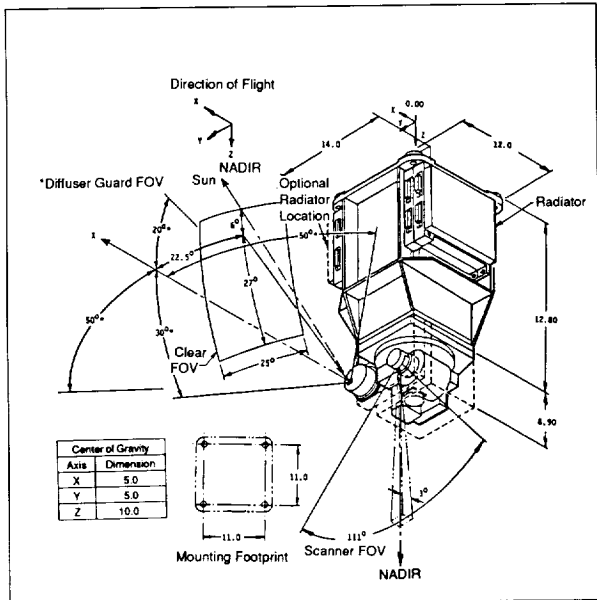
Sponsor: Office of Space Science and Applications,
Explorer Platforms

Mr. James E. Phenix has 23 years of experience at Goddard. Mr. Phenix was the Study Manager for the EES project. He also served as Head of the Structures and Mechanics Branch for the Special Payloads Division, as well as the Mechanical System Manager for the Cosmic Background Explorer (COBE). He received his BSME from the University of Maryland.

THE TOTAL OZONE MAPPING SPECTROMETER MISSIONS (TOMS)

The Total Ozone Mapping Spectrometer Missions (TOMS) are designed to continue making measurements similar to those currently being made by an instrument aboard the Nimbus-7 spacecraft, in order to produce high-resolution mapping of the global total ozone on a daily basis, as well as to detect global ozone trends to verify depletions predicted by chemical models.

In late 1993, a Goddard-managed Earthprobe mission, TOMS-EP93, containing a TOMS instrument as its only payload, will be rocketed into an elliptical parking orbit via NASA's Small Expendable Launch Vehicle. Systems



A drawing of the TOMS instrument, with dimensions shown in inches.

onboard the spacecraft will then cause it to move into a 955-km Sun-synchronous final orbit where it will operate for at least 2 years.

Requirements placed on the mission are exacting so that natural ozone changes can be separated from man-made or anthropomorphic changes. It is required that the ozone measurements be made all the way to the poles and that small-scale features and very sharp gradients in total ozone be resolved clearly. Ozone trends of 0.1 percent per year must be measured. The mission requires a spacecraft with three-axis nadir pointing capability having at least 0.1-degree pointing knowledge.

The TOMS instrument is similar to the one flown on Nimbus 7, except that it has been upgraded to accommodate electronic components which are available today. In addition, wavelength and calibration changes have been made. The instrument will provide 50-km by 50-km resolution during daytime observation.

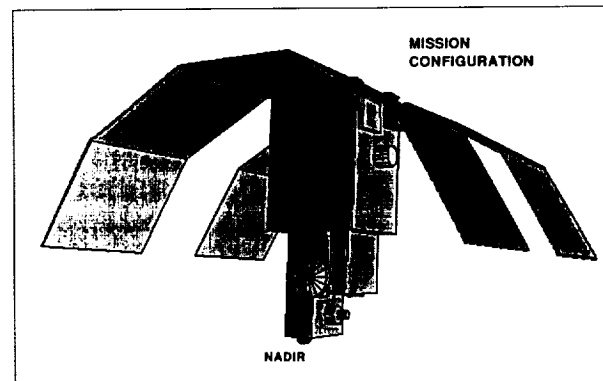
In early 1995, a similar instrument will be launched aboard the Japanese Advanced Earth Observation Satellite (ADEOS). Although this mission will be flown in a lower (800 km) orbit than the 1993 Earthprobe mission, it still is expected to provide significant ozone data.

Because of its absorption in the ultraviolet region of the spectrum, ozone is one of the most important tracer

species in the stratosphere. Ozone absorbs virtually all of the solar ultraviolet radiation incident on the Earth between the wavelengths of 200 nm and 300 nm. The amount of ozone in the atmosphere may be affected by a number of factors including man-made fluorocarbons and solar cycle variations. One of the central problems of stratospheric research is the attempt to quantify the individual roles of these factors and any possible interactions among them.

The crucial problem in global ozone trends is to separate possible anthropogenic trends from natural variability. The limiting factor is length of record, particularly with respect to defining the magnitude of the ozone change with the 11-year solar cycle as compared to steady trends due to increases in fluorocarbons and other trace gases. An important factor in the global ozone budget is the destruction of ozone in polar winter and spring. Up to 3 percent of the global ozone is destroyed in the Antarctic ozone hole.

The ultraviolet radiation received by the TOMS instrument in the total-ozone bands consists mainly of solar radiation that has penetrated through the stratosphere and has been reflected back by the dense tropospheric air and the surface. Ozone, being concentrated in the stratosphere above the region in which most of the radiation is backscattered, acts as an attenuator of this radiation. By determining the amount of this attenuation in the ozone absorption bands, the amount of ozone above the reflecting surface can be estimated accurately. More than 90 percent of the ozone is located above the tropopause, whereas all clouds, most of the aerosols, and approximately 80 percent of the atmosphere are located below it. This almost complete separation of the ozone from the scatterers and reflectors minimizes errors caused by vertical profile shape, clouds, aerosols, and other tropospheric variables.



The TOMS Phase-A configuration.

The TOMS instrument, weighing about 25 kg, is designed to be flown aboard satellites in circular orbits at altitudes between 797 and 1000 km. The instrument contains a simple, rugged Fastie-Ebert ultraviolet spectrometer subsystem together with a foreoptics telescope and scanner assembly which directs the instantaneous field of view across the Earth's atmosphere by means of a stepped scanning mirror. The nadir-viewing instrument, shown in the first figure, scans an adjustable cross-track span in 3-degree steps, with scan rates tailored to altitude for contiguous coverage with minimum overlap. For the missions identified herein, the nadir scene size varies from 42 to 50 km. The optics design is basically the same as that used on Nimbus 7 and has proved itself to be reliable and stable in more than 10 years in orbit. The spectrometer is a single grating device equipped with a wavelength selection mechanism that successively measures the radiance at preselected wavelengths with a single detector selected for its radiometric stability and low noise characteristics. Solar irradiance measurements are to be made using a diffuser plate which is equipped with a means to measure its reflectivity in the TOMS wavelength band.

The microprocessor-based instrument electronic system contains the command receiving and decoding subsystem, the telemetry formatting and interfacing subsystem, and the power conditioning and interfacing subsystems. Unregulated power is provided within the instrument.

The TOMS-EP spacecraft bus will be designed to accommodate the 1993 mission requirements and will be capable of supporting a 2-year lifetime, with a 3-year-lifetime goal.

The power subsystem will be sized to provide energy balance each orbit, with a power margin of 20 percent at the end of the 2-year mission lifetime. It will provide approximately 20 W to the instrument at voltages between 28 and 32 Vdc. The instrument will provide its own internal regulating and conditioning.

The spacecraft will be three-axis stabilized so that the instrument is nadir-pointed with about 0.5-degree control and about 0.1-degree knowledge from measured attitude data. Control will most likely be achieved using reaction wheels/scanners and magnetic torquer bars. An orbit adjust system will be used to boost the spacecraft from the parking orbit to the final orbit and to achieve a plane change to trim inclination, if required.

The mission primarily will store data and forward it later. Real-time data will be taken only to monitor spacecraft and instrument health and safety. Mass storage will accommodate up to 24 hours of data, recorded at approximately

1 Kbps. Communication to and from the ground will be via Deep Space Network compatible S-Band transponders. The links have been sized to accommodate alternate ground stations having 8- to 9-meter antennas.

The second figure shows a spacecraft concept derived from the TOMS Phase-A study. This configuration is capable of meeting all mission requirements.

The baseline TOMS ground system will use the institutional services provided by the Goddard Mission Operations and Data Systems Directorate. A POCC is planned for Goddard. It will be supported by the Data Capture Facility, the Command Management System, and the Flight Dynamics Facility. The institutional responsibilities will be for mission planning, tracking, and operation of the spacecraft.

Communications to and from the spacecraft will be accomplished via Deep Space Network stations and the Wallops Flight Facility Station since TOMS will not carry a TDRSS antenna. The possibility of an alternate ground station to fill in gaps in coverage also is being considered.

All commands to the spacecraft will be transmitted via the POCC. Received data will be processed initially by the Data Capture Facility to Level 0 and transmitted directly to the POCC for spacecraft monitoring and control, and to the Science Operations Center (SOC) for further science processing.

A SOC, similar to the one supporting Nimbus-7 and the Meteor-3 mission will be used to provide instrument mission planning, command generation, and preprocessing of the science data. This data is then forwarded by the SOC to the Science Data Facility for detailed examination and data product generation.

Contact: Donald L. Margolies (Code 450)
(301) 286-8984

Sponsor: Office of Space Science and Applications,
Earth Science and Applications Division,
Flight Programs Branch

Mr. Donald L. Margolies is Deputy Project Manager of the Explorer and Attached Payloads Project and Project Manager for the Extreme Ultraviolet Explorer. Currently, he is working for the Flight Projects Directorate on the TOMS Project. During his 27 years at Goddard, Mr. Margolies has been honored with the NASA Exceptional Service Medal and the Goddard Outstanding Performance



Award. He holds a BSEE from Rensselaer Polytechnic Institute and an MSE and an MEA from George Washington University.

LUNAR TRANSIT TELESCOPE (LTT)

The Lunar Transit Telescope (LTT) is a candidate for an early science program to be conducted as part of the Space Exploration Initiative (SEI). In addition to supplying unprecedented astronomical observations to the science community, the LTT will provide real-time viewing to high schools, colleges, and universities as educational experiences. The LTT will conduct an imaging survey of the universe with higher angular resolution and broader wavelength coverage over a larger fraction of the sky than has ever been attempted or can be attempted until this telescope is placed on the Moon.

The LTT will permit a deeper, less-biased, more statistically significant complete survey of virtually every type of astronomical object. It is an ideal instrument for statistically describing the content, structure, and evolution of the universe. The LTT will survey literally millions of objects, allowing selection of specific targets for follow up with other space- and ground-based telescopes. We often learn about the content and physical processes in our universe by studying extreme cases—the LTT will observe so many objects so completely that it will almost certainly discover extreme objects in nearly any astrophysical domain.

Because the LTT surveys such a large volume of the universe, it is a virtual certainty that the most significant contributions of this instrument cannot be predicted; they will be serendipitous discoveries.

The LTT has evolved from the CCD Transit Instrument (CTI) currently in routine operation at the Steward Observatory of the University of Arizona on Kitt Peak. As with the CTI, the LTT will have no moving parts. The optical axis will be fixed in azimuth and elevation, and lunar rotation will allow the LTT to scan the sky just as Earth's rotation provides the scanning capability of the CTI. The LTT will employ all reflective optics (a Paul-Baker three-mirror system) and image radiation from the ultraviolet through the infrared spectra. Silicon (Si) CCDs will be used as the ultraviolet and visible detectors while passively cooled HgCdTe with CCD readouts will provide the infrared detection. Pixel size will be

0.1 arc-second. The established limiting magnitudes for a signal-to-noise ratio of 10 and a 360-second integration time are $V=27$, $H=25$, and $K=24.5$.

A simple, pin-joint, open-truss structure with materials and geometry chosen to provide near-zero thermal expansion will support the telescope assembly.

Contact: John J. O'Brien (Code 402)
(301) 286-9434

Sponsor: Office of Space Science and Applications,
Astrophysics Division

Mr. John J. O'Brien, Study Manager for the LTT, has worked at Goddard for 24 years. Prior to the LTT project, he served as a technical officer for the Lyman FUSE Phase-A study and received several NASA achievement awards. He holds a BS in physics.

GEOSYNCHRONOUS ENVIRONMENTAL MISSION (GEM)

The principal objective of the Geosynchronous Environmental Mission (GEM) is to provide one or more relatively lower cost, minimum lead-time, state-of-the-art research missions in the 1990s to satisfy Earth science (land, ocean, atmosphere) needs for improved sensing capabilities in geosynchronous Earth orbit (GEO). Another major objective of GEM is to respond to Administration requests for less expensive, shorter lead-time, more frequent science missions.

The purpose of GEM is to continue advancing knowledge of the Earth sciences in concert with the goals of the Mission to Planet Earth (MPE) initiative in a time frame that fills a growing gap between prior geosynchronous environmental research missions and the first geoplatform. MPE is part of an even greater global environmental research program with many countries expected to participate in a cooperative, well-coordinated manner. Therefore, GEM research results can be expected to be of value internationally as well as domestically.

The mission can serve as a precursor to the much larger geoplatform (now referred to as the Geostationary Earth Observatory by NASA) that currently is in early stages of development. Advanced research sensors can be flown, tested, corrected, and then assessed prior to development of the 10-year-lifetime Geostationary Earth Observatory missions. Potentially high-risk technological advances also can be tested and qualified with much less impact and at lower

cost through GEM than would be the case with a larger geoplatform.

GEM would be moved to numerous worldwide longitude locations to investigate global atmospheric, land, and ocean processes. Thus, the proposed mission can be used by Earth scientists worldwide for research purposes in land, ocean, and atmosphere studies to help define requirements, not only for future remote-sensing space systems, but also for land use, environmental planning, and associated actions by local, Federal, and international agencies.

Instruments proposed for GEM can provide important regional and global near-term information for conducting research in three principal areas: rapidly evolving atmosphere change; biospheric processes and their coupling with atmospheric phenomena; and coastal and oceanic biological and physical processes.

The temporal resolution required of the data needed to support this research is available uniquely from geosynchronous altitudes.

Used in conjunction with EOS, geosynchronous satellites, and the Landsat satellites, GEM can prove a rich resource of correlative data for Earth-science analysis in a number of disciplines ranging from agriculture, forestry, and hydrology to oceanography and marine resources and the atmospheric sciences.

GEM, assuming it is launched prior to the geoplatform, will be the first land-ocean-atmosphere remote-sensing mission in GEO. And it will be the first NASA research mission in GEO in more than 20 years.

GEM shows promise of satisfying the need for improved Earth science remote-sensing capabilities by better utilization of the fundamental properties of viewing from GEO. The principal strengths of GEM are its relatively low cost and short time period from inception to launch, and its science data correlation potential with EOS and other Earth remote-sensing missions. GEM is structured to take maximum advantage of the efficiencies available through use of existing support hardware, much of which has been designed and developed on prior or present programs. A greater percentage of available resources, therefore, can be applied directly to meeting Earth-science mission goals.

GEM also could serve as a development test bed for new prototype instruments that eventually would become part

of the geoplatform payload. Testing these instruments on a smaller, less expensive spacecraft should enhance the overall chances of success of the geoplatform and minimize the disaster potential of an instrument failure on the more costly geoplatform.

GEM focuses on specific sensing advantages obtainable only from GEO, which should result in very accurate measurements of numerous atmospheric, land, and ocean qualities. These advantages include: high temporal resolution, consistent viewing angle to a given Earth location, long and flexible sensing dwell times, varying Sun angles, matching of GEO measurements with data from other sources (such as low-altitude Earth orbit (LEO) missions), and continuous stereographic measurements when two spacecraft are simultaneously surveying a common area.

If the world is moving from an inherited environment to one which must be controlled, then it is time to develop the understanding and tools to assess and manage both resource use and the affected environment on a global scale.

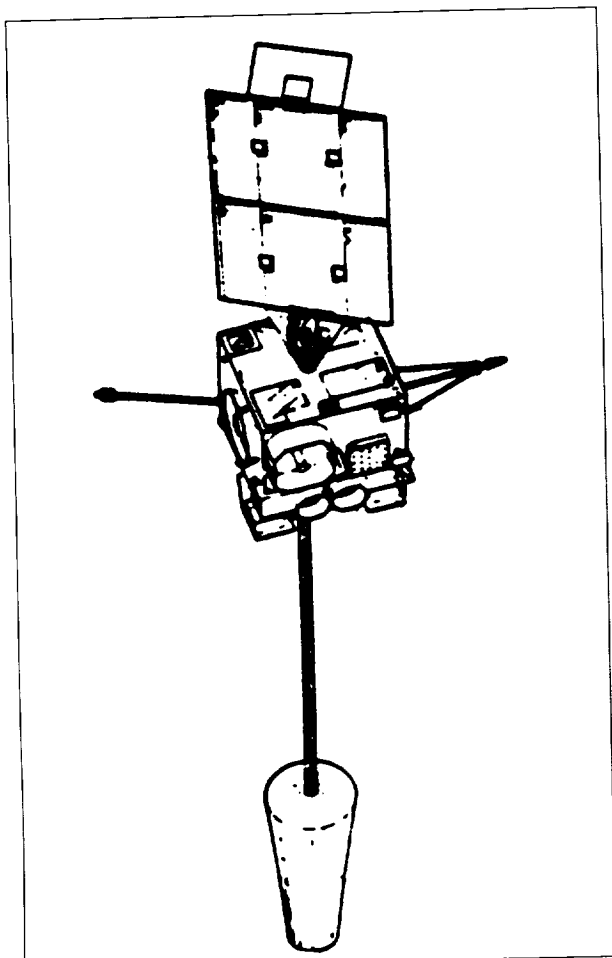
Contact: Harry Montgomery (Code 402)
(301) 286-9449

Sponsor: Goddard Space Flight Center

Dr. Harry Montgomery has worked at Goddard for 29 years. In addition to his efforts on the GEM Project, he also served as Project Manager on the Geostationary Operational Environmental Satellite Project in 1990. He holds a BS and an MS in mechanical engineering from The Johns Hopkins University and a PhD in aerospace engineering from The Catholic University of America.

THE NEXT-GENERATION GEOSTATIONARY OPERATIONAL ENVIRONMENTAL SATELLITE (GOES-N)

For most of the past two decades, U.S. operational geostationary satellites have provided timely information on rapidly evolving meteorological phenomena and unique measurements for global models over approximately half the Earth as well as significant information on the space environment and valuable communications services. While progress has been substantial, there remain many improvements and/or new capabilities which could increase sharply the value of the data to the Nation and the international community.



An artist's sketch of GOES-N.

The Geostationary Operational Environmental Satellite (GOES) is used by the National Environmental Satellite Data Information Service (NESDIS) to obtain images and soundings (temperature and moisture profiles) of the Earth's atmosphere for weather forecasting. The images and soundings are from the quintessential Visible Infrared Spin Scan Radiometer (VISSR) Atmospheric Sounder (VAS). VAS was produced by adding a sounding capability to the VISSR, which had only an imaging capability. Nominally, there is a GOES-East located at 75° E longitude and GOES-West located at 110° W longitude. Currently there is only one satellite, GOES-7, which is spin-stabilized. Since GOES-7 is a spinner operating at an altitude of about 36,000 km from which the Earth subtends only about 17 degrees, the sensors can view the Earth only about 5 percent of the time through a spin cycle. Another problem with the VAS is that it is incapable of simultaneous imaging and sounding.

The decision was made in 1983 to replace the current system with a new, three-axis stabilized system so sensors could view the Earth full time and, hence, be able to collect more data. The new system has two separate instruments: one dedicated to imaging and another to sounding; thus, simultaneous imaging and sounding are possible. The new satellites, the first of which is scheduled to be launched in early 1992, are designated as GOES I-M. GOES-N is the GOES next-generation satellite; and it will satisfy even more of the Nation's weather data needs and will replace the GOES I-M series.

Advanced Mission Analysis Office (AMAO) studies were conducted to assess the predicted performance of the GOES I-M and to compare it with the expected performance of various options of the GOES-N system. Image navigation/registration of pixels of the GOES-N are expected to be about twice as good as the GOES I-M. This should yield better estimates of winds from cloud motion and more accurate Earth location of meteorological activity.

If the advanced visible/infrared imager is on GOES-N, it will provide data in as many as nine spectral bands with resolutions as high as 0.5 km. If the high spectral resolution sounder is on GOES-N, it will sound an area of 3,000 by 3,000 km in 40 minutes.

The higher spectral resolution of 1 to 2 wave numbers for GOES-N compared to 10 to 60 wave numbers for the GOES I-M will permit higher vertical resolution of the temperature and moisture profiles. It is considered essential for the GOES-N soundings to play a significant role in the total data systems available by the late 1990s; soundings with temperature accuracies of at least 1.0 K in layers of 1 to 2 km will be needed.

Augmentation of the existing Space Environment Monitor (SEM), Data Collection System (DCS), and the Search and Rescue (S&R) system was studied.

The SEM has three main functions: measurement of magnetic field strength and direction, assessment of solar X-ray flux, and sensing of energetic particles that make up the solar wind and radiation belts around the Earth. The primary user of these data sets is the National Oceanic and Atmospheric Administration (NOAA) Space Environment Laboratory.

The purpose of the DCS is to collect environmental data in remote areas and relay the information back to a central facility for access by a variety of users. The study addressed

upgraded capabilities from the present GOES spacecraft that include an increased power budget, additional transmission rates, and a location capability.

The GOES has a limited role in providing data to locate aircraft or vessels in distress. NASA is investigating the feasibility of providing some level of location capability on the GOES-N series to provide a complement to the existing polar satellite program.

The AMAO study has resulted in a matrix of expected performance, cost, risk, and feasibility estimates for various concepts considered in response to NESDIS guidelines.

This matrix is included in the final GOES-N report to NESDIS. NESDIS management will select the particular concepts for further study and eventual inclusion into the GOES-N system.

Contact: Harry Montgomery (Code 402)
(301) 286-9449

Sponsor: Office of Space Science and Applications,
Earth Science and Applications Division

Dr. Harry Montgomery has worked at Goddard for 29 years. In addition to his efforts on the GEM Project, he also served as Project Manager on the Geostationary Operational Environmental Satellite Project in 1990. He holds a BS and an MS in mechanical engineering from The Johns Hopkins University and a PhD in aerospace engineering from The Catholic University of America.

THE TROPICAL RAINFALL MEASURING MISSION (TRMM)

The Tropical Rainfall Measuring Mission (TRMM) is an integral part of the NASA Mission to Planet Earth Program. TRMM is one of the Earth probes, a series of spacecraft designed to observe a unique subset of the total measurements required to define scientifically the Earth and observe its dynamic behavior. TRMM will be the first space mission dedicated to measurements of tropical rainfall, bearing the first precipitation radar.

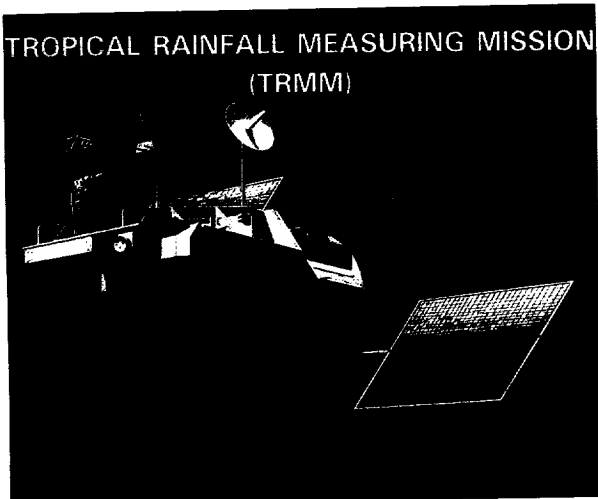
TRMM is a climate mission designed to determine the rate of rainfall and the total rainfall occurring between the North and South latitudes of 35 degrees. The primary climate data set is the monthly average rainfall with a spatial resolution of 500 km by 500 km. TRMM's instrument

ensemble will provide data that both are required for rainfall determination and are valuable independently for related research. TRMM is not required to provide meteorological operational data sets, but the ground-segment data-processing design will be sufficiently flexible to allow, if future requirements emerge, operational utilization of TRMM data.

Included in TRMM is an extensive network of ground-based precipitation observation sites. These sites will be instrumented with radars and rain gauges to provide data and allow correlation with measurements collected in space. Consideration is being given to the addition of an Earth radiant-energy measurement. This addition would greatly enrich the total scientific content of the mission by providing observations in the long-wavelength portion of the Earth's radiant-energy spectrum.

The TRMM project is a joint venture with the National Space Development Agency (NASDA) and the Communication Research Laboratory (CRL), both of Japan. The primary areas of responsibility for NASA, NASDA, and CRL are:

U.S.	Japan
Observatory (spacecraft, integration, and system tests)	Precipitation radar
Advanced Very High Resolution Radiometer (AVHRR)	Launch vehicle (H-II) and H-II-to-spacecraft adaptor
Microwave radiometers: Special Sensor Microwave Imager (SSM/I) and Electronically Scanning Microwave Radiometer (ESMR)	Observatory-to-H-II integration and test
Clouds and Earth's Radiant-Energy System (CERES)	
Telemetry, command, control, tracking, and navigation	Launch services through orbit insertion
Mission operations and control	



An artist's rendering of TRMM.

The salient features of the mission and the observatory are:

Mission:	Altitude	350 km
	Inclination	35 degrees
	Lifetime	3 years
	Eccentricity	.000454 (frozen orbit)
Observatory:	Launch mass	2850 kg
	Fuel	700 kg
	Power	1000 W
	Data rate	158 kbps
	Data format	CCSDS 102.0-B-2 packet telemetry

Data received from the TRMM Observatory via TDRSS will be Level-Zero Processed (LZP) in the TRMM Data Capture Facility and then sent to the TRMM Scientific Data Processing Center (TSDPC). The LZP data will have a latency of no greater than 48 hours after the space observation and will be made available simultaneously to both the TSDPC, located at Goddard, and the Japanese users and investigators. The entire 3-year data set will be archived permanently in the National Space Science Data Center (NSSDC) located at Goddard.

The TRMM is under active consideration for a Fiscal Year 1991 new start. With a launch on the Japan-provided H-II scheduled for 1996, the first monthly averaged data set will be available before the end of 1996. The spacecraft will be implemented with sufficient fuel storage capacity to carry, if launch mass allocation is available, greater than the planned 700 kg

of fuel, thus extending the mission life to possibly the end of the century.

Contact: Thomas Keating (Code 490)
(301) 286-7965

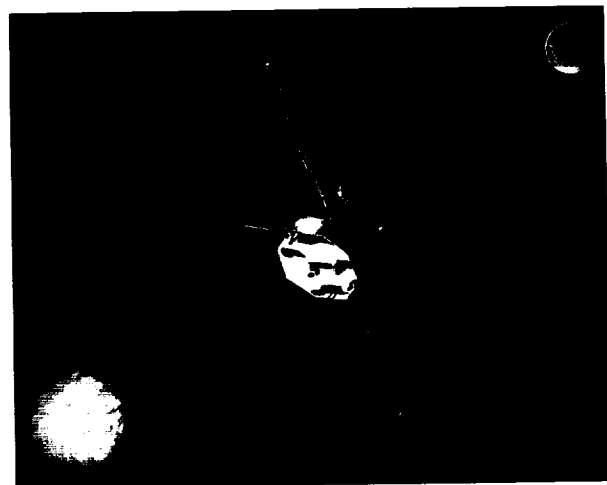
Sponsor: Office of Space Science and Applications,
Earth Probe/TRMM Project

Mr. Thomas Keating is the TRMM Systems Manager. During his 28 years at Goddard, he has received four Special Achievement Awards, a Performance Award and a Quality Increase Award. He holds a BSEE from Georgia Institute of Technology and an MSEE from The Catholic University of America.

ADVANCED COMPOSITION EXPLORER (ACE) MISSION

The Advanced Composition Explorer (ACE) mission is another in the series of Explorer missions. The prime scientific goal of this mission is to observe particles of solar, interplanetary, interstellar, and galactic origins, spanning the energy range from that of the solar wind (1 keV per nucleon) to galactic cosmic ray energies (several hundred MeV per nucleon). Definitive studies will be made of the abundance of essentially all isotopes from H to Zn (1Zn), with exploratory isotope studies extending to Zr.

The scientific instrumentation for the ACE spacecraft consists of a coordinated set of six sensor systems with unprecedented resolution and sensitivity. Instruments



Advanced Composition Explorer at L1 libration point.

include a Solar Wind Ion Mass Spectrometer, a Solar Wind Composition Spectrometer, an Ultra-low Energy Isotope Spectrometer, and a Cosmic Ray Isotope Spectrometer. In addition, three small subsystems provide solar wind electron, proton, and alpha monitoring; energetic electron, proton, and alpha monitoring; and a magnetometer.

To minimize cost, the ACE program decided to make use of existing hardware designs. Therefore, the proposed ACE spacecraft is based on designs that evolved from the AMPTE and SIMPL spacecraft. The AMPTE spacecraft was designed as a Sun-pointing bus for scientific instruments, built by The Johns Hopkins University, and successfully launched in August 1984. The orbit chosen for the ACE mission is a modified halo about the Earth-Sun interior libration point, L1. Located at L1, about 1.5 million km from the Earth, the ACE observatory is thus well positioned to undertake a comprehensive study of the elemental and isotope composition and spectral distribution of the charged particles in the interplanetary medium.

Contact: Jonathan F. Ormes (Code 660)
(301) 286-5705

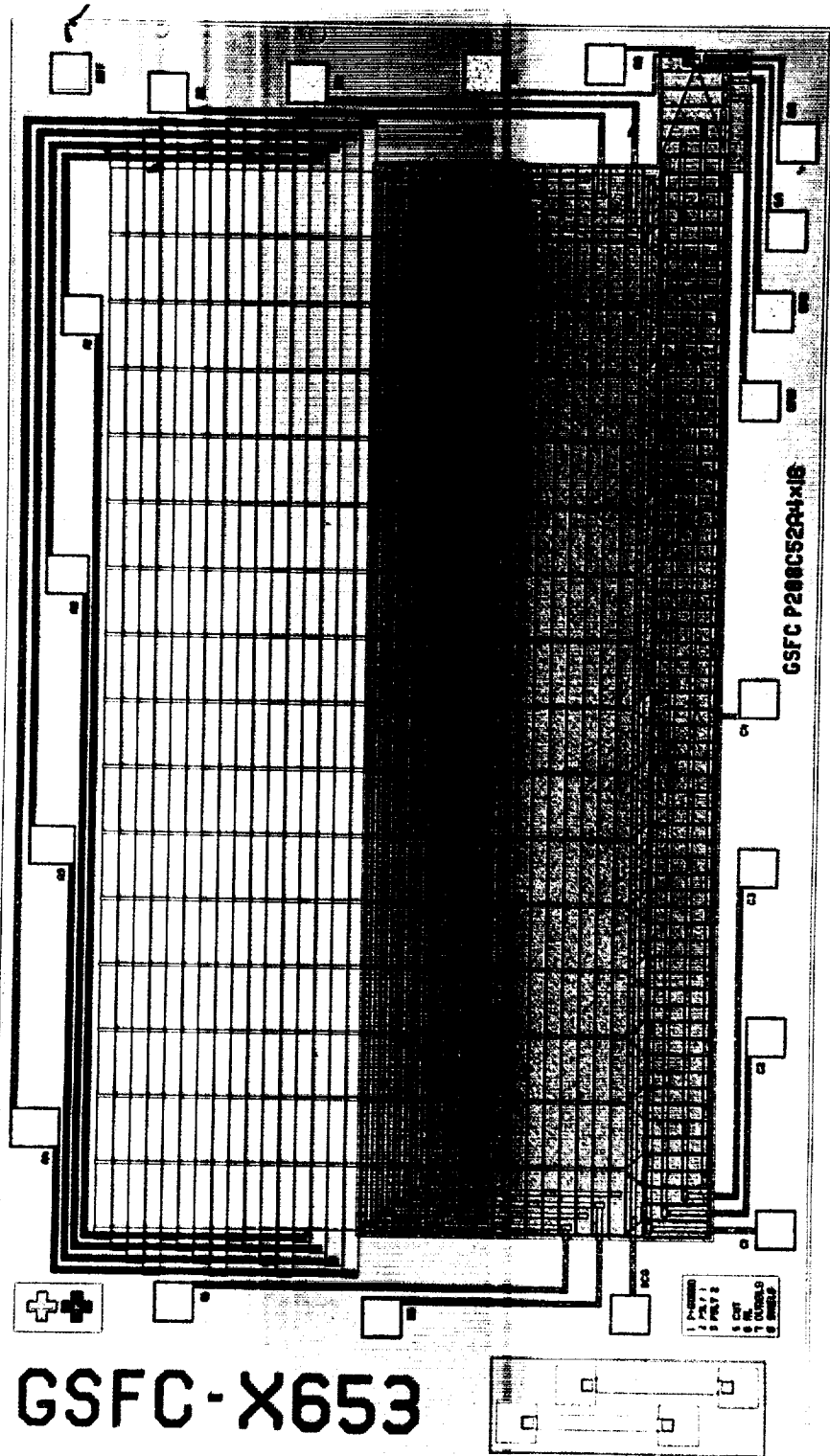
Ed Thomas (Code 410)
(301) 286-7791

Sponsor: Office of Space Science and Applications
Space Physics Division

Dr. Jonathan F. Ormes is the ACE Project Scientist and Chief of the Laboratory for High-Energy Astrophysics at Goddard. He has 22 years of experience at Goddard. Dr. Ormes received a BS from Stanford University and a PhD from the University of Minnesota.

Mr. Ed Thomas is the ACE Mission Manager and the Advanced Missions Manager for the Explorer and Attached Payloads Project. He has more than 27 years of experience at Goddard. He holds a BS in electrical engineering from Northeastern University.

Engineering Technology





"Engineering Technology is the key to progress in more sensitive instruments, more capable spacecraft, more reliable systems, and more cost-effective research."

—T. Huber

ENGINEERING TECHNOLOGY

CHARACTERIZATION OF HIGH-TEMPERATURE SUPERCONDUCTOR (HTSC) ELECTRICAL LEADS

Future NASA missions carrying payloads with sensitive instruments operating at cryogenic temperatures should benefit from the development of high-temperature superconductor (HTSC) yttrium-barium-copper-oxide (YBCO) electrical leads. Currently used leads can be responsible for as much as 50 percent of the parasitic heat load on cryogenic systems. A significant reduction of this load could be achieved with the replacement of today's conventional materials, such as copper or manganin, with HTSC ceramic electrical leads. The use of these new leads could decrease greatly the electrical noise currently observed in many of these instruments.

An increase in the efficiency of the cryogenic cooling system also would result. HTSC materials are excellent electrical conductors in the superconducting state, yet their ceramic nature makes them good thermal insulators as well. Unfortunately, it is these same ceramic properties that give HTSC leads poor ductility and strength compared to conventional metallic leads.

A comprehensive program of X-ray and mechanical testing, along with thermal and electrical work, has

been put together to meet the goal of certification and spaceflight qualification of HTSC electrical leads for future NASA missions. Samples were obtained from several sources, including Argonne National Laboratory and Clemson University. Some samples were made in-house at Goddard.

Specimens were first subjected to X-ray analysis using a Scintag X-ray diffractometer. Data collection was accomplished using time averaging, with multiple scans run on each sample. The entire process was controlled by a VAX minicomputer, which then performed a background intensity correction, followed by lattice parameter calculations using a standard data reduction program. X-ray analysis provided a good measure of the purity of a sample.

Mechanical testing of HTSC wires to determine Young's modulus and tensile strength was done using a standard Instron Tensile Tester. The results so far show significant scatter, as is typical of the strengths and moduli of ceramics. Tensile strengths have varied from 5 to 20 MPa, while Young's moduli have ranged from 50 to 100 GPa.

Testing with the Instron unfortunately is a destructive method. The Young's modulus can be obtained non-destructively using the technique of laser-generated ultrasound, where an Nd:Yag laser is used to produce

◆ *Photomicrograph of prototype Charge-Coupled Device (CCD) imaging devices for the EOS Moderate Resolution Imaging Spectrometer-Tilt (MODIS-T) program.*

pulses which generate acoustic stress waves in the sample upon impact. This method has been used successfully on carbon fibers, and it is envisioned that it will work well with HTSC electrical-lead wire specimens as well. With this method, a piezoelectric transducer is positioned on the specimen to detect the acoustic wave. A sampling oscilloscope records the time of flight of the acoustic wave, from which can be calculated its velocity. Young's modulus, E , is calculated from this by the equation $E=pv^2$, where v is the acoustic velocity and p is the sample's density.

Future plans include the implementation of the non-destructive mechanical testing described above with HTSC electrical leads, as well as the evaluation of a broader spectrum of samples to enable the spaceflight qualification of these materials.

Contact: Petar Arsenovic (Code 313)
(301) 286-8739

Sponsor: Office of Flight Assurance

Mr. Petar Arsenovic works in the Materials Branch of the Office of Flight Assurance. His interests include the study of high-temperature superconductors and the microstructure of carbon fibers used in aerospace composites. He received his MS in material science from the University of Rochester and currently is pursuing a PhD in materials science from The Johns Hopkins University. He has been at Goddard for 3 years.

A QUANTITATIVE EDDY CURRENT IMAGING SYSTEM FOR NONDESTRUCTIVE EVALUATION

The most important task of nondestructive evaluation (NDE) is to provide information about a component's serviceability, usually by measuring a material property. Most NDE methods used so far are qualitative in nature; they produce indications of a material defect but seldom yield absolute material property measurements for a specimen. Quantitative nondestructive measurement of materials is increasingly a compelling new approach, especially for spaceflight assurance.

Part of the drive for quantitative NDE is caused by the use of composite materials. Because of their high

strength- and stiffness-to-weight ratios, these materials are being used increasingly in space applications. To adequately perform spaceflight assurance measures, the detection of defects, characterization of failure modes, and measurement of material properties for these components urgently is required.

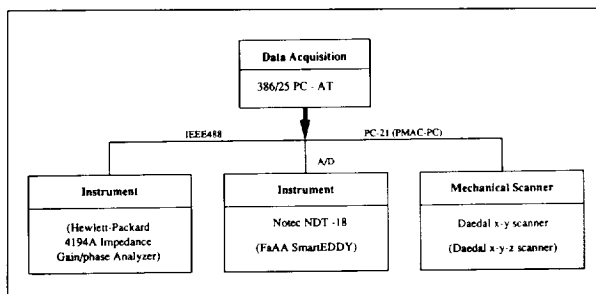
The Materials Branch of the Office of Flight Assurance has developed an eddy current imaging system using equipment on hand. (Presenting a series of NDE measurements as an image can be a powerful method of registering information gleaned from a measurement with specimen geometry.) This system uses the electromagnetic properties of a specimen to make inferences about its mechanical reliability. We have applied this system successfully to study impact damage in composite materials. The first figure shows a 0.5- in by 2.5-in eddy current image of an impact-damaged graphite/epoxy composite specimen. The resulting image clearly shows the area of damage and demonstrates the potential of eddy current imaging for evaluating impact damage in composites.

The eddy current imaging system consists of an off-the-shelf eddy current tester, an x-y mechanical scanner, and a personal computer (PC)-based data acquisition system. A block diagram of the system is shown in the second figure.

We are continuing work which will transform this system into a truly quantitative eddy current imaging system. As part of this process, each component of the system is being upgraded. The eddyscope now in use will be replaced with a digital eddy current instrument (the SmartEDDY), which has dual frequency capability, probe frequency scanning, and other advanced features. In addition, a Hewlett-Packard 4194A impedance gain-phase analyzer also will be incorporated to measure the absolute impedance of the eddy current coil and coupled material. Both instruments



Eddy current image of an impact-damaged composite specimen (scan size 0.5 in by 2.5 in).



Block diagram of the eddy current imaging system.

promise substantial improvements over the present Nor-tec eddyscope, which is only semiquantitative in nature, at best, in measuring impedance.

The scanning mechanism will be upgraded with a Daedal x-y-z mechanical scanner. The new scanner will provide control of the probe-to-sample distance (z-axis), improving the control and manipulation of the probe and the specimen. A 25-MHz 386 PC will be used as the host computer for the SmartEDDY eddy current module and associated software, in addition to serving as overall system controller.

After reviewing images obtained with this advanced eddy current imaging system, signal analysis and data processing methods will be developed to enhance the images. The advanced eddy current images acquired will be transmitted to a central image workstation for processing and correlation with other NDE results from methods such as ultrasonics, X-ray, and thermography. With the implementation of the digital eddy current imaging system and other advanced NDE techniques, the safety, reliability, and quality assurance of Goddard's spaceflight components will be improved.

Contact: E. James Chern (Code 313)
(301) 286-5836

J. Timothy Van Zant (Code 313)
(301) 286-6024

Sponsor: Office of Flight Assurance

Dr. E. James Chern is a materials engineer in the Materials Branch of the Office of Flight Assurance. He received his PhD in physics from the College of William and Mary. His prime responsibility is NDE of composite materials and structures. Prior to joining Goddard nearly

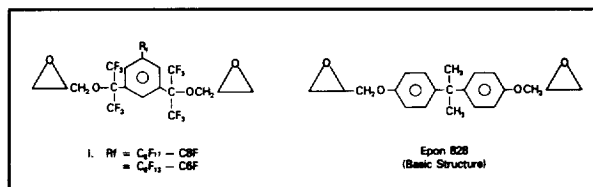
2 years ago, he was with various industrial laboratories working on NDE technology for aerospace applications.

Mr. J. Timothy Van Zant has been involved in image processing and the instrumentation of materials testing since coming to the Materials Branch in 1985. Mr. Van Zant recently received an MS in electrical engineering from The Johns Hopkins University.

A NEW, NOVEL ANTIFOAMING AGENT FOR EPOXY MATERIAL PROCESSING

The control or elimination of the foams that arise in many industrial processes can be a critical factor in industrial operations and associated cost reductions. Antifoaming agents are needed to inhibit and reduce foam formation or to defoam rapidly. The annual world market for antifoaming agents probably exceeds a quarter of a million metric tons.

Antifoaming agents are used widely in the production of monomers and polymers, in the textile industry, in the paint and latex industry and other polymer coating processes, and in the manufacture and application of adhesives. In our investigation of copolymerizing fluorodiepoxides with conventional epoxy resin Epon828, it was found that the use of diepoxides in very small amounts could break the foam bubbles and tremendously reduce the vacuum deaeration time in the preparation of the compound. Air entrainment almost always occurs when the components of an epoxy compound are mixed either manually or with a mechanical stirrer. The mixing normally is followed with vacuum deaeration to remove the entrained air from the viscous liquid compound. The deaeration process is time-consuming and involves fighting patiently with foaming. Any residual air in the compound may create a weakened bond when the material is used as an adhesive or a composite matrix, or may cause an electrical insulation failure when used for embedding or impregnation.



Copolymerizing fluorodiepoxide I and conventional epoxy resin Epon 828.

Antifoaming Effect of Fluorodiepoxides		
Epoxy Compound	Fluorodiepoxide content by wt.	Number of foam-up in vac. deaeration
Epon828/V140 (50/50)	—	>25
Epon828/V140/C8F (4)	1.09%	1/2
(5)	0.55%	1
(6)	0.23%	4
(7)	0.10%	4
Epon828/TETA (14 phr)	—	13
Epon828/TETA/C8F (8)	0.23%	1
(9)	0.096%	1
Thermoset 321	—	22
Thermoset 321, +C8F	0.19%	1/2
Scotchweld 2216	—	34
Scotchweld 2216, +C8F	0.14%	2
Epon 828/TETA/C6F	0.23%	1/2

Notes: 1. Containers used in the experiments are PE cups, 180 ml size, 6 cm depth. Epoxy compounds weighed about 30 gms and took 2 cm or less in depth in the cup.

2. V140 is Versamid 140. TETA is triethylenetetramine. Thermoset 321 and Scotchweld 2216 are the products of Thermoset Plastics and 3M Company, respectively.

3. Fluorine content of the fluorodiepoxides: C8F 58.6%; C6F 56.5%.

Fluoroepoxide I is a new fluoroepoxy resin which may be available in pilot plant quantity. Its antifoaming effect was tested with both commercial epoxy materials and our laboratory-formulated epoxy compounds, as shown in the table. Fluorodiepoxides show excellent antifoaming effects when applied at a level as low as 0.1 to 0.5 percent by weight in the epoxy compounds.

Many antifoaming agents are available commercially, but those which have few side effects are limited. Diepoxide I is valuable because it can copolymerize with a conventional epoxy resin at the same time in the same way as conventional materials, while forming an inter-crosslinking polymer network. Consequently, the antifoaming agent is not a free additive left in the cured material. Our experimental data indicate that as an antifoaming agent used only in a very small amount, Diepoxide I does not have any adverse effect on the outgassing properties and adhesive strength of either commercial adhesives tested or epoxy compounds formulated in our laboratory.

It is reasonable to expect that Diepoxide I can be used as an effective antifoaming agent in the early stage of epoxy manufacturing. It is known that foaming usually is a problem when excess reactants or solvents are

stripped. The application may not be limited to the epoxy process. A similar advantage may exist when Diepoxide I is applied as an antifoaming agent to polyurethane and other thermoset polymer processing where the functional groups of the prepolymers are reactive to the diepoxide. Their reaction also will tie the diepoxide to the crosslinked polymer network.

Contact: S. Yen Lee (Code 313)
(301) 622-3053

Sponsor: Office of Flight Assurance

Dr. S. Yen Lee, a polymer chemist, has been with Goddard since 1969. He is responsible for the development of improved or new materials to meet aerospace requirements. His publication topics include epoxy synthesis, formulation, and evaluation. Dr. Lee received his PhD degree from the University of Colorado.

PLANAR, ACTIVE-ELEMENT WAVEGUIDES IN CdTe-DOPED BOROSILICATE GLASS FOR ENHANCEMENT OF HIGH-SPEED COMPUTING PERFORMANCE

Current NASA space projects will transmit data to Earth at much faster rates than the information can be analyzed, characterized, and acted upon. Optical switches and circuits have the potential to increase data computation, access, and storage rates two to three orders of magnitude compared to conventional, lower frequency electronic systems. Optical systems also would allow noninteractive multiple data-set transmission over single data lines and would be insensitive to cosmic rays and electronic disruptions caused by high-energy X-ray radiation.

Materials currently are being sought to act as transmission media for such a process. Fused silica and other glass compositions have been used for many years as fiberoptic media for the transmission of optical and infrared communication waves over long distances. On a smaller scale, glass substrates have been effectively ion exchanged in controlled regions to produce higher refractive index areas within the substrate. Introducing focused or guided (via an optical fiber) laser radiation into the ion-exchanged region produces a guided beam in this high refractive-index region.



Redirection of the optical or infrared beam from one waveguide to another may be accomplished by introducing an optically active material into the glass composition. In this case, cadmium telluride (CdTe) is added to the glass batch. Upon quenching, the CdTe crystallizes within the bulk of the glass. CdTe is a semiconductor with a band gap of about 1.60 electron-volts (eV) in bulk form. Depending on the size of the crystallites in the glass and the ambient temperature, CdTe undergoes a slight change in refractive index at a particular threshold intensity of the incident light within a waveguided region. It is postulated that an exciton energy level within the band gap becomes saturated and causes a change in the third-order electric susceptibility, thus causing the refractive index change. This process causes localized defocusing of the guided beam. The beam is redirected out of the guided area and into an identical waveguide running parallel to the original channel. Enough intensity is lost in the transition to eliminate the saturation process and keep the beam in the second waveguide, or switching continues to occur until the intensity goes below this threshold level.

Specifically, a high Na₂O-content CdTe borosilicate glass (17-percent Na₂O, 0.5-percent CdTe, by weight) is ion exchanged by replacement of sodium ions with potassium or silver ions at the surface. A photolithographic technique may be applied to cause ion exchange only in well-defined regions, or channels, or the technique may be expanded to cause ion exchange on the whole surface to measure the bulk surface properties. Ion exchange is performed via a vacuum-deposition or salt-bath technique using pure metal (Ag) or salt (KNO₃ or AgNO₃) precursors.

Initial characterization and testing include determination of the glass transformation and subsequent CdTe crystallization and growth temperatures of the as-received substrate glass, and ultraviolet-visible-infrared transmission/absorption spectra for the as-received and ion-exchanged substrate.

Detailed characterization will include ion-exchange depth profiling for determination of the optical ion exchange process, microstructure characterization (CdTe crystallite size and morphology) and nonlinear optical property characterization of the substrate glass. The microstructure and nonlinear optical measurements will be carried out in a cooperative effort with the Optical Characterization Laboratory of the Materials Science and Engineering Department at the University of Florida.

Ultimately, single-mode and multiple-mode waveguides will be produced with a controlled-depth profile. Subpicosecond switching speeds may be achieved within the parallel, multilevel architecture inherent to the planar ion-exchange process.

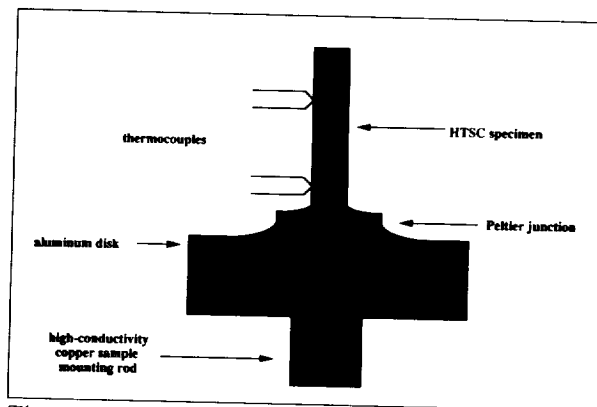
Contact: Stephen J. Pagano (Code 313)
(301) 286-8970

Sponsor: Office of Flight Assurance

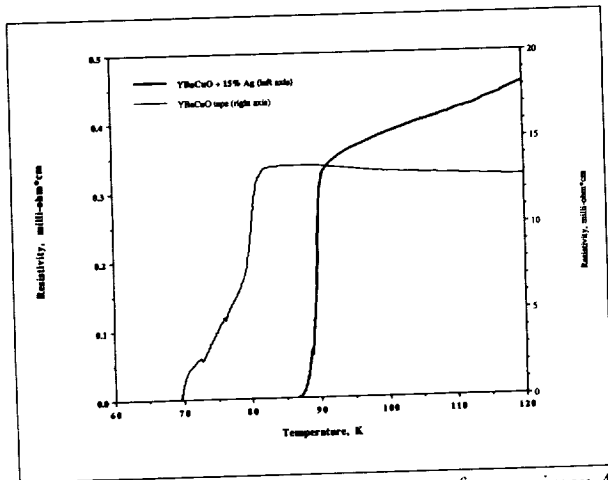
Mr. Stephen J. Pagano works as a materials engineer in the Materials Branch. He earned a BS in ceramic engineering from Alfred University and is pursuing an MS in materials engineering from the University of Florida. Mr. Pagano specializes in the science and technology of glass systems.

CRYOGENIC CHARACTERIZATION OF HIGH-TEMPERATURE SUPERCONDUCTING (HTSC) CURRENT LEADS

A program has been initiated in the Materials Branch to develop methods for characterizing candidate HTSC material for possible spaceflight use. Part of this program has been directed at measuring various physical quantities of HTSC electrical current leads that may be used with cryogenic instruments and detectors. Presently, those current leads are between 0.1 and 0.2 cm in diameter. The advantages of using current leads constructed from HTSC material over conventional current leads are high electrical conductivity and lower thermal conductivity. Higher electrical conductivity allows for



Thermal diffusivity/conductivity experimental set-up for cryogenic characterization of HTSC current leads.



Electrical resistivity versus temperature for specimen A and specimen B.

better grounding of instruments and detectors and increases resolution by reducing electrical noise. The lower thermal conductivity may increase mission life by decreasing coolant boil-off due to heat losses through the current leads.

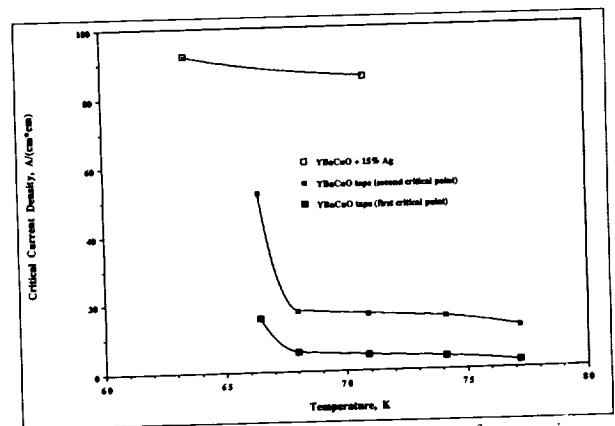
A new test facility, built around a cryostat, is used to measure the electrical resistivity, critical current density, thermal diffusivity, and thermal conductivity of HTSC specimens. A simple, four-point contact technique is used for both the electrical resistivity and critical current density measurements. As shown in the first figure, the thermal conductivity and thermal diffusivity are measured using an implementation of Angstrom's temperature-wave method. A heater is attached to one end of a specimen rod to send a periodic heat wave down the rod. Two thermometers are mounted along the specimen to follow the wave. The phase difference between the temperature oscillations at the two thermometers and the ratio of the amplitudes of these oscillations are used to calculate thermal diffusivity. By calibrating the heater (a Peltier junction) to determine the amplitude of the heat wave, the thermal diffusivity measurements can be converted to thermal conductivity.

At present, two types of $YBa_2Cu_3O_{7-x}$ HTSC material have been tested: rods with a circular cross-section made from $YBa_2Cu_3O_{7-x}$ and 15-percent (by weight) Ag (specimen A), and rods with a rectangular cross-section made from a tape of $YBa_2Cu_3O_{7-x}$ (specimen B). Currently, a survey of available HTSC current lead material is being performed.

Electrical resistivity measurements indicated that specimen A has a higher critical temperature (and a narrower transition region) than specimen B. Also, specimen A showed a much lower electrical resistivity above the critical temperature than did specimen B. According to the data plotted in the third figure, specimen A has a higher critical current density than does specimen B. Specimen B displays two critical current densities; the first critical point partially destroys the superconducting state in the specimen, and the second point completely destroys it. These two critical points can be attributed to a two-phase composition in specimen B.

Since the electrical resistivity of both specimens approaches zero below 77 K (the expected upper operating temperature for current lead applications), either specimen would perform better as an electrical conductor than copper or manganin, which are currently used as lead materials. Specimen A would be a more favorable material for current lead applications than specimen B because its transition temperature is well above 77 K and because it has a higher critical current density.

Thermal diffusivity measurements for the two specimens show that specimen B has a diffusivity that is about half the value for specimen A. This behavior correlates well with the density values in that specimen A is about twice as dense as specimen B. Thermal conductivity values for specimen A also are higher than those of specimen B. The thermal conductivity of specimen B displays typical behavior (reported by others) with respect to temperature for $YBa_2Cu_3O_{7-x}$.



Critical current density versus temperature for specimens A and B.



while the thermal conductivity of specimen A increases rapidly with temperature due to the presence of silver.

The thermal conductivity of both specimens is several orders of magnitude lower than copper, and lower than manganin as well. The thermal conductivity of specimen A was only slightly less than that of manganin, while the thermal conductivity of specimen B was about half that of manganin.

The technique used to determine the thermal conductivity of the two specimens was tested by measuring the thermal properties of a material with known values (fused silica). Fused silica was chosen since it has a low thermal conductivity value, similar to that of HTSC materials. The calculated thermal conductivity value

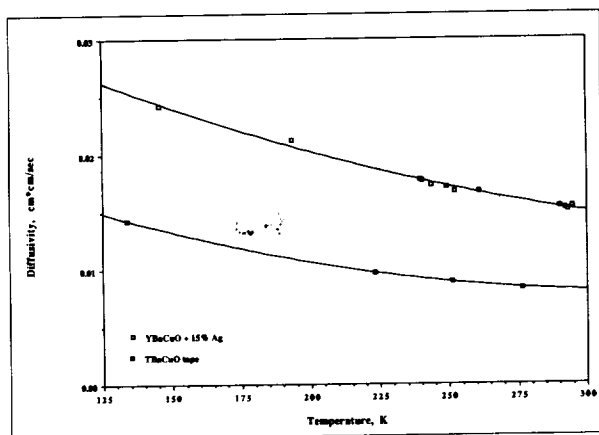
was in good agreement with literature values, illustrating that the technique can be used to measure thermal properties of HTSC specimens.

The cryogenic facility can characterize HTSC specimens effectively for electrical and thermal properties. The results of our preliminary characterization of two HTSC specimens demonstrates that HTSC materials have the potential to increase the performance of future cryogenic instruments and detectors.

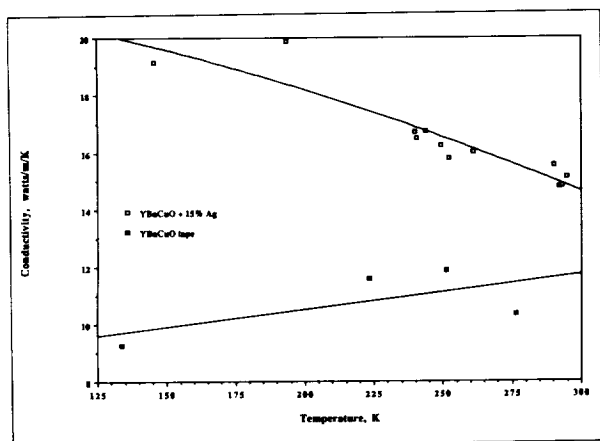
Contact: Charles E. Powers (Code 313)
(301) 286-8061

Gloria Oh (Code 313)
(301) 286-8598

Sponsor: Office of Flight Assurance



Thermal diffusivity versus temperature for specimens A and B.



Thermal conductivity versus temperature for specimens A and B.

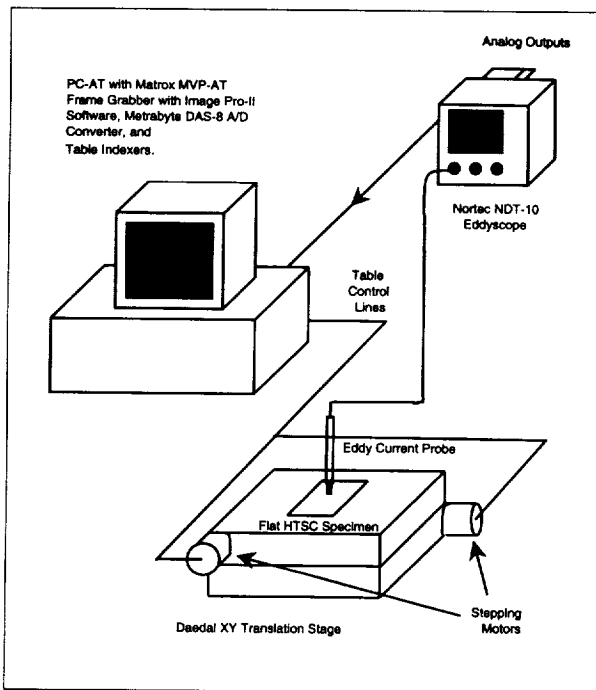
Mr. Charles E. Powers works in the Materials Branch by providing support in materials testing. During his 7 years at Goddard, he has been active in the use of computers for the automatic control and monitoring of experiments, as well as in data reduction. He holds a BS in engineering from Widener University and an MS in physics from American University.

Ms. Gloria Oh received her BS in materials engineering from Rensselaer Polytechnic Institute. She recently joined the Materials Branch, where she is involved in the characterization of ceramic and composite materials.

AN INSTRUMENT FOR SPATIAL CONDUCTIVITY MEASUREMENTS OF HIGH- T_c SUPERCONDUCTING (HTSC) MATERIALS

HTSC materials have been suggested for use in a number of space applications such as infrared bolometers and electromagnetic shielding. As part of its flight assurance role, the Materials Branch has developed an instrument capable of measuring variations in conductivity for flat samples using an eddy-current testing device and an X-Y positioning table. This instrument has been used to examine bulk HTSC samples. System improvements that would enable characterization of thin-film materials have been outlined.

Soon after the development of $YBa_2Cu_3O_{7-x}$ HTSC materials, it was discovered that for samples of identical



Schematic drawing of the eddy current testing system.

geometry, room-temperature conductivity correlated well with superconductive performance at cryogenic temperatures. Use of this method to do room-temperature screening of HTSC samples has been discussed by others.

By adding the combination of precise motion control and automated data acquisition to the eddyscope, a conductivity mapper has been developed. This instrument provides information in the form of an image about the spatial variation in conductivity in flat samples at room temperature.

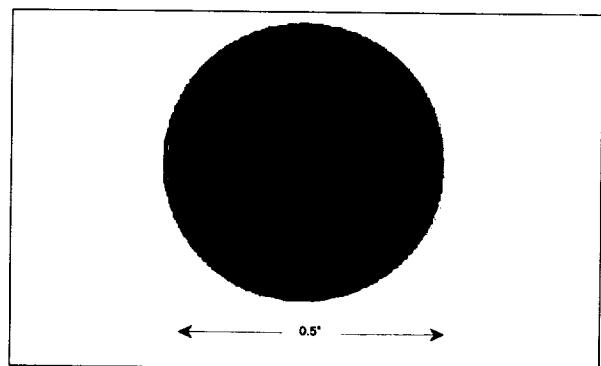
The eddy-current testing system is shown in the first figure. A conventional eddyscope is used to generate eddy currents in the HTSC samples. This instrument generates an alternating current in a coil placed over a flat specimen, thereby creating a changing magnetic field. This changing magnetic field in turn creates an electric field, and a current flows in response. This current creates a magnetic field which bucks that of the probe. An impedance bridge internal to the eddyscope attempts to balance the impedance of a reference coil and the coupled probe and sample. The eddyscope displays the measured response in two dimensions corresponding to the real and imaginary components of the effect of the specimen impedance.

Probe widths used in this test varied from 0.050 to 0.125 in; driving frequencies ranged from 100 kHz to 6 MHz. The depth of penetration of the field is inversely related to the conductivity of the sample and to the driving frequency of the coil. Assuming a conductivity of 200 siemens/cm (typical for $\text{YBa}_2\text{Cu}_3\text{O}_{7-x}$), penetration depths could vary from about 1 cm at 100 kHz to about 1.5 mm at 6 MHz.

A scan is accomplished as follows. A flat specimen is positioned on a PC-controlled, X-Y table. Command of the table is accomplished with software via subroutine calls from a Basic program. The scanning control software executes a raster scan (unidirectional scans with a nonsampling retrace) of a rectangular area with the range of travel determined at the beginning of the run. Digitization of the two eddyscope data channels is done with a 12-bit converter board which resides in the PC. Control of digitization is managed from within the same Basic program which controls table motion. Scanning dimensions and the distances between columns and rows in the resulting image can be selected prior to scanning. The software automatically computes the required sampling rate for the converter board and synchronizes data taking so that the resulting image is registered correctly.

Following the run, display of the conductivity map is done with a PC-based imaging system using a microcomputer imaging software package. This hardware is capable of displaying 512-bit by 480-bit by 8-bit images, but typical image sizes range from 100 to 200 pixels on a side.

After proper registration of the data was established, scans were done on bulk $\text{YBa}_2\text{Cu}_3\text{O}_{7-x}$ material produced in-house. These were disk-shaped specimens 12.7 mm in diameter and 2 mm thick. The second figure



Photograph of an HTSC disk with a crack in its surface.

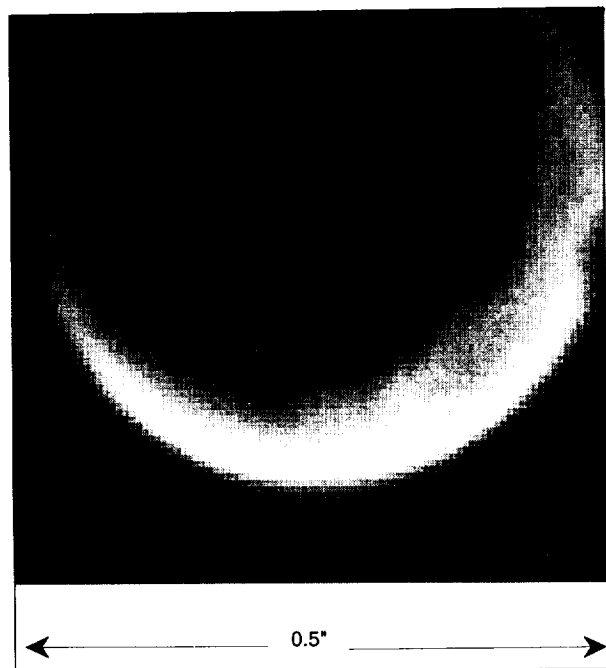


Image of HTSC disk produced by the eddy current system. The crack can be seen in the lower right-hand corner running from 3 to 5 o'clock. There also is a slight irregularity in the disk edge to the right of the crack; this corresponds to a small notch in the specimen.

shows a photograph of an HTSC disk with a crack in its surface. The third figure is the resulting image from the eddy current system. The crack can be seen in the lower right-hand corner.

Contact: J. Timothy Van Zant (Code 313)
(301) 286-6024

Sponsor: Office of Flight Assurance

Mr. Timothy Van Zant has been involved in image processing and the instrumentation of materials testing since coming to the Materials Branch in 1985. Mr. Van Zant recently received an MS in electrical engineering from The Johns Hopkins University.

DETERMINATION OF FIBER VOLUME IN GRAPHITE EPOXY MATERIALS USING COMPUTER IMAGE ANALYSIS

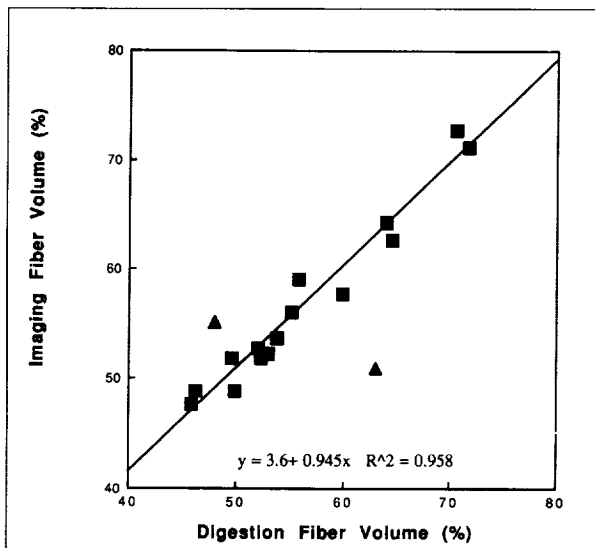
The determination of fiber content in graphite epoxy materials is required to predict accurately the mechanical properties and the thermal expansion of structural

members. Acid digestion is used traditionally to determine fiber volume. This technique requires that the cured graphite/epoxy material first be dissolved in boiling nitric acid and then washed in acetone. The environmental impact of the acid-digestion technique is twofold: the fumes generated during digestion may not be captured completely in the condenser, and the acid-digestion technique produces more than 200 mL of waste chemicals for each gram of specimen.

Optical examination is an alternative way to evaluate the fiber volume. Test specimens are cross-sectioned and polished, then analyzed using an optical microscope. The limitation of the optical technique has been that the imaging programs were available only on large computers or that the laboratory techniques available were tedious and required extensive operator interaction. Recent improvements in both personal computers and imaging software and hardware have made the use of imaging techniques a viable alternative to acid digestion.

The test specimens used in this study were acquired from various ongoing, in-house projects. All of the material evaluated was taken from panels manufactured using unidirectional prepreg material. The variety of prepreg specimens acquired enabled the evaluation of fiber volumes ranging from 45 to 70 percent. While the acid digestions reported here were performed by various individuals, all of the digestions were performed according to the American Society for Testing and Materials (ASTM) standard D3171. Specimens examined optically were taken from areas directly adjacent to those of the acid-digestion specimens. The size of the optical specimens was generally on the order of the acid-digestion specimens. The area of the cross sections examined varied from 12 to 24 mm². The optical specimens were mounted in self-curing epoxy and subsequently polished to reveal the graphite fibers.

The image analysis was performed with an imaging program titled "NIH Image." This software is public-domain shareware created at the National Institutes of Health. The program was run on an Apple Macintosh IIx computer. The images were acquired directly from a microscope via a video camera and a frame-grabber image-acquisition board. All images acquired in this study were taken at 1,000 times magnification. Preliminary studies revealed that the fiber edges could be resolved only at the greatest available magnification.



Fiber volume determined using the optical technique plotted versus fiber volume determined using the acid digestion technique.

Four basic tasks were performed to determine fiber volume. First, the subject area was selected and brought into focus. The image was then captured and corrected for variations in the light intensity using a blank-field image. The blank-field correction also was a background correction that removed artifacts on the image created by dust on the optical lens. Then, the fiber and resin areas were partitioned using a threshold operation. The thresholding operation changed the fiber area to black and the resin to white. Finally, the number of black and white pixels was measured. The ratio of black pixels to the total number of pixels in the interrogated area was the percentage of fiber area.

The fundamental assumption made is that the fiber-area percent is equal to the fiber-volume percent. The adoption of this assumption is not intended to imply that the fiber volume of the entire panel can be determined by the evaluation of a two-dimensional slice through a small portion of the panel. What the assumption does imply is that the percentage of fiber area is a good approximation of the percentage of fiber volume in the vicinity of the cross section. The information gained at the cross section must be correlated to some other physical condition of the panel. This other physical condition might be thickness or ultrasonic impedance. It should be noted that the acid-digestion technique requires a similar assumption. The acid-digestion technique evaluates only a small portion of the entire panel.

The figure shows the fiber volume determined using the optical technique plotted versus that found using the acid-digestion technique. The results were found to be in good agreement. The poor correlation of two specimens is attributable to large variations in the fiber volume of the panel from which they were taken.

This test program has shown that the percentage of fiber volume of graphite epoxy laminates can be estimated using imaging techniques. The image-analysis technique also provides an indication of the fiber distribution on a microscopic scale.

Contact: Michael J. Viens (Code 313)
(301) 286-2049

Sponsor: Office of Flight Assurance

Mr. Michael J. Viens of the Materials Branch has an MS in mechanical engineering and has worked at Goddard for 4 years. Mr. Viens conducts mechanical testing of ceramic, metallic, and polymeric materials and evaluates test results. He also is involved in nondestructive evaluation of materials and optical emission spectroscopy.

FLIGHT TELEROBOTIC SERVICER (FTS) EVOLUTION

Goddard engineers working on the Flight Telerobotic Servicer (FTS) project have a manipulator development test scheduled for flight in 1993. Over time, a planned evolution of the FTS capabilities could lead to appropriately configured elements of the FTS being used for robotic manipulation in remote satellite servicing applications, as well as in the Space Station Freedom and Lunar/Mars programs.

The current state of space technology and the general nature of FTS tasks dictate that the FTS be designed with sophisticated teleoperational capabilities for its initial primary operating mode. However, emerging technologies such as advanced computer vision and autonomous planning techniques would improve the ability of the FTS to perform autonomously in less structured work environments. Therefore, the Goddard telerobotics program covers research and development of space hardware concepts that are "robot friendly."

The FTS flight system consists of the telerobot, two workstations—one for the Shuttle orbiter and one for



Space Station Freedom—and a facility for on-orbit storage, called the Storage Accommodation Equipment.

The telerobot has two 7-degree-of-freedom manipulators and an attachment, stabilization, and positioning subsystem mounted on a compact body. The body contains internal electronic boxes that provide the power, data management, and data-processing functions. The boxes are designed as orbital replaceable units that can be replaced by an astronaut on extravehicular activity or by another telerobot. Also mounted on the body are a camera-positioning assembly with two head cameras, and holsters for storing tools and end effectors. On each manipulator wrist actuator is mounted a camera for close-up viewing. At the end of the wrist-roll actuator is a force-torque sensor for measuring forces and torques produced at the tool plate. Attached to the force-torque sensor is the end effector changeout mechanism, which will accommodate a variety of tools and end effectors.

The workstations will provide the operator with similar interfaces, including color video displays, text and graphic overlay capability, and two 6-degree-of-freedom force-reflecting hand controllers for teleoperation of the FTS manipulators. During operation, a sequence of events is displayed which the operator will use as a checklist. As commands are issued, displays provide status information and command menus. Anomalous events result in automatic caution and warning displays to the operator, along with fault diagnostics and recommended corrective actions.

A manipulator development test flight (DTF-1) precedes the deployment of the initial operational FTS system at first element launch in 1995. DTF-1, scheduled for launch in 1993, will validate the performance of the FTS manipulator design in a zero-gravity environment. Data obtained also will be used to evaluate human-machine interfaces, assess servicing interfaces with work elements, and establish the correlation between simulation and analysis results and flight performance data.

Engineering and integrating the different telerobotic technologies into an operational system that combines teleoperation and autonomy and that meets stringent performance requirements is the challenge of the FTS project. The following paragraphs summarize the major elements of these technologies.

The FTS manipulator comprises harmonic-drive actuators with brushless DC torque motors commutated by Hall effects sensors. The transmissions have 100-to-1 speed reduction and incorporate fail-safe brakes for safety purposes. A force-torque sensor attached to the manipulator tool plate measures the forces and torques exerted at the worksite and provides feedback to a force-reflecting hand controller at the workstation. It also allows the telerobot to control the forces and torques generated by the manipulator using a position-based impedance-control algorithm. This compliance-control system allows the manipulators to compensate automatically for misalignments. The operator may select position or resolved-rate control, or in special situations, single-joint control. Coordinated dual-arm control will be useful in handling large components on Space Station Freedom.

Three microprocessors are embedded in the manipulator links to control the seven joints and the end effector. Flat conductor cables carry hundreds of electrical signals through the actuators and back to the central processor in the telerobot body where the bus controller routes the commands and signals between the workstation and the telerobot. Several types of signals, including a MIL-STD-1553 data bus and the video channel from the wrist camera mounted to the wrist-roll actuator, are passed through the actuators.

The Standard Reference Model control system architecture, which has been selected for FTS, allows teleoperation and autonomous operations. Its architecture is a three-legged hierarchy of computing modules. The first leg plans and executes the decomposition of high-level goals into low-level actions. The second leg remembers, estimates, predicts, and evaluates the state of the world surrounding the telerobot. The third leg recognizes patterns, detects events, and filters and integrates sensory information. The sensory system compares the world model predictions with observations. Each level in the hierarchy has a specific function, and each receives commands from the next higher level. The first four levels of the Standard Reference Model control system will be implemented in the FTS system. Level 4 decomposes the servicing tasks into sequences of movements. Level 3, the elementary move level, plans all aspects of the manipulation. The primitive level, or Level 2, generates the time sequence of desired state vectors to produce dynamic trajectories. The servo level, or Level 1, contains the servo control loops.

Flight software, coded in Ada, interprets the operator inputs and controls the telerobot's motion, monitors health and status, and ensures the safety of the FTS. The primary control loop operates at 50 Hz, which means that all the control computations and the data transfer from the hand controllers to the manipulators back to the hand controllers must be accomplished in 20 milliseconds, including data transmission delays.

In the unstructured working environment of the FTS, current technology dictates that the FTS operational mode be primarily teleoperational. However, new technologies such as artificial intelligence planning and advanced computer vision are evolving from the research phase and could enhance significantly FTS capabilities to perform tasks autonomously in space. Therefore, the capability to evolve is designed into the FTS. In the meantime, it must use the operator for those tasks for which the human is better suited, such as vision processing and manipulator path planning.

Among the growth features being considered for controls are dual manipulator-coordinated motion, control with time delay (ground control), and increased loop speed and control bandwidth.

The operator's interaction with the FTS will be from either the Space Shuttle or the Space Station workstation where two 6-degree-of-freedom, force-reflecting hand controllers allow the operator to feel the forces and torques being generated at the tool plate of the manipulators. Color video monitors display the images from the two head cameras and the two wrist cameras. Data displays provide system status, task scripts, caution and warning signals, and fault-diagnostic information.

Evolution being considered for the operator interface includes enhancements such as stereo vision; graphics overlays, such as a shaded image of the telerobot superimposed on a computer-assisted design view of the worksite; enhanced displays of sensor data; monitoring of the activity stream at all control system levels; voice recognition; and simulation of command sequences.

Operating in the manned space environment has made safety the primary concern in the development of the FTS. Two-fault-tolerant design is used for Criticality-1 functions that could cause injury to the crew or damage to the

Shuttle orbiter or the Space Station. An independent watchdog computer monitors the telerobot systems and issues warnings or initiates system shutdown. Collision-avoidance techniques using geometric models prevent the telerobot from inadvertent contact with itself or with the environment.

The FTS provides a common interface, called the End Effector Changeout Mechanism (EECM), for all tools and end effectors so that they can be changed out autonomously on orbit. The EECM provides power, data, and video connections to the end effector or tool. The telerobot MIL-STD-1553 data bus is provided at the EECM so that future smart end effectors can communicate with the telerobot control computers.

Contact: James F. Andary (Code 409)
(301) 286-4850

Sponsor: FTS Project

Mr. James F. Andary, an engineer at Goddard for 23 years, works in the Flight Projects Directorate. He has served as a guidance and control engineer on numerous projects, including the International Ultraviolet Explorer, the Cosmic Background Explorer, and the Solar Maximum Mission. He holds a BS in mathematics from Boston College and an MS in mathematics from the University of Maryland. In 1990, he received the NASA Exceptional Service Medal.

THE GODDARD ENERGY BALANCE PROGRAM: DIRECT ENERGY TRANSFER (DET) AND MODULAR POWER SUBSYSTEM (MPS)

Two computer programs that simulate commonly used power systems for spacecraft have been tested successfully and have been submitted to NASA's distribution center for software, COSMIC.

Solar arrays are the primary electrical power source for spacecraft. Depending on the power requirements, load conditions, and intended orbit of a flight project, engineers mainly select one of two power systems, Direct Energy Transfer (DET) or Modular Power Subsystem (MPS). These power systems differ in their ability to work optimally with different size arrays, different sizes and numbers of batteries, and different flight conditions.



The DET and MPS software allow engineers to compare the two power systems under different sunlight conditions, orbital positions, operating conditions, and load conditions—and then select the optimal system for their spacecraft.

The software also provides engineers with more flexibility in designing new spacecraft and can be a valuable tool in evaluating and analyzing power system performance.

Flight projects that use either the MPS or DET power systems include: the Upper Atmospheric Research Satellite, scheduled to fly in late 1991 with an MPS system; the Small Explorer Spacecraft, now in the manufacturing phase, which will use a DET system; and various National Oceanic and Atmospheric Administration spacecraft, also powered by DET.

The computer programs that model these systems have evolved during the last 4 years. In 1990, codes were cleaned up and the final software was submitted for approval. These programs, requested by many private companies, have been ported to, and run under, VAX/VMS (using VAX Fortran) and A/UX 1.1/2.0 (using NKR Fortran).

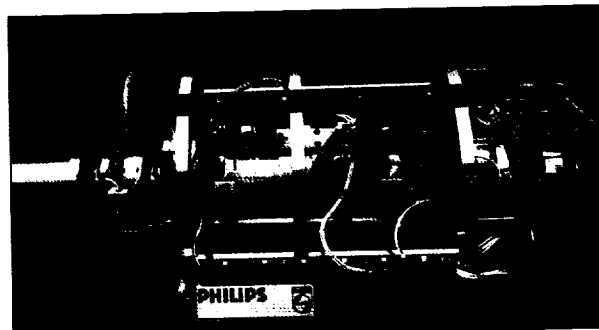
Contact: James M. Jagielski (Code 711)
(301) 286-5964

Sponsor: Various flight projects

Mr. James M. Jagielski, an electrical power system engineer with 8 years of experience at Goddard in the Space Power Applications Branch, holds a BSEE from The Johns Hopkins University. Mr. Jagielski is involved with a variety of flight projects and is considered Code 711's expert in modeling and simulation techniques of spacecraft power systems.

PERFORMANCE OF A PROTOTYPE, 5-YEAR-LIFETIME, STIRLING CYCLE REFRIGERATOR FOR SPACE APPLICATIONS

A second-generation linear Stirling cycle refrigerator for space applications, with cooling capacity of 5 W at 65 K, recently was developed. The refrigerator, designed to last 3 to 5 years, uses closed-loop controlled, moving-magnet, linear motors for the compressor and the



Prototype of the Stirling cycle refrigerator for space applications. The refrigerator was developed to have a 5-year lifetime.

Prototype Refrigerator		
Characteristics		
	Specified	Actual
Cold end temperature-5 watt load	65 K	65 K
Operating power (refrigerator only)	250 watts	140 watts
Standby power (refrigerator only)	50 watts	4.6 watts
Time to reach stable operation	5 hours	25 minutes
Ambient temperature range	5-35 °C	TBD
Radial movement of cold end (operating) - inches	10 ⁻⁵	1.4 × 10 ⁻⁴ p-p
Axial movement of cold end (operating) - inches	10 ⁻³	1.3 × 10 ⁻³ p-p
Axial movement of cold end-ambient to operating	none	TBD
24-hour cold end temperature variation	0.1 K	TBD
Weight (refrigerator only)	200 lb	185.3 lb

expander. The moving elements are contactless, being supported by active magnetic bearings with a clearance seal of 20 microns. Fiberoptic sensors are used to detect the radial position of the shafts and provide a control signal for the magnetic bearings.

The frequency, phase, and stroke of the compressor and expander are controlled by signals from precision linear variable displacement transducers (LVDTs). The vibration generated by the compressor and expander is cancelled by an active counterbalance which also uses a moving-magnet linear motor and magnetic bearings. The driving signal for the counterbalance is derived from the compressor and expander LVDTs. The efficiency of the three active members is enhanced by the use of a magnetic spring in the expander and gas springs in the compressor and counterbalance. The magnetic bearing stiffness was increased significantly from the first-generation refrigerator to accommodate Shuttle launch vibrations.

Test results are shown in the table and figure.

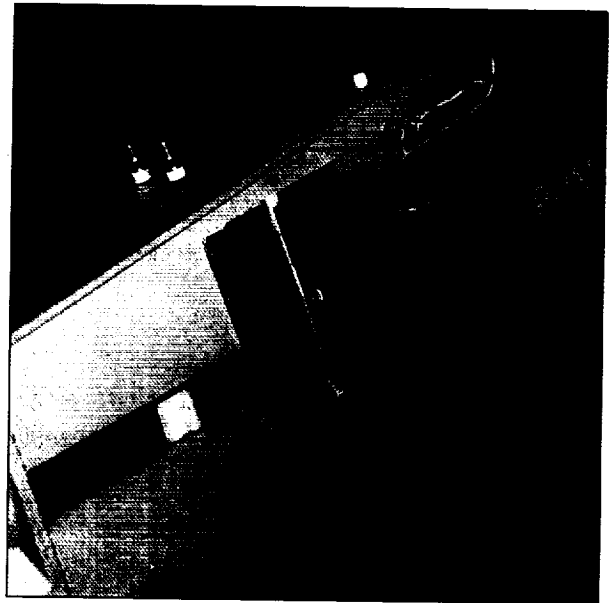
Contact: Max G. Gasser (Code 713)
(301) 286-8378

Sponsor: Office of Aeronautics and Exploration
Technology

Mr. Max G. Gasser is an aerospace engineer with 25 years of experience at Goddard. Mr. Gasser, who received his BS in chemical engineering from Virginia Polytechnic Institute, is involved with cryogenic cooler technology research and development for space applications. He received the IR-100 Award in 1983 and holds a patent on the Stirling cycle cryogenic cooler.

"CAPACIFLECTOR" COLLISION-AVOIDANCE SENSORS FOR ROBOTS

Researchers at Goddard have been developing a collision-avoidance management skin for robot arms in space using capacitance. However, a capacitive system must be very sensitive to detect the presence of objects (such as a human) at ranges sufficient for the robot to react (1 ft). To obtain such a range, the sensor typically must be "stood off" from the grounded robot arm a considerable distance (approximately 1 in). This would disfigure the robot arm, causing it to be 2 in wider and



A single-element sensor used by a robot in the lab. This capaciflector sensor could routinely detect a human or an aluminum-truss element within 1 ft of the robot. Graphite lead in a pencil was detected as close to the robot as 5 in.

thicker than necessary. It also would make cross talk between the sensor elements more pronounced and would impede the flow of heat from the robot arms to outer space (a serious problem for the FTS). The "Capaciflector," or capacitive reflector, solves these problems and, in so doing, advances the state of the art in capacitive sensor performance an order of magnitude.

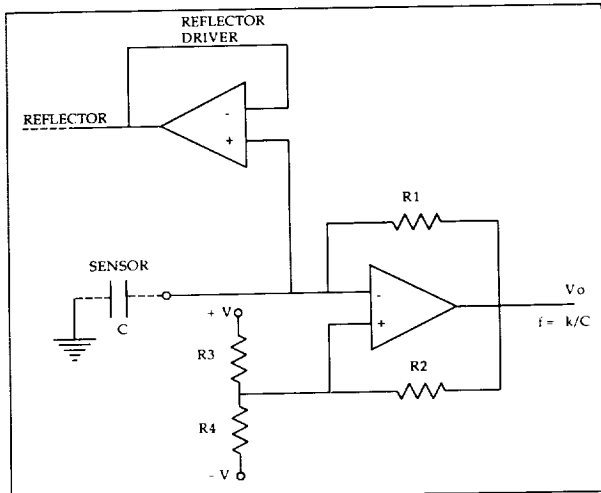
The first figure shows a single-element sensor which has been demonstrated on a robot in the Goddard lab. In this demonstration, the robot routinely detected a human or an aluminum-truss element within 1 ft of the robot, and the graphite lead in a pencil typically has been detected at ranges of 5 in.

The second figure shows the principles of operation in terms of charges and electric fields. This figure also shows a capacitive sensor not using the capaciflector principle. Since our demonstration used relatively low frequencies (approximately 20 kHz), static charges and electric field analysis could be used to determine the capacitance the sensor detected. We learned that the smaller the stand-off from the grounded robot arm, the larger the capacitive coupling between the sensor and ground. This, of course, has the effect of reducing the relative coupling between



the sensor and the object being sensed, thereby reducing sensor range and sensitivity. On the other hand, increasing the stand-off increases the bulk of the robot arm and adds wires and wiring complications. When the insulation materials are added to support the stand-off, the ability of the robot arm to dissipate thermal energy into space is reduced. When the capaciflector principle is used, the effective stand-off is approximately the width of the active shield or capacitive reflector. Thus, we can have a skin with very little thickness (on the order of 0.060 in) and a robot arm with very little bulk and still have the performance of a large stand-off.

The third figure shows the electronic circuitry involved. The capacitive coupling between the sensor and the object being sensed creates the input capacitance to tune the oscillator frequency. As an object comes closer, the capacitance increases and the oscillator frequency changes. On the other hand, the reflector is attached to the output of the voltage follower so it is electrically isolated from affecting the



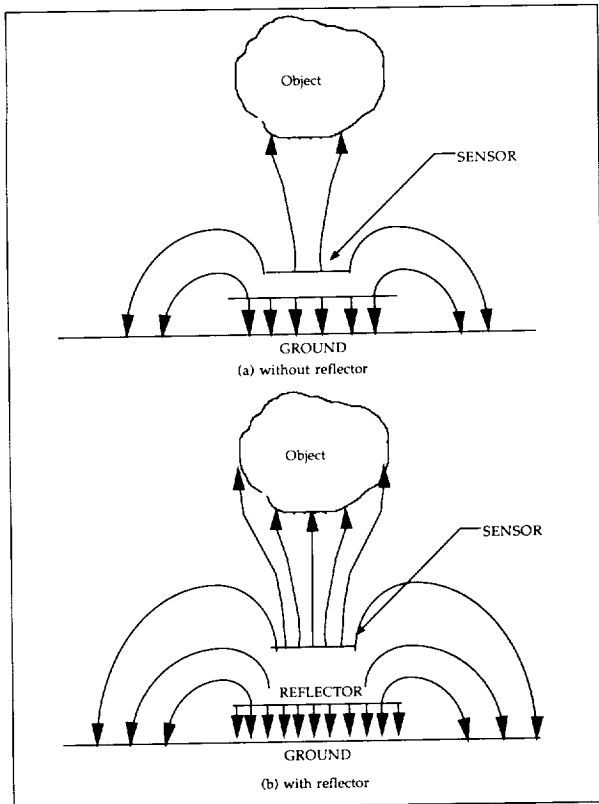
Capaciflector electronic circuitry.

tuning of the oscillator frequency. At the same time, the frequency of the reflector follows that of the oscillator. Thus, the reflector is in phase with (and reflects) the electric field of the sensor without being affected by the coupling between the sensor and an approaching object.

Contact: John M. Vranish (Code 714)
(301) 286-4031

Sponsor: Office of Space Flight

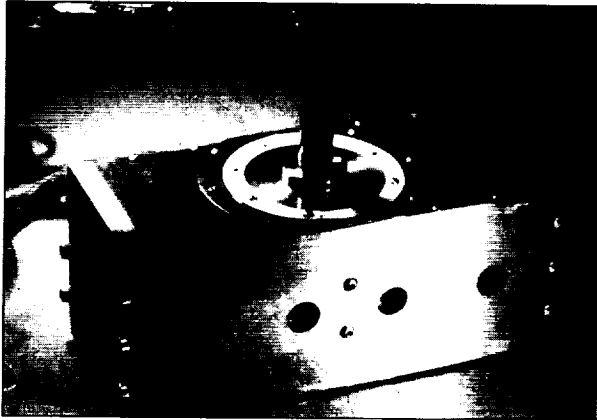
Mr. John M. Vranish, an aerospace engineer in the Electromechanical Branch, holds several patents on robotic electromechanical systems, mechanisms, and tactile proximity force sensors. His invention, the Robotic Derivator, was the top-rated Department of Defense robot innovation in fiscal year 1979. He received his MS in electrical engineering from George Washington University.



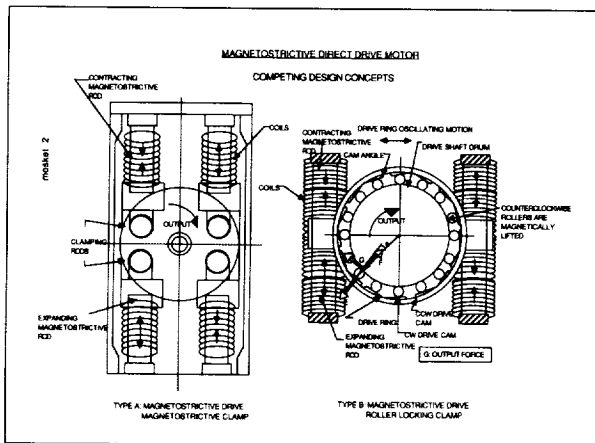
A demonstration of the difference between traditional capacitive sensors and the capaciflector.

MAGNETOSTRICTIVE DIRECT-DRIVE MOTORS

Goddard researchers are investigating the potential of a powerful new magnetostrictive material (Terfenol-D) as the basis for a direct-drive microstepping motor with torque densities comparable with industrial hydraulics and five times greater than those of the highest known performing electric motors. Such a motor would be a microradian stepper, capable of precision movements and self-braking (with the power



Photograph of magnetostrictive direct-drive motor developed using Terfenol-D, a powerful new material.

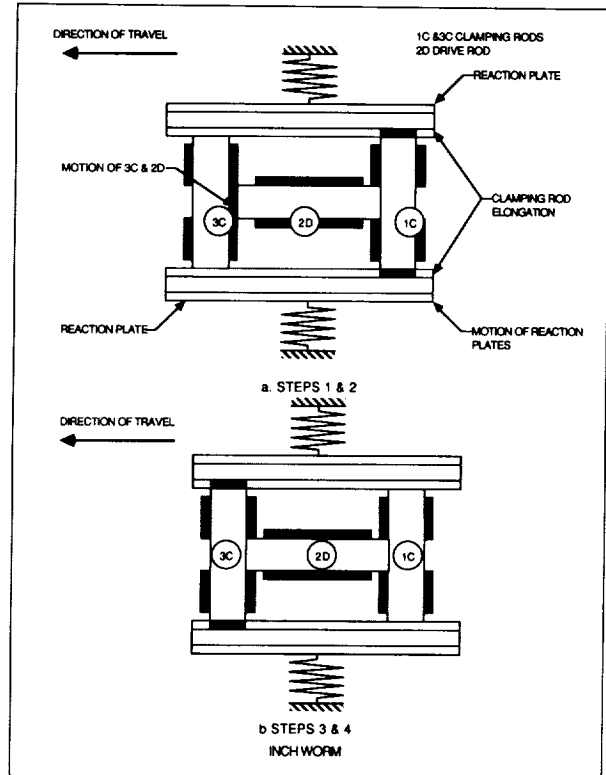


Competing design concepts for direct-drive motor prototypes.

off) so it would be safe and have a low duty cycle. Terfenol-D has impressive performance potential. It easily produces forces of 4 ksi with frequencies of 1 kHz and 0.0015 in/in travel in a magnetic field of 600 gauss.

The material is now a proven commodity in commercial production. What remains is the engineering and innovation required to turn the great potential of this material into a practical device. The immediate problem is to transmit the power and force of the short-stroke magnetostrictive-drive elements efficiently to the rotary shaft without excessive losses in structural flexures and frictional wear, and, in the meantime, to retain a lightweight, compact package.

Two competing motor prototypes are being developed and compared with each other. One prototype will be



Design for a magnetostrictive direct-drive motor based on the "inchworm technique."

based on the "inchworm technique" for linear motors, a classical and proven approach. Precision innovative mechanical and structural engineering techniques are being implemented to eliminate the parasitic flexures and clearances in previous actuators built on this principle. This will result in a practical rotary motor with the torque, speed, and precision that has not been achieved. The second, an even more promising prototype, will be based on the entirely new "roller locking principle."

The first prototype has been demonstrated to produce rotary motion. It has produced 1 ft-lbf of torque, an unprecedented number which will increase more than tenfold as follow-up devices are developed.

On the roller-locking prototype, as a pair of drive rods are actuated (to drive the device clockwise) the clockwise drive rollers will lock the drive drum and the output shaft together, producing a clockwise motion. (The counterclockwise rollers will be lifted away from the output shaft by a magnetic lifting system.) On the return stroke, the locking rollers will roll down the drive cam



back to the initial position while the drive shaft continues to rotate in a clockwise direction. The drive sequence then will repeat itself.

The roller-locking system shows several advantages over the first prototype. The magnetostrictive clamping rod system is eliminated. A magnetic lifting system is required for the drive cones, but it is much smaller and more compact than clamping rods. Also, pounding of the clamping rods is eliminated. Maximum torque is extracted from the rods because the system eliminates slip.

In addition, the use of multiple cams (the drive cones, the drive cams in the drive drum, and the output drive shaft) permits the drive rollers to act as if they are independently suspended. This permits the cones to adjust independently to wear and manufacturing anomalies while in use. This also lengthens motor life. Finally, cone roll-locking motion during the power stroke and no load-rolling motion during the return stroke minimizes the wear that does occur.

A system analysis is complete on the roller-locking motor. A detailed design and initial prototype is expected in fiscal year 1991. The two prototypes will then be tested against each other.

Contact: John M. Vranish (Code 714)
(301) 286-4031

Sponsor: Office of Aeronautics and Exploration
Technology

Mr. John M. Vranish, an aerospace engineer in the Electromechanical Branch, holds several patents on robotic electromechanical systems, mechanisms, and tactile proximity force sensors. His invention, the Robotic Derivator, was the top-rated Department of Defense robot innovation in fiscal year 1979. He received his MS in electrical engineering from George Washington University.

A NOVEL APPROACH TO ARRAY-DETECTOR TIMING GENERATION

Array detectors may require anywhere from six to 50 binary timing signals, or clocks, to move charge packets from the collection sites to the output. Dedicated instrumentation to generate the clocks is available, but it is not found commonly in electronics laboratories and

tends to be a prohibitively expensive acquisition. Timing generation has, in the past, been accomplished typically with logic or microprocessor circuits of one form or another. The implementation of timing modifications in such circuits can range from reprogramming a Programmable Read-Only Memory (PROM) to extensive wiring changes; verification typically requires the use of additional instrumentation outside the detector test fixture. Such procedures tend to be time-consuming and error-prone and, as such, make experimentation with clocking patterns in the laboratory an uninviting prospect. However, a novel technique for generating array-detector timing signals has been developed at Goddard's Detector Test Facility (DTF) which circumvents all such problems.

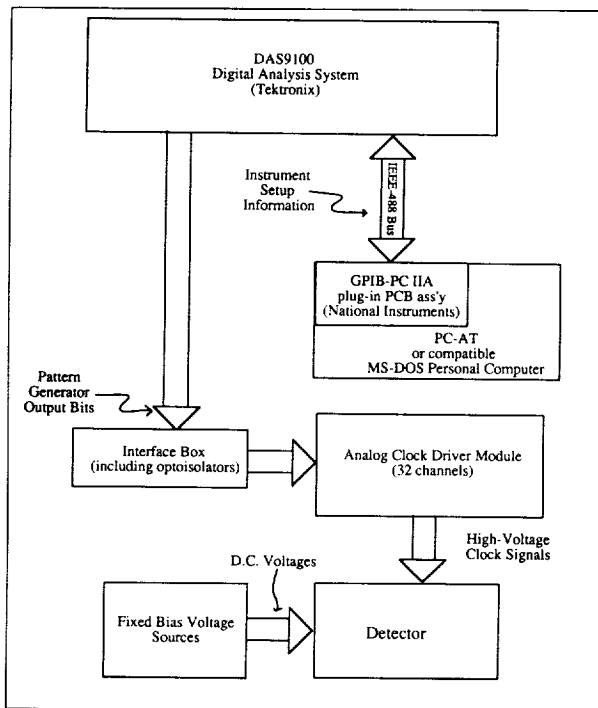
A Digital Analysis System (DAS), Tektronix model DAS9100, comprising a Pattern Generator section and an Acquisition section, is the heart of the DTF's experimental detector-drive system. The Pattern Generator simultaneously outputs a bit pattern and executes an instruction from its instruction set (NO-OP, GOTO, CALL, RETURN, REPEAT, HOLD, HALT). An algorithm thus may be created which executes the few basic detector clocking operations the correct number of times and in the correct order. After making assignments of Pattern Generator bits to the clock signals required to operate the detector, an algorithm is created and entered on the Pattern Generator screen.

The Pattern Generator output bits, in addition to being sent to a clock-driver module, are looped back into the Acquisition section of DAS9100 so that the timing patterns generated may be viewed in a graphic format for each verification.

The DAS9100 communicates with an IBM PC, model Advanced Technology (AT), over the IEEE-488 instrumentation bus, using a plug-in IEEE-488 interface card from National Instruments. Application software provided by Tektronix for this hardware configuration allows the user to store a complete description of the instrument state, including the Pattern Generator program, on the hard- or floppy-disk drives of the PC-AT in an MS-DOS compatible, compressed binary file format.

This technique has two outstanding advantages:

- It is software-based; therefore, timing patterns may be created, stored, and changed easily. This significantly reduces the lead time from the receipt of a new detector design to the start of evaluation



DTF experimental detector drive system.

procedures as compared to what is required for the design and construction of a hardware-timing generation circuit.

- It uses multipurpose equipment commonly found in electronics development laboratories—any logic analyzer with Pattern Generator and nonvolatile storage capabilities conceivably could be used to implement it. Instrumentation expenses therefore are reduced considerably relative to what would be encountered using dedicated timing-generation equipment.

This programmable timing technique has been used to evaluate a 2,048-by-2,048 pixel charge-coupled device (CCD) array detector manufactured by Ford Aerospace. We have taken advantage of the easy reprogrammability to experiment with various timing patterns, and the optimized timing determined from this experimentation has been implemented in a dedicated circuit. Currently we are generating, acquiring, and displaying images from the detector using this circuit. The technique also has been used to evaluate a frame transfer CCD array and several interline charge-coupled photodiode arrays, all of our own design, as well as various commercially available detectors. It has proven extremely useful in evaluating our detector designs

to be able to define several different frame-clocking sequences and combine them in various ways.

For the future, we intend to use programmable timing to accelerate the process of evaluation for other array detector designs as we receive them. The Pattern Generator section of the DAS9100 is capable of executing programs of up to 254 lines in length and may be configured for as many as 80 output bits. In addition, the Pattern Generator is capable of responding to external INTERRUPT, PAUSE, and INHIBIT commands, thus making the range of potential applications quite extensive. For example, the INTERRUPT command could be used to synchronize the Pattern Generator to an external exposure-timing circuit in a synchronized illumination application.

Contact: Jeffrey W. Travis (Code 724)
(301) 286-9479

Peter K. Shu (Code 724)
(301) 286-5191

Sponsor: Office of Space Science and Applications

Mr. Jeffrey W. Travis holds a BS in electrical engineering from the University of Michigan and is Head of the Detector Systems Section. He has served 3 years in the Science and Engineering Directorates at Goddard, most recently with the Detector Systems Section.

Mr. Peter K. Shu heads the Solid-State Device Development Branch of the Goddard Engineering Directorate. He directs the Detector Test Facility, where detectors are developed for various space-based scientific instruments.

THE DEVELOPMENT OF 50-MBIT/S TRANSMIT/RECEIVE ELECTRONIC COMPONENTS FOR OPTICAL COMMUNICATION SYSTEMS

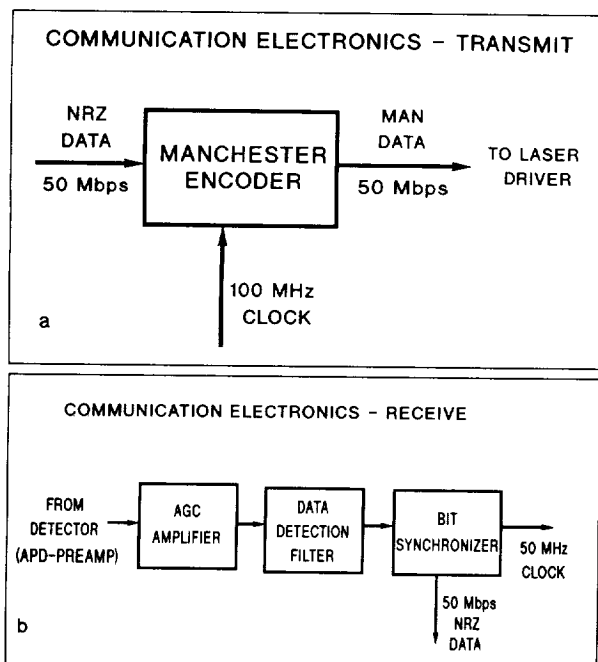
The purpose of this effort is to demonstrate an end-to-end optical communications system that will serve as a stepping stone for the LASERCOMM Flight System Development and Demonstration at 650 Mbit/s. The Communication Electronics Section of the Microwave Technology Branch has developed the communication electronics for the 50-Mbit/s LASERCOMM Brassboard Demonstration. All of the communication subsystem components have been designed, built, and tested. Manchester coding or binary pulse position modulation (BPPM), which inherently has a 50-percent duty cycle, has been selected as the signaling format because of the peak power (as opposed to



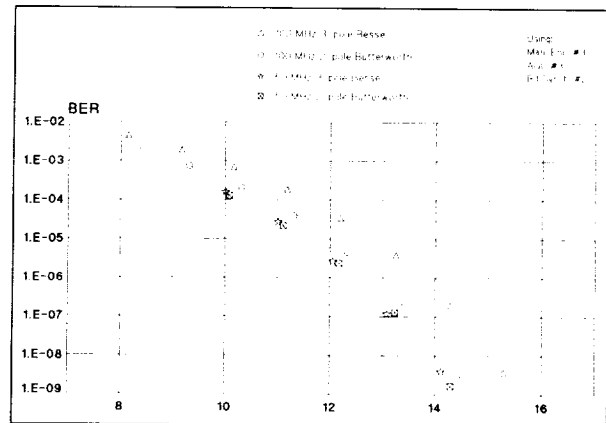
average power) limitation of laser drivers. The electronics use high-speed digital gallium arsenide (GaAs) and F100K Emitter Coupled Logic technologies.

As the first figure shows, the transmitter includes a Manchester encoder because the interface signal coding is nonreturn to zero (NRZ). The encoder must translate the incoming NRZ signal to BPPM. This is accomplished by loading the NRZ data and its complement into a shift register, and alternately shifting them out at twice the NRZ data rate (100 MHz).

The receiver consists of an automatic gain control (AGC) amplifier, a detection filter, and a bit synchronizer. Since the received optical-signal power levels are expected to vary dramatically, the AGC is necessary to provide the bit synchronizer with a constant power level. The AGC is a closed-loop feedback system in which a square-law detector converts a portion of the final signal into a voltage which is compared to a reference DC voltage. Any difference voltage is amplified and used to adjust the loss of voltage-controlled attenuators to maintain a constant signal level at the output of the AGC. The level of the constant signal output can be varied by the level-adjust potentiometer. All of the AGC components have a minimum bandwidth of 5 to 1,000 MHz, and a dynamic range of 40 dB has been achieved.



(a and b) The transmit and receive electronics for optical communications systems.



The bit-error ratio versus the signal-to-noise ratio for various data detection filters.

The data detection filter reduces the noise on the AGC output signal. It is a two-pole Butterworth or three-pole Bessel low-pass filter with a 50-MHz, 3-dB cutoff frequency.

The filtered BPPM signal then is decoded by the bit synchronizer. The bit synchronizer contains a clock and data-recovery circuit which receives the BPPM signal and extracts the clock by using a phase-locked loop. It also regenerates the BPPM data, which is then decoded into the corresponding NRZ data format by using a "maximum likelihood" detection scheme. The bit synchronizer also contains circuitry to resolve the potential 180°-phase ambiguity of the recovered clock.

Tests were performed to compare the decoded signal to the original NRZ data to determine the bit-error ratio (BER). The BER then was plotted as a function of the receiver's input signal-to-noise ratio. These results are shown in the second figure. The system recently has been integrated with electro-optics, and tests currently are being performed to measure the BER as a function of the extinction ratio of the laser.

Contact: John Maruschak (Code 727)
(301) 286-9886

Robert Patschke (Code 727)
(301) 286-6092

Michael Powers (Code 727)
(301) 286-4820

Catherine Long (Code 727)
(301) 286-8898

Mr. John Maruschak holds a BS in electrical engineering from the University of Detroit. Since coming to Goddard

in 1964, he has been involved in both the communications and instrument disciplines, including communications satellite experiments with the Applications Technology Satellite ATS-6 and the Communication Technology Satellite. Recently, Mr. Maruschak has been involved with the development and testing of microwave components and subsystems for the Differential Microwave Radiometer instruments aboard the Cosmic Background Explorer (COBE) satellite.

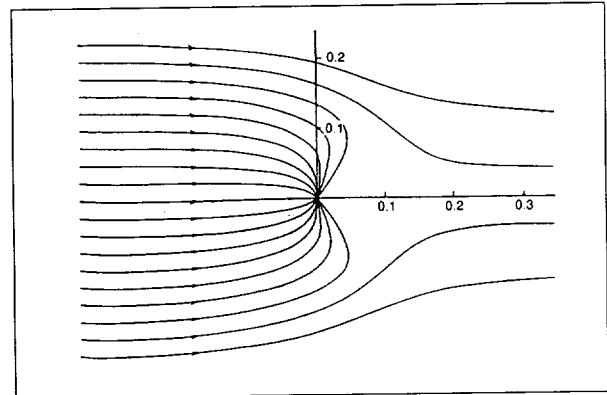
Mr. Robert Patschke is an electronics engineer with 6 years of experience at Goddard. He received a BEE degree from Pratt Institute. He has been involved primarily with the development of millimeter-wave components for future satellite communication systems.

Mr. Michael Powers graduated from the University of Delaware with a BS in electrical engineering. He has been with Goddard for 3 years. His responsibilities have included the testing of microwave receiver components, system testing of the Differential Microwave Radiometer (DMR) instruments for the COBE project, and the development of digital components for the communication electronics subsystem of the LASERCOMM project.

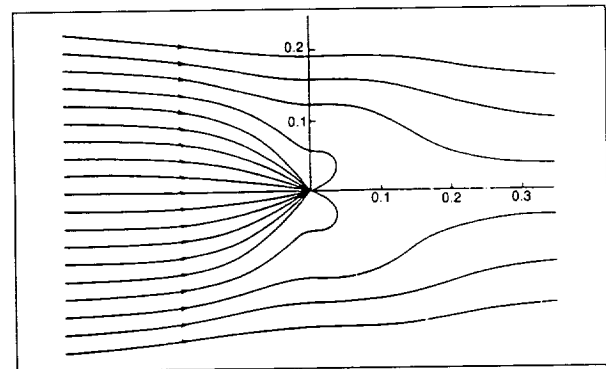
Ms. Catherine Long earned her BSEE from the University of Maryland. For 5 years, she has been working at Goddard in the Communication Electronics Section of the Microwave Technology Branch. Her responsibilities have included 60-GHz receiver development and state-of-the-art mixer/preamplifier development for the DMR instruments aboard COBE. Recently she has been involved in the design and testing of high-speed digital electronics using gallium-arsenide technology.

LOW-FREQUENCY ELECTRIC AND MAGNETIC FIELDS

In early October 1989, observations were reported on three separate occasions of ultralow-frequency (ULF) magnetic fields (0.01 to 10 Hz) near Loma Prieta, California. On October 17, a magnitude-7.1 earthquake occurred, with its epicenter located approximately 7 km from the magnetic-field monitoring site. This suggests that one might obtain valuable advance warning of impending earthquakes by continuously monitoring ULF magnetic fields near known fault zones. Since 1988, an extremely low frequency (5 to 50 Hz) Earth-ionosphere cavity resonance monitoring facility has been under development at West Virginia State College. The system



Energy flux lines in the x - y plane. The dipole located at $x=y=0$ oscillates in the z direction. Incident (from the left) is a linearly polarized monochromatic plane wave.



Energy flux lines in the x - z plane for the same physical situation as described in the first figure.

design currently is being modified to include a portion of the ULF band so that data which may prove useful for earthquake prediction can be acquired along with the cavity resonance data.

An active antenna for use as a sensor for the Earth-ionosphere cavity resonance monitoring facility is under development. It capitalizes on a little-known field-interaction phenomenon. The phenomenon is illustrated in the first and second figures. A magnetic plane wave, incident from the left, interacts with an antenna consisting of a search coil-capacitor tuned circuit, causing a current to flow around the circuit. The current generates a dipole magnetic field which, in turn, interacts with the original plane wave in such a way as to bend the magnetic lines of force toward the dipole. The result is that the Poynting vector lines, which map the flow of power, also are bent toward the dipole. This indicates that there is a resulting flow of power from a relatively large portion of



the wave front to the dipole. Because this effective area of the dipole antenna may be 100 times larger than the physical cross section of the antenna, this dipole is 10 times more sensitive than a dipole antenna in which no current is permitted to flow. This latter condition applies, for example, to an untuned search coil connected to a high-input-impedance voltage amplifier.

To enhance the effective area of a search coil antenna, then, one should maximize the current. The antenna also must be broadband enough to include the frequency band from at least 0.1 Hz to 50 Hz to provide the necessary input for the fast-Fourier transform spectrometer used for data analysis. To do this, the authors have developed an active circuit which presents a negative resistance and a negative inductive reactance to the coil to balance out the real positive winding resistance and the positive inductive reactance of the coil. The coil current and the resulting coil-plane wave interaction thereby are maximized over a band of frequencies.

Contact: John F. Sutton (Code 728)
(301) 286-5454

G. Craig Spaniol (Code 728)
(301) 286-5454

Sponsor: Office of Equal Opportunity Programs

Dr. John F. Sutton holds a BS from Union College, an MS from George Washington University, and a PhD from the American University in Washington, D.C. He designs analog electronic systems for satellite experiments. Currently he is designing active ULF magnetic field antennae. He also is developing therapy equipment for the treatment of leukemia and AIDS.

Dr. G. Craig Spaniol received a BS from West Virginia State College and a PhD from Rensselaer Polytechnic Institute. He is a professional engineer and the Chairman of the Department of Industrial Technology at West Virginia State College.

REED-SOLOMON ENCODER CONTROLLER NETWORK

Reed-Solomon encoding is used to protect the integrity of data transmitted through communication links. It encodes a block of n symbols (bits or bytes) and produces a parity block of p symbols. Codes are defined as (N,n) block codes, where N is the

sum of the input data symbols plus the parity symbols necessary to correct the input data for a given number of errors.

NASA Goddard has developed a Reed-Solomon encoder to be used in the Wide-band Transport Frame Formatter (WTFF). It has a basic block code of $(255, 223)$ eight-bit symbols, but can function in interleaved depths from one to eight. This means that block codes of length $(255n, 223n)$ where $n=1$ through 8 can be produced by the chip.

The WTFF, which formats data into standard frames specified by the Consultative Committee for Space Data Systems, uses the AHA4610 encoder, originally developed for NASA at the University of Idaho. The WTFF uses an interleave depth of five.

This article describes the controller circuitry that provides the logic necessary to use the encoder chip in a system. It allows for simple integration of the encoder into any system by providing all the timing and control logic needed for interfacing to the device.

This circuitry allows Reed-Solomon encoding to be treated as a macro-logic function for system designers and eliminates the burden of determining special interfacing requirements.

The controller network is comprised of four logic functions: an input first-in, first-out (FIFO) for buffering of the input data, the Reed-Solomon network controller programmable logic device (PLD), the AHA4610 encoder, and an output fifo memory for buffering the encoded data.

The network is operated by using the following control signals: RESET, which clears the Reed-Solomon encoder; RS-START, which initiates encoding of data contained in the input fifo; FRAME, which indicates a Reed-Solomon frame has been encoded; the input fifo control lines, WRITE and FULL; and the output fifo control lines, READ and EMPTY.

All the control logic and timing requirements necessary to transfer data from the input fifo, through the Reed-Solomon encoder, to the output fifo, are provided by the network controller PLD. To use the network, the user initially resets the system, writes data into the input fifo, tells the system to start encoding the data, and reads the encoded data from the output fifo.

Future plans for the system are to develop a flight configuration of the present design. This will entail creating flight-qualified versions of the Reed-Solomon encoder, network controller PLD, and fifos. It also is possible to develop a hybrid package of the design by using the device dies instead of the packaged devices. This will allow for a very compact system chip, which truly would make this function ideal for system designers who require Reed-Solomon encoding.

Contact: Douglas Ross (Code 728)
(301) 286-3735

Sponsor: Office of Aeronautics and Exploration
Technology

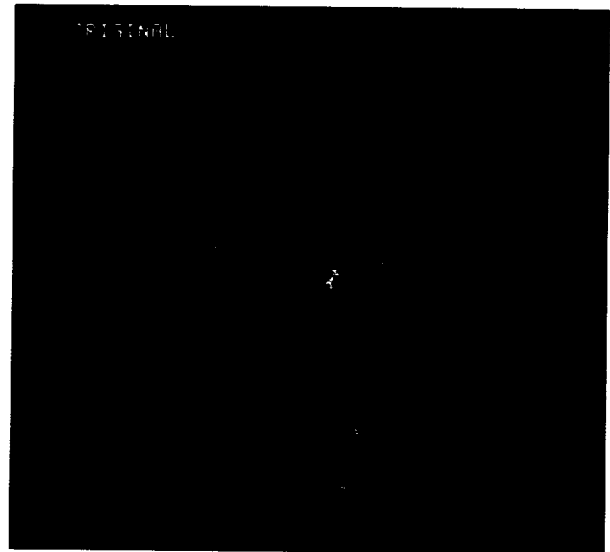
Mr. Douglas Ross has worked for Goddard since 1979 in the Instrument Electronic Systems Branch. He primarily is involved in digital-system design of research projects and advanced systems. He develops microprocessor-based systems and the software necessary to run them. Currently, Mr. Ross has a Directors Discretionary Fund project to produce a fast, versatile space-computer core. He holds a BSEE from Cornell University and an MSEE from Georgia Institute of Technology.

HIGH-COMPRESSION DATA REDUCTION SCHEME FOR SPACE APPLICATIONS

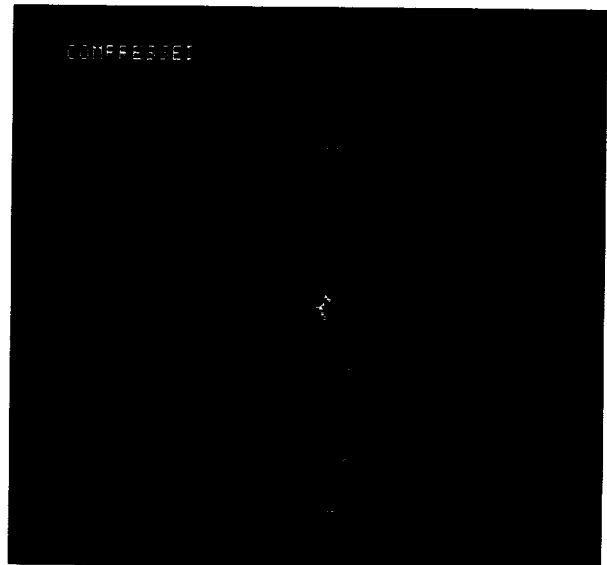
Future generations of spacecraft will accommodate a multitude of advanced sensors which will generate information at much higher rates than today's sensors. After the information is converted into a bit stream and transferred to the communications system on the spacecraft, competition exists between sensors for the limited channel capacity over data throughput. One solution is to use data compression techniques to reduce the total data rate.

Lossless data compression will reduce the redundancy in the data and guarantee full reconstruction of the original data. Its average performance on NASA's imaging data is a data reduction ratio of about 2 to 1. Development of a high-speed, application-specific integrated-circuit lossless data-compression chip was reported in the 1989 R&T report.

Situations may arise when the pointing control of a fine-resolution sensor requires knowledge of coarse-imaged surface geometric features, which would rely on a large-format image data set of more than 1,000 by 1,000 surface



High-rate data compression system.



Original and reconstructed images of the solar disk.

elements. These large data sets have to be updated frequently and without much delay. The requirement imposed on the communication channel cannot be accomplished by a mere 2-to-1 data compression. A high-compression scheme becomes necessary for such data sets.

A proposed scheme performs a block discrete cosine transform (DCT) on the data, and the transform coefficients are processed further, requantized, and coded for transmission. The scheme uses the previously developed



lossless compression chip for coding the processed DCT coefficients, thereby reducing the overall complexity involved in using most other lossless coders. The processing of the DCT coefficients would introduce distortion in the reconstructed data. However, its effect often is insignificant even at a data reduction ratio of 10 to 1 and a signal-to-noise ratio of more than 30 dB. The algorithm has been tested on various imagery, including the Orbiting Solar Laboratory full solar imagery, and shows adequate reconstructed details for locating areas of interest.

Contact: Pen-Shu Yeh (Code 728)
(301) 286-4477

Warner H. Miller (Code 728)
(301) 286-8183

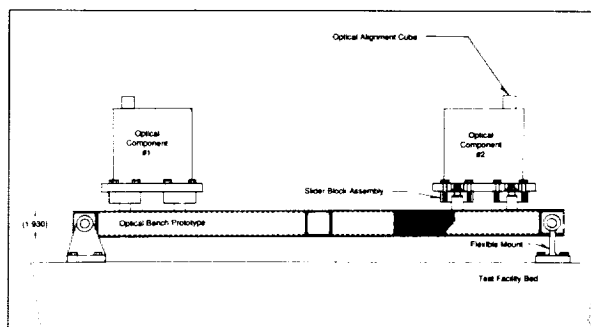
Sponsor: Office of Aeronautics and Exploration
Technology

Dr. Pen-Shu Yeh has been at Goddard for 2 years. She is conducting research in data compression and signal processing, as well as supporting flight projects in simulation. She earned her PhD in electrical engineering from Stanford University.

Mr. Warner H. Miller, who received an MS in applied science from George Washington University, has been at Goddard for 28 years. He designs advanced flight instruments for signal processing with the Instrument Electronic Systems Branch. Mr. Miller has special interests in data processing, telemetry, channel encoding, and communications.

DEVELOPMENT OF DIMENSIONALLY STABLE, FIBER-REINFORCED COMPOSITE STRUCTURAL ELEMENTS FOR USE IN SPACECRAFT AND INSTRUMENT OPTICAL SUPPORT PLATFORMS

Various Goddard groups are responsible for implementing dimensionally stable composite structures into their spacecraft and instrument designs. Goddard is developing its knowledge and capability in the area of composite materials design, analysis, and fabrication because of the urgent need to be able to respond to instrument and satellite requirements. In many cases, the performance can be achieved only with composite materials.



Optical-bench prototype test configuration. The bench design will serve as a demonstration platform for several different composite-part geometries. The design was derived from the requirements of several Goddard programs.

For this reason, a comprehensive investigation into candidate material systems and composite laminate geometries has been performed and organized into the *Composite Structural Materials Selection & Design Handbook*, which allows experienced and inexperienced composite design engineers alike to make informed decisions regarding material and geometry selection during the preliminary and detailed design phases of a project. Several PC-based computer programs were created to perform the studies which formed the design handbook. The handbook explores the laminate property variations of several composite material systems, in an incremental fashion, for a wide range of possible ply geometries. Property sensitivity due to variations in fabrication angle errors and fiber volume also are addressed. These programs will allow analyses to be performed for new material systems which are not in the handbook. The data from the analyses are linked with a spreadsheet database in order to extract the laminate geometries which are valid design candidates based on user-defined criteria ranges.

The *Composite Structural Materials Selection & Design Handbook* then was used as a guideline for the prototype hardware phase of the study project. This involved the design, analysis, and fabrication of a typical portion of a dimensionally stable optical support bench as a proof-of-concept of the component material properties generated in the design handbook. The bench design will serve as a demonstration platform for several different composite-part geometries. The design was derived from the requirements of several Goddard programs. This gave the optical-bench prototype a firm basis for implementation into other scientific instrument designs. The performance

of this design has been evaluated analytically for strength, 1-G alignment stability, thermal-distortion alignment stability, and structural dynamic frequency response. Ultimately, the prototype platform will verify, by test, these various performance predictions. The intent of the development program was to prove the feasibility of several fundamental design configurations in order for designers at Goddard and in industry to apply the results to their programs. This objective already is being met on several flight programs by using various elements of the design and by applying the knowledge gained from the development of the optical-bench prototype.

Contact: Daniel F. Mark (Code 731)
(301) 286-2704

Perry Wagner (Code 731)
(301) 286-2836

Sponsor: GSFC Director's Discretionary Fund

Mr. Daniel F. Mark holds a BS in aerospace engineering from Purdue University. He is the Mechanical Systems Manager for the Far Ultraviolet Spectroscopic Explorer (FUSE) and has 6 years of industry experience in aircraft/aerospace structures in addition to 3 years of experience at Goddard.

Mr. Perry Wagner received his BS from the University of Dayton in mechanical engineering. He is the composite materials and structures engineer for the FUSE program. Before coming to Goddard nearly 2 years ago, he worked in the composites industry at the University of Dayton Research Institute and the Air Force Materials Laboratory at Wright Patterson Air Force Base.

ATTITUDE CONTROL SYSTEM (ACS) SIMULATOR ON THE MIL-STD-1553 BUS

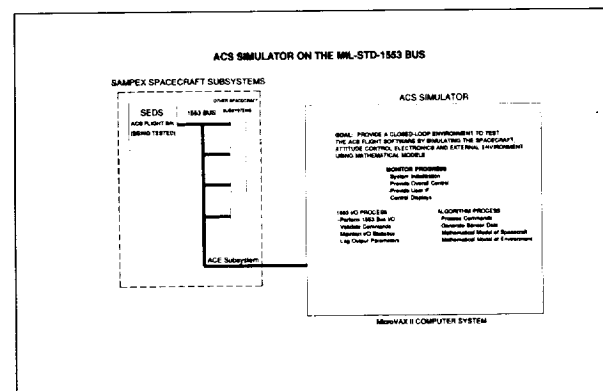
The MIL-STD-1553 bus is a digital time-division multiplex data bus that has been used successfully in avionics units on military aircraft for more than 10 years. It allows various black boxes in a system to communicate over a simple, two-wire interface, thus reducing the overall system complexity and weight. Recently, efforts have been made to adopt this interface for spaceflight use. The first of the NASA Small Explorer (SMEX) missions, the Solar, Anomalous, and Magnetospheric Particle Explorer

(SAMPEX), currently is implementing a MIL-STD-1553 bus interface into its flight system. This spacecraft is being developed at Goddard.

An attitude control system (ACS) simulator which interfaces to the MIL-STD-1553 has been developed to support the development, testing, and integration of the SAMPEX spacecraft. Its primary purpose is to provide a closed-loop environment to test the SAMPEX Small Explorer Data System (SEDS), which implements the attitude control and data-handling software. The simulator was developed on a MicroVAX II computer system and consists of a MIL-STD-1553 bus hardware interface and three main software modules. The simulator has a menu-driven user interface, and the software modules are written primarily to VAX C language.

The three main software modules consist of an input/output (I/O) module which handles all of the 1553 bus I/O and control, a display/control module which handles the user interface and the overall control of the simulator, and an algorithm module which implements the mathematical model of the spacecraft's ACS. New mathematical models could be used to simulate different spacecraft, if desired, as long as they conform to the simulator's internal interface specification.

The simulator has a variety of display pages which can be used to check or modify simulation parameters, obtain on-screen help, or monitor the progress of a simulation. The simulator has more than 100 parameters that can be



ACS simulator on the MIL-STD-1553 bus. Its primary purpose is to provide a closed-loop environment to test the SAMPEX Small Explorer Data System, which implements the attitude control and data-handling software.



set by the user to change the spacecraft attitude, rotation rates, noise factors, scale factors, sensor and actuator controls, and inertia factors. The simulation parameters can be changed in real-time by the user or loaded from a parameter command file. Initial condition files and orbital environment files also can be loaded at the beginning of a simulation to set the desired user environment. The simulator also maintains counters and snapshots of the I/O packet traffic on the 1553 bus and can time-tag and log both the spacecraft state and the 1553 bus packets to file on the disk. The spacecraft state file is provided to the user in text file format, so that the simulation results may be analyzed in the user's own lab.

Contact: Thomas P. Flatley (Code 733)
(301) 286-9942

Edward J. Hicks (Code 733)
(301) 286-2534

Thomas E. Correll (Code 745)
(301) 286-6047

Sponsor: Small Explorer Project

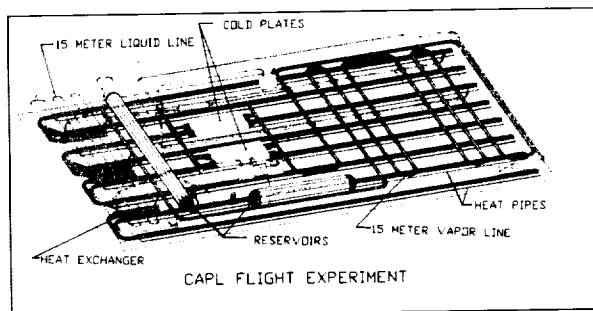
Mr. Thomas P. Flatley earned his BS in engineering from Loyola College and currently is pursuing an MS in computer science at The Johns Hopkins University. He has been working for the Electrical Engineering Branch for 5 years.

Mr. Edward J. Hicks holds a BS in computer science from Loyola College and is working on an MS at The Johns Hopkins University. He has worked in the Electrical Engineering Branch for 2 years.

Mr. Thomas E. Correll received a BS and an MS in electrical engineering from Rensselaer Polytechnic Institute and has been working for the Attitude Control and Stabilization Branch for 4 years.

THE ENHANCED CAPILLARY-PUMPED LOOP (CAPL) FLIGHT EXPERIMENT

The enhanced capillary-pumped loop (CAPL) experiment has been redesigned extensively since it was described in last year's report. The CAPL is designed as a prototype of the Earth Observing System (EOS) instrument thermal control system, which is based on



CAPL flight experiment. The most significant modification was the use of heat-pipe heat exchangers for heat rejection instead of direct condensation radiators.

capillary-pumped, two-phase heat transfer technology (CPL). This technology uses the latent heat of vaporization in a closed-loop thermal control system to transfer large amounts of heat over long distances. The system provides cold plates that are held at a nearly constant temperature by the ammonia fluid that flows through them. Both heating and cooling are available over a wide power range, and the system temperature can be adjusted to any desired level (-10° C to 50° C). Two-phase systems also offer significant weight and power savings compared to single-phase systems currently in use. The CPL is a completely passive loop in that it has no mechanical moving parts that can wear out or introduce unwanted vibrations to the platform. However, the CPL has a limited pumping capability of approximately 0.5 psi, so the system components must be designed for low-pressure losses.

Verification of CPL technology in microgravity is required prior to its implementation on the EOS platform. The effects on pressure losses, heat transfer coefficients, and fluid management must be evaluated and tested. The initial CPL Hitchhiker-G experiment proved that CPL technology can work in microgravity. However, this experiment was only a small-scale, proof-of-concept demonstration of CPL technology and did not address a number of system characteristics inherent with the larger systems required for EOS. The CAPL is a full-size prototype with features such as long fluid-transport lines and heat-pipe heat exchangers that were not tested with the first experiment.

The recent design changes to CAPL were made to update it to the latest EOS platform design. The most significant modification was the use of heat-pipe heat exchangers for heat rejection instead of direct condensation radiators.

The heat exchangers condense the ammonia vapor (remove the heat) from the CPL with the heat carried to the radiator via heat pipes. This method of heat rejection greatly reduces the vulnerability to meteoroids since the CPL fluid loop is no longer part of the radiator. Now, a meteoroid hit will result only in the loss of the portion of the radiator serviced by a heat pipe, instead of the entire thermal-control loop. Two different heat-exchanger designs are being built for ground testing; the best design will be selected for use on the flight experiment.

Another modification to the CAPL was the increase of the liquid and vapor transport lines from 10 m to 15 m in length. The tubing material was changed from aluminum to stainless steel (to reflect the latest EOS design). Also, the enhanced CAPL now carries a second, smaller fluid reservoir in addition to the original larger version. The new reservoir will demonstrate CPL operation with a reduced ammonia inventory; it is designed to operate more efficiently than the existing reservoir. Three designs are being built for ground tests, and the best one will be selected for flight. One design uses a grooved, porous, plastic material (Porex) as a fluid wick on the inside wall of the reservoir and as a vapor barrier at the inlet/exit region. The other two designs use sintered nickel as wick material, with one design using arteries for flow control and the other one using baffles.

The enhanced CAPL experiment also has three differential pressure transducers that measure the pressure drop across the heat exchangers, the vapor line, and the liquid line. A capillary starter pump and vapor-line heaters also have been added to assist in fluid management and to reduce the ammonia charge-level required to run the loop. The size of the experiment radiator was increased from 56 in by 100 in to 62 in by 100 in to increase its heat rejection capability, now predicted at 1,200 watts for the cold-case Shuttle attitude. The radiator panel will be coated with silver teflon on the interior and white paint on the exterior so that the heat exchangers will be tested with nonuniform heat sink conditions. A number of other enhancements were studied but not incorporated because they were either beyond the scope of the program or did not require microgravity performance verification.

The CAPL experiment will be flown on the Shuttle as a Hitchhiker-G payload. The experiment will be controlled from the ground with real-time data and command links to

the electronics controlling the CAPL. The mission currently is manifested for an early 1993 launch.

Contact: Dan Butler (Code 732)
(301) 286-5235

Roy McIntosh (Code 732)
(301) 286-5235

Sponsor: EOS Project

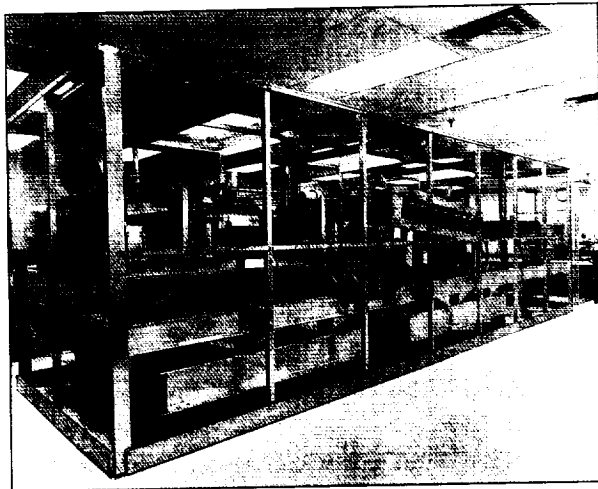
Mr. Dan Butler is a research and development engineer with the Thermal Engineering Branch with 13 years of experience at Goddard. He holds a BS in aerospace engineering from Virginia Polytechnic Institute. Mr. Butler currently serves as Program Manager for the CAPL experiment.

Mr. Roy McIntosh, Head of the Advanced Development and Flight Experiment Section, has 28 years of experience at Goddard. Mr. McIntosh, who received his education at Antioch College, has received two Exceptional Performance Awards and a NASA Exceptional Engineering Achievement Medal for work in two-phase heat transfer.

INSTRUMENT THERMAL TEST BED (ITTB)

Future large spacecraft, such as Space Station Freedom and the EOS platforms, will operate at higher powers and with longer thermal transport distances than current spacecraft do. In addition, they will have a more distributed set of loads, many of which will require very tight temperature control. Existing thermal control technology is inadequate for these applications. A new concept, two-phase thermal loops with ammonia as the heat-transfer fluid, is being developed to meet these new requirements. To support this development work, a large, easily reconfigurable test loop called the Instrument Thermal Test Bed (ITTB) has been designed and fabricated.

The ITTB is a full-scale laboratory test facility which can be used to ground test, qualify, and certify various two-phase heat transfer components and system concepts. It is very versatile and is designed in a modular manner to allow simple and rapid system reconfiguration. All of the major two-phase system concepts—capillary pumped, mechanically pumped, and hybrid—can be accommodated. Major hardware features include: standardized test ports for evaluating evaporators, condensers, and other components; numerous valves for quickly modifying system configuration; a variable transport length of 10, 20, or 30



The Instrument Thermal Test Bed, developed to support research on a new two-phase thermal loop with ammonia as the heat-transfer fluid.

meters; an optional mechanical pump; evaporator tilt capability; a capillary starter pump; and alternate locations for test reservoirs. The ITTB also is well instrumented with more than 1,000 thermocouple/pressure transducer/flowmeter channels. This wide flexibility allows a two-phase component (such as an evaporator plate, radiator, reservoir or mechanical pump) to be integrated easily into a correctly configured loop.

The primary function of the ITTB is to support the development of advanced two-phase thermal technology. Specific projects anticipated to employ this technology include Space Station Freedom and EOS. In addition to supporting hardware development, the ITTB also will be used to assist in developing control algorithms and in correlating two-phase analytical models.

Contact: T. D. Swanson (Code 732)
(301) 286-6952

Sponsor: Office of Aeronautics and Exploration
Technology

Mr. T. D. Swanson is a senior aerospace engineer with 6 years of experience at Goddard. He has a BS from Case Institute of Technology and an MS from the University of Maryland. Mr. Swanson designed and tested the first operational ammonia-based, mechanically pumped, two-phase thermal control loop. He currently is Manager of the ITTB project, and also was Chairman of the Office of Aeronautics and Exploration Technology Workshop on

Two-Phase Fluid Behavior in a Space Environment, and he currently is Vice Chairman of the Thermal Management Panel of the Interagency Advanced Power Group.

THE EFFECT OF MOLECULAR DIFFUSION ON OUTGASSING BEHAVIOR

Outgassing products from spacecraft materials can degrade system performance by condensing on critical surfaces and changing their thermal or optical properties. During spacecraft assembly, thermal vacuum bakeout is the most effective method employed to reduce the material outgassing to an acceptable level for on-orbit performance. Even after the spacecraft and its instruments have been baked out carefully, engineers remain concerned about two issues: the effectiveness of the bakeout as a function of the outgassing materials and bakeout conditions, and the on-orbit outgassing behavior after the bakeout and long-term ground storage. The long-term spacecraft outgassing will become diffusion-limited eventually. The diffusion-limited process indicates that the only way to prevent outgassing from occurring is to diffuse the molecules to the surface. The material diffusion study will help understand this behavior.

Material diffusion is a process in which molecular contaminants transport through the bulk material to the free surface, where they evaporate under vacuum conditions. Therefore, material outgassing, a result of the diffusion process, can be modeled adequately by diffusion theory. The magnitude of the outgassing rate can be determined from the geometry of the material and the diffusion coefficient of the outgassing species in the bulk material.

A transient diffusion theory based on Fick's law was developed to simulate molecular diffusion during and after bakeout. The diffusing material was packed inside a metal cylinder tube with both ends open. The equation describes the diffusion process for flow from both sides of a cylindrical tube. Because of symmetry, one-dimensional diffusion is sufficient to describe the actual diffusion process. The governing equation for both stages is exactly the same. The differences between the two stages are the initial and boundary conditions. Theoretical solutions for concentration as a function of position and time for both stages have been derived.

The plot of the solution during bakeout indicates that the concentration profile of molecular contaminants depends on the initial conditions and the molecular diffusivity. The

magnitude of the outgassing rate and total mass loss also can be determined from the changes in concentration on either side of the tube. The solution after bakeout reveals that a reverse diffusion process takes place and equilibrium inside the bulk material may occur.

Future work will concentrate on obtaining the diffusion coefficient and will involve experimental work to verify the developed theory. A series of material tests should be conducted to determine the concentration profiles. The theory and experimental data will determine future bakeout practices.

Contact: Philip T. Chen (Code 732)
(301) 286-8651

Sharon A. Straka (Code 732)
(301) 286-9736

Dannelle M. Shover (Code 732)
(606) 490-3400

Sponsor: Materials and Structures Division

Dr. Philip T. Chen has been a contamination control engineer with Goddard for 5 years. He graduated from the University of Maryland with a PhD in chemical engineering. Currently, he is responsible for supporting the X-ray Spectrometer and the Geostationary Operational Environmental Satellites project.

Ms. Sharon A. Straka has 4 years of experience at Goddard in the Applied Engineering Division. She holds a BS in chemical engineering from the University of Pittsburg. She primarily is interested in contamination of materials.

Ms. Dannelle M. Shover, an engineer completing her first year at Goddard, previously has worked on the Upper Atmosphere Research Satellite project. Her research also focuses on the contamination of materials. She received her BS in aerospace engineering from Pennsylvania State University.

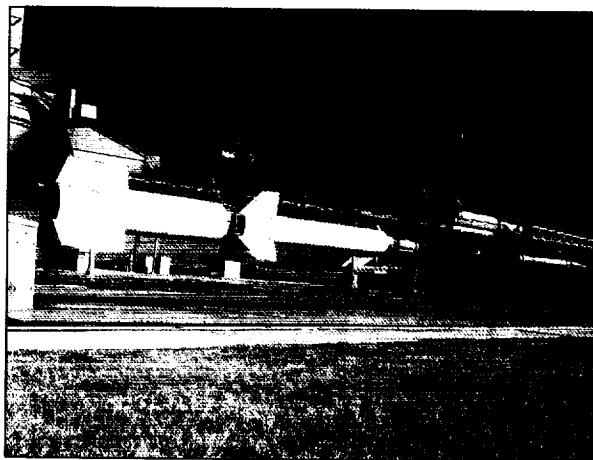
REDUCTION OF FLIGHT-TRAJECTORY DISPERSION FOR UNGUIDED LAUNCH VEHICLES UTILIZING BOOST-STAGE SPIN SYSTEM

A spin system was developed for NASA's high-performance sounding rocket launch vehicles to reduce the impact dispersion of the unguided vehicles' spent stages. The system provides a rapid-spin

acceleration, resulting in a 1-Hz spin rate immediately following launcher exit. The system provides a significant reduction in first-stage, body-fixed contributions to the flight trajectory dispersion. Upper stage impact dispersion was reduced sufficiently to allow the high-performance Black Brant XI and XII launch vehicles to be used at the Poker Flat Research Range (PFRR) in Alaska. The system proved to be highly effective during launch operations at PFRR in the winter of 1990.



Black Brant XII development test flight.



Black Brant XII sounding rocket vehicle.



The spin system for the Black Brant XI and Black Brant XII vehicles was integrated into the first-to-second-stage interstage adapter. Four XM37E1 solid-propellant rocket motors provided the force to spin the vehicles and were mounted on the external circumference of the adapter. Spin-motor ignition was controlled with an electrical system armed from the blockhouse and initiated by lanyard switches as the rocket moved the first 6 in. The lanyard switches initiated a pyrotechnic delay switch which delayed the spin-motor ignition 1 second, resulting in vehicle spin up 1/2 second after launcher exit.

The addition of the spin-motor system to Black Brant XI 39.002 UE and Black Brant XII 40.002 UE reduced theoretical 3-sigma impact dispersion of the third-stage motor from 160-km radius to 125-km radius. This reduction allowed the 3-sigma impact dispersion to be contained within the boundaries of the PFRR's allowable impact area, permitting the vehicles to be launched at PFRR.

Black Brant XI 39.002 UE and Black Brant XI 40.002 UE were launched February 1, 1990, and March 22, 1990, respectively. The 39.002 third-stage impact was 1.2 sigma from nominal, and the 40.002 UE fourth-stage impact was 1.1 sigma from nominal.

Contact: Bobby J. Flowers (Code 841)
(804) 824-1073

Sponsor: Sounding Rocket Program

Mr. Bobby J. Flowers received his BS in mechanical engineering from Virginia Polytechnic Institute in 1960. He has 30 years of experience with sounding rocket launch vehicles and payload management at NASA's Wallops Flight Facility.

SOUNDING ROCKET PAYLOAD ATTITUDE CONTROL REFERENCED TO AN UNDEFINED MAGNETIC FIELD VECTOR

Sounding rocket payload attitude control is generally a straightforward system with input from a sensor such as a gyro, magnetometer, or solar sensor. The ACS sensor used depends upon mission-specific criteria such as the need to align the payload to the Earth's magnetic field, direct an instrument at the Sun, or move the payload to a given orientation in space. Systems using gyro platforms are the most flexible since they have the ability to perform multiple maneuvers during a flight. These maneuvers are

all relative to the inertial frame at the time the gyros are uncaged. Other systems using sensors such as magnetometers and solar detectors provide a means to point accurately toward a magnetic field or the Sun but lack the ability to maneuver accurately to other orientations. Some systems use a gyro to maneuver the payload to an orientation where another sensor, such as a solar detector or star tracker, takes over control for fine pointing.

For the system discussed here, the requirements were more demanding. Mission success required accurate placement of the payload spin axis parallel to the Earth's magnetic field (**B**). The rocket was to be launched in an arctic region where the magnetic field direction was not well defined. Also, the payload was to be maneuvered to other orientations in relation to the direction of the magnetic field. These requirements defined a system with input from a magnetometer for aligning to the magnetic field, and a gyro for precise relative pointing. The scenario was to use gyro input for pointing the vehicle to the closest known magnetic-field location and from there, to use the magnetometer to lock onto the field. Then, after a specified time aligned with the field, the system would use the gyro's input to maneuver to subsequent orientations based on the measured position of **B**.

An existing ACS design using a microprocessor-based control system and a three-axis gyro platform was integrated with a three-axis fluxgate magnetometer. The ACS had sufficient A/D channels to accommodate the magnetometer, and the signal conditioning and processing were handled in software. The magnetometer was oriented in such a manner that two of the axes were orthogonal with the vehicle roll axis. This allowed a changing magnetometer signal in relation to movement in the payload pitch-and-yaw axis with a null occurring in both magnetometer channels when the payload roll axis was oriented parallel to the magnetic field. To simplify the control system, the magnetometer channels were phased and scaled so that the signals would be the same as the gyro platform signals for a given displacement. This allowed the use of the same servo software for either type of input.

Though the fluxgate magnetometers used are very accurate, they possess an inherent DC bias that is relative to many factors, including the payload structure, magnetic fields from the payload's experiments, etc. Since the actual configuration and field signature could not be determined prior to launch, a method was devised to

measure the bias in flight before switching to magnetometer control. Since the vehicle was spinning, a misalignment to the **B** field created a signal consisting of a sinusoid, produced by the Earth's **B** field, and a DC offset from the bias in the magnetometer channels.

While the payload still was pointed away from the **B** field under gyro control, this sinusoid was sampled and averaged, resulting in the channel's DC bias. This bias was then removed from subsequent measurements, leaving a signal relative to the external magnetic field only.

Once the payload was aligned with the **B** field, the gyro position data (though not being used for control at that time) was used to update the **B** field position in the ACS computer's memory. After spending a period of time at this orientation, the magnetometer's job was finished and input was once again taken from the gyro platform to make subsequent maneuvers. Since the maneuvers were to be relative to the **B** field and not to the inertial frame, the position data from the gyros stored at the time of magnetic field alignment was used to supplement the pitch-and-yaw commands previously stored in memory.

As sounding rocket experiments become increasingly complex, so do the requirements placed upon the attitude control systems. This system is a good example of the versatility and accuracy that will allow scientists to increase the scope of their experiments.

Contact: Richard Olsen (Code 841)
(818) 886-6500

Sponsor: Suborbital Projects and Operations Directorate

Mr. Richard Olsen is an ACS engineer with Space Vector Corporation. He holds a BSEE from the University of California at San Diego.

LIGHTWEIGHT, SELF-CONTAINED BALLOON MEASUREMENT INSTRUMENTATION

Measuring the dynamic forces of a scientific balloon without adding significant mass or complexity required the development of a set of instrumentation packages which will allow the high-resolution measurements of accelerations and temperatures incurred during a balloon flight. Because of constraints placed on the investigator—concerning the weight and size of the

payload relative to the available lift and flight performance of the balloon—the design of these packages demanded that the instruments be lightweight and self-powered. The design also required that these instruments contain onboard memory for data and have a flexible programming environment.

The prototype design resulted in a small, lightweight, self-contained dynamic measurement system which allows the user to tailor the programming for a myriad of applications. The stand-alone units are called Stow Away Specials (SASs). Dimensions for the units are 5 by 7 by 15 cm, and each unit weighs approximately 0.5 kg with batteries installed. The first SAS developed consists of a +/- 2.0-g accelerometer with 16-bit A/D resolution. Accelerometer resolution is 1×10^{-5} g. A single-channel scan rate is set for 10 ms sample and will collect data continuously for approximately 16 minutes. However, because the data collection software is completely programmable, the user can set up the data collection in any manner he or she chooses. (Collection routines such as peak/hold and threshold detection currently are being developed for longer flight durations.)

A second channel which records temperatures of the unit during flight has been incorporated as part of the normal flight data. A total of eight channels of data collection are available with the currently implemented logging processor. Other plans include adding an analog output for real-time collection of data as well as for test purposes. The first full-scale flight test of these units showed survivability of temperatures spanning 100° C with impact velocities up to 150 m/s. Retrieval of data consists of downloading the raw data into a PC and then transferring the data into a DEC MicroVAX for manipulation and analysis.

A second SAS was developed as a temperature measurement logger with four input channels and an 8-bit A/D resolution. This unit has been calibrated to measure temperatures in the range of -50° C to 50° C. The current scan rate is 1 s/scan, which allows measurement over a time period of approximately 30.6 hours. As with the acceleration logger, scan rates and resolution can be altered to suit the user's needs. Programs written for both types of loggers can be loaded easily in the field by writing the programs to be implemented prior to use and then burning those programs into EEPROM. This allows the investigator to make last-minute decisions and changes without having to



connect to a host computer. Any program changes therefore can be made by switching EEPROMs in the logger. All programming is written either in Basic or Assembly code. Presently, the SASs contain 230 Kbytes of memory using DRAM technology, although solid-state memory can be increased to 1.2 Mbytes. Disk storage used in less harsh environments will increase storage to 20 Mbytes.

Operating the loggers consists of three basic steps: load the intended program into the logger; install the batteries or supply power; and turn it on. Because of the flexible operating environment, logging can be initialized at the time of supplying power to the unit by commanding initialization via logic switching of the transistor-transistor logic (TTL) lines by means of contact closures, or program command. At the end of each flight, the raw data is dumped to a host in a hex format to conserve storage space and then is converted to ASCII for final analysis in engineering units. Although the SAS can be programmed to output real units, it is more economical from a memory standpoint to perform this function at the time of analysis.

Future applications include force measurement of the flight termination event, balloon film strain measurements, differential pressure measurement of the balloon gas envelope, and logging of the balloon system command function electronics.

Contact: Michael Martone (Code 842)
(804) 824-1551

Sponsor: Office of Space Science and Applications

Mr. Michael Martone is an electrical/mechanical systems technologist with 15 years of laboratory experience, including 6 years in dynamic testing. Currently with the Physical Science Laboratory of New Mexico State University, he is assigned to NASA's Wallops Flight Facility in support of the NASA Scientific Balloon Program.

DETERMINATION OF BALLOON LIFT (GAS MASS) FROM LAUNCH ACCELERATION

Mathematical modeling of balloon flight performance serves as a significant tool for prediction and analysis. Errors in agreement between calculated ascent trajectories and flight data have been inconsistent and, in several cases, have exceeded desired limits. Identified sources contributing to these ascent

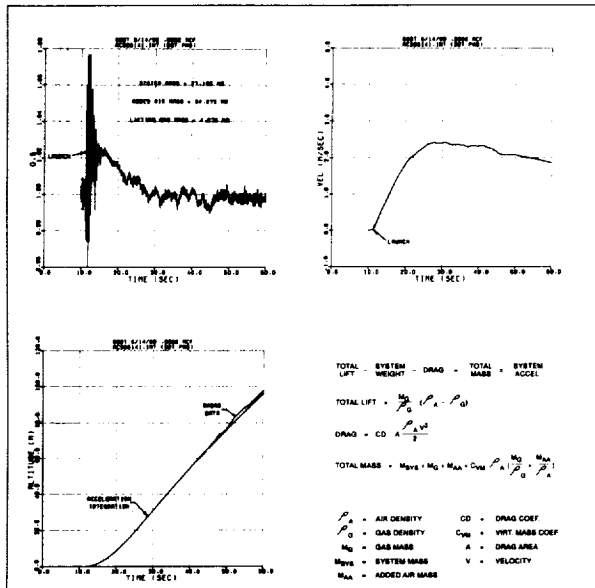
discrepancies are uncertainties in lifting gas mass, drag and virtual mass coefficients, and leaks. The primary objective of this work was to determine the feasibility of more accurately establishing the lifting gas mass from the equations of motion and from sensitive acceleration measurements during the launch transient. The secondary objective was to gain a better understanding of the retarding forces produced by drag and virtual mass considerations on a flexible balloon body. (Transient distortions of the balloon envelope effectively increase system drag beyond the classical solid-body data. In addition, some experiments have reported an increase in virtual mass with developing flow relative to the inviscid flow values applicable at flow initiation.)

Small-scale balloons (175 cubic meters) equipped with SASs were flown from a static launch, with varying lifting gas and total system mass. Balloon top and bottom accelerations, along with helium and air temperatures, were sampled and stored every 10 ms. The balloons were inflated in a hangar where lift, and balloon, payload and ballast weights could be measured within an accuracy of 9 g (typical gross inflation was on the order of 40 kg). On occasions, air was metered into the balloon envelope (with an accuracy of about 1 percent) to change significantly the displaced volume and to add mass to the system.

The figure shows typical accelerometer data with integrated results compared to radar data. Also shown is the simplified vertical equation of motion that demonstrates how the lifting gas mass can be determined from measured launch accelerations. At the instant of launch, system acceleration is maximum and system velocity is zero; therefore, incipient flow and drag are equal to zero, thus simplifying the solution.

Virtual mass is the amount of displaced fluid that exerts an additional external force on the accelerating body. For a solid sphere and ellipsoid, potential flow analysis shows that virtual mass equals half of the displaced mass, which appears at $C_{vm}\rho_a M_r/\rho_g$ in the equation of motion. The results of this work suggest that a value of $C_{vm}=0.55$ is more appropriate for zero-pressure balloons.

Leaks were a constant problem that required large amounts of recorded prelaunch and postlaunch lift data in order to improve lift-at-launch accuracy. (The scale-model balloons incorporated a lightweight, 360-m



Typical accelerometer data with integrated results compared to radar data. Also shown is the simplified vertical equation of motion that demonstrates how the lifting gas mass can be determined from measured launch accelerations.

tether for system retrieval and reuse.) Using the above virtual mass coefficient of 0.55, it was demonstrated that lifting gas mass could be determined from launch acceleration measurements with a typical accuracy of better than 1 percent.

Drag could be determined through the launch transient as well as during steady-state ascent, provided there were no significant balloon-envelope, flexible-body oscillations. In the static-launch configuration, the payload and recovery parachute suspension rigging and the balloon itself were essentially preloaded by the free lift (excess drive-up lift). At launch, this oscillator system was released into motion and, at low to normal free lifts (<14 percent), quickly damped to solid-body behavior. At excessive free lifts, the oscillations did not damp fully until well into the steady-state ascent portion of the flight. (Typical damping times are well under a minute; because damping times are insignificant, they typically are neglected during the usual 2-hour ascent.) Local balloon-envelope accelerations dissipated additional energy that was manifested as an apparently larger drag coefficient when back-calculated from the global solid-body model. The current vertical performance model assumes the balloon system behaves as a solid body.

Drag coefficients determined from solid-body behavior flight data range from 0.20 to 0.36 within a Reynolds number range of 350,000 to 1,200,000; the published solid spherical drag coefficient in this supercritical Reynolds number range is 0.2. Skin friction and form drag of the balloon rope section and recovery train afterbodies in the ascending wake account for only a few percent of these discrepancies. Work is continuing to define and predict more accurately balloon forebody geometry and to investigate a possible Froude number dependency arising from vortex-shedding-induced wave motion of the aft uninflated balloon film (essentially a flexible membrane between dissimilar fluids).

Contact: Edward Robbins (Code 842)
(804) 824-1385

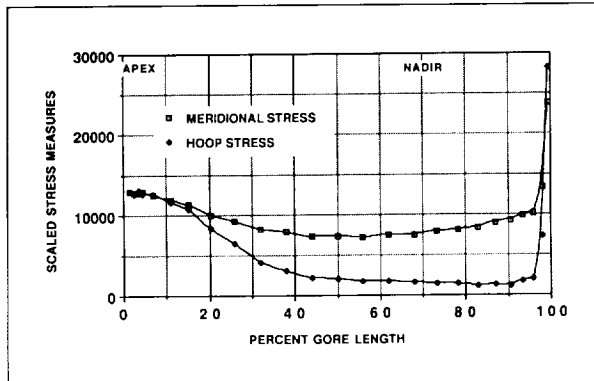
Sponsor: Office of Space Science and Applications

Mr. Edward Robbins, who holds a BSME from the University of Massachusetts, has 20 years of broad mechanical and aerospace engineering experience. Mr. Robbins currently works for the Physical Science Laboratory of New Mexico State University, but he is assigned to the Wallops Flight Facility in Virginia in support of NASA's Scientific Balloon Program.

FINITE ELEMENT SOLUTION FOR THE STRUCTURAL BEHAVIOR OF A SCIENTIFIC BALLOON

The current design methodology for scientific balloons at NASA relies on predictions obtained from a classical membrane solution approach. This approach assumes there exists an absence of hoop stresses in the skin and perfect axial symmetry. Although this approach yields the information for the tailoring of a successful balloon shape, the so-called natural shape, it cannot predict the stress field in the film. This inability to predict the actual stress field hinders the development of improved designs. An off-the-shelf nonlinear finite element code (ABAQUS) has been applied to the analysis of balloon envelopes which are tape-reinforced, very thin pneumatic membranes.

The configuration of the balloon envelope, and consequently the stress field in the balloon film, changes during ascent. The easiest problem to analyze is the fully inflated shape; it is determinate. Cyclic symmetry reduces the problem size. Skin and tapes have no bending stiffness;



Scaled stress measurements along meridional line, near gore center (isotropic skin, nonslack tape).

pressure load provides the structural stability. The non-linear finite element method permits analysis of systems where stiffness is derived from geometry and loading; however, the analysis of such systems is plagued by convergence problems. In particular, the near-zero bending stiffness coefficients in the stiffness matrix prevent the analysis from proceeding. In shells with non-zero Gaussian curvature, locally introduced bending moments die out rapidly with distance; i.e., in thin films, the in-plane stress resultants are nearly independent of the bending stress resultants. This fact is used by introducing a small artificial bending stiffness in the shell finite elements to facilitate the numerical solution without significantly affecting in-plane stress resultants.

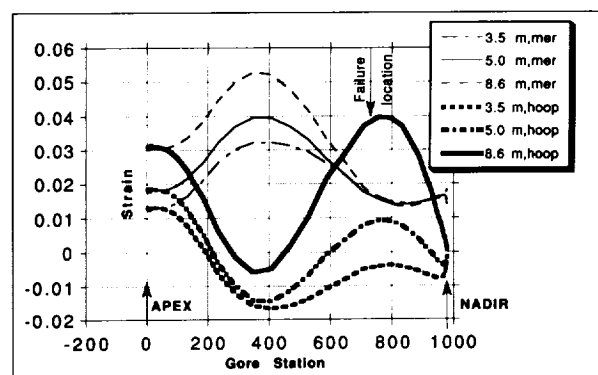
Several natural-shape models of scientific balloons have been analyzed. The stress field obtained appears to reason because:

- In an isotropic balloon envelope without a rigid top fitting, the hoop stresses and the meridional stresses at the apex are identical as suggested by the theory-of-elasticity solution for a flat disk.
- In a balloon envelope with a small number of gores, the meridional stresses rise from the apex toward the shoulder where they reach a local peak. In a similar balloon with a large number of gores, the meridional stresses decay toward the shoulder and remain near constant for the middle third of the gore length.
- The hoop stresses decay rapidly from the flat disk values at the apex to lower values dominated by gore billowing at and below the shoulder.

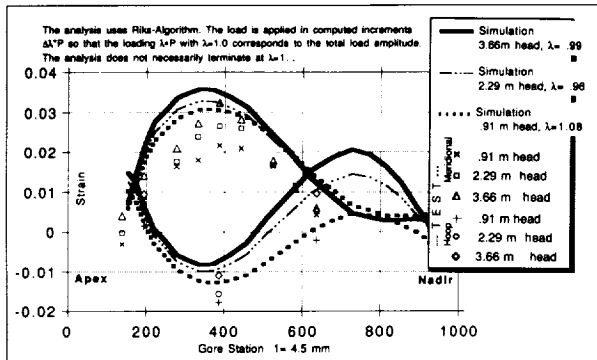
- Overpressurization studies on a 16-gore, zero-pressure, natural-shape test balloon show that failure will occur at about three-quarters of the gore length measured from the apex. While strains and stresses grow moderately with increasing pressure head in the upper section of the balloon envelope, at the failure location, the hoop stresses grow at an accelerated rate. This has been observed on a number of test balloons.
- In a balloon with zero pressure at the nadir, the hoop stresses near the nadir vanish; i.e., the film becomes slack in the hoop direction.

Local slackness in the hoop direction in the vicinity of the nadir usually prevents convergence of the finite element solution. Various modeling approaches have been used to overcome this pathology. The modeling approach used for the results presented in the first figure is a slight modification to the pressure-load distribution.

A small-scale, 16-gore, natural-shape balloon, the Structural Test Vehicle (STV), was tested to validate the analysis approach. Large manufacturing imperfections are unavoidable in the STV. Some of the observable imperfections were incorporated into the model in an approximate sense. The static analyses simulated the test scenario as closely as possible. Visco-elastic effects were accounted for by the use of an elapsed-time correction on the material properties. Tests were conducted at several pressure levels in a continuous session. Test results correlate reasonably well with the analytical predictions. The third figure shows that trends of hoop and meridional strain as a function of gore station match well. While significant



Strain at gore center in a 16-gore test vehicle for pressure heads of 3.5 m, 5.0 m, and 8.6 m. Rapidly rising hoop strain is shown at the failure location.



STV analysis versus test data. Some manufacturing imperfections are included in the analysis.

strain offsets are noted, the predicted strain increase between load levels is consistent with test results.

A number of numerical studies on balloon envelopes have been performed making convergence-forcing modeling assumptions. Some of the significant findings are:

- The current load-tape specifications which specify only the load capacity of the load tapes are inadequate. The elastic properties of the load tape and manufacturing imperfections such as slackness of the reinforcing fibers significantly affect the stress field in the balloon film.

- Accepting the validity of a maximum stress criterion for polyethylene films, it appears that natural-shape balloons designed for a given pressure level can be pressurized to some higher pressure level without undue rise in the maximum film stress. This fact can be exploited in an engineering way by optimizing balloon shapes for long-duration flights.

Contact: Willi W. Schur (Code 842)
(804) 824-1078

Joel Simpson (Code 842)
(804) 824-1070

Sponsor: Office of Space Science and Applications

Dr. Willi W. Schur earned a PhD in aerospace engineering from the University of Maryland. He has more than 25 years of experience in the structural design and analysis of industrial and marine facilities, nuclear power plants, ship structures, and balloon envelopes. He is employed by the Physical Science Laboratory of New Mexico State University and is currently assigned to the NASA Scientific Balloon Program.

Mr. Joel Simpson received his BS in aerospace engineering from the University of Maryland. He has performed analytical and experimental analysis of balloon performance and balloon structural response for 5 years while working for the Balloon Projects Branch at Wallops Flight Facility in Virginia.

Data and Communications Technology

GenSAA

The Generic Spacecraft Analyst Assistant

Mission Name:
Generic Demo

Development Utilities:

- User Interface
- Rule Base
- Data Specification

vs (root)

Save Open

Save As... Quit

Compile Build...

Next Panel

User Interface Tools

Delete

Label

Select

Define Info

Connect

User Interface Views: Grid Constants

Diplexer A

Diplexer B

Receiver 1

Receiver 2

Current Selection (click to change):

Name: Diplexer A

Telem: XRCMODE

Link to: Diplexer A

Info: (none)

Show Links

Show Infos

Done

Meters, Flags, and Objects



The GenSAA system is an indication of the wave of the future in expert system development technology. It provides, in an easy-to-use integrated package, all the tools necessary to establish the underlying knowledge base, user interface, and connections to operational data. The real-time development of expert systems for fault detection and diagnosis is at hand.

DATA AND COMMUNICATIONS TECHNOLOGY

DATA DISTRIBUTION MEDIA STUDY

The Information Processing Division (IPD) is developing a Data Distribution Facility (DDF) for distributing spacecraft data to investigator facilities, science centers, and archives. During fiscal year 1990, IPD conducted a study to select a physical medium for distributing data products in support of the International Solar Terrestrial Physics (ISTP) Program. The following options were considered: nine-track, 6,250-bpi magnetic tape; write-once-read-many (WORM) optical disks; compact disk—read-only memory (CD-ROM); 5.25-inch erasable and rewritable optical disk (magneto-optical); VHS cartridges; 8-mm helical scan tape; and 4-mm digital audio tape (DAT).

The ISTP Program will study the energetics of the near-Earth space environment with instruments on a set of integrated and coordinated space flights. The spacecraft will be built and managed by three international agencies: NASA, the Institute of Space and Astronomical Science, and the European Space Agency. When all of the ISTP instruments are operational, IPD will be processing more than two gigabytes of ISTP data per day. The DDF will package these data and distribute them to more than 100 investigators throughout the world. The investigators will

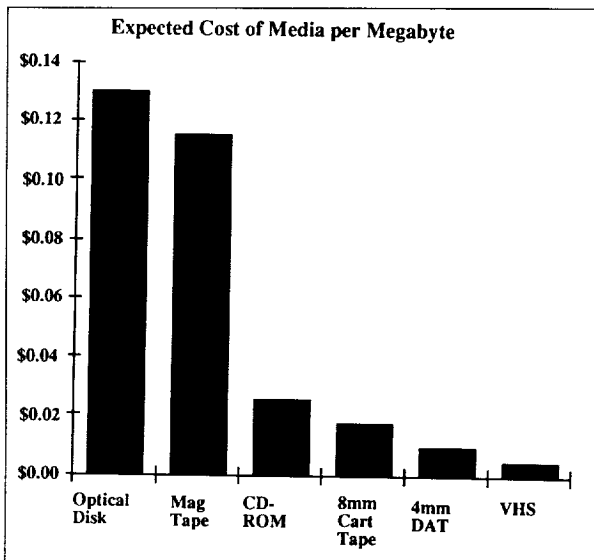
be using various computer platforms: IBM Personal Computer (PC), DEC, VAX, Sun, and Macintosh. Each investigator will receive the data from his/her own team's instrument, as well as requested data from cooperating teams' instruments and the more highly processed key parameters from all ISTP instruments.

Some of the media characteristics examined during the study are provided below.

Nine-track magnetic tape—a relatively inexpensive medium—currently is used for distributing most of IPD's products. Many investigators regularly receive data in this form, so most already have the equipment and programs needed to extract data from this medium. The concerns with this medium relate to the need to maintain tapes in a special environment and rewrite them on a regular cycle, as well as the relatively high costs to purchase and maintain the drives.

CD-ROMs are mastered and stamped at facilities set up for producing musical compact disks. The mastering charge is about \$1,300 for each disk; copies cost around \$2 each with a minimum order of 100. Drives to read a CD-ROM cost about \$500 each. An International Standards Organization (ISO) standard has been defined for the physical and logical file format of the CD-ROM; any disk conforming to this standard should be readable on any

◆ *Generic Spacecraft Analyst Assistant (GenSAA)—User Interface Design Capability.*



Predicted cost (per megabyte) of various media considered for the ISTP Program.

CD-ROM drive. CD-ROMs are expected to last 30 to 50 years, even outside a controlled environment.

For those who wish to produce only a few copies or who are concerned with the security involved in sending data to another facility for mastering, there are optical drives which can write disks in the CD-ROM format. However, these drives are more costly than other optical drives, and the lifetime of the medium they use currently is limited to 8 years.

There are no current standards across vendors for WORM media or devices; a disk written on one drive probably would not be physically readable on another vendor's drive. WORMs come in several different sizes. The 5.25-inch, 500-megabyte media cost about \$100 each now, but they are expected to decrease in price. Predicted lifetimes are in the 10- to 30-year range, and disks require a less stringent storage environment than the magnetic options.

Erasable and rewritable optical disks are a later technology than the WORMs, so they are standardized at the physical level, and they provide faster access. However, the standards do not address fully the logical file format problem, so disks need to be formatted specific to the user's platform. At least one optical drive vendor provides translation software for the platforms in which ISTP investigators are interested. The software

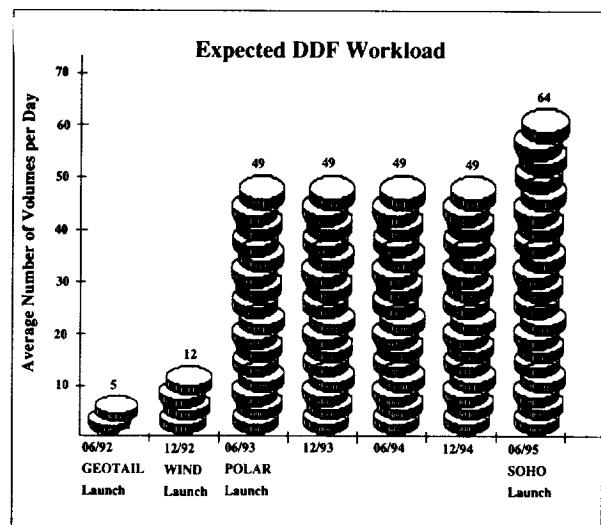
costs \$1,000, and drives cost about \$10,000. Media costs currently are about \$250 per 500-megabyte disk, but are expected to decrease to \$50 in the next few years. Predicted lifetimes range from 10 to 30 years, and the medium requires a less stringent storage environment than the magnetic options.

VHS tapes hold 2.5 gigabytes of data, making them a good medium for backup of large amounts of data, or occasional exchanges of data between users with similar platforms. Each tape costs approximately \$5; drives cost about \$6,000 each. Access is sequential.

Eight-mm cartridges vary in size from 290 megabytes to 2.6 gigabytes. The media cost between \$4 and \$45 each; drives cost about \$5,000. Access is sequential.

DATs are a fully block-addressable tape technology, whose 1.3-gigabyte tapes are expected to cost about \$8.50 each; drives cost about \$3,000 each. The main concern with this medium is the lack of experience with it.

A comparison of the media by expected cost per megabyte is shown in the accompanying graph, where the costs for the CD-ROM are based on making 100 copies of one disk, and all volumes, for all media, are assumed to be distributed full. (Note that this comparison does not include operational costs of duplicating products, except in the case of CD-ROM.)



Anticipated DDF workload, based on demands from various satellites within the ISTP Program.



Based on the study and the preferences of the investigators, IPD and the ISTP Program chose the rewritable optical disk option for distributing the data for the following reasons:

- Optical disks use industry-approved standards.
- Disks are easily transportable and are not easily damaged by environmental elements.
- Disks can be produced easily which are readable on appropriate computer platforms.
- Low-cost drives for reading and writing disks are available for appropriate computer platforms.
- Optical disks are accessible randomly at the file level.
- These technologies have been proven and are likely to be around for the life of the mission.

Based on this study and the resulting agreement with the project, hardware specifications have been prepared, and a request for proposals will be issued. To be considered, a vendor's proposal will have to pass performance benchmarks illustrating a capability to meet the anticipated production workload (shown as an average number of rewritable optical disks per day in the accompanying chart.)

Contact: Mary Reph (Code 563)
(301) 286-5037

Patricia Carreon (Code 563)
(301) 286-7766

Sponsor: Office of Space Operations

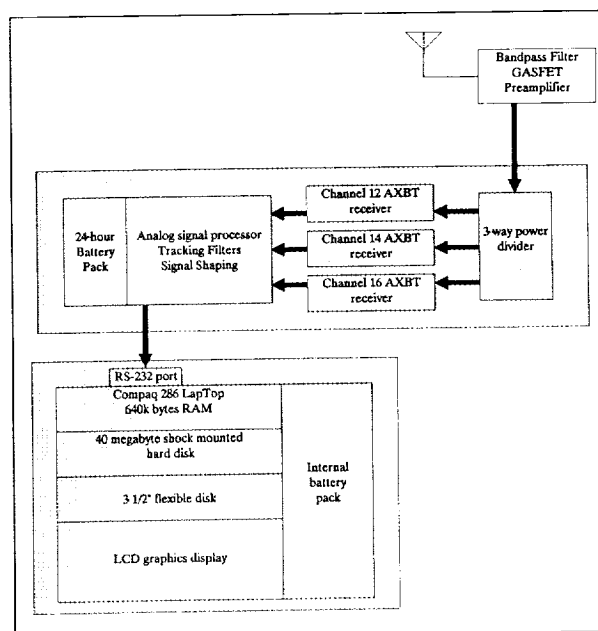
Ms. Mary Reph is Head of the IPD's Computation Systems Section. She received a BS in mathematics from the University of Georgia and an MA in mathematics from the American University. Since coming to Goddard in 1978, she has been developing systems which give scientists access to data collected by NASA.

Ms. Patricia Carreon works in the Mission Support Systems Branch. She received a BS in electrical engineering at Southern Methodist University and is working on an MS at George Mason University. She has been at Goddard for 1 year.

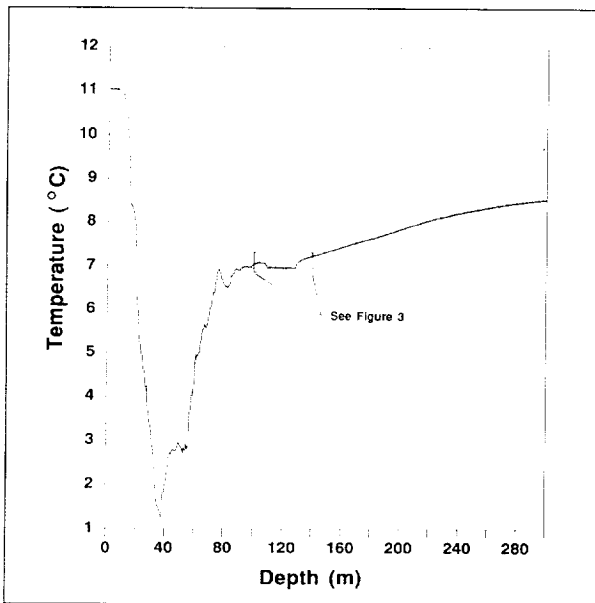
HIGHLY PORTABLE, AIRBORNE, EXPENDABLE BATHYTHERMOGRAPH (AXBT) DATA SYSTEM

A small, lightweight, and relatively portable Airborne, Expendable Bathythermograph (AXBT) data acquisition system has been developed and used on several international missions. The AXBT is an air-deployed, expendable, ocean temperature profiling probe. The AXBT consists of a temperature probe, 300 to 1,000 meters of cable, a VHF transmitter and antenna, and a salt-water-activated battery. After the AXBT hits the ocean surface and stabilizes, the transmitter is activated, and the temperature probe is released. The surface transmitter telemeters the falling probe's temperature to the data system on the aircraft.

The AXBT data system consists of a Zenith 286 battery-powered laptop computer and a briefcase containing three VHF Sonobuoy radio receivers, a battery pack, and a GAS-FET preamplifier. This AXBT data acquisition system uniquely implements a software digitizer for conversion of raw analog data to digital form. The unprocessed AXBT signal is interfaced to the laptop via the RS-232 status line inputs. The data acquisition software operation is fully automatic. AXBT casts automatically are detected, digitized, catalogued, and stored on disk for later analysis. The system also provides the operator with



A block diagram of the AXBT data system.



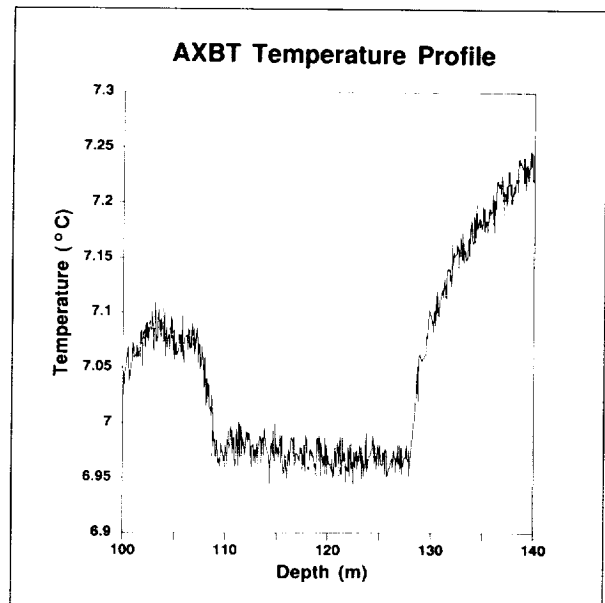
A typical AXBT temperature profile.

a real-time, fully calibrated graph of each AXBT cast. The graph may be rescaled in temperature and depth by the operator at any time. Each cast is stored in ASCII format and is calibrated in both depth and temperature.

The AXBT data system was developed during the 1989 Joint Global Ocean Flux Study (JGOFS), whose mission was to provide scientists with water-column temperature profiles along designated flight lines in the North Atlantic between the Azores, Ireland, and Iceland. These temperature profiles were valuable for interpretation of the chlorophyll distribution measured by the Airborne Oceanographic Lidar system and were used in conjunction with GEOSAT altimetry data to delineate large mid-ocean gyres affecting the JGOFS mid-Atlantic study site. The portable AXBT recording system has participated in several other NASA oceanographic missions.

In addition, the U.S. Coast Guard's International Ice Patrol and the U.S. Navy have contributed funding to the development of the flexible AXBT data recording system, and both of these agencies currently are using uniquely tailored versions of the AXBT data system on their own research aircraft.

Temperature profiles from AXBTs are a critical element in the U.S. Coast Guard's iceberg tracking program. The water-column temperature profiles are used in models along with visual observations of the ice field to provide



AXBT temperature profile, showing in detail an enlarged section of a region outlined in the second figure.

critical information on probable iceberg distributions to transoceanic shipping. The U.S. Navy uses AXBT data for a variety of applications, including acoustical modeling and satellite altimeter interpretation. The Navy has developed several AXBT data systems. However, the recently developed NASA AXBT data system represents a significant reduction in size, weight, and power consumption, thus providing dramatically improved portability. In addition, the battery-powered NASA AXBT data system eliminates the need to connect to the aircraft electrical system, which reduces the time required to install the AXBT onboard an aircraft.

Contact: Charles W. Wright (Code 972)
(804) 824-1698

Sponsor: NASA Ocean Programs, NASA Earth Sciences and Applications Division, and the Naval Oceanographic and Atmospheric Research Laboratories

Mr. Charles W. Wright has 12 years of experience at Goddard. He holds a BS in computer science from the University of Maryland, and he continues to work there on an MS in computer science. He specializes in aircraft digital data systems. Mr. Wright is the Principal Investigator for the AXBT.



DEVELOPMENT OF REAL-TIME SOFTWARE ENVIRONMENTS FOR NASA'S MODERN TELEMETRY SYSTEMS

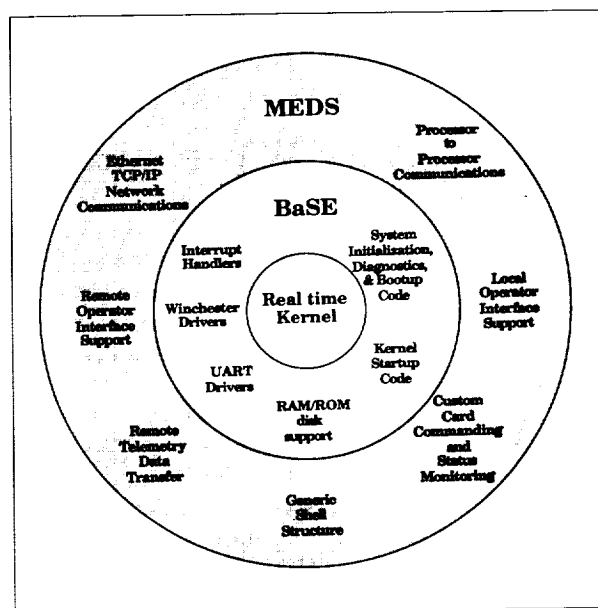
Modern real-time telemetry data systems needed to support NASA in the 1990s and beyond require state-of-the-art real-time software techniques and approaches that are tightly coupled with high-performance Very Large Scale Integration-based (VLSI) hardware systems. To this end, the Data Systems Technology Division (DSTD) maintains expertise in both high-performance VLSI-based hardware design and state-of-the-art real-time multiprocessing system software design and techniques. This knowledge base constantly is being expanded and augmented by keeping abreast of the latest commercial hardware-processing elements and systems, exploring and exploiting these technologies as they become available, and maintaining an active dialogue with commercial hardware and software system manufacturers.

The design and development of generic, low-cost, high-performance telemetry components and systems require the optimum integration of custom and standard hardware elements with a number of real-time software elements. To maintain maximum flexibility and performance for the DSTD's VLSI telemetry system elements, two special real-time system environments were developed. The Base System Environment (BaSE) supports generic system integration while the Modular Environment for Data Systems (MEDS) supports application-specific development. Architecturally, the BaSE resides just on top of a commercial real-time system kernel while the MEDS resides just on top of the BaSE, as shown in the first figure. The BaSE provides for the basic porting of various manufacturer's cards and ensures seamless integration of these cards into the generic telemetry system. With their environment, developers are assured a rich selection of available commercial components to meet their particular applications. MEDS provides the designer with a set of tested generic library functions that can be employed to speed up the development of application-specific real-time code. This article describes the philosophy behind the development of these two environments and the characteristics which define their performance and role in a final VLSI telemetry system.

To maintain their state-of-the-art aspects, NASA's next-generation telemetry systems must provide a fairly simple and fast path to future enhancements. For this reason, the

electronics hardware developed at the DSTD is based on standard open-bus architectures and makes use of multiple commercial and custom VLSI hardware-based cards that provide standard, off-the-shelf telemetry processing functions (frame synchronization, Reed-Solomon decoding, packet processing, etc.) for almost any telemetry data-handling application. BaSE allows the designer to pick and choose those open-bus products that best fit the application at hand. This environment ensures that products from different manufacturers can be used together in a "plug-and-play" fashion. It allows seamless integration of DSTD's custom telemetry processing cards into the operational environment. It contains the intelligence to configure the system automatically based on a changing hardware environment.

BaSE provides a single environment that is used for all phases of system development. Its use spans from initial hardware test and checkout, to system software development, to final operational system deployment. Its goal is to provide a cost-effective software platform that can be used for both development and operations, and can be quickly and easily tailored to meet changing system needs. BaSE works in conjunction with an unmodified, commercially available real-time, multiple-user, multiple-task kernel. This kernel lies at the core of the development system and is used to build the system software. This same kernel lies at the core of the

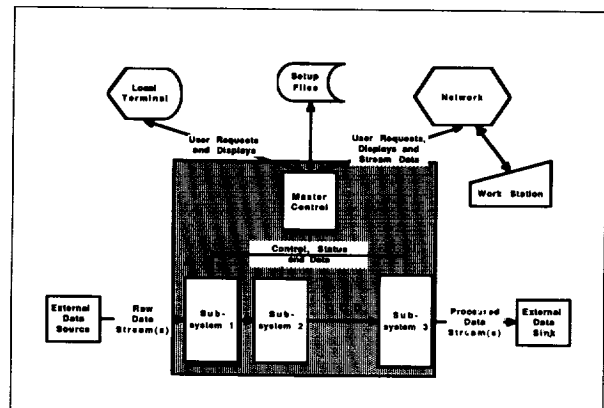


The real-time software environment provides a rich set of features.

operational system, thus ensuring that both environments are identical. This dual-purpose environment allows the system designer to develop the application directly on the target system. The use of BaSE eliminates the need for complex and expensive host software development workstations and microprocessor emulators. The real-time operating system used by BaSE provides a basic set of tools that can be used effectively to build a multiple-processor system. These tools support global events, global memory installation, and global message passing. Global events are used to synchronize tasks on different processors. The basic functions can set, clear, and test global event flags. Other functions include delayed set/clear and task suspension. Global-memory installation tools are used to install nontasking memory for use in global message passing. The basic functions can allocate, initialize, lock, and unlock a global-memory area. Global-message passing tools use prioritized queues for interprocessor/intertask message services. The basic functions can put and get messages. Other functions can create, delete, and initialize message queues.

Each central processing unit (CPU) card in a BaSE multiprocessor system is stand-alone and runs its own copy of the operating system out of its local random-access memory (RAM). The master CPU card handles all global bus interrupts and initializes all global memory. It converts global-bus hardware interrupts to software events that are set/cleared in a global memory area using operating system-supplied multiprocessing support services. Slave CPU cards suspend on these global events and thus do not have to process the actual interrupt. The master CPU card installs all global memory that is contiguous to its local memory into its memory allocation map. Slave CPU cards install only their own local memory. This way, multiple processors do not attempt to install the same global memory, which would be catastrophic if used as tasking memory. Noncontiguous global memory can be installed by a utility program into any card's memory allocation map after multitasking system operations have been started.

BaSE can be ported to virtually any Motorola MC68010/20/30-based CPU and its supporting peripheral equipment (e.g., disk drives) whether it be on a commercial card, or embedded in a custom application. It quickly is ported to new, more powerful hardware as it becomes available. The porting process is simplified because unique, card-specific code has been reduced to a mere 10 to 20 percent of the overall BaSE code. A utility



The MEDS multiprocessor platform provides a base on which to build application-specific software.

program has been developed to simplify the system generation of BaSE that allows object-oriented modifications to the default setup without changing the source code.

BaSE is supported on custom systems with multiple embedded CPUs. For example, a DSTD-developed card called the VLSI high-speed packet processor uses a ring of three MC68030 processors along two gate arrays. Each CPU runs its own private BaSE, and through the use of dual-ported RAM disks and terminal ports, each CPU has its own independent development environment. BaSE also is used in an embedded mode in the Goddard transportable telemetry workstation. This system consists of a Macintosh II equipped with several custom cards that perform various telemetry-processing functions. One of the custom cards supports a MC68030 processor running BaSE. This card has a shared port for hard-disk interface and two terminal ports for user interface allowing application-specific system development and monitoring during the prototype stage directly on the target card.

MEDS is designed as a general-purpose software platform which is expanded and customized by application programmers to suit their particular requirements. It supports the basic software functions needed in all systems—namely, the ability to set up application-specific hardware and software, process the telemetry data based on the established parameters, monitor the processing, and supply network support for remote operator interface and data transfer. This environment supplies an infrastructure to pass data between systems, processors, and tasks, as well as to provide support for operator-interface development. A complete system is



built by adding custom code to the general-purpose MEDS code. Therefore, MEDS spares the application developer the burden of creating an infrastructure for each new system and adds consistency in all system design, implementation, and maintenance.

A MEDS-based system unites and manages the data system's standard multiple-processor hardware platform. The processors are organized as a single master processor directing multiple, subordinate application-specific custom cards, as shown in the second figure. The master processor is the single point of control within the system; it interfaces with the operator, on either a local terminal or a remote workstation. Using a set of operator-defined setup files, the master processor will initialize the custom cards and monitor their processing on various status pages. Telemetry data may enter as well as exit the system via the remote interface. In any case, it is the pipeline of custom cards that actually processes the telemetry data. The basic MEDS functions include setting up the system and subsystems for processing (VLSI chip registers), controlling the application-specific processing (enable, disable, reset a card), monitoring the system and subsystems (gather and display card processing status), and streaming data transfer over the network (transfer telemetry data to/from a workstation).

The overall MEDS software design is modularized into packages which supply general-purpose system functions such as operator-interface support, status-gathering support, command-handling support, interprocessor communications, and network communications. Each package implements a set of functions that serve as a resource to the application software while hiding the details of their implementation. Consistent interfaces have been defined for each package so code within a package can be changed without affecting the application code if the functions and interfaces remain constant.

A MEDS-based system is a group of cooperating tasks built on these software packages. The tasks are spread across the processors of the system and are tightly coupled on the bus and loosely coupled on a network between the rack and the remote workstation. Some of the packages exist as linkable libraries that the programmer will use to build a task, such as a command handler. Other packages exist as customizable source code files, where the applications programmer will copy the source file, add in the application-specific code and compile, for example, a status task. In all cases, the programmer does not need to

know the details of MEDS implementation; only the interface to it. MEDS software is written in C language, and an assembler is used to interrupt handlers.

MEDS version 5.5 has been released in the last year. Expanded message passing capability is the primary feature of this new version. Through the use of a new mailbox system, telemetry data now can be passed card to card over the commercial open bus, as well as the custom telemetry data-pipeline bus. This has proved to be useful particularly when passing telemetry data to various commercial cards located on the open bus, such as high-speed data buffers and network interfaces. Additionally, this version has been optimized and modularized, providing faster porting to new telemetry systems. It has been ported to most of the existing systems.

The need for these software platforms was apparent from the outset of the VLSI telemetry-system development. Therefore, much effort was put into making every element general purpose. These elements are evolving continuously. DSTD researchers will attempt to further generalize and enhance the designs of the hardware and software platforms in each revision. The results are found in time, effort, and money saved on current and further system development and system modifications. It took 3 years to develop the first VLSI telemetry system from the VLSI circuitry to the operator interface. The current 1- to 2-year development cycles for the next-generation systems would not be possible without the environments described here.

Contact: Ward Horner (Code 521)
(301) 286-5804

Stephen Sabia (Code 521)
(301) 286-7951

Stanley Hilinski (Integral Systems, Inc.)
(301) 731-4233

Sponsor: Office of Space Operations

Mr. Ward Horner is Manager of the BaSE software platform and has 9 years of experience at Goddard. He earned a BSEET from Capitol College and received a NASA Group Achievement Award in 1989 as part of the VLSI System Design and Development Team. Mr. Horner specializes in the design of multiprocessing hardware and software implementations. He manages, coordinates, and designs a variety of sophisticated hardware- and software-oriented projects.

Mr. Stephen Sabia is Manager and designer of the MEDS software platform. He started at Goddard as a cooperative student in 1983. Mr. Sabia works on real-time telemetry data-capture systems software and is interested in hardware-software interfaces. He received a NASA Group Achievement Award in 1989 as part of the VLSI System Design and Development Team. Currently, he is pursuing an MS through the Applied Physics Laboratory of The Johns Hopkins University.

Mr. Stanley Hilinski is chief designer of the MEDS software platform. He has 15 years of software design experience. Mr. Hilinski, who started working at Integral Systems in 1985, specializes in the design and development of real-time system software platforms. He has an MS in mathematics from the University of Maryland.

FRAME SYNCHRONIZATION AT 300 MBPS

Future NASA space missions will require ever-increasing amounts of communications bandwidth. Very high data rates will be required to support NASA's future large-scale operational programs, such as Space Station Freedom and the Earth Observing System (EOS). While NASA's Tracking and Data Relay Satellite System (TDRSS) can support downlink rates of up to 300 megabits per second (Mbps) and the Advanced TDRSS is expected to support 650 Mbps, most ground-based telemetry acquisition systems can support sustained data rates of up to only a few megabits per second. To support its future programs, NASA will require new data handling systems capable of operating at rates in the hundreds of megabits per second.

As a continuation of its functional components approach and as an initial step in the development of very high rate functional components, NASA has applied advanced technologies such as application-specific, gallium-arsenide (GaAs) VLSI circuits to develop a generic High-Rate Frame Synchronizer (HRFS) capable of operating at rates of up to a minimum of 300 Mbps. This single-card design is modeled after an existing low-rate complementary metal-oxide semiconductor (CMOS) Frame Synchronizer (20 Mbps) card currently used in a number of advanced data-handling systems. In the past, the CMOS Frame Synchronizer card has demonstrated the feasibility of integrating a fully functional generic frame synchronizer on a single-card design. The HRFS maintains this same high level of physical and functional

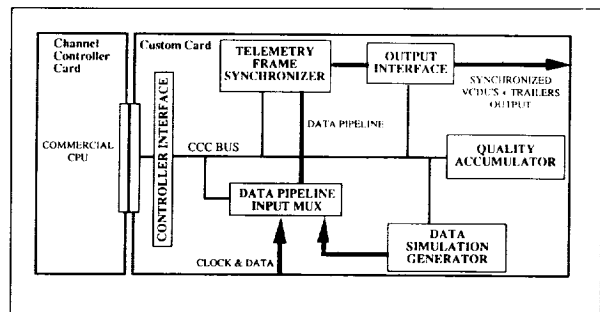
integration while demonstrating a greater-than-10-times improvement in data throughput.

The HRFS, shown in the first figure, is physically implemented on a 9U VME card. One-third of this card is a commercially available single-board computer used as the Channel Controller Card (CCC). The remainder of the card is a custom logic card that is interfaced through a side connector on the card. The CCC contains a commercial microprocessor, RAM, and VMEbus arbitration logic. The CCC acts as a dedicated processor that controls the setup, self-test, status collection, and operation of the custom logic card.

The custom logic performs the hardware functions necessary for high-speed correlation, frame synchronization, quality accumulation, and real-time trailer appendage. It also can generate simulated telemetry data at high rates for full-speed self-testing. The custom logic card can be functionally partitioned into six subsystems: Data Pipeline Input Multiplexer, Telemetry Frame Synchronizer, Output Interface, Quality Accumulator, Data Simulation Generator, and Controller Interface. Prior to operation, setup information is transferred through the Controller Interface to all the other subsystems. The setup information configures the generic subsystems to operate according to a specific mission's requirements.

The Data Pipeline Input Multiplexer provides a programmable interface between external serial data sources and the Telemetry Frame Synchronizer. During self-testing, the Data Input Multiplexer connects clock and test data from the Data Simulation Generator to the Telemetry Frame Synchronizer.

The Telemetry Frame Synchronizer accepts serial clock and test data and outputs parallel, synchronized telemetry frames and status information. It also performs reverse



High-Rate Frame Synchronizer.

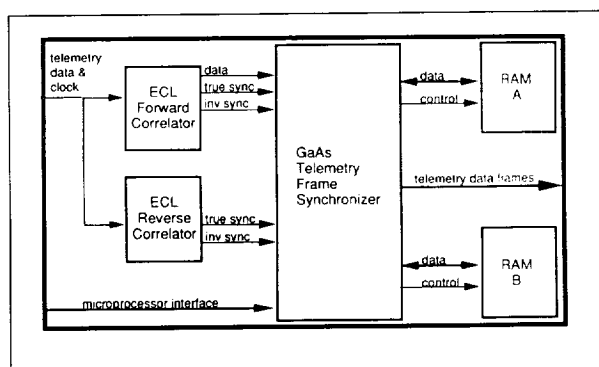


and inverted data correction and error detection. The Output Interface appends a hardware-generated, real-time quality trailer to the synchronized frames. It then selects the output path and controls the transfer of data to the next processing system.

The Quality Accumulator accepts and accumulates status-count strobes from the Telemetry Frame Synchronizer. The counts are read periodically by the CCC and formatted into a complete status block. The status block can be displayed on a terminal connected to the CCC or communicated to a higher level system controller. The Data Simulation Generator provides complete self-testing of all functions on the High-Rate Synchronizer Card with high-speed serial or parallel simulation data (300 Mbps). By comparing the status results for test runs against known correct results, the CCC can determine if the card is functioning properly before activating it for operational data.

The Telemetry Frame Synchronizer, Quality Accumulator, and Data Simulation Generator are implemented using application-specific and commercial VLSI components.

The Telemetry Frame Synchronizer subsystem, represented in the second figure, primarily consists of five VLSI circuits: two Emitter Coupled Logic (ECL) Correlator chips, one GaAs Telemetry Frame Synchronizer chip, and two commercial BiCMOS SRAMS. The serial clock data and data from the Data Pipeline Input Multiplexer are fed in parallel to each of the two ECL Correlator chips. One correlator is programmed to search for the forward synchronization pattern while the other is programmed to search for the reverse pattern. Each correlator searches for both the true and inverted cases of the sync pattern. Sync indications, clock data, and serial data are aligned and output to the



Telemetry Frame Synchronizer Subsystem.

GaAs Telemetry Frame Sync chip. If a sync pattern is matched within a programmable tolerance, a sync is signaled to the GaAs Telemetry Frame Sync (GTFS) chip, along with the number of sync errors. The GTFS chip can be programmed to accept or reject any of the four sync indications from the forward and reverse correlators (FT, FI, RT, or RI) and can be enabled to correct selectively inverted data and/or sync. Once a sync indication has been accepted, the GTFS begins its preprogrammed synchronization strategy.

The GTFS implements a programmable search, check, lock, and flywheel strategy. Upon finding sync, it creates a sync pattern search window around where it expects to find the next sync indication. The sync pattern search window allows for the programmable detection and correction of long- and short-slipped frames of up to 3 bits. Optionally, the GTFS chip can be enabled to implement a Best Match strategy. The Best Match strategy causes the GTFS chip to select the first sync pattern with the fewest errors before creating its sync pattern search window.

The GTFS implements a double buffering scheme to allow for proper status collection and time correction of reverse data, if desired. Two commercial $2K \times 9$ BiCMOS SRAMS are used to buffer frame data properly. The GTFS independently addresses each RAM, simultaneously reading from one while writing to the other. The GTFS actually can interface a variety of memory devices because of its programmable read-and-write pulse generation. Data read-out of the RAMs immediately are output on a selectable 8- to 16-bit bus along with valid data and framing control signals. Status information is collected for each frame and includes the type of frame processed (FT, FI, RT, RI), the mode of the GTFS (search, check, lock, or flywheel), sync pattern errors, slip errors, and cyclic redundancy check (CRC) errors. The status information is available to the CCC or optionally can be appended to the end of frames as they are output from the GTFS chip. The GTFS chip also delivers pulsed status events to the Quality Accumulator for quality information accumulation.

The ECL Correlator chip is a semi-custom, application-specific VLSI circuit implemented using a 6,000-gate array. The ECL Correlator chip can be programmed to correlate a programmable sync pattern of variable width from 4 to 32 bits. The ECL Correlator chip correlates for both true and inverted cases with individual programmable sync error tolerances. Unary-to-binary

conversion logic provides binary outputs of the number of errors found during each clock cycle.

The GTFS chip is a semi-custom VLSI circuit implemented using a 15,000-gate GaAs gate array. In addition to the functionality outlined above, the GTFS chip can be configured to handle variable sync word sizes (8, 16, 24, or 32 bit) and frame lengths (from 16 bits to 32 Kbits). The GTFS chip also can be configured to output data either in all cases or only during certain modes, and can be programmed for separate slip coverage during search/check and lock/flywheel modes. The CRC detection circuitry features a programmable polynomial of degree 16 and a choice of set or clear encoder initial states.

The GTFS chip accepts serial ECL clock and data input and provides a transistor-transistor logic (TTL)-compatible, 16-bit, bidirectional microprocessor interface and 16-bit frame data output interface. The GTFS chip is designed to operate at rates of up to a minimum of 300 Mbps and will dissipate one-fourth the power of ECL devices of similar integration levels.

The Quality Accumulator consists of a single Spectrum Accumulator chip. The Spectrum Accumulator is a full-custom VLSI device originally developed by The Johns Hopkins University Applied Physics Laboratory for the accumulation of sensor instrumentation events. It consists of sixteen 24-bit counters, each with programmable increment, clear, and inhibit controls. Toggling rates for each of the counters is in excess of 40 MHz. The Quality Accumulator accumulates status counts which are gathered periodically by the CCC for channel quality and status monitoring.

The Data Simulation Generator consists of the GaAs Test Pattern Generator (GTPG) chip and commercial dual-ported RAM. This chip provides for the independent generation self-test data for the HRFS. Simulated mission data is downloaded from the CCC to the dual-ported pattern data RAM.

For extensive self-testing functions, the dual-ported pattern data RAM can be accessed during GTPG operation by a control processor (the CCC). The GTPG also can partition the pattern memory into two separate buffers. In this way, a control processor can update one partition while the other partition is being output. Complete updating of the entire partition or selected updating of the data fields allows for the simulation of an extensive continuous data pattern.

Through the Data Simulation Generator, the complete card or a single function on the card can be tested without external test apparatus. Hardware and software problems on the card can be diagnosed readily and reported to a monitoring system prior to processing actual data.

The GTPG chip is a semi-custom VLSI circuit implemented using a 15,000-gate GaAs gate array. It features a TTL-compatible, 16-bit, bidirectional microprocessor interface and 16-bit memory interface with a 24-bit address space. The GTPG can be programmed to invert and/or reverse pattern data, and transfer a known number of frames or blocks through either a serial interface or through a 16-bit parallel interface. Once enabled for output, the GTPG begins its programmed sequence and acts like an independent source of data. Output data rates in discrete increments from 1 Mbps to at least 300 Mbps can be programmed into the chip.

The HRFS will find application in NASA's Second TDRSS Ground Terminal (STGT) and probably in other NASA telemetry acquisition systems such as the Data Interface Facility of the Customer Data and Operations System (CDOS). The HRFS cards also will serve as a basis for future frame synchronizers, which should operate at advanced TDRSS data rates of up to 650 Mbps. Achieving these rates will require engineers to further integrate high-speed logic into denser GaAs gate arrays, as well as to increase the pipelining in the design.

Contact: Kristin Looney (Code 521)
(301) 286-2586

Toby Bennett (Code 521)
(301) 286-5365

Sponsor: Office of Space Operations

Ms. Kristin Looney, who started at Goddard as a cooperative student in 1985, works in the Microelectronics Systems Branch. She designs and develops VLSI circuits for telemetry acquisition systems. Ms. Looney received her BS in computer science from the University of Maryland.

Mr. Toby Bennett works in the Microelectronics Systems Branch designing and developing VLSI circuits. He previously was in charge of the development of very high speed communications systems for the Internal Research and Development Department of Ford Aerospace Corporation. Mr. Bennett received his BS in electrical engineering from the University of Maryland.



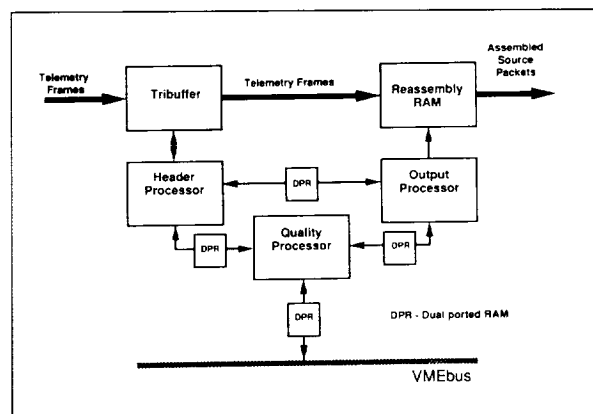
HIGH-SPEED PACKET PROCESSOR

The Mission Operations and Data Systems Directorate has completed an in-house project to develop a VMEbus-compatible Packet Processor card. The design implementation includes semi-custom VLSI devices and three microprocessors. The general requirement emphasized during the design of this card was the adaptability to extract source data from various telemetry data formats, especially packetized data, at throughput rates of up to 20 Mbps.

The throughput capability of the Packet Processor is achieved by a data pipeline consisting of two separate RAM systems controlled by specially designed semi-custom VLSI logic. The first, the Tribuffer, triple buffers input telemetry frames (up to 4 kbytes/frame) to allow a full frame period for extraction of frame- and packet-header data. The second and larger Reassembly RAM stores frame data separated by the Virtual Channel (128 kbytes/channel) and provides the capability to reassemble packets by selective readout of data pieces. This configuration has been tested successfully at rates of up to 16.5 MHz, providing data rates of up to 132 Mbps on the 8-bit-wide pipeline.

An adaptable format capability is provided by the programmability of the three microprocessors (20-MHz MC68020s) labeled Header Processor, Quality Processor, and Output Processor. The Header Processor has interface connections to the Tribuffer Controller (VLSI) and a Virtual Channel selector connection to the Reassembly RAM Controller (VLSI). The Output Processor has interface connections to the Reassembly RAM Controller. The Quality Processor does not interface with the data pipeline directly, but does communicate with the Header and Output Processors as well as with an external controller via dual-ported RAM and the VMEbus. In addition, the memory spaces of all three processors are accessible for read-and-write commands by an external controller via the VMEbus for loading software.

The Header Processor/VLSI Tribuffer Controller combination provides the following general capabilities, with the processor generating the setup controls to the VLSI device: load frame length for input data, load start and end addresses for reading output to Reassembly RAM, and read selected (header) data by loading start address and length. In addition, the VLSI Tribuffer Controller automatically cycles memory address and data buses when



Outline of the high-speed Packet Processor.

input, output, and header readings are complete and signals the processors with an interrupt.

The Reassembly RAM is partitioned for 8 Virtual Channels. The Output Processor/VLSI Reassembly RAM Controller combination provides the following general capabilities, with the processor generating output instruction codes to the VLSI device: automatically stores frame data from Tribuffer Controller into contiguous RAM for Virtual Channel identification by the Header Processor, reads pieces of data identified by instruction codes from RAM to produce reassembled output data, inserts annotation data passed with instruction codes from RAM to produce reassembled output data, inserts annotation data passed with instruction code, and inserts fill data passed with instruction code. In addition, RAM read-and-write operations can occur simultaneously, since the VLSI RAM Controller ping-pongs read/write between even and odd address spaces.

Application software has been generated for assembling packetized source data as defined by the Goddard Space Data Packetization Standard, a subset of the Consultative Committee for Space Data Systems (CCSDS) Packet Telemetry Recommendation. This standard packet format includes the contiguous insertion of variable-length source packets into telemetry transfer frames from up to eight multiplexed Virtual Channels. The locations of packets within the frame data fields are derived from a first header pointer in the frame header and packet lengths found in subsequent packet headers. This software includes verification testing and accounting functions which lead to software-limited throughput rates. Processing rates are a function of packet size (i.e., short packets require more header reading). For packet lengths of

10,200 bits (one packet per CCSDS Transfer Frame), data rates of up to 35 Mbps have been demonstrated. Future upgrades in processing rates have been anticipated in the fabrication of the card by facilitating component changes; e.g., microprocessor plug-in mezzanine modules.

Although this Packet Processor Card was designed to accomplish the packet reassembly task implied by the CCSDS recommendations, the actual function of the card is defined by the microprocessor software. This adaptability can be used to accomplish general data format conversion.

Contact: Gerald J. Grebowsky (Code 521)
(301) 286-5407

Sponsor: Office of Space Operations

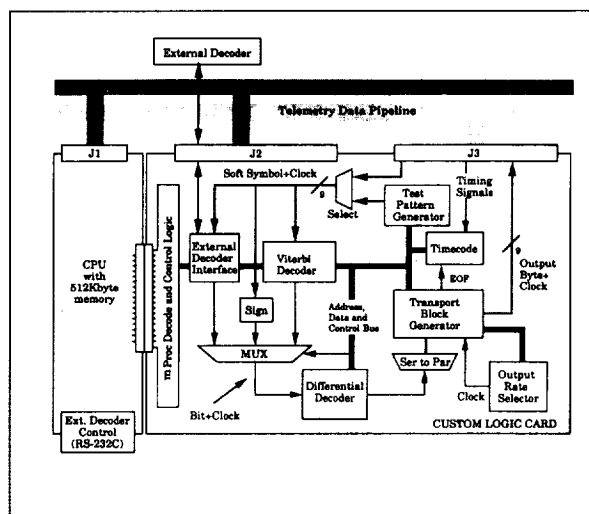
Mr. Gerald J. Grebowsky is an electrical engineer responsible for defining system processing requirements and algorithms. Mr. Grebowsky has 24 years of experience at Goddard and holds a BSEE and an MS in physics from The Catholic University of America. He has received NASA Group Achievement Awards as part of the VLSI System Design and Development Team, Image Processing Special Engineering Team, Heat Capacity Mapping Mission Project Team, Earth Resources Technology Satellite Project Team, and Large-Area Crop Inventory Experiment.

MULTIFUNCTIONAL BIT GENERATOR SUBSYSTEM

In telemetry data systems, a Bit Generator can be described as a machine that decodes symbols into bits. The Bit Generator subsystem uses the Viterbi maximum-likelihood decoding algorithm to decode symbols and correct errors. The Viterbi decoding algorithm has been used to decode convolutional encoded telemetry data streams for the last 2 decades. With the advancement of VLSI technology, this powerful decoder is available today in a single chip. One commercially available Viterbi decoder has been used to build a subsystem using the functional components approach developed by the Microelectronics Systems Branch. This subsystem complements a series of functional modules for front-end systems that can be combined to form telemetry data systems.

The Bit Generator subsystem can operate at up to 10 Mbps and provide a maximum coding gain of 5.4 dB at a 10-to-5 bit error rate (BER). The decoder chip accepts constraint lengths of $K=7$ and $K=6$ at rate $=1/2$. Both Ground Space Flight Tracking and Data Network (GSTDN) and Jet Propulsion Laboratory code vectors are supported, making this a very flexible functional component subsystem. One of the most salient features of this system is the Symbol Error Rate (SER) and BER monitoring capabilities. By re-encoding the decoded bytes the symbols (and bits) can be compared against the inputs so errors per second can be counted. By this method, the channel characteristics and the signal-to-noise ratio (SNR) can be calculated. A widely adjustable node-synchronization mechanism has been implemented in this design to provide for increased stability and control of the Viterbi decoder chip. Also, an external decoder interface is provided for use with external decoder hardware.

To fully qualify as a front-end functional component, the Bit Generator subsystem also generates generic blocks of bits at user-definable lengths. The decoded bit data is converted into a word (16-bit) packet so it can be blocked. A special time-stamp feature also is available to the user; transport blocks of data can be stamped at the end and a time-tag can then be included in the transport block. Statistical information obtained by hardware (BER and SER) can be included in the transport blocks or provided to the Monitor and Command System via the VME-bus environment.



Bit Generator subsystem functional diagram.



The Bit Generator subsystem has several functions in addition to the decoder itself. It receives input through a pipeline in byte-serial form together with a clock. This byte is called a soft symbol or quantized A/D value from a bit synchronizer source. The user selects a soft-symbol stream either from the pipeline or from an internal test-pattern generator capability. Three decoder options are available: fully VLSI-implemented Viterbi decoder, an External Decoder Interface option with control through an RS-232C interface, or a straight Sign-Magnitude bypass. The decoding method is selected by the user and then the bit stream is differentially decoded from NRZM to NRZL, NRZS to NRZL, or NRZL to NRZL. Serial-to-parallel conversion of the bit stream to 16-bit packets is completed, and then it is blocked. The data block is user-configurable, and time-tagging can be included as a header or trailer. The output is conducted back to the pipeline at a programmable rate of up to 2.4 Mbps.

The MicroElectronics Systems Branch currently is developing a prototype of the Bit Generator subsystem for a VME-based circuit board. The working prototype will be operational by spring 1991.

Contact: Caleb M. Principe (Code 521)
(301) 286-7054

Sponsor: Office of Space Operations

Mr. Caleb M. Principe, a digital hardware design engineer, has worked at Goddard since 1985. His design work focuses on the area of error-control coding and communications systems. He earned a BSEE from the University of Puerto Rico and an MSEE from The Johns Hopkins University.

HIGH-RATE VLSI-BASED LEVEL-ZERO PROCESSING (LZP) SYSTEM

In the Space Station Freedom era, telemetry data will be transported from payloads to the ground and distributed to customers by the Space Station Information System (SSIS). One primary goal of this system is to make the data transportation transparent to the customer so that the interaction with the payload takes place as if the payload were at the customer facility. The objective requires a process to remove from delivered data products all artifacts and disturbances introduced during data transport through the system. This type of processing is a

key part of what is usually referred to as level-zero processing (LZP). While the complete process of preparing telemetry data for delivery to NASA's customers requires a number of steps or levels, LZP poses a real technical challenge for NASA in the 1990s. This challenge is the result of requirements to provide real-time or near real-time LZP products at rates of up to 150 Mbps. In addition, increased use of sophisticated data formats places even more demand on NASA's future ground telemetry data systems.

The main objective of the LZP system is to restore the order of data for a given observation or collection period. Such a data set is called a data take and is delivered to the customer as an LZP product. Restoration of a data take requires one or all of the following four basic LZP functions: reassembling user packets from Virtual Channel Data Units (VCDUs); reversing "backward" playback data; merging together real-time data and playback data with proper time order; and deleting redundant data caused by the overlap between real-time and playback data.

Traditionally, such tedious LZP tasks are performed by software running on mainframe computers. To meet NASA's needs for drastically increased data speed and volume, the DSTD has proposed a new high-speed processing algorithm and architecture for the LZP system using VLSI technologies that will significantly reduce the complexity of database management necessary for reconstructing payload data streams and offer potential processing rates of up to 150 Mbps.

To achieve a low cost/performance ratio, the new architecture is based on state-of-the-art distributed real-time processing and uses a generic DSTD-developed telemetry system platform based on a functional component approach. The functional component approach uses industry-standard open bus architectures and makes use of multiple commercial and custom VLSI hardware-based cards to provide standard, off-the-shelf telemetry processing functions (frame synchronization, Reed-Solomon decoding, packet processing, etc.) for almost any telemetry data handling application.

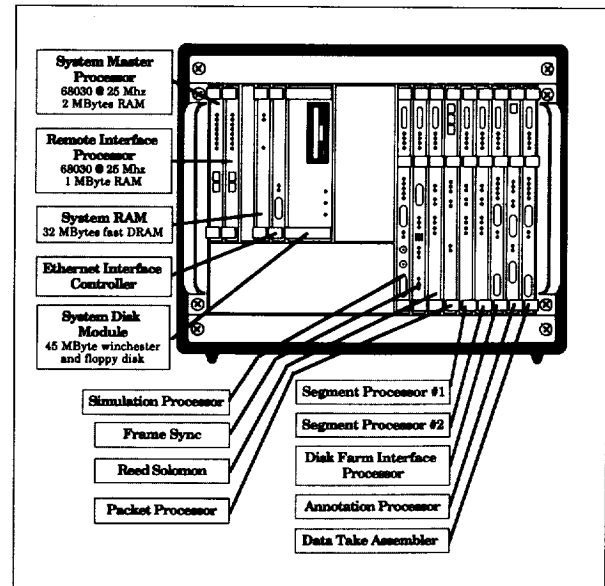
The new LZP system, called a data-take processor, is being developed in two phases. Architecturally, the systems deployed in both phases will be identical. The first-phase system will use standard, off-the-shelf 20-Mbps functional components and a 22-Gbyte, 128-Mbps

mass storage subsystem. This system is targeted for 20-Mbps operation and will be used as a testbed to streamline and optimize the LZP algorithm in preparation for phase-two development. The second-phase system will use 150-Mbps functional components currently in development at the DSTD and an 88-Gbyte, 512-Mbps mass storage subsystem that uses four 22-Gbyte, 128-Mbps mass storage subsystems in parallel.

The data-take processor will operate in three nonexclusive operational modes: real-time, quick-look, and production processing. In the real-time processing mode, customers' packets are transmitted as soon as each packet is received and reassembled. Also, the data are retained for normal production. In the quick-look processing mode, a subset of the data take will be made available to the customer within minutes of session completion. No redundancy deletion is performed. Again, the data are retained for normal production. The final and most important mode is the production processing mode. In this mode, data are processed and grouped into data takes specified by the customer through scheduling tables. The completed data take will be available to the customers within 2 minutes after data capture.

Traditionally, LZP is a two-stage process. In the first stage, a serial data stream is assembled into user packets and then stored in a mass storage buffer. The bit ordering of playback data within each packet is corrected. In the second stage, packets are sorted according to their application identification numbers (APID) and time sequence and are grouped together to form data takes.

With the data rate of 150 Mbps and average packet size of 8 Kbit, a 15-percent duty cycle operation can generate 15 million packets each orbit (assuming a 90-minute orbit). To trace every packet in the buffer would result in a huge database in the magnitude of Gbytes. The management of such a large database would be an extremely cumbersome and time-consuming task, even for a high-performance mainframe computer. Therefore, a new processing algorithm is employed that significantly reduces the size of the database. One key is to define a new class of data unit called the data segment. A data segment is a group of user packets that have identical APIDs, data direction, and a continuous time sequence. The other key is to presort packets from different sources in separate logical buffers. Accordingly, the mass storage subsystem is partitioned into a number of logical buffers. Each



The data-take processor, based on the VME dual-bus multiprocessor architecture housed in a 19- by 24-inch rack.

buffer is dynamically sized to accommodate maximum data load generated by the source for up to four orbits.

User packets from various APIDs are saved in corresponding logical buffers as data segments. Any change in the data stream that results in a reversal of data direction or a break in the time sequence for a source will result in the closing of the current data segment, opening of a new data segment, and an entry into the data segment's database. Because this action occurs relatively infrequently, the size of a data segment is significantly larger than a packet. It is reasonable to assume that there are at least 1,000 packets per segment. Thus, the data segment data base will be reduced to the level of megabytes and easily handled by microcomputers. Individual packets in a data segment are retrieved easily because the size of packets from the same source is a constant, and the starting address of a packet is a known offset from the beginning of a data segment. All processes in the second-stage LZP are simplified greatly because now they are performed on a data segment rather than on individual packets.

The data-take processor is based on a dual-bus multiprocessor architecture housed in a 19- by 24-inch rack, as shown in the first figure. The communication between microprocessors is through the VMEbus and the telemetry data flows through a custom data pipeline bus.

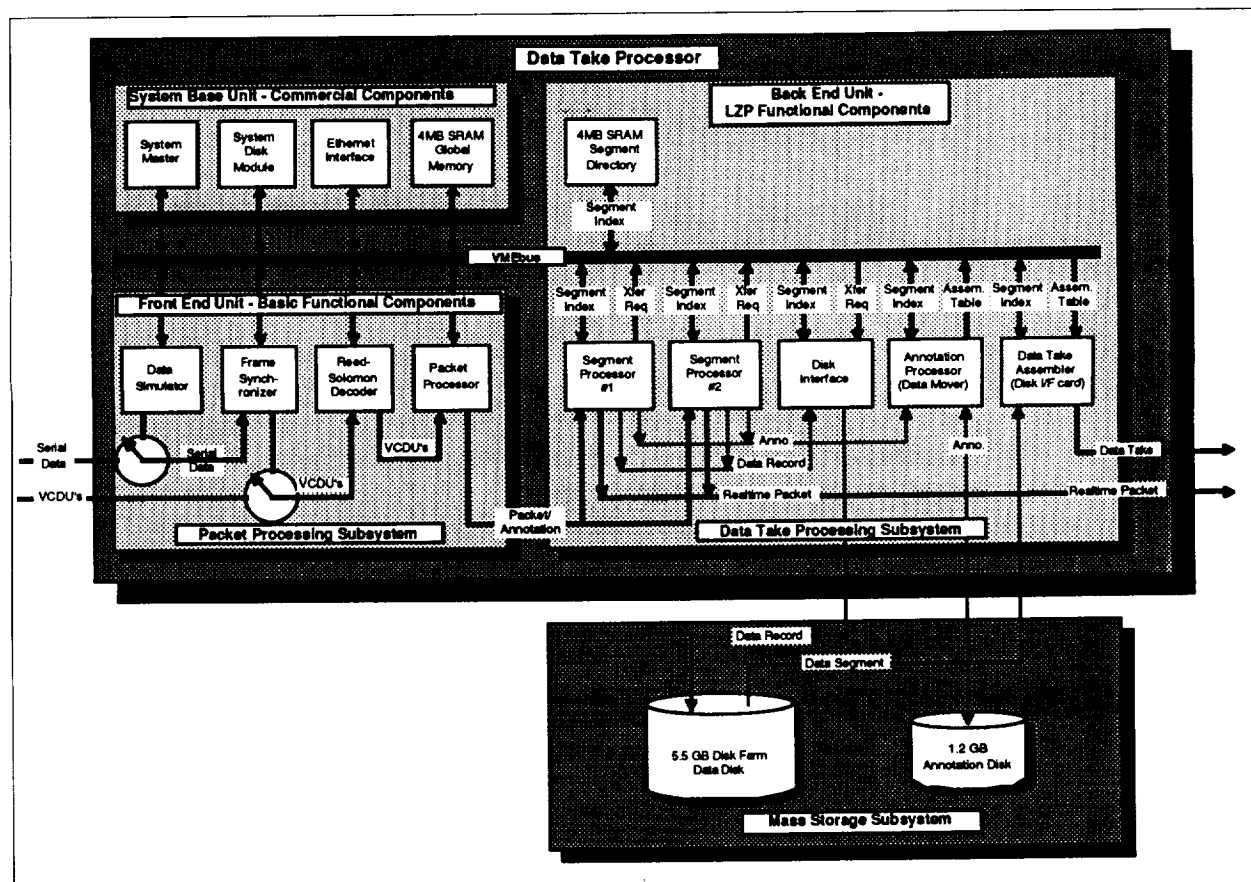


As illustrated in the second figure, the configuration of the data-take processor includes three processing units: the system base unit, the front-end unit and the back-end unit, and the mass storage subsystem.

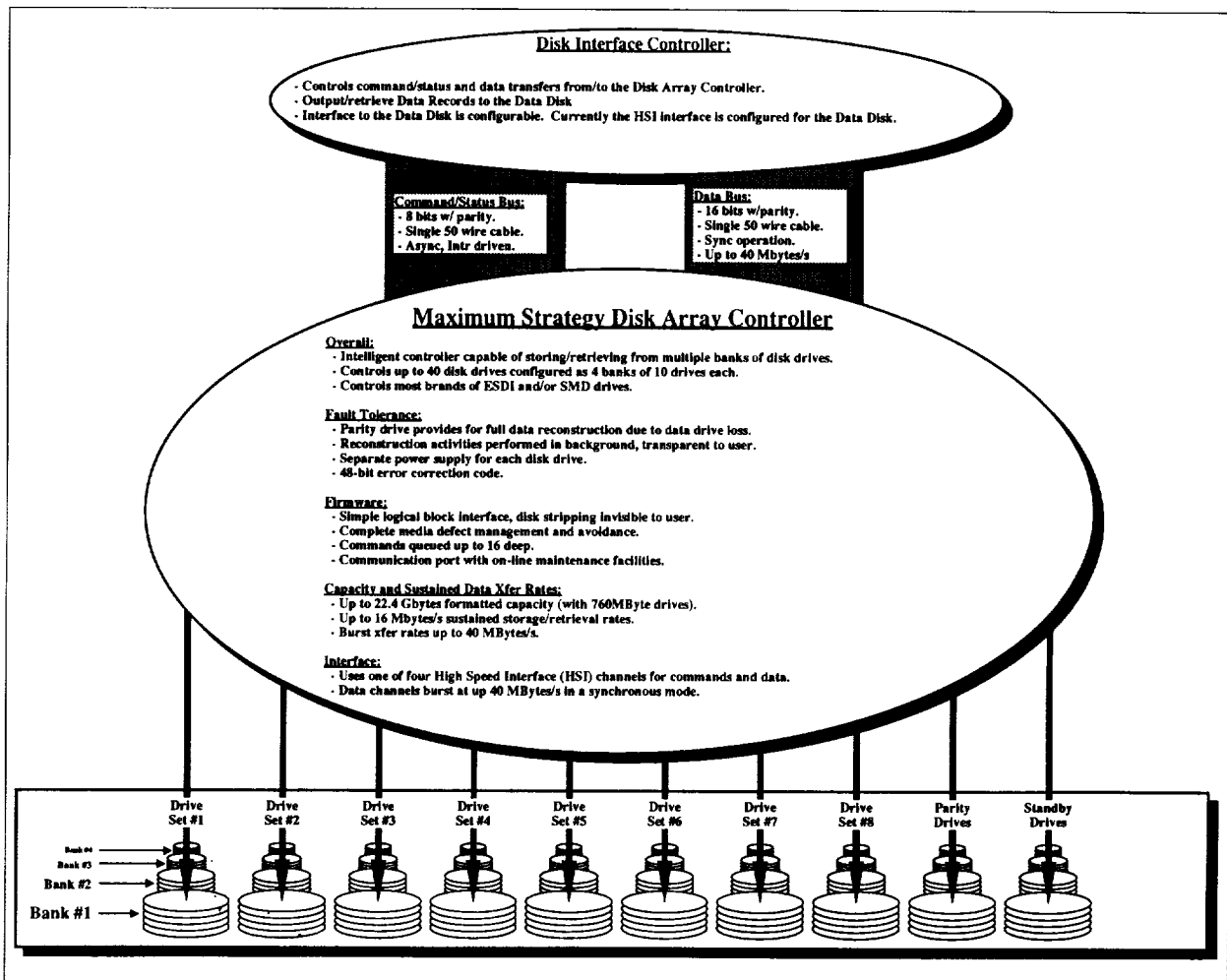
The system base unit is responsible for overall system control and serves as the system master. Through the use of BaSE and MEDS, both DSTD-developed system software packages, the operator controls LZP operations by sending commands and gathering status to and from other system components through the unit. In addition, the system base unit maintains the quality and accounting data files and production catalog files. The system base unit also provides system disk and memory, as well as the Ethernet interface to remote terminals or workstations.

The front-end unit is responsible for reassembling user packets from serial data in NASA communications

block format. It consists of the frame synchronizer, Reed-Solomon decoder, packet processor, and data simulator. The serial telemetry data is sent to the frame synchronizer and synchronized to the VCDUs. Reed-Solomon error decoding is done when coded VCDUs are passed through the Reed-Solomon decoder card. At the next processing node, the packet processor strips off the headers and trailers, reassembles user packets, reverses backward data for playback packets, and sends them to the back-end unit. The packet processor also generates quality and accounting data and annotates the packets. Meanwhile, the packet processor monitors the sequence numbers and space time of each packet to define data segments. If a change in data direction or a gap in space time is detected, the packet processor will terminate the current data segment, make a new entry in the segment directory, and start a new segment with the new packet. The data simulator generates NASA communications blocks and VCDUs used for system test and diagnostics.



The configuration of the data-take processor, including three processing units and a mass storage subsystem.



Some of the characteristics found in the mass storage subsystem and the types of functions and performance required for the data-take processor system.

The major function of the back-end unit is to reassemble the specified data takes from user packets. The five processing modules in the unit consist of two segment processors, a disk-interface processor, an annotation processor, and a data-take assembler. The segment processors separate the annotation data and user packets and sort the user packets according to their APIDs before saving them in a local memory buffer. When the data in any local memory buffer reaches a predetermined size, that data will be transferred to the disk-interface processor for storage on the mass storage subsystem. The annotation data will be passed to the annotation processor for storage on the mass storage subsystem.

The annotation processor monitors incoming packets. When all data from a source for a specified observation

have been received, it will generate a data-take assembly table and pass it to the data-take assembler. The data-take assembler uses the data-take assembly table and segment directory to assemble a data take. The table specifies data pieces in the data take, and the directory is used to compute the addresses of these data pieces on the mass storage subsystem.

The data are transferred from the disk, block by block, to a local buffer to the output port. In this way, the data can be output selectively and redundant data can be deleted. If the data segment to be output contains backward playback data, the output processor restores the order simply by transferring the last-received packet first and the first-received packet last. Furthermore, the



data-take assembler generates data-take annotations and attaches them to the data takes as either headers or trailers.

The mass storage subsystem requirements for the first-phase prototype data-take processor include sustained transfer rates of up to 128 Mbps, random-access storage in the tens-of-Gbytes range, and multiple read/write ports. Only a few years ago, storage systems which could support these requirements were either not available or were very expensive, one-of-a-kind, research tools. Today, a number of vendors offer cost-effective, off-the-shelf systems which can meet the requirements. These systems use large arrays of disk drives grouped in parallel to achieve various combinations of high speed, density, flexibility, and reliability. The third figure shows some of the characteristics found in a state-of-the-art parallel disk system and the types of functions and performance required for the data-take processor.

The prototype LZP system is configured to handle up to eight Virtual Channels and 16 sources with combined data volume of 5 Gbytes per orbit. That capacity can be expanded to 32 sources by configuring four segment processors on the system. For greater demands, multiple systems can be configured in parallel, each being called a processing channel and assigned a subset of Virtual Channels. The telemetry data stream can be steered into different processing channels in accordance with a nearly unlimited number of Virtual Channels and sources.

The prototype architecture and implementation of the high-speed LZP system has been shown. Because of the new processing algorithm and VLSI technology, the prototype system features compact size, low cost, high processing throughput, easy maintainability, and increased reliability. Though extensive control functions have been done by hardware, the programmability of processing tasks makes it possible to adapt the system to different data formats and processing requirements.

Contact: Ward P. Horner (Code 521.1)
(301) 286-5804

Jianfei Shi (RMS Technologies, Inc.)
(301) 286-5322

Sponsor: Office of Space Operations

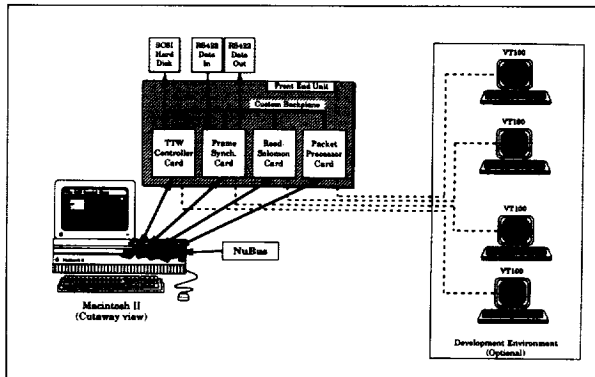
Mr. Ward P. Horner is Manager of the Data Storage Technology RTOP and has 9 years of experience at Goddard. He earned a BSEET from Capitol College and received a NASA Group Achievement Award in 1989 as part of the VLSI System Design and Development Team. Mr. Horner specializes in the design of multiprocessing hardware and software implementations. He manages, coordinates, and designs a variety of sophisticated hardware- and software-oriented projects.

Mr. Jianfei Shi is chief designer of the LZP system. He has 6 years of experience designing complex telemetry data systems and has been with RMS Technologies, Inc., for 3 years. He earned an MSEE from the University of Adelaide in Australia. He received a NASA Group Achievement Award in 1989 as part of the VLSI System Design and Development Team. Mr. Shi specializes in system design and implementation.

TRANSPORTABLE TELEMETRY WORKSTATION (TTW) SYSTEM

NASA has responded to the Space Station Freedom era with a continuing effort to combine a modular design approach with state-of-the-art VLSI technology in order to develop telemetry data-processing systems capable of meeting customers' needs for many years. As part of this effort, the DSTD, in cooperation with Clemson University, has developed a Transportable Telemetry Workstation (TTW) for performing a number of telemetry data-processing functions such as synchronization, Reed-Solomon encoding, etc., at moderate data rates of 1 to 5 Mbps. These functions can be combined to provide for such data handling capabilities as telemetry and command (TAC) and LZP. LZP will require back-end functions for removing all data disturbances and will be added in the future to make the TTW a complete data-take processor.

The front end of a data-take processor is primarily responsible for assembling user packets from serial data in NASA Communications Division block format. It consists of the frame synchronizer, Reed-Solomon decoder, packet processor, and data simulator (which is provided on the frame synchronizer in the TTW).



TTW system architecture.

The TTW is primarily an adaptation of the VLSI telemetry components and architectures already developed by NASA's DSTD to the system architecture of the Macintosh II family of computers and its NuBus implementation. The figure illustrates the general architecture of this next-generation telemetry system.

The TTW front-end unit consists of four cards: the TTW controller card, the frame synchronizer card, the Reed-Solomon decoder card, and the packet processor card. All cards are resident in a Macintosh II and operate completely independent of the Macintosh system with status information and special telemetry data segments being passed to the Macintosh user-interface application across the NuBus.

The TTW controller card is a real-time controller responsible for configuring and monitoring the status of other cards in the system based on user-input received from the Macintosh application. The controller card also possesses a small computer system interface (SCSI) controller so that incoming telemetry data can be stored in real-time for later retrieval as needed.

The frame synchronizer card has been implemented using NASA's VLSI telemetry processing chip set. As a set, these devices perform high-speed NASA communications block processing, telemetry frame synchronization, real-time trailer appendage, and cumulative data quality generation. Telemetry data enters the TTW through the frame synchronizer in the form of an RS422 interface; an RS422 output path also exists on this card. This output path can allow real-time data to be passed through the TTW so that systems may be chained together, or stored data (from the SCSI disk) may be transmitted, allowing

the TTW to perform as a data-rate changer if needed. These are only two of the many possible uses for this extremely flexible configuration.

The Reed-Solomon card is responsible for detecting and correcting errors in the telemetry data stream. This card receives its data input primarily from the frame synchronizer and transfers the corrected data to the packet processor card, whose primary responsibility is to transform the telemetry data blocks received as input into user packets for storage on the system's SCSI disk.

The custom backplane shown in the figure actually consists of four completely independent buses, each of which also operates independent of the NuBus. The custom backplane possesses a von Neumann-type bus consisting of 24 address bits and 16 data bits. This bus is used exclusively by the controller card for communicating with other cards in the system. Also part of the custom backplane are two custom-protocol FIFO buses to be used for transferring telemetry data among the cards of the front-end system. Finally, there is a daisy-chain bus to be used primarily for communications between two physically adjacent cards in the system.

Each card in the system has one or more Motorola 68020s under the control of a real-time, multitasking operating system which provides many multi-processing functions such as task synchronization. Also, each card's application software executes within the DSTD-developed BaSE and the MEDS environments. These environments are part of DSTD's Functional Components Approach-specific software environments and provide many functions necessary to system operation.

A development interface also is found on every card in the form of a VT100-compatible terminal interface. This interface can be monitored during system integration and troubleshooting and can be used for software maintenance as needed. Finally, the controller card also can serve as a development system for the other cards in the system. Since this card already has an SCSI controller, disk-possessing development tools can be attached to the controller card, and a driver placed into the controller card's operating system will allow the controller card to have access to all tools necessary for application development.



The user-interface software is in the form of a standard Macintosh application and serves to isolate the user from many of the tedious details of configuring the TTW for operation. The user is responsible for providing key pieces of information specific to a particular mission. Once setup is complete, the information is transferred to the controller card. The controller card then configures the remaining cards in the system and monitors system operation. Status information is gathered by the controller and then transferred to the user application for monitoring overall system performance.

Development of the TTW began in summer 1989 and will continue through 1991. The ultimate goal of the TTW is to provide full data-take processing functions for moderate data rates at a low cost to consumers. The prototype architecture for the TTW has been presented. This architecture takes advantage of state-of-the-art VLSI technology and multiprocessing techniques to produce an extremely compact, low-cost, and flexible system which can be maintained easily and customized to meet future telemetry processing needs.

Contact: Carol Dominy (Code 521)
(301) 286-5406

Kevin Kay (Code 520)
(301) 286-5356

Sponsor: Office of Space Operations

Ms. Carol Dominy has been the Project Manager of the TTW since 1989. She received her BS in electrical engineering from the University of Tennessee. She has been at Goddard for 6 years, during which time she has been involved in the design and implementation of several real-time hardware components used for telemetry data processing. Her interests include microprocessor system design and high-speed computer architectures.

Mr. Kevin Kay received his BS and MS in computer engineering from Clemson University. He has been an employee of RMS Technologies for 1 year, but has worked with the TTW project since 1989 when he was a graduate student. Mr. Kay has worked extensively in the areas of real-time hardware and software development and also is interested in the performance analysis of alternative computer architectures.

OPEN SYSTEM FOR COORDINATING AUTOMATED RESOURCES (OSCAR)

As the development of distributed systems for heterogeneous processing systems becomes more common, the need for tools above and beyond low-level network routines becomes apparent. The Open System for Coordinating Automated Resources (OSCAR) provides development support and run-time management of distributed tasks and communications. OSCAR consists of a library of high-level programming interfaces, a set of utilities, and a run-time kernel for each processing node. A prototype of the OSCAR library has been developed for Sun workstations using TCP/IP protocols, and a port to the Apple Macintosh is under development.

The OSCAR library is a set of C++ classes providing a consistent programmer interface across different hardware platforms. In OSCAR, a programmer creates an agent object. Through this agent object, a programmer can register a name, look up the names of other agents, send data to other agents, and receive data from other agents. OSCAR handles the low-level details such as interfacing to the underlying network and buffering incoming messages. OSCAR also provides a mapping of symbolic names of agents to their physical network addresses. This enables applications in a distributed system to be moved easily among machines without the need to reconfigure network addresses. As an aid to network management, agents keep track of traffic statistics (such as the number of messages received and sent) and log errors to files.

The class design isolates network, operating system, and protocol-specific information to one or two classes, which are not accessed directly by a user application. Such modularity allows easy porting of the OSCAR library to new machines while providing support for different network protocols. Even more importantly, applications which use OSCAR can be ported to other platforms with no changes to the communications code.

OSCAR is being developed to support a number of projects within the Data Systems Technology Division, including the Intelligent Control Center project and the Ground Operations Technology Testbed. Future plans are to build utilities which will allow the user to graphically construct components such as distributed agents, task specifications, script-driven stubs, and node-to-node protocol specifications. Run-time utilities will support the

automatic assignment of tasks to machines and provide network management support for automated failure recovery and reconfiguration.

Contact: Robert E. Dominy (Code 522)
(301) 286-4196

Sponsor: Office of Space Operations

Mr. Robert E. Dominy has 5 years of experience in Goddard's Automation Technology Section. He currently develops technology for distributed knowledge-based systems. His research interests include artificial intelligence and machine learning. Mr. Dominy earned a BA in computer science from the University of Tennessee. He received a Group Achievement Award as a member of the Space Station Flight Telerobotics System Phase-B Study Team.

POLYNOMIAL TIME ALGORITHM FOR SINGLE-RESOURCE SCHEDULING

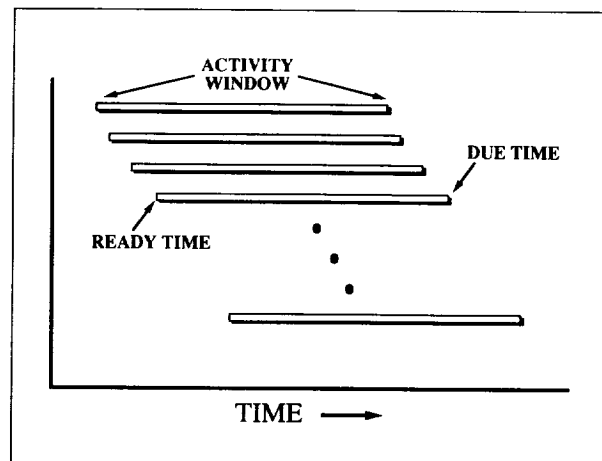
NASA repeatedly encounters activity scheduling problems. These problems involve the allocation of limited resources to activities of finite duration, often subject to constraints which restrict the specific time each activity may be scheduled. A common approach to solving these problems has been to use heuristics in an expert or knowledge-based system. An alternative, which has been considered infrequently, is to use mathematical optimization techniques. Although many activity scheduling problems are not solved feasibly with an optimization algorithm, others are solved efficiently and effectively. The number of activity scheduling problems with computationally feasible solutions continues to increase.

The general case of maximizing the number of activities with specified ready and due times which are scheduled on a single resource is known not to have a polynomial time solution; i.e., a solution where the number of arithmetic steps is a polynomial of the number of activities. A Goddard-supported study of the application of combinatorial optimization techniques to activity scheduling determined the existence of a polynomial time solution for a special case of this single-resource scheduling problem. Further investigation resulted in the development of polynomial time algorithms for two previously unsolved special

cases. Each algorithm provides an optimal solution in a finite number of arithmetic steps for one of these two special cases. The number of steps does not exceed a third-order polynomial function of the number of activities, denoted $O(n^3)$ where n is the number of activities. A combination of these two algorithms also provides a near optimal, polynomial time solution for the general case.

The polynomial time solution uncovered in the activity scheduling study is for the special case where the sequence of activities, ordered by increasing ready times, is identical to the sequence of activities ordered by increasing due times. The first figure illustrates this special case. The algorithm for this special case is based upon the theoretical result that, for any feasible schedule, the sequence of scheduled activities has start times ordered by increasing ready times (or by increasing due times). In solving this special case of the single-resource scheduling problem, the number of computations does not exceed a second-order polynomial function of the number of activities, $O(n^2)$.

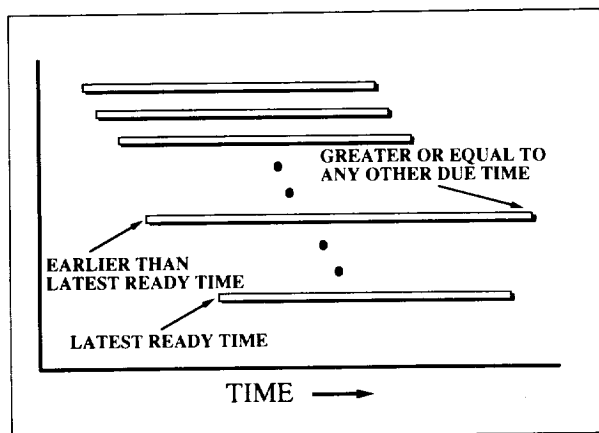
In the first previously unsolved special case, the sequence of activities ordered by increasing ready times is identical to the sequence of activities ordered by increasing due times with the exception of one activity with a ready time earlier than the latest ready time and a due time equal to or greater than the



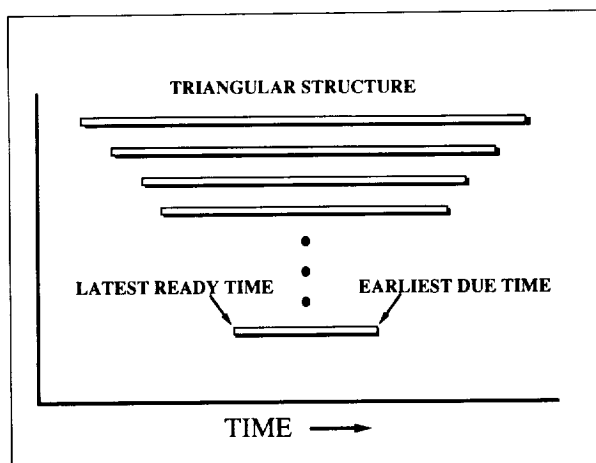
A special, single-resource scheduling case where the sequence of activities, ordered by increasing ready times, is identical to the sequence of activities ordered by increasing due times.



due time of any other activity. The second figure illustrates this previously unsolved special case. This special case is solved by replacing the original problem with an equivalent set of independent subproblems of the form shown in the first figure and solving each of these subproblems with the $O(n^2)$ algorithm. Since the number of subproblems is smaller than



A special case solved by a polynomial time algorithm, in which the sequence of activities ordered by increasing ready times is identical to the sequence of activities ordered by increasing due times with the exception of one activity with a ready time earlier than the latest ready time and a due time equal to or greater than the due time of any other activity.



A second, special case solved by the polynomial time algorithm, in which the sequence of activities ordered by increasing ready times is identical to the sequence of activities ordered by decreasing due times.

or equal to the number of activities in the original problem, the optimal solution for this problem is determined in a maximum of $O(n^3)$ computations.

In the second previously unsolved special case, the sequence of activities ordered by increasing ready times is identical to the sequence of activities ordered by decreasing due times. The third figure illustrates this special case. The algorithm for the special case is based upon the theoretical result that, when the activities to be scheduled exhibit the specific triangular structure shown, any feasible schedule can be (re)arranged such that the start times of activities starting prior to the earliest due times are in a sequence of increasing ready times and such that the end times of activities ending after the latest ready time are in a sequence of increasing due times. A total of $2n$ sequences must be evaluated to solve this problem. Since each evaluation requires $O(n^2)$ steps, the optimal solution for this problem also is determined in a maximum of $O(n^3)$ computations.

The importance of this work extends beyond the specific single-resource scheduling problem addressed in this investigation. Single-resource scheduling problems arise in practice, for example, when scheduling jobs on a uniprocessor computer and scheduling observations for an independent, space-based pointing instrument. A multiple-resource scheduling problem may be treated effectively as a single-resource scheduling problem if one resource, acting as a bottleneck, determines the solution. An example is scheduling assembly of sensitive components at a facility with one clean room. Some multiple-resource scheduling problems can be decomposed into multiple, single-resource scheduling problems. A hybrid approach which employs heuristics to decompose an otherwise intractable real-world activity scheduling problem into a sequence of single-resource scheduling problems may provide a near-optimal solution. Scheduling requests for TDRSS is an excellent example of the type of problem which appears potentially amenable to the hybrid approach.

Recently, the algorithms developed in this investigation have been embedded in a PC-based, proof-of-concept prototype which schedules requests for the TDRSS. These requests model the workload projected for the 1995 time period. Running on an 8-MHz PC-Advanced Technology (AT) without a math coprocessor, the prototype schedules 1 week of requests for TDRSS resources (1,584 requested activities) in approximately 4

minutes. The prototype is sufficiently general to be tested on other, similar scheduling domains such as the Deep Space Network.

Contact: Larry Hull (Code 522)
(301) 286-3009

Sponsor: Office of Space Operations

Mr. Larry Hull is a senior computer engineer with more than 20 years of experience at Goddard in areas as diverse as real-time operational support for manned and unmanned spaceflight missions, computer performance and capacity management, discrete event simulation of computer and communications systems, expert systems, activity scheduling, and project management. He received a BS in mathematics from Worcester Polytechnic Institute, an MS in physics from Northeastern University, and both an ME in engineering administration and an ME in computer science from George Washington University. Mr. Hull's primary research interests focus on artificial intelligence and human-computer interaction.

THE TDRSS ONBOARD NAVIGATION SYSTEM (TONS) SIMULATED FLIGHT ENVIRONMENT SOFTWARE

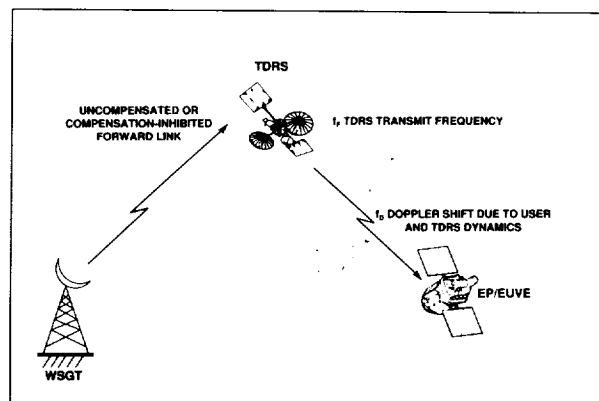
Currently, TDRSS supports user orbit determination through ground-based, two-way tracking. Future user mission needs, however, will require increased user autonomy, real-time navigation, and improved navigation accuracy. In the TDRSS Onboard Navigation System (TONS) experiment, the capability to flight-demonstrate one-way, forward-link TDRSS navigation service for on-board navigation of user spacecraft will be performed. The TONS experiment includes hardware components flown onboard the Explorer Platform/Extreme Ultraviolet Explorer (EP/EUVE) spacecraft and the ground-system data-processing segment.

In support of this experiment, a major research effort to investigate the feasibility of performing onboard navigation using one-way, forward-link TDRSS data has completed its initial phase of a ground demonstration model called the TONS Ground Support System (TGSS). The TGSS is designed to satisfy the TONS experiment objectives, which are to verify the accuracy, performance, and architectural concepts of performing high-precision orbit determination onboard user spacecraft by the use of TDRSS data. Such an

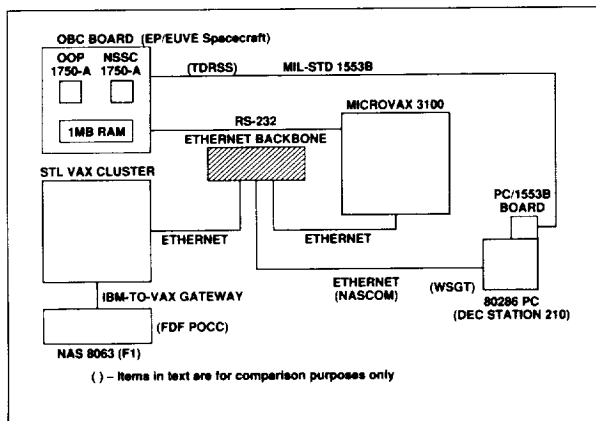
experiment could replace ground tracking stations, thus providing a cost-effective NASA alternative to the classic ground support system for orbit determination.

The most challenging objective of the TONS experiment, which was assigned to the TGSS, was to develop flight navigation software to model the flight environment onboard the EUVE spacecraft. Since the flight software will be used in future missions in conjunction with the TONS experiment, there were several key operational and performance requirements that had to be taken into consideration which were unique and difficult to implement. For example, the flight software shall reside on a specific 1,750-A microprocessor with limited memory; it shall interface with the existing EP Coprocessor Flight Executive (COP); it shall be implemented in Ada language in order to interface with software on several different computers; and it shall process specified amounts of tracking data in a certain amount of time using a limited percentage of the computer resources. As a result, the TGSS is comprised of various hardware components and complex software algorithms to model the spacecraft environment.

The hardware components were selected in such a manner as to closely duplicate the hardware architecture onboard EUVE so that TDRSS one-way, forward-link Doppler tracking data extracted onboard EUVE and downlinked in the EUVE telemetry stream to Goddard's Flight Dynamics Facility can be simulated. In the second figure, the National Advanced Systems (NAS) 8063 and the DEC VAX cluster model the EUVE Payload Operations Control Center by capturing and processing the extracted EUVE telemetry data. Next, the MicroVAX



Drawing of the planned TDRSS one-way, forward-link tracking system.



Hardware configuration model of the TONS simulated flight environment software.

3100 minicomputer is used to provide report screens of uplinked commands and downlinked data and to simulate data communications from the NAS and DEC computers to the DEC Station 210 PC. Then, the PC models the ground processing functions of the White Sands Ground Terminal facility for the TONS experiment. Finally, the two Military Standard 1,750-A microprocessors simulate the communications and data handling portion of the onboard computer of the EP/EUVE spacecraft.

Support software, which consisted of a communications prototype, was built successfully and demonstrated the ground and spacecraft communications data link using the selected hardware architecture. The second figure illustrates how the communications prototype software along with the various hardware components were used to simulate the telemetry path of extracted EUVE spacecraft data.

Likewise, the TGSS software is comprised of several individual software components to satisfy the TONS experiment objectives. The onboard software component emulates the onboard processing of extracted Doppler data for orbit determination. The experiment data-processing and analysis software and the operational support software components simulate the TONS telemetry and perform various tasks relating to telemetry processing, orbit determination comparisons, and data-quality analyses.

The following capabilities were implemented in the initial phase of the TGSS. The onboard orbit determination algorithms were verified, the communications data loop was prototyped to test the new hardware fully, and the experiment data-processing and analysis software was

completed. This effort will enable us to port the navigation software to the 1,750-A and to introduce the COP in the later phase of the TGSS. The project is targeted for completion by the end of May 1991.

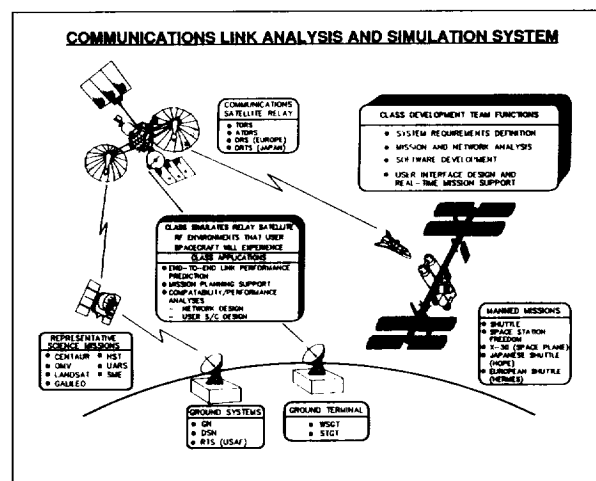
Contact: Terri L. Wood (Code 552)
(301) 286-7527

Sponsor: Office of Space Operations

Ms. Terri L. Wood coordinates and manages (and participated in the development of) the TGSS software in the Flight Dynamics Division of the Systems Development Branch. Ms. Wood has worked at Goddard for 7 years and earned a BS in mathematics from the University of Maryland.

SATELLITE COMMUNICATION HARDWARE EMULATION SYSTEM (SCHES)

The Communications Link Analysis and Simulation System (CLASS) has been developed by Goddard's Networks Division to provide a tool for evaluating the performance of space communication links through the network communications and tracking support elements, especially TDRSS. Subsequent enhancements and extensions of the system have expanded the CLASS system capability to provide a general-purpose communications system analysis and design tool for use by both the network and the network user. CLASS models all elements



CLASS, developed to evaluate the performance of space communication links through network communications and tracking support elements.



elements enables us to observe the effects these changes have on the overall channel performance. In particular, it affords us the ability to characterize the transient features of TDRSS.

When large amounts of data have been collected on the behavior of a particular hardware module, a true hardware simulation for that hardware subsystem may no longer be necessary. Instead, the simulation can be replaced with a functional model that uses appropriate statistics to corrupt the digital data stream. This functional model can provide the same accuracy as the direct emulation model, when predicting steady-state channel performance, but with the potential for enormously increased simulation run speeds.

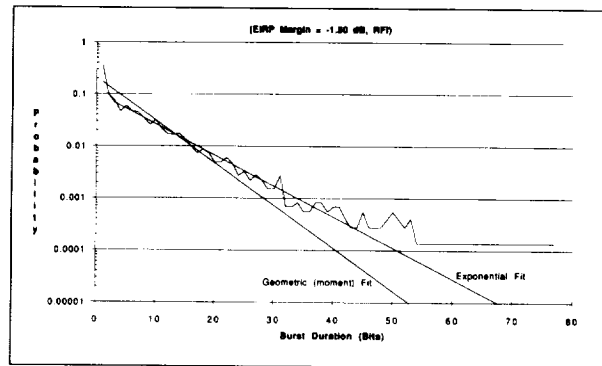
The computational support for SCHES is provided by software hosted on an HP9000 computer, running under a UNIX operating system environment. The system includes a user-friendly interface for run control, provided on a Macintosh II. The capability to visually monitor test run activities is supported through the use of a video monitor.

SCHES was tested during the course of a task to develop a complete model simulation of the Orbital Maneuvering Vehicle (OMV) video telemetry return link. OMV was to be a remotely piloted spacecraft, designed to be part of the space transfer system.

The OMV video signal needed to be extremely robust to allow the pilot on the ground to view a target. Video compression and forward error correction, as described below, ensured the quality of the picture at the ground terminal. The camera's video signal was first digitized and compressed by 2-D differential pulse code modulation and Huffman coding. Error resistance was added through the use of Reed-Solomon encoding and Helical interleaving. A rate-1/2 convolutional code was added with periodic convolutional interleaving so that the data could be relayed via TDRSS. Then, from White Sands Ground Terminal, the data was sent to Johnson Space Center via DOMSAT.

The pilot's commands to the OMV vehicle were transmitted by the forward link. Errors in the data transmission, however, were expected to result primarily from thermal noise and radio frequency interference (RFI) corruption of the TDRSS S-band return link between the OMV flight vehicle and the TDRSS spacecraft.

The essential concepts of the SCHES model of the OMV channel simulation are illustrated in the second figure.



Exponential and geometric fits to burst duration statistics.

The model is separated into three subsystems: the video compression unit and video reconstruction unit, which are modules unique to OMV; the Reed-Solomon coder-encoder subsystem; and the TDRSS link subsystem, which is part of standard CLASS. Each subsystem is further divided into modules. Each module simulates a hardware function and produces a data file which, in turn, drives the next module.

The DOMSAT link was not discretely modeled in the SCHES simulation because the BER through this link was reduced, through forward error correcting, to a very low value. The other blocks in the system were exact, bit-by-bit hardware emulations of the actual system and together were used to characterize both transient (synchronization) behavior as well as static behavior of the channel.

More than 20 simulations of the OMV return video link were completed, each requiring 25 hours of run-time. Runs were made with 50 frames apiece of data (approximately 5 million bits), and had varying effective isotropic radiated power (EIRP) margins and RFI environment conditions. The hardware simulation and the many test points provided the user with equivalent information to that acquired from actual hardware tests. Statistical processing was done by manipulating the data files after the simulation was over and by producing plots, histograms, and tables.

Statistics from different runs were plotted versus EIRP margin for each RFI condition. This data provided an easily understood statistical display of the actual performance characteristics of the video channel under varying environmental conditions.

**Summary of OMV when Operating with a 1.5-dB EIRP Margin
in a Worst-Case TDRS-East Environment**

Channel Characteristics	Units	Value
Analysis ID	-	A908041411
RFI	-	SSA,TDRS.EAST
EIRP Margin	dB	-1.5
Data rate	Kbps	972
Number of lines per subframe	-	20
Initial stepsize	-	16
Number of frames	frames	50
Number of codewords transmitted	codewords	2390
Number of (convolutionally coded) symbols	symbols	9,751,200
Statistics Before DE-PEI	Units	Value
Mean Clock Jitter	% of symbol	-0.57
Standard Deviation of the Clock Jitter	% of symbol	2.18
Symbol Slip Rate	-	0
Random Error Rate	-	1.17E-2
Number of Bursts	bursts	186,577
Burst Window	symbols	12
Mean Burst Error Duration	symbols	13.68
Standard Deviation of Burst Error Duration	symbols	11.10
Mean Errors Per Burst	symbols	3.96
Standard Deviation of Errors Per Burst	symbols	2.43
Mean Space Between Errors in a Burst	correct symbols	3.54
Standard Deviation of Space Between Errors in a Burst	correct symbols	3.12
Error Rate Due to Burst	-	7.58E
<u>(# of Bursts) (Mean # of Errors Per Burst)</u> Number or Symbols Transmitted		
Total Error Rate = (Error Rate Due to Bursts) + (Random Error Rate)	-	8.7E-2
Transition Probabilities		
Pr(0/1)	-	.61274
Pr(1/1)	-	.12864
Pr(2/1)	-	.09934
Pr(3/1)	-	.06842
Pr(4/1)	-	.04940
Pr(5/1)	-	.02341
Pr(6/1)	-	.01091
Pr(7/1)	-	.00714
Pr(7/0)	-	.61286
Pr(6/0)	-	.12810
Pr(5/0)	-	.09973
Pr(4/0)	-	.7571
Pr(3/0)	-	.04215
Pr(2/0)	-	.02348
Pr(1/0)	-	.01075
Pr(0/0)	-	-.00722
Predicted Viterbi Decoder Error Rate	-	2.64E-3
Analysis ID	-	A908041411



**Summary of OMV when Operating with a 1.5-dB EIRP Margin
in a Worst-Case TDRS-East Environment**

Statistics After DE-PEI	Units	Value	
Random Error Rate		1.17E-2	
Number of Bursts	bursts	198,021	
Burst Window	symbols	12	
Mean Burst Error Duration	symbols	14.93	
Standard Deviation of Burst Error Duration	symbols	12.20	
Mean Errors Per Burst	symbols	3.73	Standard
Deviation of Errors Per lburst	symbols	2.17	
Mean Space Between Errors in a Burst	correct symbols	4.10	
Standard Deviation of Space Between Errors in a Burst	correct symbols	3.08	
Error Rate Due to Bursts	-	7.57E-2	
Statistics After the Biterbi Decoded	Units	Value	
Total Error Rate	-	5.219E-3	
In-Sync Error Rate	-	5.219E-3	
Number of Bursts	bursts	4730	
Burst Window	bits	6	
Mean Burst Error Duration	bits	7.96	
STandard Deviation of Burst Error Duration	bits	6.84	
Mean Errors Per Burst	bits	4.77	
Standard Deviation of Errors Per Burst	bits	3.75	
Longest Burst	bits	57	
Statistics After the Reed Solomon Decoding	Units	Value	
Uncodable Codewords in-Sync	Codewords	162	
Uncodable Codewords Out-of-Sync	Codewords	28	
Decodable Codewords In-Sync	Codewords	2209	
Decodable Codewords Out-of-Sync	Codewords	0.0	
In-Sync Codeword Error Rate	-	.068	
First In-Sync Codeword	-	20	
a) The first 8 codewords are dummy data used in initialize the helical interleaver.			
b) A codeword is declared in-sync when its sync counter value stays at 15 for two codewords.			
First Decodable Codeword After Declaring In-Sync	-	29	
Number of Freewheeling Events	-	47	Lowest
Freewheeling Value	-	14	
Max Sync Counter Value	-	2	
Number of Subframe Replacements During Initial Sync	Subframes	24	
Number of Subframe Replacements After Initial Sync	Subframes	148	
Total Number of Subframes	Subframes	600	



Analysis Section. He is responsible for the development of the CLASS program and RF analyses for all major NASA spaceflight programs. In 1989, he received the NASA Exceptional Achievement Award for his contributions.

AN INTERFERENCE MITIGATION METHODOLOGY FOR SCHEDULING IN SPACE COMMUNICATIONS

Projected or planned increases in the number of user spacecraft and data rates supported by TDRSS in the S-band and in the Ku-band could result in significant mutual interference and communications schedule conflicts. More attention must be paid to this problem in terms of scheduling. An interference mitigation methodology that considers all relevant communications parameters and that helps avoid severe restrictions on both network and user resources in communications scheduling has been developed.

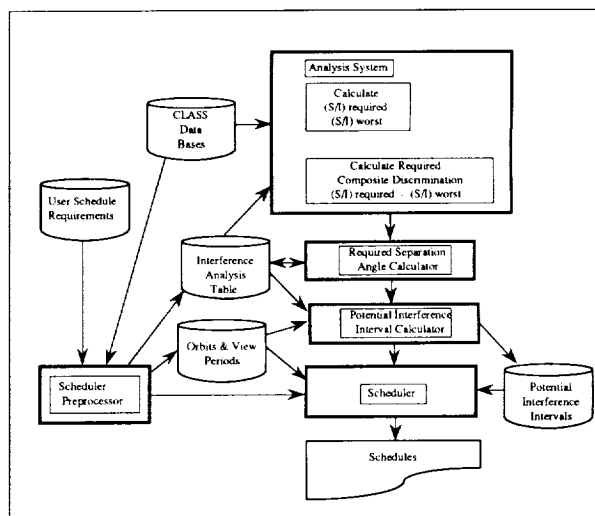
This methodology calculates required separation angles between the desired user and interferer spacecraft and produces potential interference intervals, leading to schedules free of unacceptable interference. It can be used as the basis for analysis, evaluation, and organization of user schedules with respect to communications performance.

The method of producing schedules to mitigate interference while minimizing restrictions on use of network and user resources is described by the following steps and is referred to as the interference mitigation methodology:

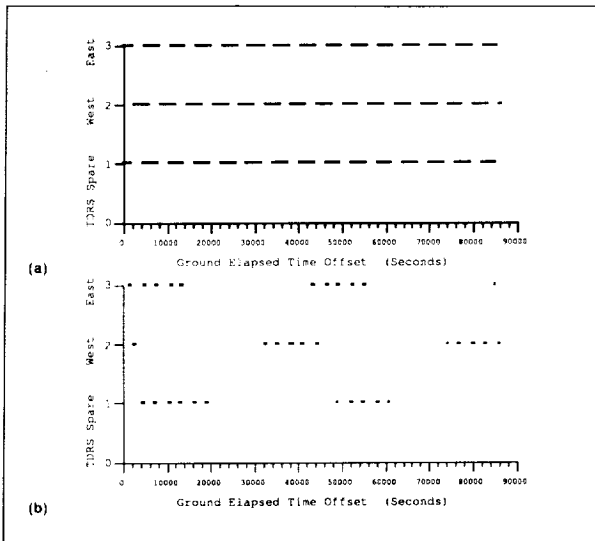
- For every given pair of desired user and interferer links, determine the discrimination required to guarantee nonnegative BER link margin. This discrimination value is equal to the required S/I minus the worst S/I. S/I designates the signal-to-interference-level ratio, which is determined by EIRP, antenna gain, polarization rejection, pseudonoise processing gain, and stochastic factors, such as multipath RFI.
- "Required S/I" is the value of S/I such that the degradation of the desired user signal equals the worst-case channel margin. The worst-case channel margin is a parameter that characterizes the desired user link performance.

- "Worst S/I" is determined by formulating S/I as a function of the separation angle between interferer and desired user. "Worst S/I" designates the global minimum of this function.
- For every given pair of desired user and interferer links, calculate the required separation angle (the largest separation angle between the desired user and the interferer that provides the required discrimination as determined in the first step. This calculation utilizes the TDRS antenna gain pattern adjusted as necessary to reflect polarization rejection of the interferer signal.
- Based on the separation of angles obtained in the second step, find all potential interference intervals; that is, intervals during which unacceptable interference is likely.
- Use the potential interference intervals from the third step as a constraint to a scheduler for generating schedules free of unacceptable interference. The effect of this constraint is to preclude the scheduling of a desired user/interferer link combination during any potential interference interval associated with that combination.

Interference between two forward links, or between a forward link and a return link, is unacceptable now.



Block diagram of the proposed interference mitigation scheduling system. The modules represented by the shaded blocks produce the potential interference intervals and have been implemented in CLASS.



Potential interference intervals at (1) TDRSS Spare, (2) TDRSS West, and (3) TDRSS East when the desired user is Space Shuttle Columbia and the interferer is Space Station Freedom. (a) The users have identical orbits, so that the separation angle is always 0 degrees during TDRSS view periods. Thus, potential interference occupies 100 percent of in-view time. (b) The users have identical orbits except for a 20-degree difference in their main anomalies. In each orbit, there are two times when they are separated by less than the required separation angle: once just after appearing above the horizon as seen by the TDRSS, and once just before disappearing below the horizon.

Interference mitigation is concerned only with pairs of return links.

The interference mitigation methodology as given uses BER margin degradation, as a function of S/I, as the parameter to determine the channel communications performance for a link pair.

The S/I in dB for TDRSS is a function of the separation angle between the desired user and the interferer as seen from the TDRSS. This is a consequence of the fact that as the separation angle changes, the interferer signal power is affected both by the change in TDRSS antenna gain in the direction of the interferer, and by the change in the polarization rejection of the interferer signal (if it has a different polarization).

Software to produce potential interference intervals has been implemented within Goddard's CLASS environment, as an initial step toward development of a scheduling system that incorporates the interference

mitigation methodology described in this article and illustrated in the first figure. CLASS is a software tool for the prediction and evaluation of TDRSS/user spacecraft communications link performance.

The interference mitigation methodology has been applied to planned missions involving EOS, the Space Station Freedom, and the Space Shuttle. All missions operate at Ku-band with carrier frequency equal to 15.0034 GHz, unspread. The Space Shuttle operates in Data Group 2, Mode 1, with right circular polarization. Channels 1 and 2 are rate-1/2 convolutional coded and channel 3 is uncoded. Space Station Freedom operates in Data Group 2, with left circular polarization, with data rates of 300 Mbps and 25 Mbps. EOS operates in Data Group 2, with right circular

Space Shuttle Orbiter Link Characteristics			
Channel	Data Rate (kbps)	EIRP (dBW)	Link Margin (dB)
Channel 1: Subcarrier Q	192	52	19.0
Channel 2: Subcarrier I	2,000	52	13.5
Channel 3: Baseband	50,000	52	1.5

Space Station Manned Base Link Characteristics				
Link ID	Channel	Data Rate (Mbps)	EIRP (dBW)	Link Margin (dB)
SSHDRL1	I	150	60.1	3.0
	Q	150	60.1	3.0
SSHDRL2	I	25	60.1	10.8
	Q	25	60.1	10.8

Earth Observing System Link Characteristics				
Link ID	Channel	Data Rate (Mbps)	EIRP (dBW)	Link Margin (dB)
KSA8	I	150	60.1	3.6
	Q	150	60.1	3.6



		Case 1	Case 2
Desired User	User ID	Columbia	Columbia
	User Link ID	Ku-Band, 1, 3Chan	Ku-Band, 1, 3Chan
	Channel	Z	Z
	Polarization	RHC	RHC
	Worst-Case Margin	1.5	1.5
Interferer	User ID	EOS	SSMB
	User Link ID	KSA8	SSHDL2
	Polarization	RHC	LHC
	Axial Ratio (dB)	1.5	2.1*
TDRS	SA Antenna ID	DEFLT	DEFLT
S/I	Required (dB)	6.2**	9.01**
	Boresight (dB)	-11.6	4.0
	Worst Case (dB)	-11.6	4.0
	Required Discrimination (dB)	17.8	5.01
Required Separation Angle (deg)		0.74	0.92

**NOTE: The axial ratio for the interferer's antenna is a calculated value based on an assumed value of 15 dB for the polarization rejection of the interferer's link on the boresight of the TDRS SA antenna.*

***NOTE: The required S/I is obtained by computer simulation.*

polarization, with data rates of 300 Mbps. See tables 1 through 3 for link characteristics.

Table 4 presents the results of interference analysis. Note that there is no unacceptable interference for Space Shuttle channels 1 and 2 and no unacceptable interference between the Space Station 300-Mbps link (I + Q) and the Space Shuttle channels 1, 2, and 3. It also is noted in the table that even though the required discrimination in Case 2 is less than that in Case 1, the required separation angle is greater. This is explained by the presence of polarization rejection of the interfering signal in Case 2.

Potential interference intervals depend heavily on the choice of orbits of user spacecraft. The second figure illustrates this dependency by showing the intervals for two choices for the user orbits. By changing the orbital spacing interval of the users from a spacing of 0 degrees to a spacing of 20 degrees, the total of the potential interference intervals goes from 100 percent of the in-view time—approximately 813 minutes during the 24-hour scheduling period—to approximately 61 minutes.

The methodology presented in this article represents a feasible, general approach to mutual interference mitigation as a means for generating schedules free of unacceptable interference. The effect of multiple interferers is not considered.

A scheduling system incorporating the methodology described in this article is being developed in the CLASS environment for use in mission planning and in communications performance optimization of user schedules.

Contacts: Yen F. Wong (Code 531)
(301) 286-7446

James L. Rash (Code 531)
(301) 286-3595

Sponsor: Communications Link Analysis and Simulation System (CLASS)

Mr. Yen F. Wong has 6 years of experience at Goddard in the Networks Division. He holds an MSEE from the City College of New York City. His research interests focus on computer-aided modeling and analysis of communications systems, as well as space communications and signal processing. He has developed several software models for the CLASS project.

Mr. James L. Rash has worked in the Telecommunication Systems Branch of the Networks Division for 6 years. He currently is involved with developing artificial intelligence applications for CLASS. He received a BA in mathematics and physics and an MA in mathematics from the University of Texas at Austin.

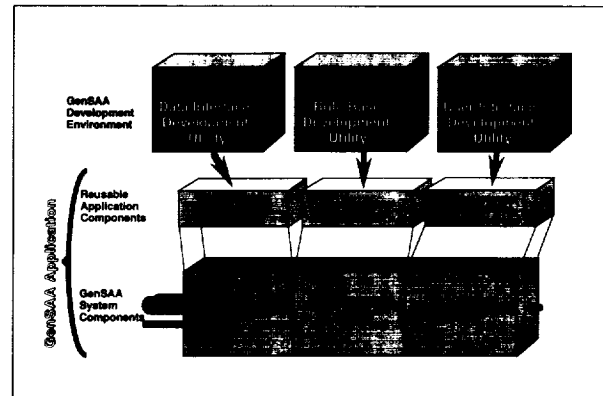
THE GENERIC SPACECRAFT AND ANALYST ASSISTANT (GenSAA)

The Flight Operations Analysts (FOAs) in the Payload Operations Control Center (POCC) perform the operational activities that are necessary to monitor the satellite's health and safety. This responsibility demands that these analysts monitor real-time data looking for combinations of telemetry parameter values, trends, and other indications that may signify a problem or failure. As satellites become more complex and data rates continue to increase, it is understandable that these analysts quickly are approaching a level of information saturation.

The FOAs in the spacecraft control center for the Cosmic Background Explorer (COBE) satellite currently are using a fault-isolation expert system developed to assist them isolate and correct faults in the communication links. This system, the Communications Link Expert Assistance Resource (CLEAR), is the first real-time expert system to be used in the operational environment of a satellite control center at Goddard. CLEAR monitors real-time spacecraft and ground-system performance parameters in search of configuration discrepancies and communication link problems. When such a discrepancy or problem is detected, CLEAR graphically displays where the problem exists and provides advice on how to resolve it swiftly and effectively.

Conventional methods employed for the development of expert systems typically use a specialized knowledge engineer who is responsible for obtaining the expertise from the domain expert and translating it into a syntactical form (called the knowledge representation) suitable for execution by the computer. Furthermore, specially trained programmers are required to integrate the resulting expert system with the operational system. The extraction of the knowledge from the domain expert is an iterative process that is usually tedious, time consuming, and costly. This is compounded by the fact that spacecraft analysts who possess the expertise desired to be embedded in an expert system either are not readily available or not fully acquainted with the domain knowledge until shortly before launch.

Based on the success of CLEAR and several other systems in the control center domain, numerous expert systems will be developed to support control center operations during the 1990s. To facilitate the development of these systems, a project has been initiated to



A spacecraft analyst will use the GenSAA development utilities to create application-specific components. These components then are integrated with the real-time system components, resulting in an expert system capable of supporting spacecraft monitoring and diagnosis.

develop an integrated, domain-specific tool, the Generic Spacecraft Analyst Assistant (GenSAA), that will allow FOAs to rapidly create simple, highly graphical expert systems.

GenSAA will insulate the spacecraft analysts from the complicated programming details of the systems with which the expert system will have to interface. Perhaps more importantly, this tool will promote use of previously developed rule bases and system components, thus facilitating software reuse and further reducing development time and effort.

The GenSAA tool will consist of a development environment and system components. The system components include an inference engine, a display driver, and a process that manages the reception of data. The development environment is composed of three utilities: a data-interface development utility, a rule-base development utility, and a user-interface development utility. Collectively, these utilities will be used to create or modify an instance of an expert system.

GenSAA will use a highly graphical, point-and-select method of interaction. The expert system developer will use the data-interface development utility to select the telemetry parameters to be monitored, the rule-base development utility to define the rules which will act on the values of these telemetry parameters, and the user-interface development utility to layout a simple graphical representation of the subsystem or process being



monitored. The graphical elements of the user interface subsequently can be connected to telemetry points and/or rules for animation during operation.

The components generated by the development utilities are called application-specific components. They will be integrated with the GenSAA System Components to create a GenSAA Application. A GenSAA Application is an expert system that will be executed during spacecraft contacts to monitor the selected telemetry parameters and to notify the flight operations analysts of faults inferred from these data.

To demonstrate the advantages of software reuse and to involve the user in the tool definition, the project team decided initially to focus on a class of missions managed by Goddard. A study of upcoming missions was conducted to identify a series of missions that have sufficient commonality to enable reuse of expert-system software from mission to mission. The Small Explorer (SMEX) and ISTP families of missions were determined to be ideal target groups due to the appropriate time frame of these programs, the low-cost nature of the missions, the emphasis on system reuse, and the rapid turnaround between missions. All of these factors correlate closely with GenSAA's objectives.

GenSAA is intended to be used by FOAs in a POCC. The expert systems created with GenSAA will assist flight operations analysts greatly with the tedious task of data monitoring, thereby allowing them to focus on other, higher level responsibilities during real-time contacts with the satellite. By facilitating the reuse of expert system elements from mission to mission, GenSAA will reduce development costs, preserve expertise between missions and during periods of personnel turnover, and provide a reliable and more accurate level of operation of our rapidly advancing satellites.

Contact: Peter M. Hughes (Code 522)
(301) 286-3120

Sponsor: Office of Space Operations

Mr. Peter M. Hughes, who works in the Automation Technology Section, received his BS in computer science from the College of William and Mary and is currently pursuing an MS in the same discipline at The Johns Hopkins University. His technical interests are in the areas of artificial intelligence, human factors, and software engineering. Mr. Hughes was the chairman of the 1990

Goddard Conference on Space Applications of Artificial Intelligence. He has 6 years of experience at Goddard. Mr. Hughes received a Goddard Exceptional Achievement Award for his contributions to the development of the CLEAR Expert System.

ADVANCED TELEMETRY-PROCESSING TECHNOLOGY RESEARCH AND TECHNOLOGY OPERATING PLAN

The Advanced Telemetry-Processing Technology Research and Technology Operating Plan will evaluate alternative approaches to high-rate packet telemetry processing for parallel and nonparallel computer architecture developments applicable to Space Station-era data systems. The plan will study telemetry processing functions, higher levels of telemetry processing, and telemetry-processing system architecture requirements. To evaluate alternative approaches to telemetry processing, computer architecture will be matched to high data-rate telemetry-processing requirements. Critical telemetry functions will be selected for benchmarking, and computer architecture performance then will be evaluated. Programming techniques, software conversion, and higher levels of telemetry processing also will be evaluated.

During fiscal year 1990, critical telemetry-processing functions were selected from the results of the telemetry-processing functional analysis performed in fiscal year 1989. The benchmarks developed in fiscal year 1990 (and 1991) as a result of the critical telemetry-processing functional analysis are a packet telemetry simulator/reassembly benchmark, data-storage benchmark, and system benchmark. The simulator/reassembly benchmark was developed by converting existing packet telemetry software. These benchmarks were adapted to execute on the following machines: Sun 2, Multiflow Trace 14/300, MIPS M/2000, IBM System 6000, Convex C-120, CRAY II, CRAY XMP, Alliant, and Sequent.

The results of these benchmarks varied widely among the different machines with no single machine performing extremely well on both benchmarks.

Contact: James A. Pritchard (Code 564)
(301) 286-7785

Sponsor: Office of Space Operations/Advanced Systems Office

Mr. James A. Pritchard has 24 years of experience at Goddard. He currently works in the Information Processing Division on data-processing systems. Mr. Pritchard, who holds a BS in electrical engineering from the University of Tennessee, is responsible for directing research on the application of parallel processing to high-rate telemetry systems.

COMMUNICATIONS DATA FORMATTER (CDF) ENHANCEMENT

One of the Digital Systems Section's many responsibilities is to provide tracking stations with digital data-processing equipment to receive and transmit spacecraft telemetry data formatted into 4,800-bit NASA Communications data blocks. One particular device that has been used to perform these functions is the Communications Data Formatter (CDF). The CDF is a single-chassis device which has a central processing unit (CPU) circuit board with an Intel Z80 microprocessor. Each CDF can be configured with different circuit boards according to the function the CDF has to perform. The set of circuit boards available includes frequency-synthesizer boards, RS-232 and RS-422 transmit-and-receive boards, timing boards, and Block Error Detector boards.

When the CDF first was built, its function was to support a single project's telemetry communications requirements. As a result of this and the limitation of the available technology, the CDF was provided only 16 Kbytes of ROM for storing its software program and 8 Kbytes of RAM for storing and processing data. This small memory capacity restricts the size of programs for the CDF so that only one project can be supported at a time without replacing the programmed ROM.

Over the years, the CDF has been installed at a variety of locations where it was needed to support only one project's requirement. In the tracking stations at Dakar and the Dryden Flight Research Facility, the CDF is used for Space Shuttle support. At the Merritt Island tracking station, five CDFs support several projects, including the Space Shuttle, Gamma Ray Observatory, Magellan, and Galileo programs.

A CDF was installed at the Onizuka Air Force Base's tracking station to support the launch of one of the National Oceanic and Atmospheric Administration's satellites. It did not take long before requests arrived from several other projects to use this station and its CDF for support requirements.

As a result, it was necessary to redesign the CDF so it could perform multiple functions. The Bendix Field Engineering Corporation's Data Systems Group was directed to provide a recommended design approach for this challenge. Their proposal was to expand the CDF's memory capacity by taking advantage of advances in memory chip technology.

The CDF's CPU board has been redesigned so that it can hold 128 Kbytes of ROM and 16 Kbytes of RAM. Now, several programs to support different projects can be stored at the same time, each in its own memory bank. To allow selection of a memory bank so that a given program may be run, an operating system has been developed as well.

The new CPU board and operating system are being installed in the CDF at Onizuka Air Force Base's tracking station. In addition, several programs have been developed to provide support for the various projects' telemetry and communications requirements.

As pointed out earlier, the Merritt Island tracking station has five CDFs. This number resulted from the many requirements that this site has because of its unique position for providing pad testing and launch support. With this memory expansion, it will be possible to provide the same support capability with just two or three CDFs.

Contact: Lou F. Kalil (Code 531)
(301) 286-9368

Sponsor: Networks Division

Mr. Lou F. Kalil has been employed at Goddard since 1980. In that time, he has worked on all the major data systems in the Ground Network, which include tracking, timing, command, telemetry, and communications. He has been involved in several major projects, and he was Data Systems Manager for the Vandenberg Air Force Base tracking station installation for Shuttle support and



for the Systems Utilization and Enhancement project. He is responsible for the sustaining engineering and software development of all telemetry and communications data systems in the Ground Network. He also is responsible for software development for the command data systems. Mr. Kalil received a BA in mathematics and physics from Vanderbilt University and an MACT in physics from Auburn University. He was awarded the Silver Snoopy Award in 1989 for his contributions to the success of the Space Shuttle Transportation System.

A MULTIPLE-ACCESS (MA) CALIBRATED RECEIVER USING PROGRAMMABLE CHARGE-COUPLED DEVICES (CCDs)

The Networks Division is involved in the investigation of advanced communications signal processing techniques that are applicable to the TDRSS and advanced TDRSS. One such activity is the design and development of a state-of-the-art receiver which uses programmable charge-coupled device (CCD) correlator technology as the basis for novel signal processing. This process encompasses rapid pseudo-noise (PN) signal acquisition, as well as PN tracking and carrier/symbol synchronization.

Under a NASA Goddard Small Business Innovative Research (SBIR) contract, Stanford Telecommunications, Inc. (STel), has developed a CCD receiver in laboratory hardware. The programmable CCD analog-digital correlator used in this effort was developed by the Massachusetts Institute of Technology's Lincoln Laboratories and contains 256 stages.

This CCD correlator can be used to implement a PN-matched filter (PNMF) that can be matched to virtually any PN code and can provide an effective parallel processing capability to a degree equal to the number of stages. It is this PNMF flexibility, coupled with its high-level parallel processing capability, that makes the CCD correlator so attractive for TDRSS signal processing applications.

CCD correlator operations involve the voltage-to-charge transformation of input signals, followed by the propagation of these charge packets from one delay time stage to the next, at a rate controlled by an external clock. Accordingly, the CCD correlator is inherently an analog processing device since it introduces no

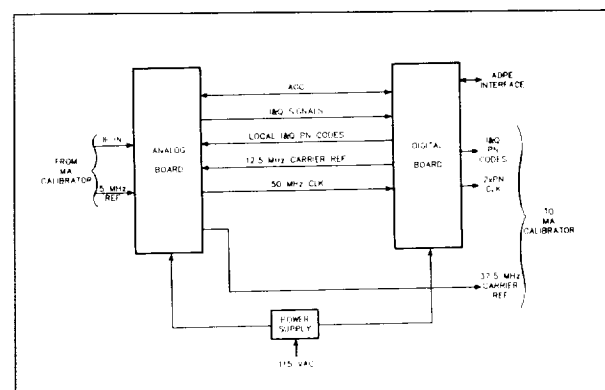
amplitude quantization. The PNMF property arises from the tapping, weighting, and summing of the charge packets at each clock cycle.

What makes the CCD receiver especially unique is its ability to apply the same circuitry and the same signal information to implement all key PN, carrier, and symbol synchronization functions. The analog CCD correlator outputs are analog-to-digital converted and subsequent digital processing is used to implement all acquisition and tracking functions.

The first phase of the STel SBIR effort involved the implementation of the rapid PN acquisition feature of the CCD receiver. The principal capability demonstrated was the achievement of a 2-second PN acquisition time at a 90-percent probability.

The second phase of the SBIR effort focused on the remainder of the receiver signal processing functions, which included the PN, carrier and symbol tracking, and data detection. The hardware test results indicated that the CCD receiver incurs relatively little implementation loss and operates within 1 dB of theory. The results of this proof-of-concept effort demonstrate that a low-complexity, high-performance, and operationally flexible receiver for TDRSS applications is attainable. Key operational benefits are achieved by the judicious use of digital signal processing and the application of embedded microprocessors.

The CCD receiver circuits shown in the figure are divided between an analog board and a digital board. The analog board receives the 35-MHz IF IN from the



CCD receiver block diagram. CCD circuits are divided between an analog board and a digital board.

Multiple Access (MA) calibrator and a 5-MHz reference. It develops I-and-Q PN code samples for processing by the digital board, a 50-MHz clock to drive the circuits on the digital board, and a 37.5-MHz carrier reference for the MA calibrator. The digital board, under control of a microprocessor and firmware, provides local I-and-Q PN codes and a 12.5-MHz carrier reference to the analog board, exchanges automatic gain control signals with the analog board, and sends both correlated I-and-Q PN codes and $2 \times$ PN clock to the MA calibrator. The digital board also interfaces with the system for acquisition start-up and status.

The CCD receiver is a state-of-the-art design and contains some unusual micro-logic circuits. The CCD correlator on the analog board is a chip containing CCDs. Except for the microprocessor circuits, the digital board is made up exclusively of XILINX chips, which are very large programmable logic arrays. Each chip has an associated programmable read-only memory containing its program code which configures the chip at power on and reset.

Contact: Harley Mann (Code 531)
(301) 286-4343

Sponsor: Office of Space Operations

Mr. Harley Mann has 26 years of experience at Goddard. He holds a BSEE from the University of Maryland. Mr. Mann is Project Manager for hardware for the White Sands Ground Terminal Enhancements Project. His research focuses on radio frequency communication.

THE MULTISATELLITE OPERATIONS CONTROL CENTER (MSOCC) APPLICATIONS AND RESOURCE SCHEDULER (MARS)

The Multisatellite Operations Control Center (MSOCC) provides Payload Operations Control Center (POCC) functions for launch and operations of various scientific satellites. The MSOCC is comprised of shared hardware, software, and facilities which are allocated to the various projects and spacecraft missions.

These resources are first allocated to support operational (real-time) events involving the telemetry and commanding of near-Earth satellites. MSOCC users, people associated with projects that are being supported by the

MSOCC, can request the remaining resources for development, testing, or integration of their software systems.

The current scheduling method is purely manual. MSOCC users request the use of resources by filling out a form which is distributed and collected by the scheduler. The requests are then checked for accuracy and completeness. The scheduler also obtains a hard copy of the TDRSS pass schedule as well as copies of the Space Network, Ground Network, and Deep Space Network schedules for the given week. The scheduler then starts to process all of the inputs and the schedule development begins. During the scheduling process, the scheduler allocates the MSOCC resources based on the following priority scheme:

- Launch Support
- Spacecraft Support
- Spacecraft and Mission Tests
- Software Deliveries
- Preventive Maintenance
- Software Testing
- Training
- Software Development
- Demonstrations, miscellaneous

These priorities, which are based on the status of current projects and missions, change frequently and further complicate the current manual method of scheduling. Finally, a daily and weekly paper schedule, showing the MSOCC resource usage, is posted to support the real-time events and user requests.

The MSOCC Applications and Resource Scheduler (MARS) Project was initiated in response to a need for automating the resource scheduling process within the MSOCC. The MARS Project Team is responsible for designing and developing a prototype scheduling system for the MSOCC. The prototype system will address two principal tasks—user request-form management and request scheduling—and in doing so, will automate much of the labor-intensive scheduling task, which



now is performed manually. The main goals of the MARS Project are to demonstrate the feasibility and practicality of automating the scheduling process and to gather functional requirements for an operational system.

The MARS prototype will be implemented as two software systems hosted on separate computers. The first system, the User Request Entry System (URES), will enable users to develop schedule requests, validate the requests (check for syntax errors), and automatically ship requests to the scheduling system. The second system, the Scheduling System (SS), will contain the user interface software and the scheduling software used to create the schedule.

In operation, an MSOCC user starts up the URES on a Macintosh II located near the MSOCC. The user then enters the necessary request data. The system checks the user's request form for syntax problems. The form is then stored on the local machine and sent electronically to the scheduling system where it is stored in the database. At the appointed time (when the scheduler starts up the SS), the scheduler starts the scheduling process in automatic mode. In this mode, each request is extracted from the database and scheduled based on the priority scheme and the encoded heuristics of the scheduler. In the other mode, interactive mode, single requests can be manipulated (deleted, inserted, or moved) by the scheduler. The end result is a daily and weekly schedule that details the MSOCC hardware and facility resource usage.

During the design and implementation of the prototype, several technology areas have been highlighted. They are user-interface technology, scheduling methodology, and knowledge representation. The prototype will present effective user-interface technology, including windowing, color, icons, graphical displays, and mouse input. The prototype's knowledge base will provide a model for representing schedule information such as resources, priorities, and scheduling heuristics (encoded as rules). The scheduling procedure will be accomplished using Nexpert (an expert system software development tool from Neuron Data Corporation) rules and control structures.

Using the technology areas described above, the project team will be able to investigate a majority of the capabilities envisioned for an operational MSOCC

scheduling system. The MARS prototype includes the following capabilities:

- simplified entry of requests by MSOCC users into the system;
- allocation of MSOCC equipment to users based on guidelines formulated by the scheduling operators;
- scheduling of several jobs on shared equipment;
- ability to explain why a particular request was not scheduled;
- modification of guidelines by the scheduling operator;
- modification of scheduled events by the scheduler;
- generation of hard copies of resource requests, equipment schedules; and
- processing of requests for additional support on an existing schedule such as additional equipment support resulting from a launch slip.

However, because of time constraints, there are several functional areas that will not be explored. The functions that will not be explored, but which are recommended for the operational MSOCC scheduling system, are:

- generation of separate operator shift schedules;
- generation of MSOCC support events directly from Space Network, Deep Space Network, and Ground Network schedules;
- modification of previously submitted schedule requests by the requestor;
- distribution of the final schedule to terminals other than the scheduling workstation;
- automatic input of continuing services from a previous week.

The first demonstration of the prototype is scheduled for early fiscal year 1991. Comments will be solicited from reviewers as well as the MSOCC scheduling staff after the demonstration. Enhancements will then be made, and the first prototype will be delivered. Plans are already underway for a second-phase prototype.

It is expected that MARS will demonstrate that automation of the MSOCC scheduling process can be achieved. While MARS is not intended to replace the schedulers—human interaction always will be necessary in this operational environment—it will reduce to a minimum the tedious tasks such as request-form management. MARS will enable schedulers to increase their efficiency greatly by allowing them to automatically schedule standard requests and by reducing their paper load.

Contact: Mike Bracken (Code 522.3)
(301) 286-7896

Sponsor: Office of Space Operations

Mr. Mike Bracken holds a BS in mathematics from the College of William and Mary and is pursuing an MS in computer science from The Johns Hopkins University. He has been a member of the Automation Technology Section at Goddard since 1988. Mr. Bracken specializes in the application of expert system technology.

THE TRANSPORTABLE APPLICATIONS ENVIRONMENT (TAE)

Fiscal year 1990 was a year of significant technical achievement for the Transportable Applications Environment (TAE) Project. After several years of developing prototype and beta versions of a user-interface development and management system, called TAE Plus, a production-quality version (TAE Plus V4.1) was completed and delivered to COSMIC for immediate availability to the general public at a nominal distribution fee.

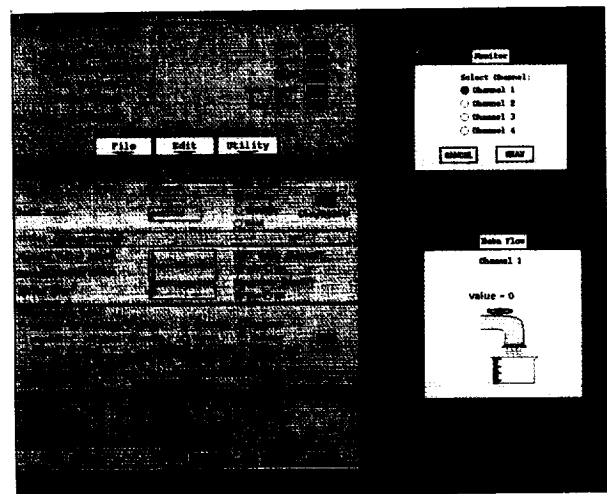
TAE Plus is a tool for designing, building, and tailoring an application's user interface and for controlling the designed user interface throughout the application's execution. The main component of TAE Plus is a WYSIWYG user-interface designer's WorkBench that allows an application developer to construct interactively the look and feel of an application screen by arranging and manipulating user entry, informational, and data-driven interaction objects (e.g., radio buttons, menus, icons, help dialogue boxes, gauges, dials, etc.). A WorkBench user specifies the windows and interaction objects that will make up the user interface and

specifies the sequence of the user interface dialogue. A rehearse capability allows the developer to review the user interface during the earlier stages of the development process. At the end of the WorkBench session, the designed user interface is saved into resource files, which are then accessed by the TAE Plus services (called WPTs, WindowProgramming Tools) during runtime to display and control the user interface.

As an aid to the developer going from the user-interface design process into the application-implementation phase, the WorkBench provides the option to generate fully annotated and operational code which will display and manage the entire work bench-designed user interface. Currently, code generation is available for C, Ada, and Fortran programming languages. This code provides the skeleton program into which the application programmer can insert or branch to application-specific logic.

The WorkBench and the runtime services are written in the object-oriented C++ programming language and use the MIT X Window System as the underlying windowing standard. Because of the growing popularity of the Open Software Foundation's Motif™ user-interface style, work is underway on upgrading and tailoring TAE Plus to support the Motif user-interface style. The TAE Plus supporting Motif™ (TAE Plus V5.0) is expected to be completed by the end of 1990.

The base development of the graphic-oriented TAE Plus software is being done on Sun workstations under



Building a user interface with TAE Plus WorkBench.



UNIX. TAE Plus is designed to be portable to any UNIX graphic workstation known to be operating on the Apollo, VAXStation II, DECStation 3100, Macintosh II, HO, IBM PS/2, Masscomp, and Silicon Graphics IRIS. In fiscal year 1990, a port of TAE Plus operating in the VAX/VMS environment was completed and delivered to COSMIC for distribution.

TAE Plus popularity continued and user sites grew by more than 60 percent from the previous year. Currently, there are more than 725 TAE installations, of which 193 are NASA-sponsored sites, 160 are other government sites, 120 are university sites, and 260 are private industry sites. Applications cover a wide range of disciplines, such as operations, simulation, production systems, network

management, real-time command and control, planning and scheduling, data base management, image processing, science/analysis services, prototyping activities, and office automation.

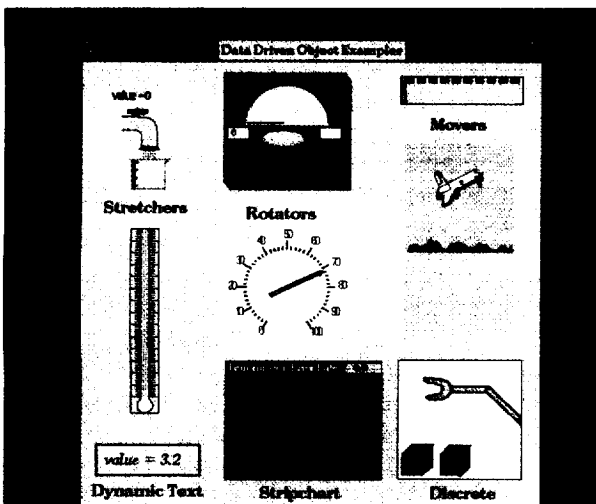
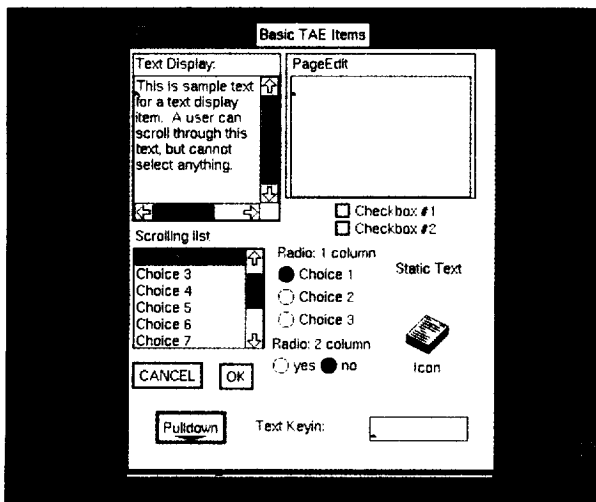
In fiscal year 1990, the Eighth TAE User's Conference was held near Johnson Space Center and provided an excellent exchange of ideas between the users and the TAE Plus developers. An assortment of excellent papers was presented. Topics ranged from using TAE Plus for developing land analysis systems and an expert system real-time controller application to tutorials on adding new interaction objects to the WorkBench and the use of the TAE Command Language.

TAE Plus is an evolving system and future plans include delivery of the TAE Plus Version 5.0 with Motif™, C++ code generation from the WorkBench, on-line tutorial and training tools; introduction of hypermedia technology; integration of expert system technology to aid in making user-interface design decisions; and implementation of additional user-interface designer tools, such as WYSIWYG graph builder. TAE Plus is continuing to play a significant role in improving productivity in the development and management of application user interfaces.

Contact: Martha R. Szczur (Code 522)
(301) 286-8609

Sponsors: Office of Space Operations

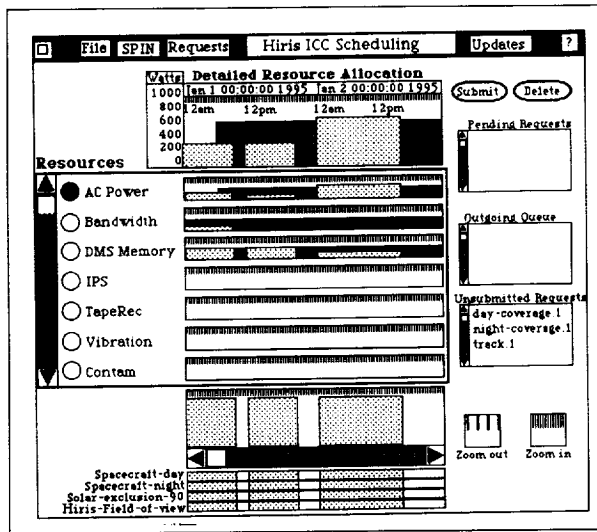
Ms. Martha R. Szczur, Manager of the TAE Project since 1984, has more than 28 years of experience in the development of Goddard software systems and has a BS in mathematics. Her professional interests focus on graphical user interface technology, emphasizing human factors and development support tools.



TAE Plus user interaction objects.

THE SCHEDULING CONCEPTS, ARCHITECTURE, AND NETWORKS (SCAN) TESTBED

The Scheduling Concepts, Architecture, and Networks (SCAN) testbed was created to evaluate planning and scheduling concepts in the Space Station Freedom era. The planning and scheduling process is highly complex; it must support both spacecraft operations and science. The planning and scheduling system must provide for optimal use of onboard resources,



ICC main screen. The underlying functionality of the ICC workstation was designed and implemented using an object-oriented design methodology. This provided for easy modification and upgrading typical of a testbed environment. The coding was done in an object-oriented extension of the C programming language, called C++.

interactive and responsive scheduling and rescheduling, and interaction with and between geographically distributed users. The SCAN testbed operates in a distributed environment designed to model various operations concepts of this scheduling process.

Platform planning and scheduling are driven by a set of guidelines derived from the Science Tactical Plan, platform and payload operations requirements, and user science objectives. Resource availability constrains the planning and scheduling of these operations. One objective of the SCAN testbed is to investigate innovative alternatives for planning and scheduling for platforms. One alternative automates the process by allowing the scientist to make requests from a remote site, thus eliminating the need to meet face-to-face with the planning and scheduling team. The planning and scheduling for the mission can be done electronically. The EOS platform was chosen as a representative platform mission. To demonstrate this alternative method of planning and scheduling, the following scenario was used in the first phase of the testbed.

The Science Tactical Plan, developed by the Instrument Working Group, provides each instrument a reservation of resources; i.e., a share of resources proportional to the

science priority of that instrument, to be used as a guideline for activity creation. These resource reservations, along with orbit constraints and TDRSS contact data, are sent to the EOS Operations Center (EOC) for distribution to multiple Instrument Control Centers (ICC). An ICC provides tools the scientist uses to create activity requests for the instrument, such as a request to look at a particular point on Earth from various angles. These requests are sent to the EOC and merged with the activity requests of other ICCs into a schedule for the platform. An instrument schedule is extracted and returned to each ICC.

With the SCAN testbed, the scientist interacts with the ICC workstation via a graphical interface designed and built using the Transportable Applications Environment (TAE) Plus, a user-interface management system. This interface provides the scientist with the capability to create instrument activities by directly manipulating the necessary display elements. The scientist views resource usage over a specific time interval displayed on a graphical timeline. The scientist is provided with menus to generate requests for mission visibility data or other pertinent data required to make an intelligent request. These requests are sent to the EOC, and the instrument schedule is returned to the ICC. This information is displayed graphically on the ICC main screen.

Contact: Karen Thorn (Code 522)
(301) 286-3737

Sponsor: Office of Space Operations

Ms. Karen Thorn has 6 years of experience at Goddard in the Data Systems Technology Division. She holds a BS in computer science from the University of Maryland.

ADVANCED COMMAND MANAGEMENT SYSTEM

The autonomous operation of a spacecraft while it is out of contact with the ground is driven by a set of commands that are stored on board. A single set of contiguous commands, known as a command load, is generated on the ground to cover a specific load period, usually 1 day, and uplinked to the spacecraft during a contact. The ground element that generates the command loads is called the command management system (CMS). It is the responsibility of the CMS to merge requests for



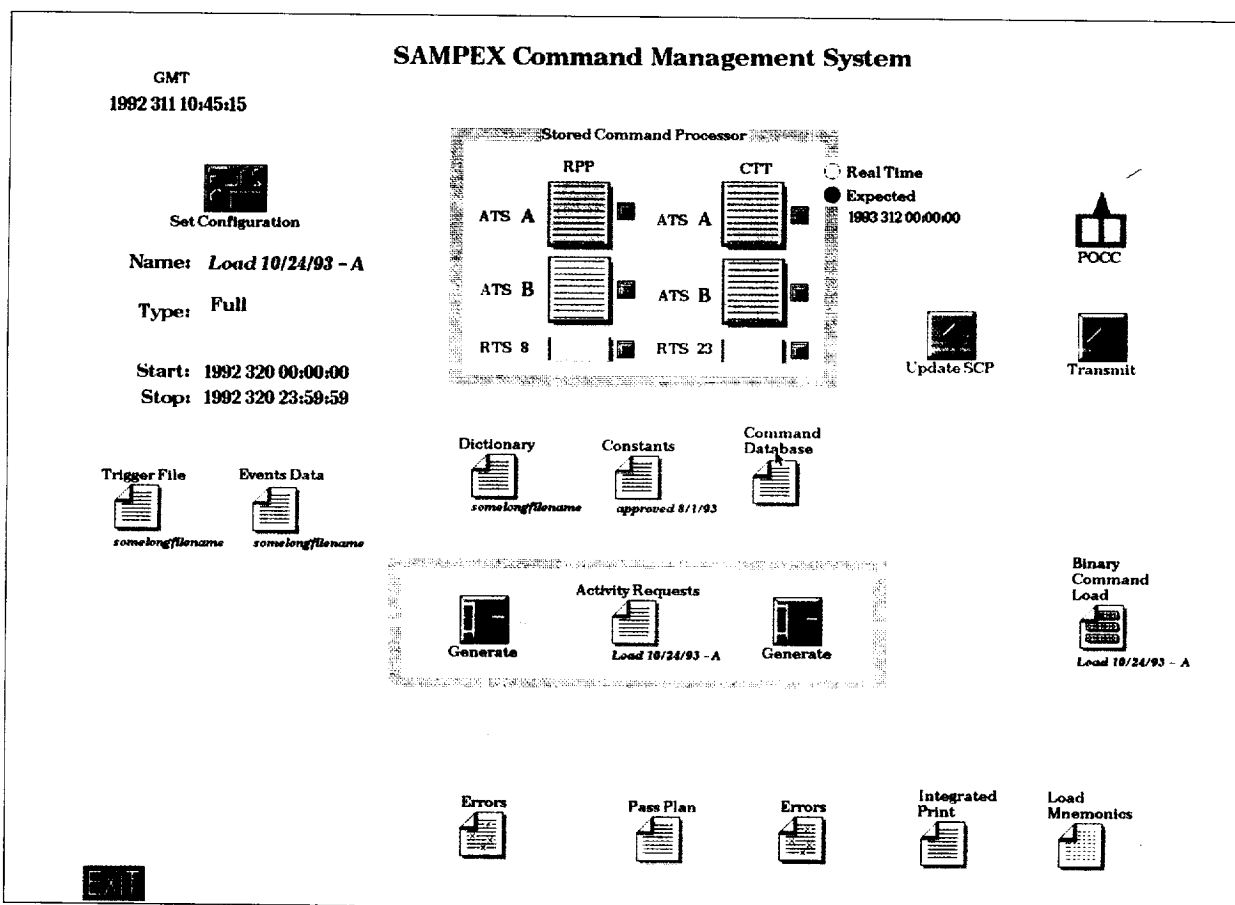
activity and spacecraft status information from the project scientists, the POCC, the Flight Dynamics Facility, and other sources to produce command loads that are consistent, safe, and reasonable given current ground and onboard resources.

The CMS normally is operated by a specially trained staff, located in its own command management facility. CMS processing is largely batch-oriented. A set of input files representing available commands, desired activity, ground-station availability, spacecraft status, and other relevant data are identified for a target load period. The CMS then produces the command load, identifying any errors and inconsistencies in load generation reports. The operation of a CMS requires a certain amount of expertise, since the relation of the input files to the output files and reports can be quite complex and unintuitive. In addition, the process by which some input files are created can be prone to errors.

The requirements for the CMS that will support the Solar, Anomalous, and Magnetospheric Particle Explorer (SAMPEX) are somewhat unique. This CMS is to be located in the mission operations room and operated by the same flight operations team that operates the POCC system. SAMPEX is also the first in a series of Small Explorer missions, and it is desired that all or part of the SAMPEX CMS be reusable for those future missions.

To meet these requirements, the Spacecraft Control Programs Branch, which has the responsibility to produce and maintain Goddard command management systems, has enlisted the Software Automation Systems Branch to apply several advanced technologies to the problem.

Since the CMS operators will not be command management experts, the use of the CMS must be simple and intuitive. Toward this end, the CMS will be built with a direct-manipulation graphical user interface. The display



SAMPEX Command Management System.

will attempt to give the user an overview of the load generation process. Important functions and objects will be represented with icons. Full-screen text editors will not be used. Instead, specific graphical editors will be created for each type of input file that must be created. Typing will be kept to a minimum; the user most often will use the mouse to select from a list of options at each point. A series of dialogues will guide the user through the system. All of these interactive graphics will be produced with the Transportable Applications Environment (TAE) Plus, a user interface management system developed by Goddard's Data Systems Technology Division.

A prototype of this user interface was developed during the requirements analysis phase. It was shown to various groups involved with command management, including the SAMPEX flight operations team. The prototype proved to be a valuable tool, as it helped to clarify some of the important system concepts very early in the software development life cycle.

To provide a system that can be tailored for future missions, the CMS will be implemented with the C++ programming language, an object-oriented extension of C language. The software will be based on a library of reusable objects that have been developed by the Data Systems Technology Division. In particular, several of these objects provide a simple, object-oriented application programmer interface to TAE Plus that allows elaborate user interfaces to be created with a very small amount of code. This also will help the development team to meet its very tight schedule.

The SAMPEX CMS represents a large departure from traditional systems of this type. However, the use of new approaches such as these will help pave the way to more reliable, more easily built ground operations systems.

Contact: Stephen G. Edwards (Code 522)
(301) 286-6676

Sponsor: Office of Space Operations

Mr. Stephen G. Edwards has 5 years of experience at Goddard. He holds a BSE in computer science and engineering from the University of Pennsylvania. His research focuses on user-interface design and object-oriented programming.

COMBINED OPERATIONAL MISSION PLANNING AND ANALYSIS SYSTEM (COMPASS)

The Goddard Flight Dynamics Division develops and operates software systems providing a wide range of analysis, attitude (orientation), orbit, and monitoring support for space missions. As with many organizations, the Flight Dynamics Division builds similar systems for each mission. However, there has been enough variability in mission requirements, especially for attitude support, that software costs have risen significantly during the last decade. Thus, the Flight Dynamics Division initiated the Combined Operational Mission Planning and Analysis System (COMPASS) project to develop a highly generalized system which would minimize mission-specific support costs, while retaining the flexibility necessary to meet division institutional requirements into the next century.

COMPASS will provide an integrated framework of application software systems to perform mission analysis and supply attitude-related flight dynamics products. COMPASS will incorporate sophisticated concepts, techniques, and methods based on completed and ongoing work in the Flight Dynamics Division on generalized systems, reusable software, advanced user interfaces, networking, and distributed processing. Further, COMPASS will take full advantage of proven industry standards and commercial products in these areas.

The basic COMPASS approach is to separate the software that implements application functionality from the software that provides a common computational environment. The latter environment, known as the user interface/executive (UIX), will be based on a hardware architecture of networked PC workstations and mainframes. The UIX will provide a common user interface on the workstations that allows access to software running on any of the networked computers. An initial system architecture based on this concept was defined during fiscal year 1990. Preliminary UIX requirements also were outlined. These will provide the basis for prototyping activities to be carried out in fiscal year 1991.

Generalized COMPASS application software will be designed specifically to fit into this UIX environment. Thus, requirements and specifications for the application software can take UIX capabilities for granted. This allows the application software specifications to focus fully on the application domain. These specifications are to be



written in a very general way based on project-standard, object-oriented specification concepts.

The COMPASS specification concept provides methods for specifying models for classes of objects in the application domain. Generality is fostered by grouping related classes into categories and having other models depend on the categories rather than on the specific classes. For example, the generalized specifications include classes for each kind of spacecraft sensor supported by the Flight Dynamics Division, grouped into a sensor category. Other specifications then may be written in terms of this general sensor category, rather than assuming a mission-specific complement of sensors.

A document defining the specification concept was completed during fiscal year 1990. A considerable amount of domain analysis of Flight Dynamics Division attitude support also has been completed using these concepts, leading to drafts of the generalized specifications in this area. Final versions of the COMPASS specification documents are expected in fiscal year 1992.

The object-oriented nature of the COMPASS specifications will allow a close correspondence between the specifications and the actual application software, which is expected to be written in the Ada programming language. According to the developing COMPASS implementation concepts, models and categories in the specifications will map directly into reusable software components. To support a specific mission, an analyst will choose appropriate models from the generalized specifications. This decision also will select corresponding software components that may be configured automatically based on a standard software architecture, resulting in an executable program. Multiple programs will be configured to support a mission, all running in the common UNIX environment.

Through use of this configuration concept, it is the goal of the COMPASS project to reduce by 80 percent the amount of software that the Flight Dynamics Division needs to develop specifically for each mission, reduce by 50 percent the mission-specific analysis and development costs, and reduce by 30 percent the mission-specific operations and maintenance costs. In addition, the generalized software will evolve to meet the Flight Dynamics Division's needs during a 30-year lifetime.

Developing COMPASS obviously will be a major undertaking, and the full system will not be completed before fiscal

year 1997. However, even taking into account the cost of developing and maintaining the system, COMPASS is expected to reduce the cost of Flight Dynamics Division mission support considerably in the next century.

Contact: Ed Seidewitz (Code 552)
(301) 286-7631

Sponsor: Office of Space Operations

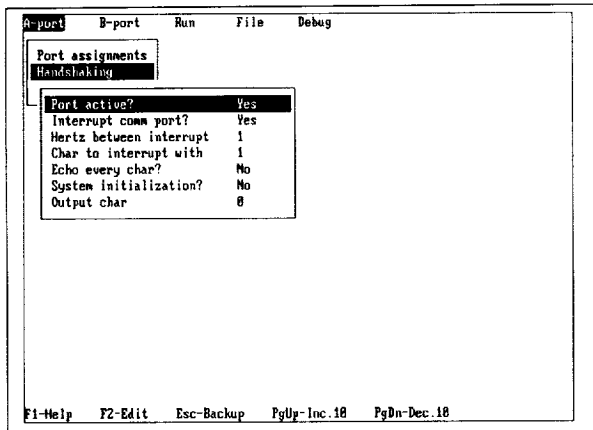
Mr. Ed Seidewitz is a software systems engineer and COMPASS Project Manager. He has a BS in aeronautics and astronautics, as well as a BS in computer science and engineering from the Massachusetts Institute of Technology. He has worked in the Flight Dynamics Division for more than 6 years and has been active in the development of object-oriented methods and applications of Ada.

A PERSONAL COMPUTER-BASED, MULTITASKING DATA-ACQUISITION SYSTEM

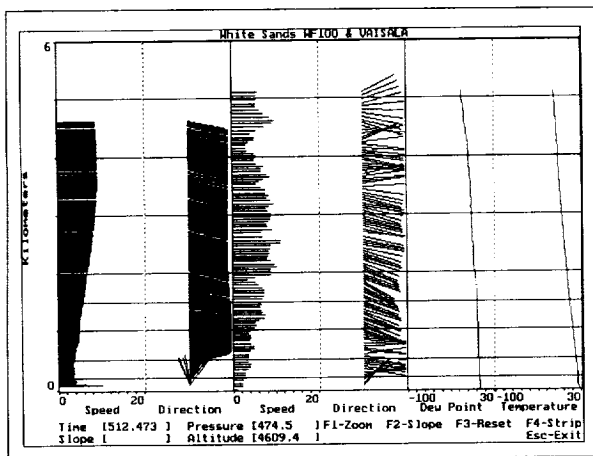
A multitasking data-acquisition system was written to collect meteorological radar and telemetry data simultaneously from two sources. This system is based on PC architecture. Data is collected via two asynchronous serial ports and is deposited to disk. The system is written in both the C programming language and in Assembler. It consists of three parts: a multitasking kernel for data collection, a shell with pull-down windows as a user interface, and a graphics processor for editing data and creating coded messages.

The main goal of this programming project was to design a well-structured, user-friendly data system. This system had to be easily adaptable to any asynchronous serial data source and had to run on any PC or PC clone. As illustrated in the first figure, the user interfaces with the system via a series of pull-down windows. It is here that startup variables and system parameters are entered. Also at this level, the system can be programmed to collect and frame any type of asynchronous serial data.

Once system setup is complete, data collection is initiated from another window. At this point, data is gathered and written to disk in the background. This allows the user to move freely from window to window without worry of data corruption. The user also can move to the DOS prompt, where programs not interfering with the serial ports can be run simultaneously with data collection.



Example of user interface with pull-down windows.



Graphics screen for creation of METBZ coded message using WF-100 radar and VAISALA TM system.

A separate program called a graphics processor was written to complement the data system and is illustrated in the second figure. The program can be run before, during, or after data collection. It simply reads a file and displays the appropriate information graphically. Since DOS files can be shared by more than one program, the graphics processor can read and display data while that data is being written by the data system.

The graphics processor also allows the user to edit data graphically. An area of interest can be "zoomed in" on for closer study. Noisy data can be edited out by use of a cursor. A running average can be applied to data as well as the creation of several meteorological coded messages.

Although this data system was designed originally to collect and process meteorological data, its modularity

allows for easy adaptability to other data sets. At present, this data system has been field tested and works as planned. It also has been adapted for use by three other projects.

Contact: Steven A. Bailey (Code 972)
(804) 824-1429

Sponsor: Atmospheric Sciences Laboratory, White Sands Missile Range

Mr. Steven A. Bailey works on software engineering for several remote-sensing projects in the Observational Science Branch of the Laboratory for Hydrospheric Processes. His technical interests include writing data acquisition systems using PCs. Mr. Bailey received a BA in geology from Slippery Rock State University and a BS in computer science from the University of Maryland. He has 6 years of experience at Goddard's Wallops Flight Facility.

INTELLIGENT TUTORING SYSTEMS

The Data Systems Technology Division is involved in the area of intelligent tutoring, the field which applies knowledge-based technologies to various forms of training and operational support. Currently, there are two major, ongoing activities.

The first is the application of intelligent tutoring technology to NASA command and control language training. Historically, NASA has relied on on-the-job training for POCC personnel to become proficient with the System Test and Operation Language (STOL). Estimates of the time taken to acquire acceptable levels of proficiency using existing training methods range up to 4 months. The objective of this effort is to develop and demonstrate a prototype intelligent tutoring system (ITS) for assisting NASA control room operators in learning to use STOL.

STOL is the primary interface between NASA control center operators and ground-based and on-orbit equipment. STOL provides the capability for the operators to command and control equipment, process telemetry, display data, and perform various support functions that are common to the MSOCC environment.

The STOL ITS will be used to deliver introductory and refresher STOL training. As part of tutoring, the STOL ITS will provide the trainee with four aids to facilitate



learning. The first aid will be an alternative representation of STOL that is graphically oriented, consisting of dynamic icons and graphics that represent the various elements of the Gamma Ray Observatory (GRO) environment. This graphical representation will be used to facilitate learning STOL and will be treated as an intermediate step between the trainee's current way of thinking about the system and the way he or she will have to use STOL in the actual control room.

The second aid will be context-sensitive advice. This advice will be selected by the tutor module according to the learning styles and requirements of the student. The advice or tutoring provided to the trainee will be tailored to the individual trainee's status in the current session as well as his or her learning/tutoring record. The objective is to make the advice as brief and helpful as possible to the specific individual, based on previous problems and current needs.

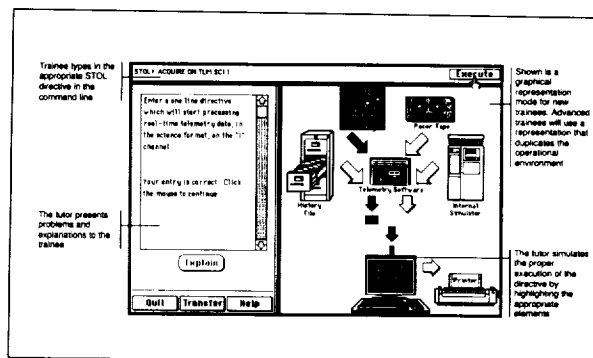
The third aid will be an intelligent editor which will assist the student in developing STOL procedures that are syntactically correct. The fourth aid will be a glossary of STOL directives, containing semantics, syntax, and examples.

Since the project is primarily a research effort, several research questions will be addressed, including:

- The feasibility of developing a general-purpose STOL tutor which can be used effectively in a wide range of POCC environments;
- Evaluation of the relative effectiveness of alternative knowledge representations for tutoring a command-and-control language;
- Evaluation of the relative effectiveness of alternative user-interface modes for students with varying skill levels.

In conjunction with the Control Center Systems Branch, a preliminary version of the STOL ITS has been developed for the Macintosh and is being used to evaluate various approaches to the human-machine interface issues associated with such systems.

To date, this activity has produced several microcomputer-based tools currently being used by the GRO flight operations team for training and certification. The STOL glossary was used in classroom training and serves as a reference resource. A STOL Certification Tool was developed to automate the operator certification process.



A sample screen from the ITS prototype. A prototype was developed on an Apple Macintosh with HyperCard to demonstrate the capabilities and interaction techniques of an ITS in a STOL environment.

This activity also has helped stimulate a cooperative work arrangement with the Johnson Space Center, which has an active program in ITS technology.

The second major activity is longer in range and deals with the broad issues associated with the development, installation, and use of ITS technology in operational spacecraft control centers. Particular emphasis is being given to the role that knowledge-based systems, incorporating normative models of operator interaction, could play in such operational environments. Based on observations made in the MSOCC, the researchers have developed real-time scenarios which detail the operator functions and the information required to successfully carry out those functions.

A major tool in this research is the Operator's Function Model Expert System. This system provides an architecture for an intelligent operator's associate. This associate provides assistance to the human operator of a complex dynamic system. Using this tool, the intent is to develop an ITS which both teaches novices the principles and procedures for ground-system control and evolves into an operator's assistant as the student's skill level increases.

Contact: Troy J. Ames (Code 522)
(301) 286-5673

Sponsor: Office of Space Operations

Mr. Troy J. Ames performs research and development in advanced technologies concerning artificial intelligence and human factors. He has been at Goddard for 6 years

and currently works in the Automation Technology Section. He holds a BS in computer science and a BS in mathematics from the University of Idaho.

COMPUTING CENTER ACQUIRES CRAY SUPERCOMPUTER

In December 1989, NASA/GSFC awarded the contract for the NASA Center for Computational Sciences (NCCS)(formerly NASA Space and Earth Sciences Computing Center, NSESCC) class 7 advanced supercomputer to Cray Research, Inc. (CRI) of Calverton, MD. The new system, based on the CRAY Y-MP8/432 supercomputer, was benchmarked at more than 10 times the production and throughput levels of the Computing Center's CYBER 205. It is expected that this acquisition will keep the Earth and space science communities within NASA at the forefront of supercomputing over the next decade. The contract will allow the NCCS to upgrade system performance from 10 to up to 60 times that of the CYBER 205.

The CRAY Y-MP8/432 was delivered to GSFC on June 18, 1990, as part of NCCS's plan to replace the CYBER 205, which was installed in 1982. The supercomputer system successfully completed the pre-acceptance performance benchmark and system functional demonstrations in early July. On July 10, the acceptance test period for the CRAY began, and the NCCS opened the system to pilot users.

The initial configuration of the CRAY Y-MP included 4 Y-processors with a 6-nanosecond clock cycle, 32 megawords of processor memory, 128 megawords of solid-state storage device (SSD) auxiliary memory, and 25 gigabytes of disk storage. In comparison, the CYBER 205 has a 20-nanosecond clock cycle, 4 megawords of processor memory, and 11 gigabytes of disk storage.

The CRAY also includes the following network interfaces: a Network Systems Corporation EN643 TCP/IP gateway, a Digital Equipment Corporation VAX 9000-410 gateway, and channel-speed VM and MVS CRAY station software interfaces for NCCS IBM and IBM-compatible systems.

The contract includes options to upgrade from 4 to 6 and 8 processors in the Y-MP8 technology, providing increases to 15 and 20 times the CYBER's processing capability. When the CRAY Y-MP16, or CRAY C90, becomes avail-

able (projected for 1993), the Computing Center may upgrade to this new technology with 8 and 16 processors to achieve 40 to 60 times the CYBER's capability.

The Computing Center may increase processor memory to 64, 128, 256, and 512 megawords. Auxiliary (SSD) memory is expandable to 256, 512, and 1024 megawords, and disk storage may be increased to 45, 86, 169, and 335 gigabytes.

The contract also included an option to install a CRAY high-speed channel interface to a network of very high-speed Ultranet hubs. The hubs are being installed in various buildings at GSFC and will be linked by fiberoptic cables. This network will have a peak bandwidth of 1 gigabit per second and will provide future channel-speed interconnection of the major large-scale scientific computing nodes at GSFC.

Additional interface options include a second TCP/IP gateway and support for ISO/OSI and FDDI standard interfaces when they become commercially available.

Plans and preparations for acquiring a class 7 supercomputer for the NCCS began more than 2 years prior to delivery. In July 1989, GSFC released the RFP (Request for Proposal) for the supercomputer. The RFP limited competition to U.S. manufacturers and called for proposals and benchmark results to be submitted in early September. A GSFC technical evaluation panel then reviewed the proposal for conformance to RFP criteria and presented their results to the procurement and selection officials. In November 1989, Cray Research, Inc. of Calverton, MD, was selected for negotiations, and a goal to complete the contract by the end of 1989 was established.

In October of 1989, at the request of NASA Headquarters, and in conjunction with the General Services Administration (GSA), the NCCS agreed to support the class 7 supercomputer requirement of NASA/Lewis Research Center's (LeRC) Computer Services Division (Cleveland, Ohio). Subsequently, GSFC, LeRC, GSA, and NASA Headquarters personnel collaborated to add a second CRAY Y-MP8/432 with the same configuration to the GSFC contract.

Negotiations with CRI began in December 1989, and the final contract for the two supercomputers was signed at GSFC on December 29, 1989. The combined contract saved both NASA centers substantial dollars, as well as



effort, and significantly accelerated the LeRC acquisition. LeRC scientists will use their CRAY system for modeling advanced aerodynamics, such as computational fluid dynamics.

Contact: Mr. Christopher E. Bock (Code 931)
(301) 286-8707

Sponsor: Office of Space Science and Applications

Mr. Christopher E. Bock currently is a computer scientist in the NASA Center for Computational Sciences (NCCS). As supercomputing project leader and senior technical advisor on supercomputers for NCCS, he is responsible for long-range planning, acquisition, implementation, and support of scientific supercomputer systems. He has 23 years of experience in large-scale scientific computer systems at Goddard. He received a BS in mathematics from the University of Maryland.

Acronyms

AASE	Airborne Antarctic Ozone Experiment	DET	Direct Energy Transfer
ACS	attitude control system	DIRBE	Diffuse Infrared Background Experiment
ADEOS	Advanced Earth Observation Satellite	DMR	Differential Microwave Radiometers
AGN	active galactic nuclei	DSTD	Data Systems Technology Division
AIRS	Atmospheric Infrared Sounder	DTF	Detector Test Facility
AOL	Airborne Oceanic Lidar		
APIDS	application identification numbers	ECL	Emitter Coupled Logic
ASI	Agenzia Spaziale Italiana	ECS	EOSDIS Core System
AVHRR	Advanced Very High-Resolution Radiometer	EES	Expendable Explorer Spacecraft
AXBT	Airborne Expendable Bathythermograph	EGRET	Energetic Gamma Ray Experiment Telescope
		EIRP	effective isotropic radiated power
BaSE	The Base System Environment	EOC	EOS Operations Center
BATSE	Burst and Transient Source Experiment	EOS	Earth Observing System
BBXRT	Broad Band X-Ray Telescope	EOSDIS	EOS Data and Information System
BER	bit-error rate	EP/EUVE	Explorer Platform/Extreme Ultraviolet Explorer
		EROS	Earth Resources Observation Systems
CCD	charge-coupled device	ESMR	Electronically Scanned Microwave Radiometer
CDP	Crustal Dynamics Project		
CERES	Clouds and Earth's Radiant-Energy System	FIRAS	Far Infrared Absolute Spectrophotometer
CFCs	chlorofluorocarbons	FTS	Flight Telerobotic Servicer
CLASS	Communications Link Analysis and Simulation System	FUSE	Far Ultraviolet Spectroscopic Explorer
CLEAR	Communications Link Expert Assistance Resource		
COBE	Cosmic Background Explorer	GALE	Genesis of Atlantic Lows Experiment
COMPASS	Combined Operational Mission Planning and Analysis System	GARP	Global Atmospheric Research Program
		GCM	General Circulation Model/Global Climate Model
DAAC	Distributed Active Archive Center	GEM	Geosynchronous Environmental Mission
DARPA	Defense Advanced Research Projects Agency	GenSAA	Generic Spacecraft and Analyst Assistant
DCS	Data Collection System	GHRS	Goddard High-Resolution Spectrograph
DDF	Data Distribution Facility	GISS	Goddard Institute for Space Studies
		GLA	Goddard Laboratory for Atmospheres

PRECEDING PAGE BLANK NOT FILMED

207 INTENTIONALLY BLANK

Acronyms

GLOBE Global Aerosol Backscatter Experiment
GLRS Geoscience Laser Ranging System
GOES Geostationary Operational Environmental Satellite
GRO Gamma Ray Observatory

HEAO-1 High-Energy Astronomy Observatory
HEASARC High-Energy Astrophysics Science Archive Research Center
HIRIS High-Resolution Imaging Spectrometer
HRTS High-Resolution Telescope Spectrograph
HST Hubble Space Telescope
HTSC high-temperature superconductor

ICAR Integrated Camera and Radiometer System
ICCs Instrument Control Centers
IMP Interplanetary Monitoring Platform
IRAS Infrared Astronomical Satellite
IRIS Infrared Interferometric Spectrometer
IRTF Infrared Telescope Facility
ISCCP International Satellite Cloud Climatology Project
ISTP International Solar Terrestrial Physics
IUE International Ultraviolet Explorer

JGOFS Joint Ocean Global Flux Study

KISS Kiepenheuer Institut Solar Spectrograph
KPVT Kitt Peak Vacuum Telescope

LASP Laboratory for Astronomy and Solar Physics

LAWS Laser Atmospheric Wind Sounder

LEAP Low-Energy Antiproton experiment
LG Local Group of galaxies
LTT Lunar Transit Telescope
LZP Level-Zero Processing

MABL Marine Atmospheric Boundary Layer
MEDS Modular Environment for Data Systems
MMS Multimission Modular Spacecraft
MODIS Moderate Resolution Imaging Spectrometer
MOXE Monitoring X-ray Experiment
MPE Mission to Planet Earth
MSOCC Multisatellite Operations Control Center

NCAR National Center for Atmospheric Research
NDE nondestructive evaluation
NDSC Network for Detection of Stratospheric Change
NDVI Normalized Difference Vegetation Index
NESDIS National Environmental Satellite Data Information Service
NIST National Institute of Standards and Technology
NIXT Normal-Incidence X-ray Telescope
NLS Neptune longitudinal system
NOAA National Oceanic and Atmospheric Administration
NSO National Solar Observatory
NSSDC National Space Science Data Center

OLR outgoing longwave radiation

OSL Orbiting Solar Laboratory

OSSE Oriented Scintillation Spectrometer

Acronyms

PC	personal computer	SSM/I	Special Sensor Microwave/Imager
POCC	Payload Operations Control Center	SWADE	Sea Wave Dynamics Experiment
PSCs	polar stratospheric cloud particles		
<hr/>			
RAM	random-access memory	TAE	Transportable Applications Environment
RFI	radio frequency interference	TDRSS	Tracking and Data Relay Satellite System
ROM	read-only memory	TGSS	TONS ground support system
ROSAT	Roentgen Satellite	TOMS	Total Ozone Mapping Spectrometer
<hr/>			
SAMPEX	Solar, Anomalous, and Magnetospheric Particle Explorer	TONS	TDRSS Onboard Navigation System
SAS	Stow Away Specials	TRMM	Tropical Rainfall Measuring Mission
SCAN	Scheduling Concepts, Architecture, and Networks	TTL	Transistor-transistor logic
SCF	Science Computing Facility	TTW	Transportable Telemetry Workstation
SCHES	Satellite Communication Hardware Emulator System	<hr/>	
SDOC	Science Data Operation Center	UARS	Upper Atmosphere Research Satellite
SECS	Small Experiment Communications Satellite	UIT	Ultraviolet Imaging Telescope
SEDS	Small Explorer Data System	<hr/>	
SERTS	Solar EUV Rocket Telescope and Spectrograph	VAS	VISSR Atmospheric Sounder
SMMR	Scanning Multichannel Microwave Radiometer	VISSR	Visible Infrared Spin Scan Radiometer
SOHO	Solar and Heliospheric Observatory	VLBI	Very Long Baseline Interferometry
SSIS	Space Station Information Systems	VLSI	Very Large-Scale Integration-based
<hr/>			
		WTFF	Wide-band Transport Frame Formatter
<hr/>			
		XUVI	X-ray Ultraviolet Imager

Author Index

<i>Author</i>	<i>Page</i>	<i>Author</i>	<i>Page</i>
M. H. Acuña	23	Carol Dominy	173
John E. Allen Jr.	41	Robert E. Dominy	175
Troy J. Ames	200	Anne R. Douglass	47
James F. Andary	130	Jeff Dozier	103
George Anikis	107	Dean G. Duffy	82
Petar Arsenovic	121	Stephen G. Edwards	196
Steven A. Bailey	199	William M. Farrell	25
Daniel N. Baker	17	F. Ferguson	42
Toby Bennett	164	Carl E. Fichtel	97
Nancy W. Boggess	2	F. M. Flasar	26
Elihu Boldt	7	Thomas P. Flatley	144
Mike Bracken	192	Bobby J. Flowers	148
Dan Butler	145	Michael S. Fox-Rabinovitz	53
William J. Campbell	77	Max G. Gasser	133
Barbara E. Carlson	21	Anthony D. Del Genio	62
Patricia Carreon	157	Bruce M. Gentry	59
Donald J. Cavaliere	77	Daniel Y. Gezari	30
Alfred Chang	70	Per Gloersen	77
Benjamin Fong Chao	87	Robert Godfrey	179
Philip T. Chen	147	M. L. Goldstein	16
E. James Chern	122	Gerald J. Grebowsky	167
Ming-Dah Chou	67	Joseph M. Grebowsky	76
Shu-Hsien Chou	51	Brian D. Gross	53
Regina J. Cody	41	Isadore Harris	49
Josefino C. Comiso	77	Sara R. Heap	34
J. E. P. Connerney	23	Edward J. Hicks	144
B. J. Conrath	26	Stanley Hilinski	161
Thomas E. Correll	144	Paul M. N. Hintzen	9
Prabhakara Cuddapah	71	Walter R. Hoegy	76
John J. Degnan	84	Frank E. Hoge	75
Drake Deming	38	Brent Holben	57
Michael D. Desch	25	Ward Horner	161,169

Author Index

<i>Author</i>	<i>Page</i>	<i>Author</i>	<i>Page</i>
Peter M. Hughes	188	John Maruschak	138
Larry Hull	176	Roger A. Mattson	98
Stanley D. Hunter	97	Hans G. Mayr	13,49
James M. Jagielski	132	G. R. McConaughy	106
Michael F. Jasinski	90	Thomas J. McGee	65
Donald E. Jennings	38	Roy McIntosh	145
Harrison Jones	36	A. G. Michalitsianos	10
Robert Joyce	32	James A. Miller	12
Lou F. Kalil	190	Warner H. Miller	142
Ted Kaplan	179	Takamitsu Miyaji	7
Yoram Kaufman	57	Harry Montgomery	113,114
Kevin Kay	173	Carol Moralejo	41
Thomas Keating	116	David F. Nava	22
Richard Kelley	32	Jay P. Norris	96
Alex Klimas	17	J. A. Nuth	42
Donald A. Kniffen	95,96	John J. O'Brien	113
Chester J. Koblinsky	71	Gloria Oh	125
C. Laurence Korb	59	Ronald J. Oliversen	9
Randal Koster	93	Richard Olsen	149
Andrew A. Lacis	64	Jonathan F. Ormes	5,117
S. Yen Lee	123	Manfred Owe	80
L. Lilleht	42	Stephen J. Pagano	124
Catherine Long	138	Chung-Kyu Park	54
Kristin Looney	164	Claire L. Parkinson	77
Jeremiah H. Madden	103	Robert Patschke	138
G. M. Madejski	6	Walter A. Payne	22
Paul Mahaffy	29	W. Dean Pesnell	49
Harley Mann	191	Robert F. Pfaff, Jr.	19
Stephen P. Maran	1	James E. Phenix	109
Donald L. Margolies	110	B. R. Pincus	100
Daniel Mark	143	Charles E. Powers	125
Michael Martone	150	Michael Powers	138

Author Index

<i>Author</i>	<i>Page</i>	<i>Author</i>	<i>Page</i>
J. E. Pownell	100	Robert E. Streitmatter	5
Caleb M. Principe	168	Max Suarez	93
James A. Pritchard	189	John F. Sutton	140
H. K. Ramapriyan	106	T. D. Swanson	146
James L. Rash	185	Martha R. Szczur	194
J. J. Rast	100	Didier Tanré	57
Mary Reph	157	T. D. Taylor	106
Edward Robbins	151	Otto W. Thiele	69
D. Aaron Roberts	16,17	Ed Thomas	117
Richard B. Rood	47	Roger J. Thomas	39
Daniel Rosenfeld	69	Karen Thorn	195
Douglas Ross	141	Hendrik L. Tolman	82
William B. Rossow	60	Jeffrey W. Travis	137
Sasan S. Saatchi	89	T. Jane Turner	6
Stephen Sabia	161	J. Timothy Van Zant	122,127
Kenneth H. Schatten	13	Michael J. Viens	129
Siegfried Schubert	54	A. F. Vinas	16
Willi W. Schur	152	John M. Vranish	134,135
Ed Seidewitz	198	Perry Wagner	143
Jianfei Shi	169	Edward J. Walsh	71
David A. Short	69	A. L. Weir	26
Dannelle M. Shover	147	Yen F. Wong	185
Peter K. Shu	137	Terri L. Wood	178
Joel Simpson	152	Charles W. Wright	159
Craig G. Spaniol	140	Man-Li C. Wu	73
James Spinhirne	56	Pen-Shu Yeh	142
Louis J. Stief	22	H. Jay Zwally	77
Steven J. Stochaj	5		
Sharon A. Straka	147		

